



HAL
open science

Calorimetry and W mass measurement for future experiments

Marina Béguin

► **To cite this version:**

Marina Béguin. Calorimetry and W mass measurement for future experiments. High Energy Physics - Experiment [hep-ex]. Université Paris Saclay (COmUE), 2019. English. NNT : 2019SACLS393 . tel-02490574

HAL Id: tel-02490574

<https://theses.hal.science/tel-02490574>

Submitted on 25 Feb 2020

HAL is a multi-disciplinary open access archive for the deposit and dissemination of scientific research documents, whether they are published or not. The documents may come from teaching and research institutions in France or abroad, or from public or private research centers.

L'archive ouverte pluridisciplinaire **HAL**, est destinée au dépôt et à la diffusion de documents scientifiques de niveau recherche, publiés ou non, émanant des établissements d'enseignement et de recherche français ou étrangers, des laboratoires publics ou privés.

Calorimetry and W mass measurement for future experiments

Thèse de doctorat de l'Université Paris-Saclay
préparée à l'Université Paris-Sud

Ecole doctorale n°576 Particules, Hadrons, Énergie, Noyau, Instrumentation,
Imagerie, Cosmos et Simulation (PHENIICS)
Spécialité de doctorat: Physique des Particules

Thèse présentée et soutenue à l'Orme-des-Merisiers, le 10 décembre 2019, par

MARINA BÉGUIN

Composition du Jury :

| | |
|--|-----------------------|
| Maarten Boonekamp Directeur de Recherche, CEA Saclay | Président |
| Alain Blondel Professeur des Universités, Université de Genève | Rapporteur |
| Sylvie Braibant-Giacomelli Professeur des Universités, Dipartimento di Fisica e Astronomia, Bologna | Rapporteur |
| Sjöstrand Torbjörn Professeur des Universités, Department of Astronomy and Theoretical Physics, Lund | Examineur |
| Patrick Janot Directeur de Recherche, CERN (EP) | Co-directeur de thèse |
| Elizabeth Locci Directeur de Recherche, CEA Saclay | Directrice de thèse |
| Luca Malgeri Directeur de Recherche, CERN (EP) | Co-directeur de thèse |

*A great discovery does not issue from
a scientists brain ready-made, like
Minerva springing fully armed from
Jupiter's head; it is the fruit of an
accumulation of preliminary work.*
Maria Skłodowska-Curie

A ma famille

Acknowledgements

This report, even if written by a single person, is the result of continued interactions, discussions, debates and interrogations that took place over the three last years, whether during meetings or through informal conversations. The results presented in this paper were obtained thanks to the support, the encouragements and the help of many fantastic people who joined me through the journey of this PhD. Each of them significantly contributed to my professional and personal development.

Consequently, similarly to large scientific collaborations, I have chosen to name the people who took part, in one way or an other, to this great adventure. Before going into the details, I would like to thank CERN, CEA-Saclay and Université Paris-Sud for giving me the opportunity to complete this research project. I would like to address my warmest thanks to CERN for its hospitality during these three years as well as for funding this project through my selection for the Doctoral Student Program.

Patrick Janot¹, Elizabeth Locci^{1,2}, Luca Malgeri¹,

Paolo Azzurri^{3,7,8,33}, Quentin Barrand^{4,13}, Florian Beaudette⁵, Colin Bernet⁶,
 Alain Blondel^{7,8,9,33}, Maarten Boonekamp³³, Subhadip Bouri¹⁰, Sylvie Braibant-Giacomelli^{9,33},
 Rene Brun¹¹, Katarzyna Dyga-Krajewska¹², Famille Barrand^{13,14}, Famille Béguin^{13,15},
 Francesco Fiori¹⁶, Antonio Gonzalez Puertas¹⁷, Ilya Gorbunov^{18,19}, Clement Helsens²⁰,
 Jan Kieseler^{19,21}, Adam Krajewski¹², Sofiane Lablack^{10,22}, Clemens Lange^{19,23,24}, Anna Lipiec¹²,
 Jenny List²⁵, Artur Lobanov⁵, Carlos Lourenco²⁶, Arabella Martelli¹⁹, Predrag Milenovic^{19,23},
 Lorenzo Moneta¹¹, Hubert Odziemczyk¹², Martine Oger²⁷, Felice Pantaleo¹⁹, Marco Rovere^{19,28},
 Jean-Baptiste Sauvan^{5,29}, Felix Sefkow³⁰, Pedro Vieira De Castro Ferreira Da Silva^{19,31},
 Torbjörn Sjöstrand^{32,33}, Adam Sosnowski¹², Roberto Tenchini^{7,8}, Georges Vasseur²⁷,
 Valentin Volkl²⁰, and al.³⁴

¹ I wish to express my deep gratitude to the three of you for giving me the chance to become a scientist in this exciting field of research. I really enjoyed working on this multi-faceted subject from which I learned a lot and in which I developed significantly. Thank you for sharing your deep knowledge with me, for your kindness, your help and your continued support. I am also very thankful for offering me to present my results at several worldwide conferences.

² Special thanks goes to Elizabeth who has been a precious and untiring advisor, from my very first day at CERN as Master's student until the very end of this thesis. You were an excellent supervisor who offered assistance, provided encouragements, relevant advices and guidance. You initiated me to the challenging environment of research and thesis, and I will always be grateful for that. Thank you for your continued availability and your understanding when receiving last-minute texts to proofread over the last weeks.

³ It was a real pleasure to work with you on the FCC-ee project. Many thanks for our enlightening discussions, your relevant suggestions and your help on the W mass measurement. Grazie mille, spero che avremo ancora l'opportunità di lavorare insieme.

-
- ⁴ Merci à toi Quentin, pour ton soutien quotidien indéfectible. Merci de m'avoir encouragé dans les moments difficiles et remotivée lors des grosses baisses de moral. Merci aussi pour ton aide en informatique. Je pense que sans toi certains programmes seraient toujours en train de tourner.
- ⁵ Your help on the HGCal Fast simulation was precious. Thank you for providing me the first version of this software and for your time when answering my numerous questions.
- ⁶ Merci pour le logiciel HEPPY, indispensable à mon étude de la masse du boson W à FCC-ee. Un grand merci également pour toutes les explications portant sur son utilisation et son fonctionnement.
- ⁷ Thanks a lot for offering me to present at several conferences abroad. Even though I was always very stressed, I really enjoyed communicating about my work, my results and my conclusions.
- ⁸ Many thanks for your interest and your feedbacks during the WG working group meetings.
- ⁹ Thank you for agreeing to review this manuscript as referee.
- ¹⁰ I would like to thank the Master students I supervised, for bringing a great atmosphere during my last months as PhD candidate. I specially thanks them for their patience with my limited experience as a supervisor.
- ¹¹ Many thanks for providing a precious help with the ROOT framework, the keystone of Physics research.
- ¹² Warm thanks to the Polish friends I met at CERN. All our week-ends, dinners and parties cruelly missed me during the last months of this project, and I am looking forward to seeing you more often. My Polish is not good enough to express all my gratitude, but *dziękuję bardzo, moi przyjaciele*.
- ¹³ On ne peut jamais remercier assez sa famille. Vos encouragements m'ont été d'un grand réconfort et ont sans aucun doute contribué à l'aboutissement de ce travail.
- ¹⁴ Un chaleureux merci pour votre soutien, votre affection, vos encouragements et tout l'intérêt que vous avez porté à mon travail. A bientôt à Nantes !
- ¹⁵ Je voudrais remercier ceux avec qui tout a commencé. Mes profonds remerciements vont à mes parents, mon frère et ma soeur pour leur soutien inconditionnel. Merci à toi Papa, et à toi Maman, de m'avoir toujours soutenu, encouragé et aidé tout au long de mon cursus. Merci d'avoir su me donner toutes les chances pour réussir; voyez en ce travail l'aboutissement de tous vos efforts. Merci pour votre investissement à essayer de comprendre la physique des particules ainsi que les tenants et les aboutissants de mon travail. Merci enfin à Camille et Axelle pour leur temps, celui que je n'ai pas passé à leurs côtés et que j'ai sacrifié au profit d'études loin de la maison. Je vous souhaite autant de réussite que moi dans votre vie personnelle et professionnelle.
- ¹⁶ Un vero amico che ho incontrato durante la mia prima esperienza al CERN in 2015. Mi hai fatto conoscere la fisica delle particelle, non lo dimenticherò mai. Grazie infinitamente. Hai ancora la mia e-mail per un caffè !

- ¹⁷ A huge thank you for the visit in the LHC tunnel - I will never forget the chance that I had to go as close as possible to this wonderful machine. Thank you for your exceptional kindness and good luck for your Master's studies. ¡Muchas gracias por el paseo en bicicleta!
- ¹⁸ Thanks for accepting to implement the HGCal fast simulation software into the general CMS software.
- ¹⁹ Thanks to all the members of the CMG group and more particularly the perf/sim group for their feedback during the weekly meeting. Thanks to all the very interesting presentations in these meetings, I gained great insights into various aspects of High Energy Physics.
- ²⁰ A huge thank you for your help in the use of PYTHIA within the FCC software. My study of the systematic uncertainty on the W mass due to FSI would not have been possible without your help.
- ²¹ Thank you for all your precious explanations on Machine Learning techniques and for taking the time to answer my questions.
- ²² Merci d'avoir continué mon travail sur la masse du W à FCC-ee et pour les résultats de l'étude de la contamination du background.
- ²³ You are the first scientists with whom I interacted at the very beginning of this PhD, three years ago. I would like to thank both of you for your warm welcome.
- ²⁴ Thanks you for the precious help on HTCondor and your perpetual availability. It was a real pleasure to work with you.
- ²⁵ Many thanks for your help on the ISR treatment in the kinematic fit; it significantly improved my results.
- ²⁶ I could always count on my exceptional officemate. Thank you Carlos for enlightening my working days with your good mood. Thank you for your friendliness, our pleasant coffee breaks and for all the interesting discussions we had, on both Particle Physics and unrelated topics. Those three years were unfortunately insufficient to improve my Portuguese, but muito obrigado por ser um ótimo colega. Pense em beber quando eu for embora !
- ²⁷ Une thèse, c'est aussi beaucoup de procédures administratives, un phénomène amplifié lorsque l'on appartient à plusieurs laboratoires. Un grand merci pour votre disponibilité et votre aide en ce qui concerne les documents du CEA.
- ²⁸ Thank you for dedicating your study of the jet resolution implementation in the updated version of the CMS software to me, and for your availability to answer my questions.
- ²⁹ Thank you for the review of the full implementation and validation of the HGCal fast simulation.
- ³⁰ Thanks for your help with the tricky modelling of the hadronic shower profile in the HGCal fast simulation.
- ³¹ I would also like to thank you for your patience and your availability. I really enjoyed working on the recoil reconstruction and that would not have been possible without your help.

³² Thank you for your help with PYTHIA and for the quick correction of its source code, which made my study of the systematic uncertainty on the W mass introduced by the FSI possible.

³³ Thank you for accepting to join the examining committee.

³⁴ Last but not least, I would like to thank all the friends, physicist or not, that I have met all along this PhD, at CERN, at the ICFA Summer School or during conferences. I also thank the CMS guides, with whom I enjoyed discussing Particle Physics every Saturday as well as the visitors I guided, for their numerous and interesting questions.

Finally, I would like to apologise to anybody that contributed to this work and that I forgot to name in this section. May they be thanked.

General introduction

The description of the electromagnetic and weak interactions in a single unified model was proposed by Glashow, Weinberg and Salam [1] in the 1960s, predicting that the electromagnetic and weak forces are different manifestations of the same force, the electroweak source, into which they would merge above a given energy threshold. The model postulated the existence of two charged and one neutral weak bosons. This latter raised the issue of neutral currents, for which there was no experimental evidence. The first experimental evidence of the electroweak theory was obtained in 1973 with the observation of neutrino interactions suggesting the presence of weak neutral current [2]. This discovery provided a first measurement of the weak mixing angle, θ_W , and allowed, despite a large experimental uncertainty, a first quantitative prediction of the weak bosons masses ; from 60 to 80 GeV for the W boson and from 75 to 92 GeV for the Z boson. The Large Electron Positron (LEP) collider was not even a project and the mass ranges were inaccessible at that time. Therefore, Rubbia, Cline and Mc Intyre proposed to transform the Super Proton Synchrotron (SPS) into a proton-antiproton collider to reach the unprecedented energy level of 540 GeV, required for the production of such heavy particles. In January 1983, the European Organisation for Nuclear Research (CERN) scientists announced the discovery of the W boson to the world after the observation of six and four W events by the UA1 and UA2 Collaborations respectively [3, 4]. Despite a few number of events, UA1 and UA2 measured the W mass with a precision of about 5 GeV/c². A few months later the Z boson was discovered. The observation of these two weak bosons brought a masterpiece to the electroweak theory.

The study of production and decay of the Z boson was a critical test of the Standard Model. For that purpose, the LEP collider, still the largest ever built, was designed and put into operation in 1989. In 1995 LEP was upgraded to reach the energy at which W bosons could be pair-produced. The collider's energy eventually reached 209 GeV in 2000. By combining the measurements of the four LEP experiments (ALEPH, DELPHI, L3, OPAL), the W mass was then measured with a precision of 33 MeV/c² (roughly 50 MeV/c² per experiment) [5].

In 1984, the Tevatron started colliding protons and antiprotons at a centre-of-mass energy of 800 GeV and ultimately reached 1.8 TeV in 1986. The W mass was measured by the two experiments, CDF [6] and D0 [7], with a precision of roughly 20 MeV/c², leading to a combined measurement with a 16 MeV/c² uncertainty (15 MeV/c² when combined with LEP).

The construction of the Large Hadron Collider (LHC) started immediately after the dismantlement of the LEP, in the tunnel of which it was installed. Contrarily to the SPS collider and the Tevatron, the LHC, entered in operation in 2009, collides protons. After an initial period at 2.4 TeV, it reached the centre-of-mass energy of 7 TeV, then 8 and 13 TeV with a high luminosity. A Toroidal LHC ApparatuS (ATLAS), one of the two general purpose experiments has published

a measurement of the W mass with an uncertainty of $19 \text{ MeV}/c^2$ [8]. The combination with the W mass measured by the other general experiment, Compact Muon Solenoid (CMS), should yield an accuracy comparable to or better than that of the Tevatron.

Figure 1 summarises all these results since the LEP measurements.

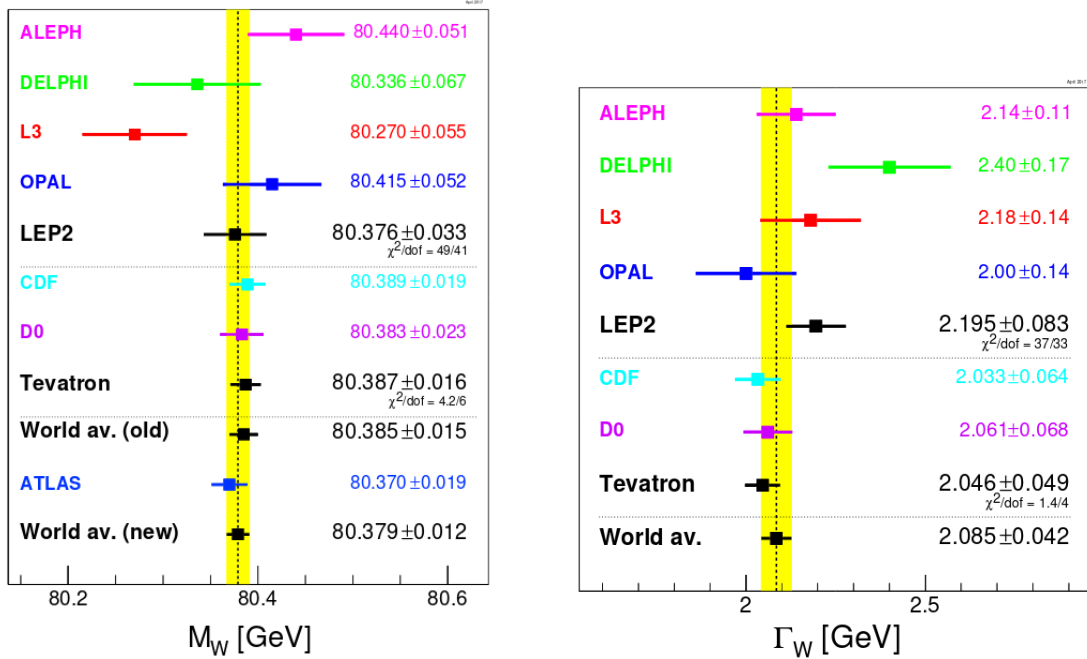


Figure 1 – Measurements of the W mass and width by the LEP, Tevatron and LHC experiments [9].

The W mass measurement is now largely dominated by both experimental and theoretical systematic uncertainties and efforts are going on to ultimately bring both of them below $1 \text{ MeV}/c^2$.

An intermediate step towards such accuracy is the upgrade of the LHC into a most powerful machine, the High Luminosity-LHC (HL-LHC). Expected to start in 2026, it will operate at a higher luminosity, increasing the volume of data by a factor ten for each experiment. Such a high statistics will allow several ancillary measurements necessary to reduce the experimental uncertainties and to improve the parametric inputs to the theoretical predictions in order to refine the knowledge of the W mass and other parameters of the Standard Model. The full exploitation of the LHC is the first priority for the European Strategy but the future of particle physics is also under consideration and the Strategy called for an ambitious post-LHC accelerator complex at CERN. Among the various possibilities to increase the precision of measurements done at LHC, a future circular electron-positron collider (FCC-ee), first step towards a 100 TeV hadron collider, offers the best potential to deliver a huge number of W bosons. With more than 2×10^8 W pairs produced at the WW threshold and above (6×10^7 pairs at 161 GeV), FCC-ee will be a W factory that would be adequate to reach such a level of accuracy.

The precise measurement of the W mass will be discussed in the context of two future experiments: i) the CMS-detector upgrade with the high-granularity endcap calorimeter to be installed for the HL-LHC and ii) a detector for the FCC-ee project.

This document is organised in three parts. The first four chapters give the context of the W mass measurement in this study. Chapter 1 provides an introduction to the Standard Model of Particle Physics and highlights the importance of a precise measurement of the W mass for both Standard Model consistency and new physics discovery. Chapter 2 is completely focused on the W boson production and decay mechanisms in hadron and lepton collisions. It also describes the different methods to measure the W mass in each decay mode. Chapter 3 briefly presents the experimental facilities: the LHC and HL-LHC colliders and the CMS experiment as well as the Future Circular Collider (FCC) project and the CLIC-like detector (CLD). In Chapter 4, the simulation and reconstruction software used to generate data in these analyses are presented.

The second part discusses the W mass precision expected at the HL-LHC. The W mass is reconstructed only from the $W \rightarrow l\nu_l$ decays. The recoil, computed from all reconstructed particles in the event but the lepton, is a key component in the accurate W mass measurement. Its reconstruction is challenging and its resolution depends on: the definition model, the detector effects and the particle-flow (PF) algorithm used for the reconstruction. Assuming a perfect reconstruction of the PF candidates, Chapter 6 evaluates the effect of the High-Granularity Calorimeter (HGCal) parameters on the recoil reconstruction, improved with machine learning techniques, and gives an estimation of the precision expected on the W mass measurement at CMS with respect to the present measurement at LHC. Before evaluating the effect of the detector performance on the recoil, the full geometry and parameters had to be tuned in order to achieve the best particle reconstruction required by different physics benchmarks. In Chapter 5 the implementation of a fast simulation tool of the HGCal, developed to undertake this kind of study as a complement to the full simulation and reconstruction framework of the CMS detector, is described.

The last part discusses the W mass precision expected at the FCC-ee. In this study, the mass of the W boson was measured with the direct reconstruction method in the semi-leptonic and hadronic decay channels. Several kinematic procedures were employed to get the best statistical precision on the W mass. At the FCC-ee quite a few running scenarios are planned and extremely large samples of W -pairs will be collected both near the threshold centre-of-mass energy ($\sqrt{s} \sim 2M_W$) and at larger energies, up to $\sqrt{s} = 365$ GeV. The kinematic reconstruction of the W -pair events with FCC-ee data in both decay channels and for all energies in the centre-of-mass are presented in Chapter 7. With precisions below the MeV level, the measurements will be most likely limited by the systematic uncertainties. The most important source of uncertainty expected at the FCC-ee is due to Quantum Chromodynamic (QCD) effects occurring in the fragmentation process of the hadronic decay channel. The contribution of this source of uncertainty and the treatment to reduce its impact on W mass precision is discussed in Chapter 8.

Contents

| | |
|--|-----------|
| Acknowledgements | i |
| General introduction | v |
| List of Figures | xiii |
| List of Tables | xvii |
| Acronyms | xix |
| 1 Theoretical framework | 1 |
| 1.1 The Standard Model | 2 |
| 1.1.1 Matter and interactions | 2 |
| 1.1.2 The Lagrangians of the Standard Model | 3 |
| 1.1.2.1 The electromagnetic interaction | 3 |
| 1.1.2.2 The electroweak interaction | 4 |
| 1.1.2.3 The strong interaction | 5 |
| 1.1.2.4 Spontaneous symmetry breaking | 6 |
| 1.1.2.5 Free parameters of the Standard Model | 7 |
| 1.2 A precise measurement of the W mass as a probe of the Standard Model | 7 |
| 2 W boson production and decay | 11 |
| 2.1 Hadron colliders | 12 |
| 2.2 Lepton colliders | 15 |
| 2.2.1 On-shell W-pair production | 16 |
| 2.2.2 Off-shell W-pair production | 17 |
| 2.2.3 Corrections to lowest order W-pair cross-section and decay | 18 |
| 2.2.3.1 Pure QED corrections | 19 |
| 2.2.3.1.1 Initial State Radiation (ISR) | 19 |
| 2.2.3.1.2 Coulomb correction | 20 |
| 2.2.3.1.3 Intermediate and Final State Radiation (WSR and FSR) | 20 |
| 2.2.3.1.4 Non-factorisable virtual corrections | 21 |
| 2.2.3.2 QCD corrections | 21 |
| 2.2.3.3 Final State Interactions (FSI) | 21 |
| 2.2.3.3.1 Colour Reconnection | 21 |
| 2.2.3.3.2 Bose-Einstein Correlation | 22 |
| 2.3 Comparison of W production at hadron and lepton colliders | 22 |

| | | |
|-----------|---|-----------|
| 2.3.1 | Mass and width from direct reconstruction | 23 |
| 2.3.1.1 | Hadron collisions | 23 |
| 2.3.1.2 | Lepton collisions | 24 |
| 2.3.2 | Mass and width from cross-section at threshold | 26 |
| 3 | Current and future CERN experiments | 29 |
| 3.1 | The LHC and HL-LHC | 30 |
| 3.1.1 | The machines | 30 |
| 3.1.2 | The CMS detector | 33 |
| 3.1.2.1 | Structure | 33 |
| 3.1.2.2 | HL-LHC upgrades | 36 |
| 3.1.2.3 | The High-Granularity Calorimeter | 36 |
| 3.2 | The Future Circular Collider project: FCC | 39 |
| 3.2.1 | Overview of the project | 39 |
| 3.2.2 | The FCC-ee machine | 42 |
| 3.2.3 | The CLD | 44 |
| 4 | Events simulation and reconstruction | 47 |
| 4.1 | LHC and HL-LHC | 48 |
| 4.1.1 | CMSSW | 48 |
| 4.1.1.1 | Event simulation | 48 |
| 4.1.1.2 | CMS event reconstruction at LHC | 49 |
| 4.1.1.3 | CMS event reconstruction at HL-LHC | 50 |
| 4.1.1.3.1 | Event reconstruction | 50 |
| 4.1.1.3.2 | Performance of the physics objects reconstruction | 51 |
| 4.1.2 | Delphes | 52 |
| 4.2 | FCC-ee | 54 |
| 4.2.1 | Event simulation | 54 |
| 4.2.1.1 | Generator step | 54 |
| 4.2.1.2 | Detector step | 56 |
| 4.2.1.2.1 | Detector implementation | 56 |
| 4.2.1.2.2 | Particle interactions in the detector | 58 |
| 4.2.2 | Event reconstruction | 60 |
| 5 | A fast simulation for the CMS HGCal Upgrade | 65 |
| 5.1 | Geometry implementation | 66 |
| 5.1.1 | Geometry model | 66 |
| 5.1.2 | Geometry in FastSim | 67 |
| 5.2 | Particle interactions through the detector | 69 |
| 5.2.1 | Parametrisation of the electromagnetic and hadronic showers | 69 |
| 5.2.1.1 | Longitudinal profile | 69 |
| 5.2.1.1.1 | Electromagnetic showers | 69 |
| 5.2.1.1.2 | Hadronic showers | 70 |
| 5.2.1.2 | Transverse profile | 70 |
| 5.2.1.2.1 | Electromagnetic showers | 70 |
| 5.2.1.2.2 | Hadronic showers | 71 |
| 5.2.2 | Hits generation | 74 |

| | | |
|----------|---|------------|
| 5.3 | A very fast simulation | 75 |
| 5.4 | Software validation | 77 |
| 6 | W mass measurement at the HL-LHC with CMS | 83 |
| 6.1 | Recoil definitions | 84 |
| 6.1.1 | Traditional definitions | 84 |
| 6.1.2 | Recoil resolution | 85 |
| 6.1.3 | Improvement of the recoil definition | 86 |
| 6.1.3.1 | Principle | 87 |
| 6.1.3.2 | Regression targets | 88 |
| 6.1.3.3 | Quantile regression | 90 |
| 6.1.3.4 | Corrections | 91 |
| 6.2 | Recoil study | 91 |
| 6.2.1 | Input variables | 91 |
| 6.2.2 | Comparison of the estimators | 94 |
| 6.3 | Effect of the HGCal parameters on the W mass | 96 |
| 7 | W mass measurement at FCC-ee | 101 |
| 7.1 | Kinematic reconstruction methods | 102 |
| 7.1.1 | Kinematic rescaling | 102 |
| 7.1.2 | Kinematic fit | 103 |
| 7.1.2.1 | Principle | 103 |
| 7.1.2.2 | Object parametrization | 106 |
| 7.1.2.3 | Correlation matrix | 107 |
| 7.1.2.4 | Constraints | 109 |
| 7.1.2.5 | Fit goodness | 110 |
| 7.1.2.6 | Analogy between the kinematic fit and the kinematic rescaling . . . | 112 |
| 7.2 | Principle of the statistical uncertainty evaluation | 112 |
| 7.3 | Hadronic channel | 115 |
| 7.3.1 | Jets pairing | 115 |
| 7.3.2 | ISR and beamstrahlung treatment | 116 |
| 7.3.2.1 | Photon parametrization | 118 |
| 7.3.2.2 | ISR treatment evaluation | 118 |
| 7.3.3 | Mass and width extraction | 119 |
| 7.4 | Semi leptonic channel | 120 |
| 7.4.1 | Mass and width extraction | 121 |
| 7.5 | Discussions | 123 |
| 8 | Study of the Final State Interactions effect | 127 |
| 8.1 | Monte Carlo models | 128 |
| 8.1.1 | Colour Reconnection | 129 |
| 8.1.2 | Bose-Einstein Correlation | 129 |
| 8.2 | Effect on M_W | 130 |
| 8.2.1 | Systematic uncertainty | 130 |
| 8.2.2 | Effect on the statistical uncertainty | 132 |
| 8.3 | Treatment using a cone analysis | 132 |
| 8.3.1 | Cone reconstruction | 133 |

| | | |
|---|--|------------|
| 8.3.2 | Effect of the cone on M_W and on the statistical uncertainty | 134 |
| 8.3.3 | Final State Interactions effect on the W mass with a cone | 134 |
| Conclusion and perspectives | | 137 |
| Bibliography | | 139 |
| Appendix A Complements to the HGCal fast simulation | | 149 |
| A.1 | HGCal layers implementation in the fast simulation | 149 |
| A.2 | Fit of the hadronic radial shower profile of 40 GeV pions in the HGCal | 149 |
| Appendix B Complements to the W mass measurement at FCC-ee | | 153 |
| B.1 | Relation between the FOM and the W mass statistical uncertainty | 153 |
| B.2 | Kinematic fit procedure | 155 |
| B.3 | Off-diagonal terms covariance matrix | 157 |
| B.4 | Comparison before/after cut in probability | 158 |
| Appendix C Résumé en français | | 159 |

List of Figures

| | | |
|------|--|----|
| 1 | Measurements of the W mass and width by the LEP, Tevatron and LHC experiments [9]. | vi |
| 1.1 | The particles of the Standard Model | 3 |
| 1.2 | Feynman diagrams of radiative corrections of the W boson propagator | 8 |
| 1.3 | 68% and 95% confidence level prediction of M_W as a function of m_{top} obtained from electroweak fit, including (blue region) and excluding (grey region) the Higgs boson mass, and compared to the direct measurement (vertical and horizontal green bands) [10] | 8 |
| 2.1 | Leading-order production mechanism of the W boson in hadron colliders [11] | 12 |
| 2.2 | Contributions of the different quark flavours to the W production at the Tevatron (left) and LHC (right) [12] | 13 |
| 2.3 | First-order QCD-correction contributions to the W boson [13] | 13 |
| 2.4 | Cross-section for different processes in hadron colliders as a function of centre-of-mass energy [14] | 14 |
| 2.5 | Differential cross-sections as a function of p_T^W for W^+ and W^- production initiated with different parton flavours and evaluated with CuTe at NLO+NNLL (next-to-next-to-leading logarithmic) [15] | 15 |
| 2.6 | Decay of the W boson in fermion-antifermion pair | 15 |
| 2.7 | W pair production in e^+e^- collisions | 16 |
| 2.8 | W-pair decay into four-fermion final states (CC03 diagrams) | 17 |
| 2.9 | Example of four-fermions states which are not produced through the W-pair decay . | 18 |
| 2.10 | Electroweak radiative corrections [16] | 19 |
| 2.11 | Photon emissions in Coulomb correction [17] | 20 |
| 2.12 | Cross-section for different processes in lepton colliders as a function of the centre-of-mass energy [18] | 23 |
| 2.13 | Transverse mass distribution for the events $W \rightarrow e\nu$ at ATLAS [19] | 25 |
| 2.14 | Dependence of the W pair-production cross-section on W mass (2.14a) and width (2.14b) as a function of the centre-of-mass energy in the threshold region | 26 |
| 3.1 | CERN's accelerator complex | 31 |
| 3.2 | Schematic representation of the CMS detector structure in Run II [20] | 34 |
| 3.3 | Expected radiation dose over the current calorimetry of the CMS detector in HL-LHC conditions [21] | 37 |
| 3.4 | Longitudinal upper half structure of one of the endcap calorimeters. The electromagnetic part (CE-E) is the closest to the interaction point, followed by the hadronic part (CE-H) | 37 |

| | | |
|------|---|----|
| 3.5 | Layout of a full silicon (left) and hybrid silicon-scintillator (right) layers of the HGCal detector | 38 |
| 3.6 | Schematic view of the 100 km Future Circular Collider in the Geneva area [22] | 40 |
| 3.7 | Schematic implementation of the FCC-ee (left) and FCC-hh (right) infrastructures and a zoom on the particle trajectories in the G interaction point region at FCC-ee (middle of the left layout) [22] | 41 |
| 3.8 | FCC integrated project technical schedule [22] | 42 |
| 3.9 | Luminosity as function of the centre-of-mass energy for FCC-ee summed over two interaction points, compared to the estimated luminosities of the other e^+e^- collider projects [23] | 43 |
| 3.10 | Longitudinal top right quadrant view of the CLD detector concept [24] | 44 |
| 3.11 | Transverse momentum resolution of the tracker for single muons as a function of the momentum at a fixed polar angle [24] | 45 |
| 4.1 | Jet resolution as function of p_T obtained for different models of the charged hadrons momentum | 52 |
| 4.2 | Jet resolution as a function of p_T for different η values and computed for different models of the charged hadrons momentum | 53 |
| 4.3 | Comparison of the lepton (left) and recoil (right) p_T , η and ϕ reconstructed using CMSSW and DELPHES | 55 |
| 4.4 | Interaction of a $ee \rightarrow WW \rightarrow q\bar{q}q\bar{q}$ event, generated at $\sqrt{s} = 240$ GeV with PYTHIA, through the CLD detector using the PAPAS simulation | 57 |
| 4.5 | Comparison of the lepton energy before an after FSR association | 60 |
| 4.6 | Jet resolution of CLD simulated with HEPPY | 61 |
| 4.7 | Reconstruction of the jet energy and theta angle by the CLD detector simulated with HEPPY | 62 |
| 4.8 | Reconstruction of the missing energy with the CLD detector simulated with HEPPY | 63 |
| 5.1 | Hexagon and square cells telling as implemented in the FastSim | 68 |
| 5.2 | Electromagnetic longitudinal shower profile of 50 GeV electrons in the HGCal, generated with CMSSW | 70 |
| 5.3 | Hadronic longitudinal shower profile of 100 GeV pions in the HGCal, generated with CMSSW | 71 |
| 5.4 | Radius, ρ , containing 68% and 90% of the energy deposited in a silicon layer (EE) as a function of layers | 72 |
| 5.5 | Fit of the radial profile of a shower initiated by 100 GeV pions in the HGCal | 72 |
| 5.6 | Radius, ρ , containing 68% and 95% of the energy deposited by the hadronic shower in the HGCal | 73 |
| 5.7 | Energy fluctuations of 100 GeV pions in the HGCal | 74 |
| 5.8 | Principle of the Quadtree data structure applied on the hexagon geometry in the fast simulation | 76 |
| 5.9 | Wrong hit and cell distribution within Quadtree leaves | 77 |
| 5.10 | Comparison of the distributions from the fast simulation to CMSSW results for 50 GeV electrons | 79 |
| 5.11 | Comparison of the distributions from the fast simulation to CMSSW results for 50 GeV photons | 80 |

| | | |
|------|---|-----|
| 5.12 | Comparison of the distributions from the fast simulation to CMSSW results for 100 GeV pions | 81 |
| 6.1 | Resolution of the transverse momentum of the recoil from Z events as function of the number of vertices for particle-flow and track recoil definitions for simulated data and data samples [25] | 85 |
| 6.2 | Distribution of the track recoil resolution of $W \rightarrow l\nu$ events represented in two reference frames | 86 |
| 6.3 | Recoil resolution of $W \rightarrow l\nu$ events estimated with $ \Delta\vec{h} $ and reconstructed with track and particle-flow recoil definitions | 87 |
| 6.4 | Scheme of a deep dense neural network | 88 |
| 6.5 | Definition of the magnitude and azimuthal angle correction coefficients, $e_{1,2}$ | 89 |
| 6.6 | Recoil correction coefficient distributions using the track definition | 89 |
| 6.7 | Evolution of the loss function of the quantile regression of the recoil components as a function of Epoch | 91 |
| 6.8 | Correction of the track-based recoil using multivariate quantile regression | 94 |
| 6.9 | Recoil scale and direction at 13 TeV at CMS for the Phase II reconstructed from a multivariate quantile regression using different estimators | 95 |
| 6.10 | Event-by-event resolution and bias variation as a function of the recoil scale reconstructed with different models without PU (left) and with 200 PU (right) | 96 |
| 6.11 | Event-by-event resolution and bias variation as a function of the recoil direction reconstructed with different models without PU (left) and with 200 PU (right) | 97 |
| 6.12 | Energy resolution as a function of energy from a standalone simulation of incident electrons on an HGCAL [21] | 98 |
| 6.13 | Effect of the HGCAL parameters on the recoil scale at 0 PU (left) and 200 PU (right) | 98 |
| 6.14 | Average bias and resolution for the estimated recoil scale (left) and direction (right) on an event-by-event basis | 99 |
| 7.1 | Double-sided Crystal-Ball fit of the parameters distributions to determine the diagonal terms of the covariance matrix of the kinematic fit in the hadronic channel at $\sqrt{s} = 162.6$ GeV | 108 |
| 7.2 | Distribution of the χ^2 probability of the 4C kinematic fit at $\sqrt{s} = 162.6$ GeV | 110 |
| 7.3 | Pull distributions of the parameters of the 4C kinematic fit at $\sqrt{s} = 162.6$ GeV in the hadronic channel, fitted with a Gaussian distribution | 111 |
| 7.4 | Analogy between the kinematic rescaling and kinematic fit (4C) methods for the W masses reconstruction | 113 |
| 7.5 | W mass reconstructions for extreme templates ($M_W = 80.385 \pm 1$ GeV/ c^2) | 113 |
| 7.6 | Distribution of the W mass for good and wrongly-paired jets at various energies | 117 |
| 7.7 | Kinematic fit probability distribution for good and bad jets pairings at 162.6 GeV | 118 |
| 7.8 | Fitted radiated photon energy compared to the MC simulated one for different centre-of-mass energies | 119 |
| 7.9 | Effect ISR treatment at 365 GeV | 120 |
| 7.10 | Invariant mass distributions of the smaller (left) and the larger (right) di-jet mass of the hadronic decay channel for different centre-of-mass energies and different reconstruction techniques | 122 |

| | | |
|------|--|-----|
| 7.11 | Invariant mass distributions of the W mass for the W leptonic decays (left) and for the W hadronic decays (right) in the semi-leptonic decay channel for different centre-of-mass energies and different reconstruction techniques | 124 |
| 8.1 | M_W shift due to CR effect, modelled using the SKI scenario ($k_I = 0.6$) at 240 GeV . | 131 |
| 8.2 | Effect of a cone (R=0.4 rad) on the reconstructed mass at different energies | 135 |
| A.1 | Fit of the radial profile of a shower initiated by 40 GeV pions in the HGCal. | 149 |
| B.1 | Full flowchart of the kinematic fit procedure as used in the current study of W mass reconstruction at FCC-ee. | 155 |
| B.2 | Off-diagonal terms of the covariance matrix of the kinematic fit ($\sqrt{s} = 162.6$ GeV) . | 157 |
| B.3 | Comparison pull before and after cut | 158 |
| B.4 | Comparison W mass distributions reconstructed with the kinematic fit 4C (top figures) and 5C (bottom figure), adding or not the cut in fit probability ($P < 0.03$) at $\sqrt{s} = 365$ GeV | 158 |
| C.1 | Coupe longitudinale (partie haute) de l'un des deux HGCal. La partie électromagnétique (CE-E), la plus proche du point d'interaction, est suivie de la partie hadronique (CE-H) | 161 |
| C.2 | Comparaison des distributions obtenues avec la FastSim et la FullSim pour des pions générés à 100 GeV | 164 |
| C.3 | Corrections du recul défini à partir des traces en utilisant la régression quantile multivariée | 166 |
| C.4 | Masse invariante de la plus petite des masses du canal hadronique (gauche) ainsi que la masse leptonique (droite) du canal semi-leptonique reconstruites à 240 GeV en utilisant les différents estimateurs. | 169 |

List of Tables

| | | |
|-----|--|-----|
| 3.1 | Properties of the active material for full silicon layers [21] | 38 |
| 3.2 | Properties of the active material for hybrid layers, with both silicon and scintillators [21] | 39 |
| 3.3 | Run plan for FCC-ee operations in the configuration of two interaction points | 43 |
| 4.1 | Parameters of the transverse momentum parametrization (Eq. 4.6) in PAPANAS | 58 |
| 4.2 | Main characteristics of CLD detector as implemented in PAPANAS | 59 |
| 5.1 | HGCal parameters differences between the current geometry and the model used in the fast simulation (2016 geometry frozen for the TDR studies) | 67 |
| 5.2 | Fast simulation run time (seconds) | 77 |
| 6.1 | Input features of the DNN estimating the correction on the recoil components | 93 |
| 7.1 | Integrated luminosity L_{int} , W-pair production cross-section σ_{WW} and number of W pairs ($N_{WW} = L_{int} \times \sigma_{WW}$) expected at FCC-ee for different centre-of-mass energies | 114 |
| 7.2 | Efficiency of the χ^2 pairing for the various centre-of-mass energies | 116 |
| 7.3 | Expected statistical uncertainties on the W boson mass and width for the hadronic decay channel at FCCee (full luminosity with 2 IPs) with the CLD detector for different centre-of-mass energies and different reconstruction methods | 121 |
| 7.4 | Expected statistical uncertainties on the W boson mass and width for the semi-leptonic decay channel at FCC-ee (full luminosity with 2 IPs) with the CLD detector for different centre-of-mass energies and different reconstruction methods | 123 |
| 8.1 | Statistical and systematic uncertainties on the W mass and width in the hadronic and semi-leptonic channels for the combined LEP2 results obtained with the direct reconstruction method | 128 |
| 8.2 | Estimated systematic uncertainties [MeV/c ²] introduced by the CR (SKI with $k_I = 0.6$ and SKII models) and BEC in the hadronic decay channel for different centre-of-mass energies | 131 |
| 8.3 | Effect of the CR (SKI with $k_I = 0.6$ and SKII models) and BEC on the W mass and width statistical uncertainties in the hadronic channel for different centre-of-mass energies and for the full FCC-ee luminosity [MeV/c ²] | 132 |
| 8.4 | Effect of a cone (R=0.4 rad) reconstruction on the mass and width statistical uncertainties in the hadronic channel for different centre-of-mass energies and full FCC-ee luminosity [MeV/c ²]. No FSI were included in the simulation | 134 |
| 8.5 | Estimated systematic uncertainties [MeV/c ²] introduced by the CR (SKI with $k_I = 0.6$ and SKII models) and BEC after a cone cut (R = 0.4 rad) on the four jets of the hadronic decay channel for different centre-of-mass energies | 135 |

| | | |
|-----|---|-----|
| 8.6 | Effect of a cone ($R = 0.4$ rad) reconstruction on the mass and width statistical uncertainties [MeV/c^2] in presence of CR (SKI with $k_I = 0.6$ and SKII models) and BEC in the hadronic channel for different centre-of-mass energies and full FCC-ee luminosity | 136 |
| C.1 | Détérioration de la masse et de son incertitude statistique due à l'ajout d'un cône de sélection sur les jets | 168 |

Acronyms

CMSSW CMS Software

ALICE A Large Ion Collider Experiment

ATLAS A Toroidal LHC ApparatuS

BEC Bose-Einstein Correlation

BEH Brout-Englert-Higgs

BH Back Hadronic

BSM Beyond Standard Model

CE-E Endcap Calorimeter Electromagnetic

CE-H Endcap Calorimeter Hadronic

CERN European Organisation for Nuclear Research

CLD CLIC-like detector

CLIC Compact Linear Collider

CM centre-of-mass

CMS Compact Muon Solenoid

CR Colour Reconnection

DNN deep dense neural network

ECAL Electromagnetic Calorimeter

EE Endcap Electromagnetic

FCC Future Circular Collider

FH Front Hadronic

FOM Figure Of Merit

-
- FSI** Final State Interaction
- FSR** Final State Radiation
- HCAL** Hadronic Calorimeter
- HGCal** High-Granularity Calorimeter
- HL-LHC** High Luminosity-LHC
- IDEA** International Detector for Electron-positron Accelerators
- ILC** International Linear Collider
- IP** interaction point
- ISR** Initial State Radiation
- LEIR** Low Energy Ion Ring
- LEP** Large Electron Positron
- LHC** Large Hadron Collider
- LHCb** Large Hadron Collider beauty
- MC** Monte Carlo
- NLO** next-to-leading-order
- NNLO** next-to-next-to-leading-order
- PDG** Particle Data Group
- PF** particle-flow
- PS** Proton Synchrotron
- PU** pile-up
- PV** primary vertex
- QCD** Quantum Chromodynamic
- QED** Quantum Electrodynamics
- SiD** Silicon Detector concept for ILC
- SM** Standard Model of Particle Physics
- SPS** Super Proton Synchrotron

Chapter 1

Theoretical framework

*"If one is working from the point of view of getting beauty into one's equation,
... one is on a sure line of progress."
Paul A.M. Dirac*

Contents

| | | |
|------------|---|----------|
| 1.1 | The Standard Model | 2 |
| 1.1.1 | Matter and interactions | 2 |
| 1.1.2 | The Lagrangians of the Standard Model | 3 |
| 1.1.2.1 | The electromagnetic interaction | 3 |
| 1.1.2.2 | The electroweak interaction | 4 |
| 1.1.2.3 | The strong interaction | 5 |
| 1.1.2.4 | Spontaneous symmetry breaking | 6 |
| 1.1.2.5 | Free parameters of the Standard Model | 7 |
| 1.2 | A precise measurement of the W mass as a probe of the Standard Model | 7 |

The Standard Model of Particle Physics (SM) [26, 27, 28], describing the constituents of matter (fermions) and the mediators (bosons) of fundamental interactions acting between them, has demonstrated its extraordinary predicting power. Since the building of the Standard Model, 50 years ago, all the bricks that were then missing have been found: the gluon (1979) [29], the W and Z bosons (1983) [3, 4], the top quark (1995) [30], the neutrino (1955-2000) [31, 32, 33] and the Brout-Englert-Higgs (BEH) boson (2012) [34]. Despite the striking success of the SM, particle physics still misses a theory that would fully describe our universe.

A major shortcoming of the SM is that it includes only three of the four fundamental forces, omitting gravity. It fails at explaining the large disparity of particle masses and of strength of fundamental forces: the so-called "hierarchy problem". In addition, in the SM, neutrinos are massless whilst the observation of neutrino oscillation demonstrates that they are massive particles. The SM does not explain the matter-antimatter asymmetry. The SM model only describes visible matter, which has been estimated to be less than 5% of the universe, while the rest would be made of unknown matter (25% dark matter) and energy (69% dark energy), which manifest themselves through gravitational effects.

This chapter is a brief introduction to the SM and more particularly of the electroweak part, perfect tool to test its internal consistency and search for new physics. In particular, the mass of the W boson is one of the most important observable to bring to light any deviance of the model. The relevance of the W boson mass in the SM is discussed in Section 1.2.

1.1 The Standard Model

1.1.1 Matter and interactions

The Standard Model describes all the fermion and boson interactions and is based on a gauge quantum field theory including the internal symmetries of the unitary product group,

$$SU(2)_L \otimes U(1)_Y \otimes SU(3)_C, \quad (1.1)$$

where $SU(3)_C$, $SU(2)_L$, $U(1)_Y$ are respectively the Quantum Chromodynamic (QCD), weak where L stands for left-handed interaction, and the hypercharge (Y) group.

The first generation of fermions is a representation of the gauge group given in Equation (1.1) and contains all the constituents of ordinary stable matter. Fermions are spin 1/2 particles, which obey the statistics of Fermi-Dirac [35]. Although there is no strong theoretical argument supporting additional generations, the experimental observation has led to include two other families, which differ from the first generation by their higher masses. Fermions belonging to these generations are only observed in cosmic rays and accelerators. They are unstable and eventually decay into the first generation particles. Thus the standard model contains twelve fermions split into two categories: the leptons (charged e , μ , τ and their associated uncharged neutrinos ν_e , ν_μ , ν_τ) and the quarks (u, d, s, c, t, b). Consequence of the Dirac equation of quantum mechanics describing the dynamics of fermions [35], all twelve fermions have their antiparticle with the same mass but opposite quantum numbers.

The fermions interact by exchanging gauge bosons, also called vector bosons, which are spin 1 particles obeying the statistics of Bose-Einstein [35]. Electromagnetism is mediated by the photon, which couples to fermions having an electric charge (charged leptons and quarks). The weak interaction is mediated by the W and Z bosons, which couples to all fermions including neutrinos unable to interact via any other force. The strong force is mediated by gluons, which couple to particles having a color charge (conventionally red, green, blue), i.e. quarks and gluons themselves. As the strength of the interaction increases with its distance scale, quarks only appear in bound states of integral charge state and zero total colour-charge: mesons (2 quarks), baryons (3 quarks). There

are thus such twelve bosons.

Without the so-called "spontaneous symmetry breaking mechanism" W and Z bosons would be massless, as the photon. The Higgs mechanism introduces a quantum field that causes spontaneous symmetry breaking through which W and Z bosons interacting with this field acquire a mass. The spin 0 scalar boson, the BEH boson, is associated to the Higgs field as is the photon to the electromagnetic field. The elementary particles of the SM are represented on Figure 1.1.

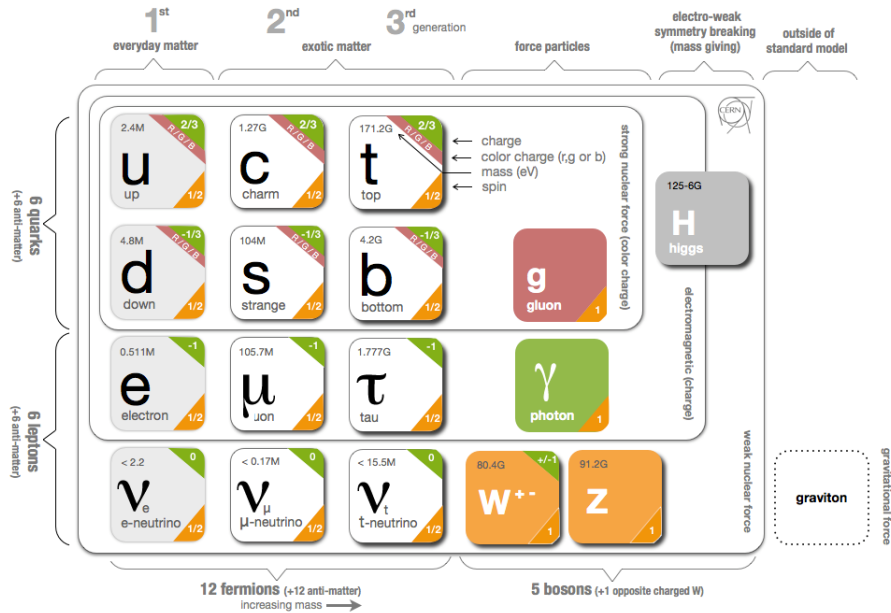


Figure 1.1 – The particles of the Standard Model

For each particle, the charge, mass and spin are given. The fermions of the ordinary matter are shown in grey while the exotic matter is in white boxes. The gauge bosons appear in coloured boxes. The graviton, mediator of the gravitational force, is also introduced in this figure as an outside SM particle (Credit: CERN).

The gravity completes the picture of the common physical phenomena. Defined by the Albert Einstein's general relativity theory, this force describing the universe at very large scale is possibly mediated by the graviton, a massless spin-2 particle. Conversely to the other bosons this particle has never been observed because the gravitation between two particles is extremely small (the relative strength for particles at a distance 1 fm, roughly the proton radius, is 10^{-37} against 10^{-8} for the weak force). The gravitation force between two particles is then neglected at the Particle Physics scale and the quantum gravity is not described by the SM theory.

1.1.2 The Lagrangians of the Standard Model

The relativistic quantum field theory of interacting particles is described with Lagrangian formalism.

1.1.2.1 The electromagnetic interaction

The Quantum Electrodynamics (QED) is an abelian gauge theory with the symmetry group $U(1)$. The gauge field mediating the interaction between the charged-fermion fields is the electromagnetic

field. The interaction of these fields involves the exchange of photons and is described by the relativistic Lagrangian [36]:

$$\mathcal{L}_{QED} = \bar{\psi}(i\gamma^\mu D_\mu - m)\psi - \frac{1}{4}F_{\mu\nu}F^{\nu\mu}, \quad (1.2)$$

where,

- ψ is the field representing the charged fermions of mass m ;
- γ^μ are the Dirac matrices, built with the Pauli matrices σ_i ;
- $D_\mu = \partial_\mu + ieA_\mu Q$ is the gauge covariant derivative with Q the electric charge operator ($Q\psi = q\psi$) and e the electric charge, the coupling strength of the field ψ with the electromagnetic field. A_μ is the covariant four-potential of the electromagnetic field generated by the electron;
- $F_{\mu\nu} = \partial_\mu A_\nu - \partial_\nu A_\mu$ is the electromagnetic field tensor;

A mass term for the photon would break the gauge invariance. The photon must therefore be massless and the range of the interaction is infinite.

1.1.2.2 The electroweak interaction

In 1933, Enrico Fermi suggested that beta decay might be explained by a four-fermion interaction, into which an electron and a (not yet discovered) neutrino would be created, in analogy with the nuclear photon decay. In this interaction, the electric charge e was replaced by the Fermi's constant G_F . This new coupling constant was associated to a new force: the weak force. After the experimental observation of the non-conservation of parity in weak interactions, the Fermi's Lagrangian needed to be modified to take into account the fact that only left (right) handed (anti) fermions are involved in these interactions. The analogy with electromagnetism suggested that the weak interaction might be carried by a vector boson which would play the role of the photon. As the weak interaction has a short-range, the mediator should be heavy, and, as the beta decay changes the charge, it should be a charged particle. The four-fermion point-like interaction imagined by Fermi was then replaced by a charged-particle exchange (W^+W^-).

Electromagnetic and weak interactions are now described in the single framework of the electroweak theory [1], based on the gauge symmetry group $SU(2)_L \otimes U(1)_Y$. The generator of the $U(1)_Y$ group is the hypercharge Y related to the generator Q of $U(1)_{QED}$ and to the charge associated to $SU(2)$, the weak isospin T_3 , by the relation $Y = 2(Q - T_3)$. This generator is associated to the gauge boson B_μ , which is not the photon. The generators of the $SU(2)_L$ are the three Pauli matrices σ_i associated to the three gauge bosons W_μ^i (two charged and one neutral bosons). The Lagrangian of the electroweak interaction can be written as [36]:

$$\mathcal{L}_{EW} = i\bar{\psi}\gamma^\mu D_\mu\psi - \frac{1}{4}W_{\mu\nu}^i W_i^{\mu\nu} - \frac{1}{4}B_{\mu\nu}B^{\mu\nu}, \quad (1.3)$$

where,

- ψ is the left-handed fermion field transformed as the doublets $\begin{pmatrix} \nu \\ \ell^- \end{pmatrix}$ and $\begin{pmatrix} q_u \\ q'_d \end{pmatrix}$ under $SU(2)$. q_u (q'_d) is representing the three generations of quark up (down) and $q'_d = \sum_j V_{ij}d_j$ with V_{ij} the Cabibbo-Kobayashi-Maskawa (CKM) mixing matrix [9]. The right-handed fermion fields are invariant under $SU(2)$;

- γ^μ are the Dirac matrices;
- $D_\mu = \partial_\mu - ig\frac{\sigma_i}{2}W_\mu^i - ig'\frac{Y}{2}B_\mu$ is the gauge covariant derivative with $g(g')$ the weak (electromagnetic) coupling constant.
- $W_{\mu\nu}^i = \partial_\mu W_\nu^i - \partial_\nu W_\mu^i + g\epsilon_{ijk}^i W_\mu^j W_\nu^k$, the gauge bosons (i, j and k) linked to $SU(2)_L$. ϵ_{ijk}^i are the structure constants of the gauge group.
- $B_{\mu\nu} = \partial_\mu B_\nu - \partial_\nu B_\mu$ the gauge boson linked to $U(1)_Y$.

The physical particles, the photon field, A_μ , as well as the neutral, Z_μ , and charged, W_μ^\pm , weak boson fields are linear combinations of W_μ^i and B_μ :

$$\begin{aligned} W_\mu^\pm &= \frac{1}{\sqrt{2}}(W_\mu^1 \pm iW_\mu^2) \\ \begin{pmatrix} A_\mu \\ Z_\mu \end{pmatrix} &= \begin{pmatrix} \cos \theta_W & \sin \theta_W \\ -\sin \theta_W & \cos \theta_W \end{pmatrix}, \begin{pmatrix} B_\mu \\ W_\mu^3 \end{pmatrix}. \end{aligned} \quad (1.4)$$

θ_W is the weak mixing angle defined as:

$$\cos \theta_w = \frac{M_W}{M_Z}. \quad (1.5)$$

Identifying A_μ with the photon field which only couples to the charge Q with the electric charge e implies the relation:

$$g \sin \theta_W = g' \cos \theta_W = e. \quad (1.6)$$

1.1.2.3 The strong interaction

QCD describes the strong interactions of coloured quarks and gluons exemplified by nuclear binding forces. It is a non-abelian gauge theory, whose $SU(3)_c$ is the symmetry group. The generators of $SU(3)_c$ are the eight Gell-Mann matrices λ_j [9] associated to the eight massless gauge bosons G_μ , called gluons. As quarks, gluons carry a colour charge (red, green, blue).

The Lagrangian of the strong interaction can be written as [36]:

$$\mathcal{L}_{QCD} = \sum_q \bar{\psi}_i^q (i\gamma^\mu D_{\mu, ij} - m_q \delta_{ij}) \psi_j^q - \frac{1}{4} F_{\mu\nu}^a F^{a\mu\nu}, \quad (1.7)$$

where,

- ψ_i^q are the field of the quark of flavour q and mass m_q with colour index i that runs from 1 to 3 (three colours);
- γ^μ are the Dirac matrices;
- $D_{\mu, ij} = \partial_\mu \delta_{ij} + ig_s t_{ij}^C G_\mu^C$ is the gauge covariant derivative where $g_s (\equiv \alpha_s)$ is the strong coupling constant. The generators of the $SU(3)$ group are $t_{ij}^C = \lambda_{ij}^C/2$ with C , running from 1 to 8, the eight kind of gluons;
- $F_{\mu\nu}^a = \partial_\mu G_\nu^a - \partial_\nu G_\mu^a - g_s \epsilon_{bc}^a G_\mu^b G_\nu^c$ is the gluon field tensor where ϵ_{bc}^a are the structure constants of the $SU(3)$ group. G_μ^a corresponds to the gluon fields.

1.1.2.4 Spontaneous symmetry breaking

The Lagrangian of the electroweak theory given in Equation (1.3) obeys local gauge invariance, however the lowest-energy vacuum solutions are allowed to violate this invariance. For these solutions, the symmetry $SU(2)_L \oplus U(1)_Y$ may be broken around that vacuum while the whole Lagrangian may remain symmetric. Without this spontaneous symmetry breaking, also called Higgs mechanism, as the photon, the W and Z bosons, quarks and leptons would be massless whilst they have been observed with non-zero masses.

The symmetry is spontaneously broken by the introduction of a complex scalar field ϕ , whose the Lagrangian can be written as [36]:

$$\mathcal{L}_{BEH} = (D^\mu \phi)^\dagger (D_\mu \phi) - V(\phi), \quad (1.8)$$

where,

- $D_\mu = \partial_\mu + igT^i W_\mu^i + ig'Y B_\mu$ is the gauge covariant derivative where W_μ^i and B_μ are the gauge bosons of $SU(2)_L$ and $U(1)_Y$ respectively and T^i and Y the associated charges. $g(g')$ are the weak(electromagnetic) coupling constants;
- $V(\phi)$ is the Higgs potential defined in Equation (1.9).

$$V(\phi) = \lambda(\phi^\dagger \phi)^2 - \mu^2(\phi^\dagger \phi), \quad (1.9)$$

where λ is the strength of the interaction ($\lambda > 0$). If $\mu^2 < 0$, the bilinear term is an ordinary mass term and $V(\phi)$ has the form of a parabola with an unique symmetric minimum ground state for $\phi = 0$. Therefore, for spontaneous symmetry breaking, μ^2 must be chosen positive. The potential has the shape of a "Mexican hat" with an infinite number of degenerate ground states. The minima energy are found from the derivative of the potential:

$$\frac{dV(\phi)}{d\phi} = 2\lambda(\phi^\dagger \phi) - \mu^2 = 0. \quad (1.10)$$

Then all ground states have the same absolute value,

$$v = |\phi_0| = \sqrt{\frac{\mu^2}{2\lambda}}, \quad (1.11)$$

and differ by their different orientations in the complex plane. The scalar field is redefined in terms allowing small perturbations around the ground state:

$$\phi(x) = (v + H(x))e^{i\eta(x)}, \quad (1.12)$$

where $H(x)$ is the Higgs boson. When replacing $\phi(x)$ by the expression given in Equation (1.12) in the Lagrangian, through the covariant derivative the Higgs field couples to the gauge bosons W_μ and B_μ , which acquire a mass proportional to the vacuum expectation value of the Higgs field, v :

$$\begin{aligned} M_W &= \frac{vg}{2}, \\ M_Z &= \frac{v\sqrt{g^2 + g'^2}}{2}. \end{aligned} \quad (1.13)$$

Similarly through the Yukawa interaction between the Higgs field and massless quark and lepton fields, quarks and leptons acquire a mass proportional to v [9]. The $U(1)_{QED}$ and $SU(3)$ symmetries remaining unbroken, the photon and the gluons do not interact with the Higgs field and remain massless.

1.1.2.5 Free parameters of the Standard Model

There is no consensus on the number of free parameters of the SM, i.e. parameters that are not fixed by the model but are determined experimentally. This number usually varies between 18 and 29, more or less arbitrarily chosen. We will limit ourselves to 18 parameters.

They are:

- the nine charged-fermion masses: m_e, m_μ, m_τ and $m_u, m_d, m_s, m_c, m_b, m_t$;
- three mixing angles and a phase from the quark mixing matrix (CKM) determining the probability of changing the quark flavour in weak interactions;
- three gauge coupling-constants: g' (electromagnetic), g (weak), g_s (strong);
- two parameters to characterise the Higgs potential: v (vacuum expectation value) and λ (Higgs self-interacting coefficient).

g', g_s and v are often replaced by α_{QED} (the fine structure constant), M_Z (the Z-boson mass) and G_F (the Fermi coupling constant), which are better measured experimentally. The parameter λ may also be replaced by M_H (the Higgs mass).

1.2 A precise measurement of the W mass as a probe of the Standard Model

After the discovery of the W and Z bosons in 1983 and Higgs boson in 2012, all the parameters of the SM have been measured with different levels of precision and no deviation from SM predictions has been observed within the limit of experimental and theoretical uncertainties. All direct searches for physics beyond the SM have been so far unsuccessful.

This suggests that the energies where new particles could be produced on-shell, have not yet been reached. In this context two complementary approaches are pursued:

- increasing the energy (and luminosity) by building larger colliders such as HL-LHC or FCC-hh with the hope of seeing new particles popping up;
- increasing the precision by building clean machines (e^+e^-) and ultra-powerful detectors with the goal of detecting visible effects of new physics through virtual exchanges.

Indeed quarks and bosons induced-radiative loops appear in the self-energy vector of the W boson, as shown on Figure 1.2. Then the W, top quark and Higgs masses are interdependent through the one loop diagrams and the loop-level expression of the W mass is [9]:

$$M_W^2 = \frac{\pi \alpha_{QED} (M_Z^2)}{\sqrt{2} G_F \sin^2 \theta_W} \frac{1}{1 - \Delta r} \quad (1.14)$$

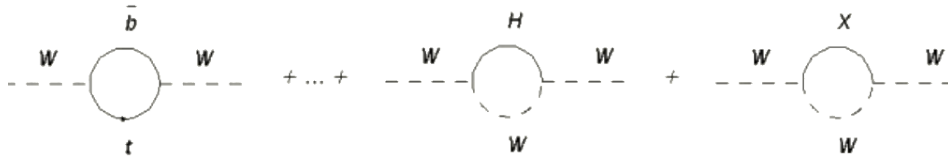


Figure 1.2 – Feynman diagrams of radiative corrections of the W boson propagator
Only the one-loop radiations are shown

Electroweak radiative corrections to physical observables, Δr , are computed in perturbation theory and they depend on the top-quark mass quadratically and on the Higgs and Z masses logarithmically:

$$\Delta r = -\frac{\cos^2 \theta_W}{\sin^2 \theta_W} \Delta \rho + \frac{\alpha}{3\pi} \left[\frac{1}{2} - \frac{1}{3} \frac{\sin^2 \theta_W}{1 - \tan^2 \theta_W} \right] \log \frac{m_H^2}{m_Z^2} + \dots \sim 1\% \quad (1.15)$$

$$\Delta \rho = \frac{\alpha m_t^2}{\pi m_Z^2} - \frac{\alpha}{4\pi} \log \frac{m_H^2}{m_Z^2} + \dots \sim 1\%.$$

The global electroweak fit [10] is able to gather all measured observables from LEP, Tevatron, LHC, such as masses, partial widths, asymmetries, couplings, into one single χ^2 , to obtain the most precise evaluation of the parameters of the SM. Figure 1.3 shows the comparison of the direct measurement (green) to the electroweak global fit prediction of the W mass as a function of the quark top mass, including (blue) and excluding (grey) the mass of the Higgs boson. Currently, the prediction and experimental measurements are in agreement within 1σ as shown on Figure 1. Any deviation of the measurements with respect to predictions and among themselves would reveal the existence of new, weakly interacting particles through global fits of the electroweak sector.

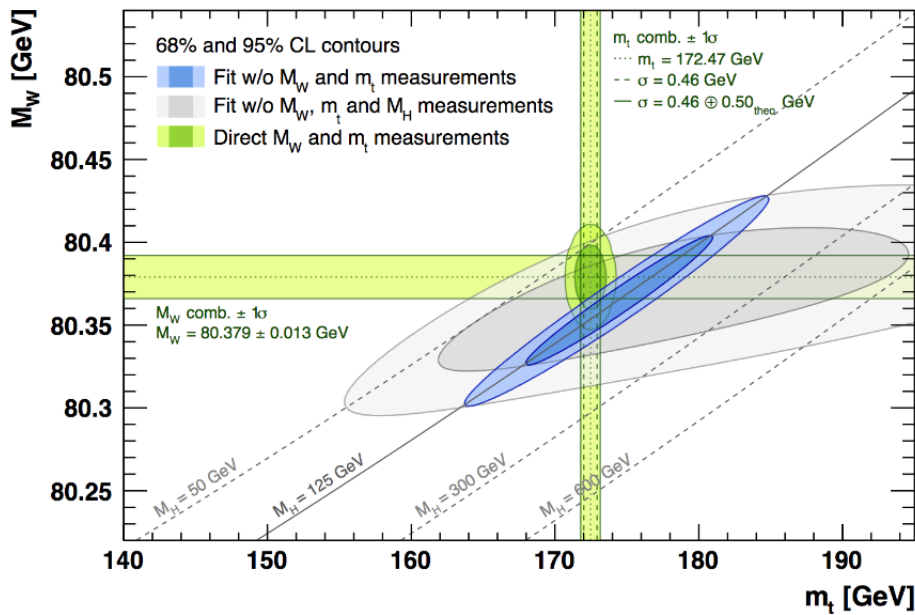


Figure 1.3 – 68% and 95% confidence level prediction of M_W as a function of m_{top} obtained from electroweak fit, including (blue region) and excluding (grey region) the Higgs boson mass, and compared to the direct measurement (vertical and horizontal green bands) [10]

The current world average of the W mass value is [9]:

$$M_W^{meas} = 80.379 \pm 0.012 \text{ GeV}/c^2, \quad (1.16)$$

and the SM prediction is [9]:

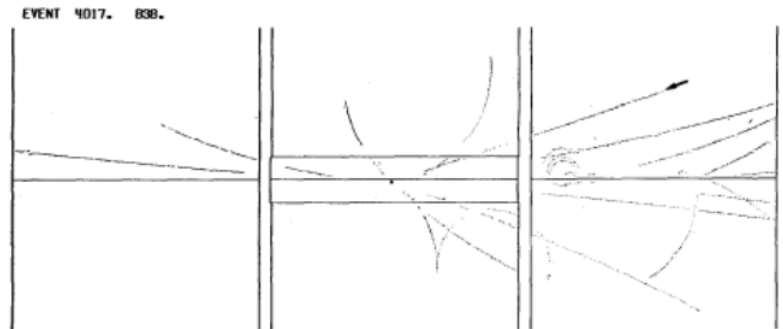
$$M_W^{theo} = 80.358 \pm 0.004 \text{ GeV}/c^2. \quad (1.17)$$

Improving the accuracy of the W-mass measurement at the level or beyond the accuracy of the theoretical prediction would be a crucial test of the internal consistency of the SM and any failure might reveal the emergence of new physics beyond the SM.

The precise measurement of the W mass will be discussed in the context of the CMS experiment at LHC and in that of future experiments at HL-LHC and FCC-ee. Chapter 2 will be devoted to the properties of the W boson and the methods to measure its mass in these different types of collisions. Chapter 3 will give a description of the respective experimental contexts.

Chapter 2

W boson production and decay



Display of UA1 $W \rightarrow e\nu$ event.

Contents

| | | |
|------------|--|-----------|
| 2.1 | Hadron colliders | 12 |
| 2.2 | Lepton colliders | 15 |
| 2.2.1 | On-shell W-pair production | 16 |
| 2.2.2 | Off-shell W-pair production | 17 |
| 2.2.3 | Corrections to lowest order W-pair cross-section and decay | 18 |
| 2.2.3.1 | Pure QED corrections | 19 |
| 2.2.3.1.1 | Initial State Radiation (ISR) | 19 |
| 2.2.3.1.2 | Coulomb correction | 20 |
| 2.2.3.1.3 | Intermediate and Final State Radiation (WSR and FSR) | 20 |
| 2.2.3.1.4 | Non-factorisable virtual corrections | 21 |
| 2.2.3.2 | QCD corrections | 21 |
| 2.2.3.3 | Final State Interactions (FSI) | 21 |

| | | |
|------------|--|-----------|
| 2.2.3.3.1 | Colour Reconnection | 21 |
| 2.2.3.3.2 | Bose-Einstein Correlation | 22 |
| 2.3 | Comparison of W production at hadron and lepton colliders | 22 |
| 2.3.1 | Mass and width from direct reconstruction | 23 |
| 2.3.1.1 | Hadron collisions | 23 |
| 2.3.1.2 | Lepton collisions | 24 |
| 2.3.2 | Mass and width from cross-section at threshold | 26 |

The W-boson production mechanisms at hadron and lepton colliders differ in many ways, and consequently the experimental contexts of detection of the W events and the techniques for the W mass measurement. In the following, the production and decay mechanisms will be examined and compared for these different types of collisions.

2.1 Hadron colliders

At hadron colliders, the leading order production mechanism of electroweak gauge-bosons (W, Z) is the parton-parton hard scattering from the constituents of the colliding hadrons. This mechanism, shown on Figure 2.1, is called Drell-Yan process [11].

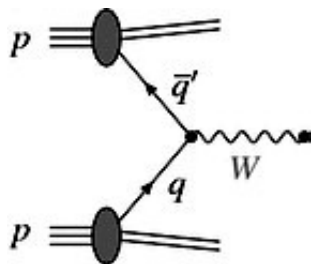


Figure 2.1 – Leading-order production mechanism of the W boson in hadron colliders [11]

Hadrons are characterised by the so-called valence quarks: a proton is formed from two quarks up and a quark down. In addition to the three valence quarks, hadrons contain a sea of quark-antiquark pairs (so-called sea quarks), which participate to the global properties of the hadrons, such as the mass for instance. These constituents are bound together by the constant exchange of virtual soft gluons (quark confinement).

W and Z bosons are produced through the annihilation of a quark and an anti-quark and both valence and sea quarks participate in the process. Nevertheless in proton-antiproton collisions vector bosons are predominately produced through valence-quark interactions, whilst in proton-proton collisions the participation of at least one sea quark is required. Figure 2.2, displaying the contributions of different quark flavours to W production at LHC compared to the Tevatron, shows that at the LHC the contribution of *c* and *s* quarks is quite significant with respect to *u* and *d* quarks.

At the leading order, the colliding partons are assumed to be perfectly collinear with the colliding hadrons and the gauge bosons are then produced with no transverse momentum. The QCD

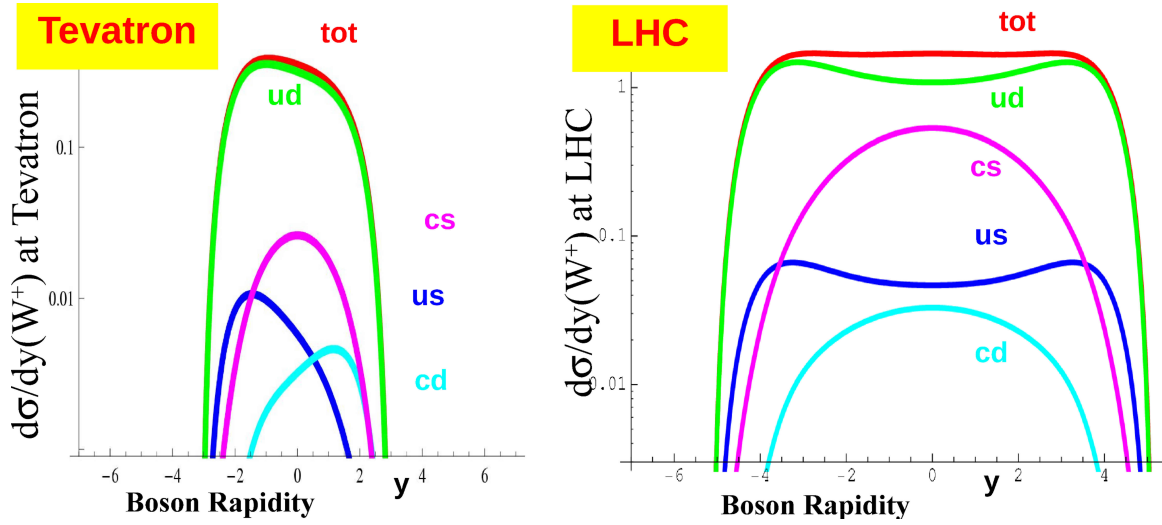


Figure 2.2 – Contributions of the different quark flavours to the W production at the Tevatron (left) and LHC (right) [12]

factorisation theorem (Drell-Yan) allows to express the cross-section for the hard-scattering process $pp \rightarrow V$ as the incoherent sum of all the possible fermionic sub-processes, weighted with the probability distribution of these fermions in the colliding hadrons [37]:

$$\sigma(A + B \rightarrow W + X) = \sum_{a,b} \int_0^1 dx_a \int_0^1 dx_b f_a/A(x_a) f_b/B(x_b) \hat{\sigma}(a + b \rightarrow W), \quad (2.1)$$

where $\hat{\sigma}(a + b \rightarrow W)$ is the parton cross-section and $f_a/A(x_a)$ is the probability to find the constituent a in the hadron A carrying the fraction x_a of the longitudinal impulse of that hadron. In the sum $\sum_{a,b}$, the quark pair ab runs over all possible combinations of quarks.

At the leading order the effect of strong interactions has been neglected. However the emission of non collinear hard-gluons will give a transverse momentum to the W, much higher than the momentum that would result from the Fermi motion of the constituents inside the hadrons. The contribution of the first-order QCD-corrections are shown on Figure 2.3.

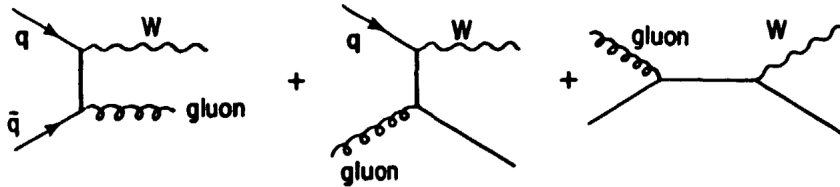


Figure 2.3 – First-order QCD-correction contributions to the W boson [13]

Calculations are available up to next-to-next-to-leading-order (NNLO) in QCD and include electroweak corrections at next-to-leading-order (NLO) [38, 37]. The cross-section predictions at the LHC and at the Tevatron are compared in Figure 2.4. They depend on the parton distribution functions (PDFs).

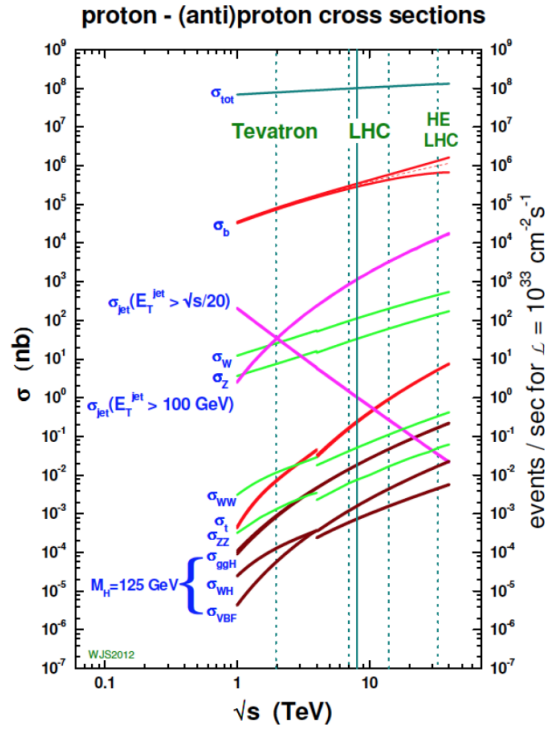


Figure 2.4 – Cross-section for different processes in hadron colliders as a function of centre-of-mass energy [14]

The dotted lines correspond to the different centre-of-mass energies. The break point in the curves is the difference of estimated cross-section between pp and $p\bar{p}$ collisions.

Figure 2.5 shows the predicted transverse momentum of the W boson, p_T^W , for different initial parton flavours. The higher is the mass of the contributing parton(s), the harder will be the p_T^W spectrum, and consequently the transverse momentum of the decay products.

The short lived (3.2×10^{-25} sec) W boson quickly decays to any fermion-antifermion pair (Figure 2.6), but not a top quark, whose mass is larger than M_W . The remaining partons (quarks and gluons), which do not participate into the production of the gauge bosons, will form hadrons through the process of hadronisation. This additional activity is what is usually called the underlying event.

The branching ratios for each of these decays are [9]:

$$\begin{aligned}
 \Gamma(W \rightarrow e\bar{\nu}) &= 10.71 \pm 0.16\% \\
 \Gamma(W \rightarrow \mu\bar{\nu}) &= 10.63 \pm 0.15\% \\
 \Gamma(W \rightarrow \tau\bar{\nu}) &= 11.38 \pm 0.21\% \\
 \Gamma(W \rightarrow q\bar{q}) &= 67.41 \pm 0.27\%
 \end{aligned}
 \tag{2.2}$$

Although the W boson decays mostly into hadrons, because of the largest branching ratio, this decay cannot be identified in the huge QCD background generated in hadron collisions. In these collisions, the electroweak process is then rather identified with the leptonic decay. Therefore, the signature of a W boson produced in hadronic collisions is a lepton with a large momentum emitted at wide angle from the beam axis and a large missing transverse momentum, carried away by the

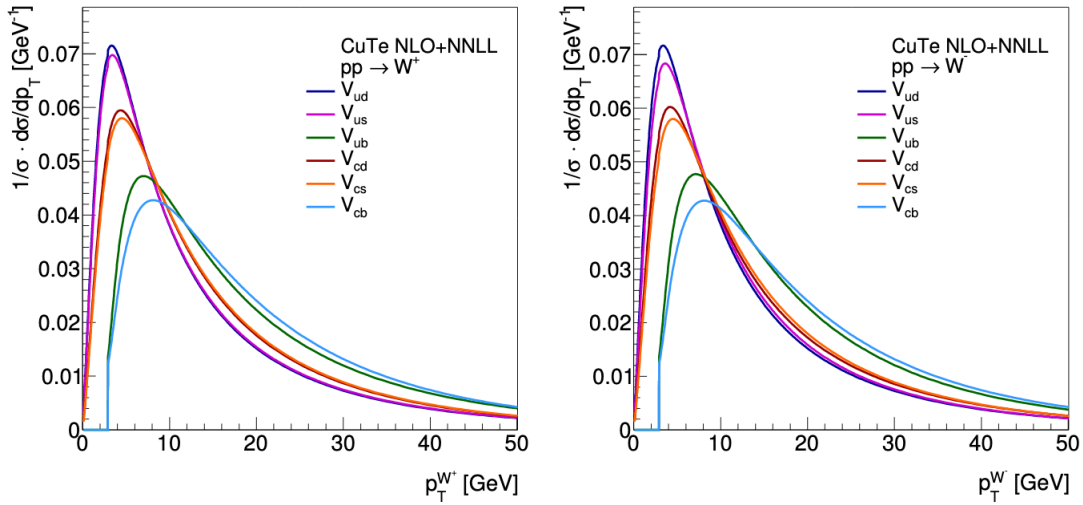


Figure 2.5 – Differential cross-sections as a function of p_T^W for W^+ and W^- production initiated with different parton flavours and evaluated with CuTe at NLO+NNLL (next-to-next-to-leading logarithmic) [15]

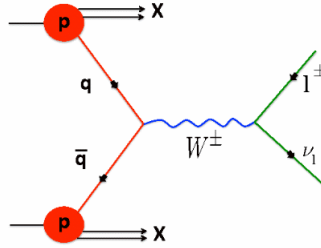


Figure 2.6 – Decay of the W boson in fermion-antifermion pair

neutrino. In the lepton selection only the electron or muon can be used because the tau lepton cannot be reconstructed with an acceptable accuracy.

2.2 Lepton colliders

In electron-positron collisions, the W bosons are pair-produced by electron-positron annihilation for $\sqrt{s} = 2M_W$. The W mass can be measured either from the total W-pair cross-section close to the threshold, where its size is most sensitive to the mass, or from the measured momenta of the decay products of the two Ws. In the first method the cross-section must be accurately predicted and in the second one a precise knowledge of the W-pair centre-of-mass energy is crucial. Given the high level of accuracy (10^{-4}) required by both methods and the size of the radiative corrections (see section 2.2.3), these corrections are indispensable for the measurement of the cross-section and the determination of four-momentum computed by energy-momentum conservation. Full radiative corrections to the final state of four fermions from the decays of the two Ws do not exist.

W-pair production can be described in three steps:

- The on-shell W pair production, $e^+e^- \rightarrow W^+W^-$, which at tree level is described by the

diagrams of Figure 2.7. At this level the complete $\mathcal{O}(\alpha)$ radiative corrections are known, including the virtual one-loop corrections and the real-photon bremsstrahlung [15, 16]. Once the on-shell W-pair production has been described, the on-shell W-decay can be attached to it. The radiative corrections to this decay are known [39, 40, 41, 42].

- The off-shell production of W pairs, which then decay into four fermions. The initial and final state radiations can be implemented in the leading-log approximation, but the full set of virtual corrections is still missing.
- The full $\mathcal{O}(\alpha)$ corrected evaluation of all possible four-fermion states. Also QCD corrections are needed particularly for the fully hadronic final states.

All these steps will be shortly described in this chapter. A complete discussion can be found in [43].

2.2.1 On-shell W-pair production

The lowest-order cross-section determines the essential features of the W-pair production. The total cross-section for the process $e^+e^- \rightarrow W^+W^-$ is:

$$\sigma = \sigma_{Born}(1 + \sigma_{EW} + \sigma_{QCD}), \quad (2.3)$$

where:

- σ_{Born} (Born cross-section) is the lowest order cross-section (tree-level) in the on-shell approximation, i.e. neglecting the decay of the W boson;
- σ_{EW} is the electroweak higher-order electroweak radiative corrections such as loop-corrections or real photon emission; a complete set of $\mathcal{O}(\alpha)$ corrections is available.
- σ_{QCD} is the higher-order QCD corrections to WW final states with quark pairs. They can generate additional jets in the final state.

In the Born approximation, the process $e^+e^- \rightarrow W^+W^-$ is described at the lowest order (tree-level) by the Feynman diagrams shown on Figure 2.7.

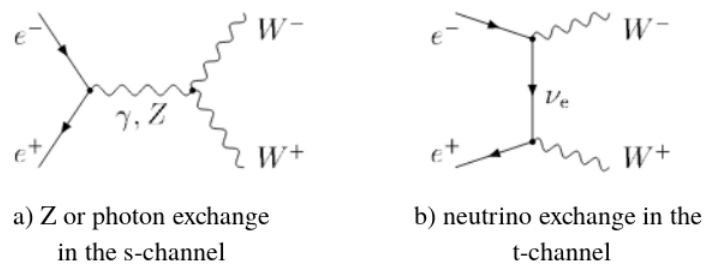


Figure 2.7 – W pair production in e^+e^- collisions

These diagrams represent the on-shell production of the W boson. This state, where the W decay is neglected, is also called Born approximation.

Then the differential and total on-shell cross-section near the threshold (the W velocity $\beta = \sqrt{1 - 4M_W^2/s} \ll 1$) can be written as [44]:

$$\left(\frac{d\sigma}{d\Omega}\right)_{Born} \sim \frac{\alpha_{QED}^2}{s} \frac{\beta}{4\sin^2\theta_W} \left[1 + 4\beta \cos\theta \frac{3\cos^2\theta_W - 1}{4\cos^2\theta_W - 1} + \mathcal{O}(\beta^2)\right]. \quad (2.4)$$

s is the total energy of the initial electron-positron system squared, θ_W is the weak mixing angle defined in Equation (1.5), θ is the parametrization of the unit sphere ($d\Omega = d\cos\theta d\phi$) and α_{QED} is the fine-structure constant. The total cross-section is given by:

$$\sigma_{Born} \sim \frac{\pi\alpha_{QED}^2}{s} \frac{4\beta}{\sin^4\theta_W} + \mathcal{O}(\beta^3). \quad (2.5)$$

The term proportional to β originates from the t-channel diagram only and the contributions from s-channel and s-t interference are proportional to β^3 . Therefore at the production threshold, $\beta \sim 0$ and the W bosons are isotropically produced, whilst they will be more and more often produced in the forward direction as the centre-of-mass energy increases.

2.2.2 Off-shell W-pair production

In the Born approximation, W bosons are considered as stable particles, whilst the W bosons are not stable but decay within 3.2×10^{-25} sec, corresponding to a finite decay width of about $2.085 \text{ GeV}/c^2$.

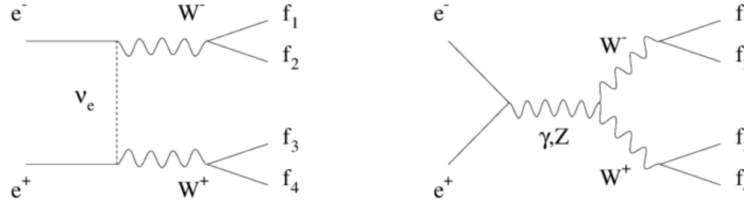


Figure 2.8 – W-pair decay into four-fermion final states (CC03 diagrams)

Each W decays into a pair of fermions, as shown on Figure 2.8, according to the branching ratios given in Equation (2.2) and producing a four fermions final state:

- $q\bar{q}q'\bar{q}'$ with a branching ratio of 45.5%. The quarks will hadronise and lead to a 4-jet final state (hadronic channel).
- $q\bar{q}l\nu$ with a branching ratio of 43.9%. This semi-leptonic channel is characterised by two jets, an energetic lepton and a large missing energy, carried away by the neutrino.
- $l\nu l'\nu'$ with a branching ratio of 10.6%. The leptonic-channel signature is two energetic leptons and a very large missing energy because of the generation of two neutrinos.

The leading-order off-shell cross-section (taking finite W width into account) can be expressed as [43]:

$$\sigma_{off-shell}(s) = \int_0^s ds_1 \rho(s_1) \int_0^{(\sqrt{s}-\sqrt{s_1})^2} ds_2 \rho(s_2) \sigma^0(s, s_1, s_2). \quad (2.6)$$

s is the square of the energy in the centre-of-mass, s_1 and s_2 are the invariant masses squared of the two virtual W-bosons. ρ_s is the Breit-Wigner function associated to the W propagator defined as a function of the full width of the W boson, $\Gamma(s)$ [43]:

$$\rho(s) = \frac{1}{\pi} \frac{\sqrt{s}\Gamma(s)}{(s - M_W^2)^2 + M_W^2\Gamma^2(s)}. \quad (2.7)$$

$\sigma_0(s, s_1, s_2)$ is the cross-section for the W pair with invariant masses s_1 and s_2 at the leading order. It contains CC03 diagrams of Figure 2.8 and their interferences. The four-fermion final states are not only produced through the three doubly resonant CC03 diagrams of the W-pair production, but also through diagrams with the same initial and final state, although different intermediate states, such as those shown on Figure 2.9.

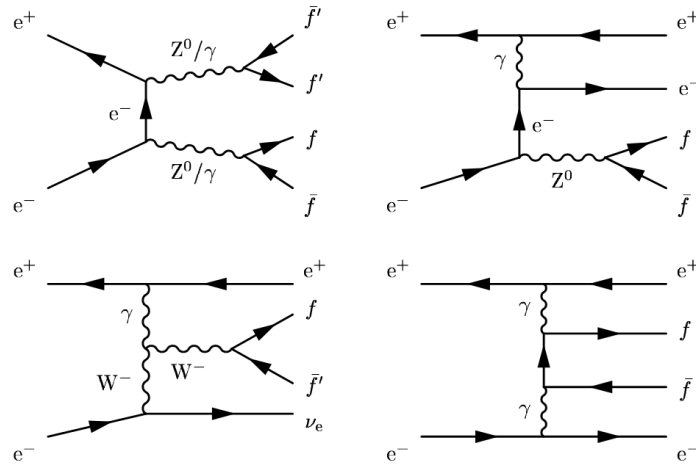


Figure 2.9 – Example of four-fermions states which are not produced through the W-pair decay

These processes are background to the CC03 signal:

- The ZZ production is a potential background source in the fully hadronic decay channel.
- The single-Z production has a large cross-section and is an important potential background to the semi-leptonic channel. There is also interference in the final state $e^+\nu e^-\bar{\nu}$.
- The single-W production leads to final states that are undistinguishable from $e^+\nu e^-\bar{\nu}$.
- The $\gamma\gamma$ production is a source of undistinguishable background for the fully leptonic final states.

2.2.3 Corrections to lowest order W-pair cross-section and decay

The process $e^+e^- \rightarrow W^+W^- \rightarrow 4f$ may be accompanied by:

- Emission of photons in the initial, intermediate and final states, so-called electroweak radiative corrections. The main radiative corrections at the order $\mathcal{O}(\alpha)$ are represented in Figure 2.10 [16].

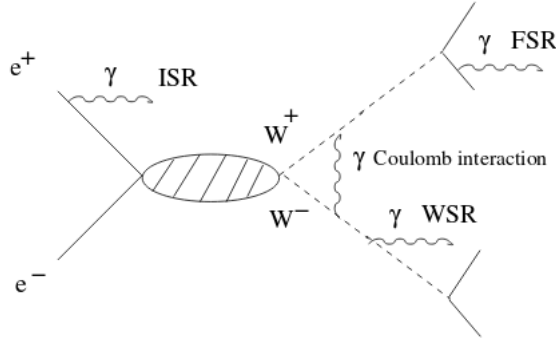


Figure 2.10 – Electroweak radiative corrections [16]

The main electroweak radiative corrections of order $\mathcal{O}(\alpha)$ are represented: Initial State Radiation (ISR), W intermediate State Radiation (WSR), Final State Radiation (FSR) and Coulomb correction

- Emission of gluons in the hadronic final state, so-called QCD corrections; These emissions will involve reconnection effects in fragmentation and hadronisation: colour reconnection and Bose-Einstein correlations.
- Virtual corrections at various stages of the process.

2.2.3.1 Pure QED corrections

2.2.3.1.1 Initial State Radiation (ISR) The Initial State Radiation (ISR), also known as bremsstrahlung is the collinear radiation of one or more photons from the incoming electron or positron.

In the s-channel production (above threshold), the ISR gives rise to a dominant logarithmic universal, factorising, process-independent contribution. In the t-channel, the gauge-invariance is violated because of non-conservation of the electromagnetic current by bremsstrahlung emission. In order to compensate and construct a conservative current at threshold, photon emissions in all stage of the process would have to be considered [45]. The photon radiation corrections in this channel are non-universal, non-factorising, process-dependent ISR.

The ISR corrected cross-section can be written with the structure-function approach [46]:

$$\frac{d^2\sigma_{ISR}(s)}{ds_1 ds_2} = \int_{(\sqrt{s_1} + \sqrt{s_2})^2}^s \frac{ds'}{s} \rho(s_1) \rho(s_2) \left[b \left(1 - \frac{s'}{s}\right)^{b-1} (1 + \mathcal{S}_a) + \mathcal{H}_a \right], \quad (2.8)$$

where,

$$b = \frac{2\alpha}{\pi} \left(\ln \frac{s}{m_e^2} - 1 \right). \quad (2.9)$$

\mathcal{H}_a is the contribution of the hard photon emission and \mathcal{S}_a corresponds to the virtual and soft real photon emission. Both of them are split into the universal, function of the Born cross-section and non-universal part, $\sigma_{ISR}^{\text{non-univ}}$. The explicit expressions of \mathcal{S}_a and \mathcal{H}_a , as well as $\sigma_{ISR}^{\text{non-univ}}$ can be found in [45].

The ISR correction is the largest QED correction to the W-pair production cross-section. The ISR emissions are included into the present analysis of the W mass.

2.2.3.1.2 Coulomb correction Another large photonic correction, which is not associated to the initial state, is due to the Coulomb singularity in the threshold region. Close to the threshold, the two bosons move slowly and the exchange of virtual photons may occur between them before they decay into fermions (Figure 2.11). It corresponds to the exchange of virtual photon between the two W bosons before they decay into fermions. This correction is inversely proportional to their velocity, β , in their centre-of-mass system. In the on-shell approximation, the Coulomb correction to the cross-section is:

$$\sigma_{Coulomb, on-shell} = \frac{\alpha\pi}{2\beta}\sigma_{Born}, \quad (2.10)$$

where σ_{Born} is the total on-shell cross-section defined in Equation (2.5) [47]. At threshold, $\beta \sim 0$ (the W bosons are then stable) and the Coulomb interaction diverges. This singularity is balanced in the off-shell approximation by the finite-width of the W boson where the correction of the Coulomb interaction is [47]:

$$\sigma_{Coulomb, off-shell} = \sigma_{Born} \frac{\alpha\pi}{2\beta} \left[1 - \frac{2}{\pi} \arctan \left(\frac{|\beta_M|^2 - \bar{\beta}^2}{2\bar{\beta}Im\beta_M} \right) \right], \quad (2.11)$$

with,

$$\begin{aligned} \bar{\beta} &= \sqrt{1 - 2(s_1^2 + s_2^2)/s + (s_1^2 - s_2^2)^2/s^2}, \\ \beta_M &= \sqrt{1 - 4(M_W^2 - iM_W\Gamma_W)/s}. \end{aligned} \quad (2.12)$$

In the on-shell approximation, the Coulomb interaction introduces a maximum correction to the cross-section of about 6% at nominal threshold and decreases above (1.8% at 190 GeV). This correction produces a shift at the level of 5-10 MeV/c² on the reconstructed W mass. However, bound states of the two W bosons do not have time to form because of their limited lifetime [17]. Therefore, this effect has been neglected in the present study of the W mass measurement.

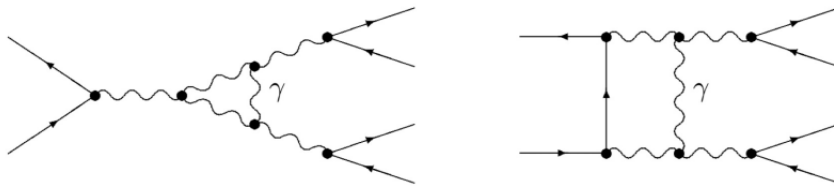


Figure 2.11 – Photon emissions in Coulomb correction [17]

2.2.3.1.3 Intermediate and Final State Radiation (WSR and FSR) WSR and Final State Radiation (FSR) photons will influence the angular distribution of their parent particles and then the differential cross-section. The W mass is not affected by these radiations as the photon can always be associated. In the hadronic decay channel, these photons are embedded in the parton shower describing the first phase of the hadronisation. The relative uncertainty is considered included in the jet and fragmentation one. In the leptonic decay, the FSR is not lepton

universal. The electron will be then more sensitive to the FSR than the muons and taus. In the reconstruction of the muon decay of the semi-leptonic channel for the study of the W mass at the FCC-ee, the FSR photons were combined to the muon as explained in Section 4.2.2.

2.2.3.1.4 Non-factorisable virtual corrections These corrections correspond to the exchange of virtual photons between any pair of charged particles throughout all the stage of the process. The contribution to the cross-section was computed in [48] at NLO and the impact on the cross-section has been estimated to be about 0.1%. Therefore, the effect on the present study of W mass has been neglected.

2.2.3.2 QCD corrections

The one-loop QCD radiative corrections, together with the gluonic bremsstrahlung, affect the hadronic partial width adding a factor $\alpha_s(M_W^2)/\pi$ in $\mathcal{O}(\alpha)$. By extension, the total width of the W propagators, Γ_W , is corrected including a normalisation factor in the parton-level calculation [17]:

$$\Gamma_W = \frac{3}{2\sqrt{2}\pi} G_F M_W^3 \left(1 + \frac{2\alpha_s(M_W^2)}{3\pi} \right). \quad (2.13)$$

The QCD corrections are included in the PYTHIA event generator [49] used in the study of the W mass at FCC-ee.

The W mass uncertainty is currently dominated by systematic uncertainties that present a major challenge in accurate W mass measurement [50]. With the threshold scan method, presented in Section 2.3.2, a statistical precision of 0.23 MeV/c² on the W mass is achievable only with a precision level of 2×10^{-4} (0.8 fb) on the theoretical cross-section [51]. Currently the four-fermions cross-section at the W-pair production threshold is known with a 1.5 fb precision [52], introducing a shift on the W mass of about 5 MeV/c². The global fit of the best measured observables of the SM predicts the W mass with a precision of about 4 MeV/c² [53]. Assuming that the two-loop electroweak corrections are known, an estimation of the missing three-loop electroweak corrections shows that the theory precision could reach 0.3 MeV/c² on the W mass at threshold [54].

2.2.3.3 Final State Interactions (FSI)

As a consequence of the W short lifetime, the typical separation between the decay vertices is about 0.1 fm, much smaller than the typical hadronisation scale (1-10 fm), and the fragmentation of the two W's may not be independent.

Two different physical effects are involved: the statistical correlation between identical particles from the two decays at hadron level, named Bose-Einstein correlation, and the QCD interactions between particles from different cascades at parton level, the Colour Reconnection effects. The wrong particles association resulting from these effects induces the highest systematic uncertainty on the W mass at LEP (Table 8.1), traduced by a shift of the invariant mass distribution.

2.2.3.3.1 Colour Reconnection A naive approach is to consider that each $q\bar{q}$ -pair from the W decay products forms a colour singlet which hadronises independently from the other one. Due to the phase-space overlap, the four partons may be assumed to be produced at the same point and

due to colour confinement, they are not free. Hence, in addition to the real pairing $q\bar{q}$ and $q'\bar{q}'$, the alternative systems $q\bar{q}'$ and $q'\bar{q}$ can be created. This kind of interconnection of the two Ws through their decay products, called Colour Reconnection (CR), affects the reconstructed W mass in the hadronic channel.

At LEP, the uncertainty due to CR on the hadronic W mass was estimated to $35 \text{ MeV}/c^2$ [5].

2.2.3.3.2 Bose-Einstein Correlation The hadronic decays of the W pair mostly contain pions, which obey the Bose-Einstein statistics. According to the Bose-Einstein statistics, identical bosons with the same charge and from close space-time regions become indistinguishable and coherent effects appear between them. Such effects lead to the enhancement of the production of identical bosons which occur mainly between low-momentum pions from different Ws. This particle mix between the two W bosons is named Bose-Einstein Correlation (BEC).

At LEP, the uncertainty due to BEC on the hadronic W mass was $7 \text{ MeV}/c^2$ [5].

In W-pair production, these interconnection effects introduce a large systematic uncertainty on the W mass. In order to reduce this uncertainty, several data reconstruction methods have been developed during the W mass study at LEP [8, 5]. The Final State Interaction (FSI) phenomena are not well described by QCD and several phenomenological models have been developed and implemented in Monte Carlo (MC) programs to describe CR [55, 56, 57] and BEC [58, 59] effects in the hadronic decays of W bosons in e^+e^- collisions. The philosophies of the PYTHIA [49] toy models as well as the method applied to reduce the effects of the FSI on the W mass at the FCC-ee are discussed in Chapter 8.

The cross-section of the most important processes in the centre-of-mass energy range of FCC-ee are summarised in Figure 2.12. These cross-sections contain all the corrections discussed above.

2.3 Comparison of W production at hadron and lepton colliders

Production of on-shell W bosons at hadron colliders (UA's, Tevatron, LHC) is tagged by the high p_T charged lepton from leptonic decays. Owing to the unknown parton-parton effective energy and missing energy in the longitudinal direction, the hadron-collider experiments reconstruct the transverse mass of the W, and derive the W mass from comparing the lepton transverse momentum or/and the transverse mass distribution with Monte Carlo predictions as a function of M_W . These analyses use the electron and muon decay modes of the W boson.

In e^+e^- -colliders (LEP, FCC-ee) a precise knowledge of the beam energy enables the determination of the $e^+e^- \rightarrow W^+W^-$ cross-section as a function of the centre-of-mass energy, as well as the precise reconstruction of the W mass precisely from its decay products. Close to the W^+W^- threshold (161 GeV), the dependence of the W-pair production cross-section on M_W is large, and this is used to determine M_W . At higher energies this dependence is much weaker ; W-bosons are directly reconstructed and the mass determined as the invariant mass of its decay products, the resolution being improved by a kinematic fit.

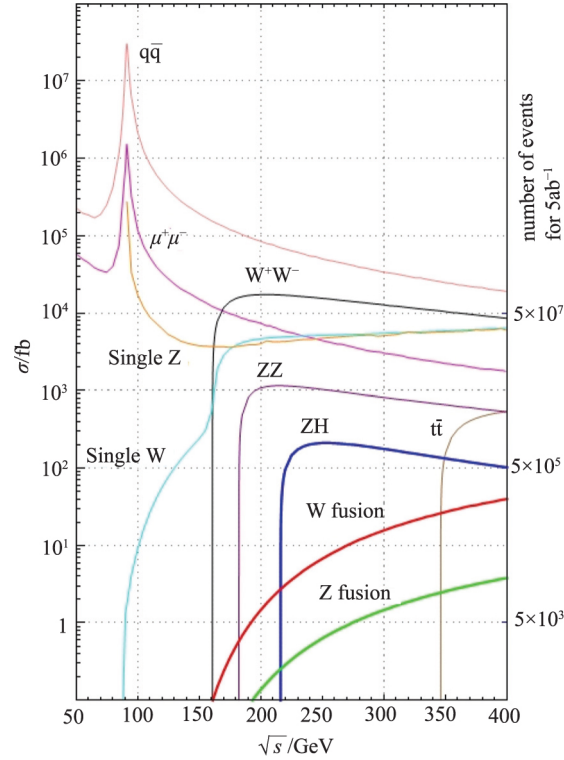


Figure 2.12 – Cross-section for different processes in lepton colliders as a function of the centre-of-mass energy [18]

2.3.1 Mass and width from direct reconstruction

2.3.1.1 Hadron collisions

Only the leptonic decay of the W is identified in hadronic collisions, hence the W mass is reconstructed from the higher energetic lepton (electron or muon) and its neutrino. The former is well measured while the latter is undetected and is associated to the missing energy. Because most of the other hadronic products resulting from the collision, X, escape along the beam axis, the longitudinal component of the momentum of the missing energy cannot be measured. Therefore only the transverse components of the four-vectors is used.

A first observable used to determine the mass of the W boson is the transverse momentum of the charged lepton, \vec{p}_T^ℓ . The \vec{p}_T^ℓ distribution rises up to $p_T \sim M_W/2$ and falls rapidly after. This shape is called Jacobian peak and can be interpreted as follows: in the rest frame of the W boson, the W decays into a lepton and its neutrino. The decay angle, 90° with respect to the beam axis, leads to the maximal transverse momentum for the lepton which is equals to $M_W/2$ by energy-momentum conservation. With a similar approach, another usable observable is the transverse momentum of the neutrino, \vec{p}_T^ν . The shape of the distribution of \vec{p}_T^ν also has a Jacobian peak with a maximum at $p_T \sim M_W/2$.

These observables are sensitive to the angular distribution of the W boson decay in its rest frame and to the p_T -boost of the boson, $W-p_T$ [15]. Moreover, $W-p_T$ is not theoretically known with the required precision. It is possible to mitigate this uncertainty by measuring the transverse momen-

tum of the recoil, \vec{h} , the hadronic product of the collision. By definition, the recoil is equal to the opposite of the W transverse momentum, therefore measuring precisely the recoil means measuring W - p_T . A precise recoil reconstruction method at CMS is discussed in Chapter 6.

The recoil is the 2D vectorial sum in the transverse plane of the momenta of all particles but the lepton:

$$\vec{h} = \sum_i \vec{p}_{T,i}. \quad (2.14)$$

By imposing the transverse momentum balance, the transverse momentum of the neutrino is:

$$\vec{p}_T^W = \vec{p}_T^\ell + \vec{p}_T^\nu = -\vec{h}. \quad (2.15)$$

Combining \vec{p}_T^ν , \vec{p}_T^ℓ and ϕ , the opening angle between the projections of the charged lepton and the missing momentum in the transverse plane, the transverse mass is defined:

$$m_T = \sqrt{2\vec{p}_T^\nu \vec{p}_T^\ell (1 - \cos \phi)}. \quad (2.16)$$

Using the relation derived from Equation (2.14), the transverse mass can be rewritten:

$$\frac{m_T^2}{2} = p_T^\ell (p_T^\ell + |\vec{p}_T^\ell + \vec{h}|) + \vec{p}_T^\ell \cdot \vec{h}. \quad (2.17)$$

This dependence with the recoil makes the transverse mass less sensitive to the W transverse momentum than the other observables [15]. As the transverse momentum of the lepton (or the neutrino), the m_T distribution exhibits a Jacobian peak with a maximum at $m_T \sim M_W$. Figure 2.13 shows the transverse mass distribution reconstructed at ATLAS.

From these transverse distributions, the W mass and width are finally extracted by adjustment of simulated Monte-Carlo templates, generated at different masses and widths, on the data distributions. Using several observables has the advantage to cross-check the results since the estimators have different systematic uncertainties. For example, the m_T distribution is less affected than the lepton p_T by the W boson p_T but is sensitive to the systematic uncertainty associated with the measurement of the recoil. A precise recoil reconstruction and the accuracy expected with CMS at HL-LHC are discussed in Chapter 6.

2.3.1.2 Lepton collisions

With enough statistics, the W mass and width can also be measured by direct reconstruction in electron-positron collisions. The W bosons are pair-produced and the mass is determined from the kinematic reconstruction of the W-pair decay products. Since the final states of the electron-positron collisions are very clean and the kinematics is completely determined, the W mass can be estimated by simply forming the invariant mass. However, only the hadronic and the semi-leptonic decay channels are usable because of the large missing energy (unmeasurable) due to the two neutrinos of the full-leptonic channel. Moreover, the tau lepton of the semi-leptonic channel decays quickly into secondary leptons and neutrinos (with a branching ratio of 35%) or into collimated hadrons (highly boosted), therefore extracting the W mass and width from the $W^+W^- \rightarrow \tau\nu q\bar{q}$ decay is more delicate and is not considered in this study.

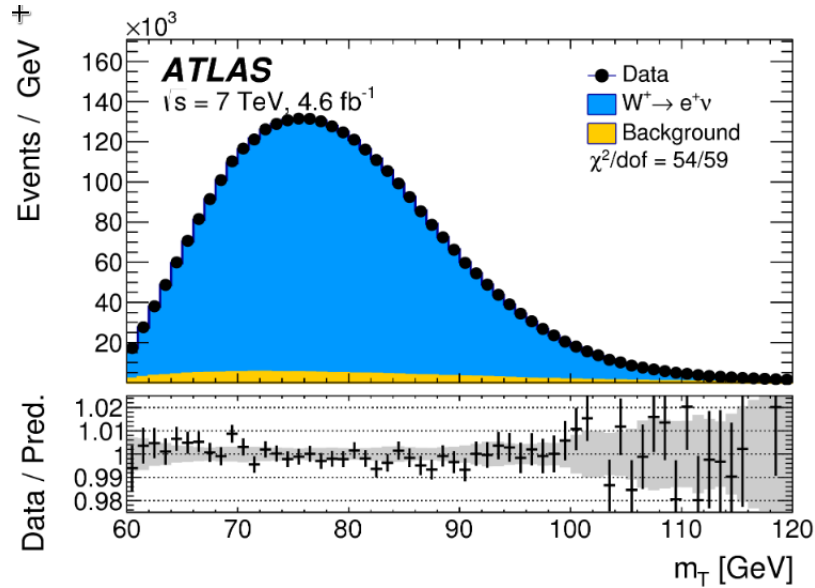


Figure 2.13 – Transverse mass distribution for the events $W \rightarrow e\nu$ at ATLAS [19]

Data (black dots) are compared to the Monte-Carlo simulation (blue histogram), including the signal and the background (yellow). The ratio given below the distribution compares the measured and simulated data. The statistical uncertainty on the measurement is represented by the error bars while the grey part shows the systematic uncertainty on the prediction.

Since the W are pair-produced, there are two reconstructed invariant masses, m_{inv} , per event. With E_i and P_i the energy and momentum, estimated by reconstruction, of the fermion i , each m_{inv} is computed as:

$$m_{inv} = \sqrt{(E_1 + E_2)^2 - (P_1 + P_2)^2}. \quad (2.18)$$

The jets are clustered with the DURHAM (k_T) jet algorithm [60], the lepton is associated with the most energetic lepton of the decay and the missing momentum, computed by energy-momentum conservation, is attributed to the neutrino. A precise description of the event reconstruction can be found in Chapter 4.

M_W and Γ_W are extracted by a fit of the distribution of measured event-by-event invariant masses with MC templates. The precision of this measurement is strongly correlated to the accurate theoretical knowledge of the dynamics of the production and decay stages in the $e^+e^- \rightarrow W^+W^- \rightarrow hadrons$ process. In the hadronic channel, the two pairs of quarks undergo a QCD cascade, called fragmentation, that produces the set of final-state hadrons. Because of the large W width, the fragmentation of the two pairs are not completely independent but may be interconnected by QCD interference effects resulting in a large systematic uncertainty on the W mass and width measurements. There are two types of phenomenological interconnection sources and both of them are modelled in MC generators in order to minimise discrepancies between data and MC events. These effects have been discussed in Section 2.2.3.3.

The invariant mass resolution is mainly degraded by detector effects. Several techniques have been developed in e^+e^- collisions to improve the mass resolution [5] over that obtained by simple reconstruction, also called raw mass. In particular, a constraint kinematic fit imposing the energy and momentum conservation, together with the equality of the two W masses in an event, is a

very powerful technique [61] in both hadronic and semi-leptonic decay channels. In the hadronic decay channel, a jet four-momenta rescaling (4C kinematic rescaling), satisfying the total energy-momentum conservation while keeping jet angles and velocities fixed to their measured values, is also a good primary improvement. However, this method cannot be used in the semi-leptonic channel as the neutrino momentum is computed using energy-momentum conservation. A more detailed description of both techniques and their effects on the W mass resolution can be found in Chapter 7.

2.3.2 Mass and width from cross-section at threshold

In addition to the direct reconstruction, the e^+e^- collisions offer the possibility of a measurement at the W pair-production threshold, from the WW cross-section measurement.

Figure (2.14) shows the $e^+e^- \rightarrow W^+W^-$ off-shell cross-section as function of the energy in the centre-of-mass. The effects of radiative corrections discussed in 2.2.3 are not included in this cross-section computation. The smallness of the cross-section near the threshold is compensated by the sensitivity to the W mass in this region. That is illustrated on Figure 2.14a where the W^+W^- excitation curve is drawn for different values of the W mass. Therefore, a measurement of the cross-section in this region directly yields a measurement of M_W . As shown on Figure 2.14b, the cross-section is also sensitive to the W width, whose variation introduces an inflection point around the threshold. This double sensitivity of W pair-production cross-section to the mass and width of the W boson allows a simultaneous determination of these two parameters.

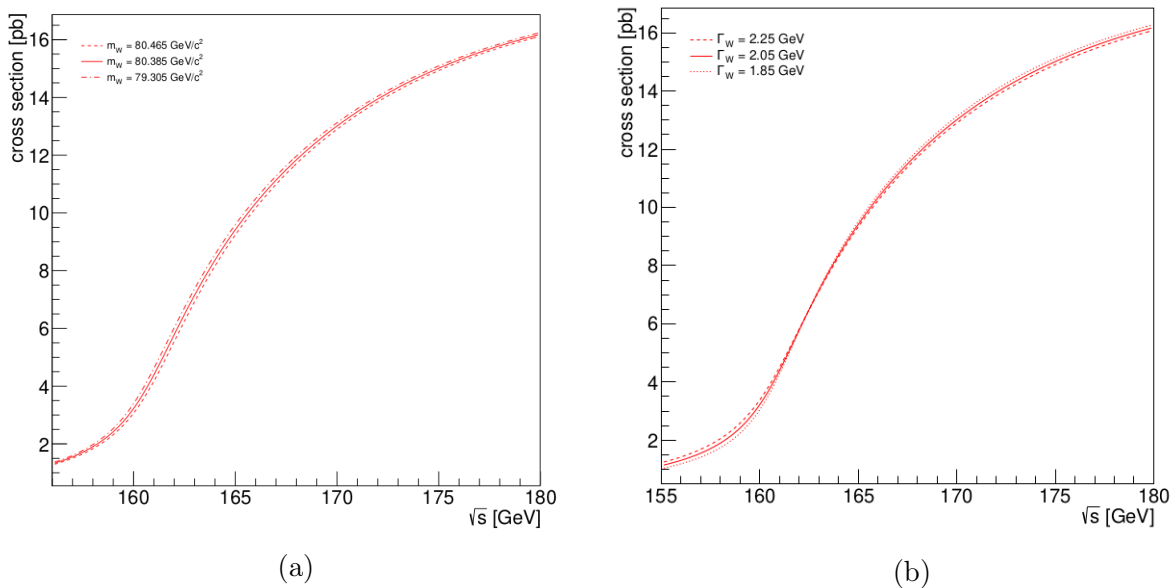


Figure 2.14 – Dependence of the W pair-production cross-section on W mass (2.14a) and width (2.14b) as a function of the centre-of-mass energy in the threshold region

The sensitivity of the W mass is enlightened with a W mass variation around the PDG value while the dependence to the width is shown with a variation of $\pm 0.2 \text{ GeV}/c^2$. The radiative corrections are not included.

To minimise the statistical uncertainty on the W mass and width, the optimal strategy for the data-taking has to be determined by choosing the optimal collider energies. If only the mass is measured, a single cross-section measurement can be made, whereas for the extraction of the mass

and width, the cross-section requires a measurement at two (or more) energy points. The parameter values are then extracted from cross-section templates generated for different mass and width values. For these measurements, all the decay channels of the W-pair can be used, even the full-leptonic channel unusable with the direct measurement.

The evaluation of the W mass precision reachable at the FCC-ee with the threshold method shows that the W mass could be measured with a statistical uncertainty of $0.23 \text{ MeV}/c^2$ at the optimal centre-of-mass energy 161.4 GeV . In case of simultaneous measurements of the W mass and width, the optimal data taking configuration has been estimated to $E_1 = 157.10 \text{ GeV}$, $E_2 = 162.34 \text{ GeV}$ and $f = 0.40$, where E_1 and E_2 are two optimal energy points and f is the data luminosity fraction delivered at the first energy. With this combination, the statistical uncertainties on the W mass and width could respectively reach $0.4 \text{ MeV}/c^2$ and $1.2 \text{ MeV}/c^2$. Such precisions are achievable with a control of systematic uncertainties on the background, acceptance, luminosity, theoretical cross-section and beam energy measurement [51, 62].

The experimental context of the precise measurement of the W mass in current and future experiments is presented in the following chapter.

Chapter 3

Current and future CERN experiments

*There is no result in nature without a cause;
Understand the cause and you will have no need of the experiment.
Leonardo Da Vinci*

Contents

| | | |
|------------|--|-----------|
| 3.1 | The LHC and HL-LHC | 30 |
| 3.1.1 | The machines | 30 |
| 3.1.2 | The CMS detector | 33 |
| 3.1.2.1 | Structure | 33 |
| 3.1.2.2 | HL-LHC upgrades | 36 |
| 3.1.2.3 | The High-Granularity Calorimeter | 36 |
| 3.2 | The Future Circular Collider project: FCC | 39 |
| 3.2.1 | Overview of the project | 39 |
| 3.2.2 | The FCC-ee machine | 42 |
| 3.2.3 | The CLD | 44 |

This chapter focuses on the experimental facilities used in this study.

In hadron collisions, the W mass is determined from transverse quantities such as the transverse mass, m_T . As explained in Chapter 2, the recoil is one of the components entering in m_T computation and is the most important parameter to mitigate the uncertainty on the transverse mass. The recoil is defined from all the reconstructed particles in the event except for the lepton. Therefore, its reconstruction strongly depends on the performance of the detector. The effect of the HGCal

resolution, granularity and acceptance on the recoil reconstruction, and by expansion, the expected performance of the CMS detector at HL-LHC in the W mass measurement are assessed in Chapter 6. The first part of this chapter introduces the LHC and its high luminosity phase, expected entering in operation in 2026. An overview of the CMS detector together with the upgrade of its forward calorimeter, designed to handle the challenging HL-LHC environment, are presented in the following section.

In the context of a precise measurement of the W mass at a post-LHC e^+e^- collider discussed in Chapter 7 and 8, a short summary of the FCC-ee project and a potential detector, CLD, used in this study are also introduced.

These experimental apparatuses are and would be the most complex ever built. As the result of the efforts of thousands of people over a long period, a meticulous presentation of each sub-system would be extremely long. Therefore, this chapter only gives a brief overview of the experimental framework used. More details can be found in [63, 21, 64, 65] for the HL-LHC and experiment upgrades and in [23, 66, 67, 24, 68, 69] for the overall FCC programme.

3.1 The LHC and HL-LHC

3.1.1 The machines

The Large Hadron Collider (LHC) is a particle collider (Figure 3.1) designed to accelerate protons and heavy ions to a centre-of-mass energy of $\sqrt{s} = 14$ TeV and $\sqrt{s} = 5.52$ TeV per nucleon, respectively. It is installed in a 27 kilometres circumference tunnel, about 100 metres underground, which previously hosted the LEP, at CERN on the Franco-Swiss border, near Geneva. It is the world's largest and most powerful particle collider ever built. The collisions take place at four crossing points, occupied by experiments designed for specific physics programmes. The two general-purpose and high-luminosity experiments ATLAS and CMS are dedicated to precise measurements of the SM quantities (including Higgs boson research) and searches for Beyond Standard Model (BSM) physics. The other two experiments, A Large Ion Collider Experiment (ALICE) and Large Hadron Collider beauty (LHCb), are mainly focused on the study of heavy ions and heavy-flavour physics respectively.

The protons, produced by ionising hydrogen atoms, are injected in the linear accelerator LINAC 2, which brings their energy to 50 MeV. They are then sent to a first circular pre-accelerator, the Proton Synchrotron Booster, where the incident beam is split and distributed into four stacked rings to reach 1.4 GeV. The beams are recombined into a single beam, which is transferred to the Proton Synchrotron (PS) pre-accelerator and accelerated up to 25 GeV. Finally, the protons are conveyed to the last pre-accelerating device, the SPS, where they reach an energy of about 450 GeV before they are introduced into the LHC via two independent vacuum pipes in opposite directions. After 20 minutes of acceleration with superconducting radio-frequency cavities operating at 400 MHz, the proton energies reach 7 TeV and the beams enter in collisions into the four detectors.

The same complex is also used for the lead ions injection which are accelerated into the LINAC 3 and the Low Energy Ion Ring (LEIR) before being transferred directly into the PS and then following the same acceleration path as protons.

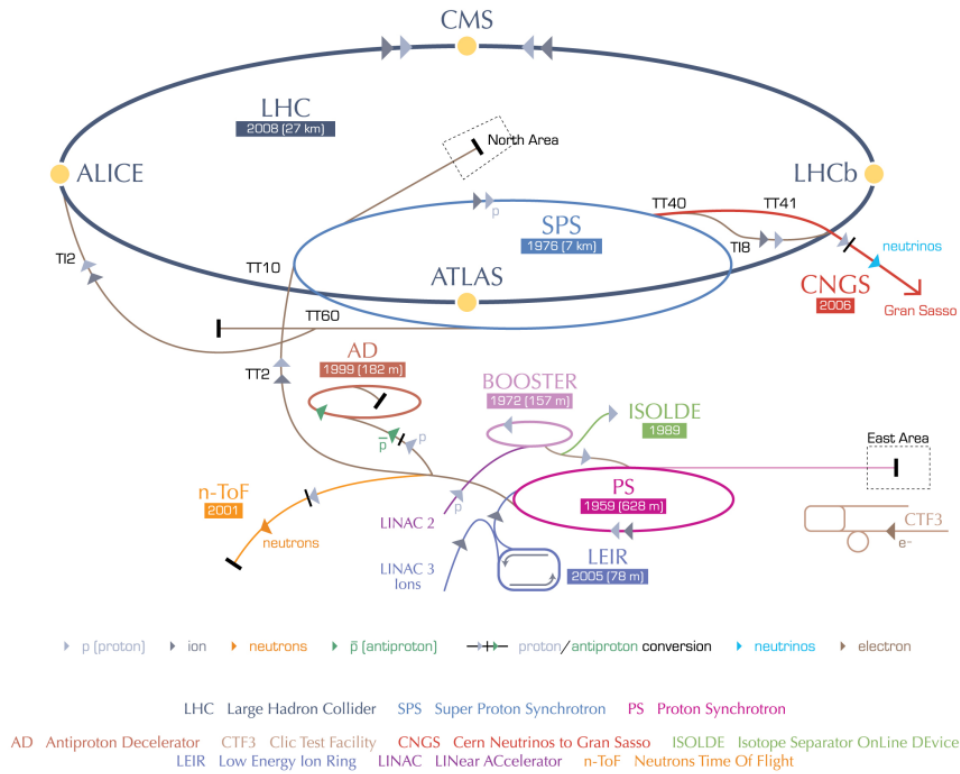


Figure 3.1 – CERN’s accelerator complex

The LHC, its pre-accelerators and its major experiments (yellow dots) are represented. The direction of hadrons from their injections into the LINAC 2 to the PS, SPS and LHC are indicated with blue arrows. Other CERN experiments are also drawn. Credit: CERN

After 12 to 24 hours of collisions, the overall beam quality gets degraded and it becomes unstable. The protons start interacting with residual gases inside the beam pipe or the beam spreads because of intra-beam interactions. The beam is then dumped and the LHC is filled with new particles.

The beam is not continuous but organised in 5 centimetre-long bunches of 1.14×10^{11} protons (before the first collisions) with a transverse section of about $10 \times 100 \mu\text{m}^2$ at the interaction point (IP). Bunches are separated by 25 ns, i.e. about 7.5 m for ultra relativistic particles. The particle beams are bent by a magnetic field of about 8.6 T generated by 15 metre-long superconducting magnets operating at a temperature of 1.9 K. To prevent collisions with stray molecules in the beam pipe, the hadrons circulate in a vacuum maintained at 10^{-13} atm. Besides the 1232 dipole magnets, sextupole and octupole magnets are respectively used to correct for chromatic effects and to stabilise the beams. Before each collision, the superconducting quadrupole magnets are also used to squeeze particles closer together in bunches and focus the beam to reach the highest possible luminosity.

With the beam energy, the instantaneous luminosity of the colliding beams, \mathcal{L} ($\text{cm}^{-2}\text{s}^{-1}$), is an important feature of a collider. The LHC is able to deliver a high instantaneous luminosity, key to the search for rare production and decay processes, or the study of standard model processes, such as the W and the Z bosons, with high accuracy. Under the hypothesis that the LHC is a

perfect circular machine with Gaussian bunches of transverse dimensions σ_x, σ_y , the luminosity can be expressed as [70]:

$$\mathcal{L} = f_{rev} \frac{N_1 N_2 n_b}{4\pi \sigma_x \sigma_y}, \quad (3.1)$$

where,

- $N_{1,2}$ are the number of protons per bunch. $N_1 = N_2 = 1.14 \times 10^{11}$;
- $N_b = 2808$ is the number of bunches per beam;
- $f_{rev} = 14$ MHz is the revolution (collision) frequency of two bunches;
- $\sigma_x = 100 \mu\text{m}$ and $\sigma_y = 10 \mu\text{m}$ are the transverse beam sizes at the IP.

These parameters lead to $\mathcal{L} = 3.10^{33} \text{ cm}^{-2}\text{s}^{-1}$. The exact definition of a collider instantaneous luminosity can be found in [64].

The integrated luminosity, \mathcal{L}_{int} (in b^{-1}), defining the statistical precision of a measurement over a certain period of time is defined as:

$$\mathcal{L}_{int} = \int \mathcal{L}(t) dt. \quad (3.2)$$

With σ the cross-section of a given process, the expected number of events of this process is directly linked to \mathcal{L}_{int} :

$$N_{evt} = \sigma \cdot \mathcal{L}_{int}. \quad (3.3)$$

The first proton-proton collisions in the LHC were recorded in 2009 at $\sqrt{s} = 900$ GeV and the first complete data-taking period (Run-I) occurred between 2010 and 2012. The accelerator operated at $\sqrt{s} = 7$ TeV during the first two years and at $\sqrt{s} = 8$ TeV in 2012, delivering an integrated luminosity of 6 fb^{-1} and 23 fb^{-1} respectively. During the first Long Shutdown (LS1), several modifications were made to the collider and its experiments, for a second data-taking period that took place between 2015 and 2018 (Run-II), starting at $\sqrt{s} = 13$ TeV and raised close to $\sqrt{s} = 14$ TeV. During this period, the instantaneous luminosity reached about $2 \cdot 10^{34} \text{ cm}^{-2}\text{s}^{-1}$ although the LHC was only designed to deliver $\mathcal{L} = 1 \cdot 10^{34} \text{ cm}^{-2}\text{s}^{-1}$. New upgrades to be implemented between 2019 and 2021 (LS2), will enable the machine to deliver a higher luminosity ; 300 fb^{-1} are expected by the end of Run-III in 2023.

The full exploitation of the LHC capacities is the first priority for particle physics in the European strategy [71]. Therefore, following Run-III, the machine and its experiments will be improved to deliver and handle a decisive luminosity increase. During this Phase-II of the LHC exploitation, the instantaneous luminosity is expected to reach $5 \cdot 10^{34} \text{ cm}^{-2}\text{s}^{-1}$. The machine would deliver 250 fb^{-1} per year with the objective of 3 ab^{-1} at mid-2030 ; ten times more than the LHC. The corresponding average pile-up (PU), mean number of collisions per bunch crossing, at this luminosity is 140 (with $1 \cdot 10^{34} \text{ cm}^{-2}\text{s}^{-1}$, the LHC average PU is 27). By design, the HL-LHC machine has the potential for 50% higher instantaneous and integrated luminosities, at the expense higher radiations and PU (up to 200 interactions per bunch crossing).

To face the harsh conditions generated by the highest luminosity or because they will be close to the end of their lifetime, several systems will be replaced and/or improved. The upgrade phase is therefore crucial not only for the full exploitation of the LHC physics potential, but also to enable the operation of the collider beyond 2025. A detailed description of the HL-LHC upgrade project, its technological and operational challenges as well as the physics opportunities are detailed in [64]. With the objective of maintaining excellent performance while collecting ten times more data in a challenging environment, the experiments will be improved as well. The next section gives a brief overview of the current structure of the CMS detector and briefly presents the sub-system upgrades for the HL-LHC. The last part of this section gives more details about the upgrade of the CMS endcap calorimeters.

3.1.2 The CMS detector

The CMS experiment is one of the two LHC multi-purpose detectors. It was designed for a rich physics programme detailed in [72] whose the guidelines are a precise study of the SM parameters (including the Higgs boson research) as well as the search for BSM phenomena. The Higgs boson has been discovered in 2012 by both CMS and ATLAS detectors.

3.1.2.1 Structure

The CMS detector [73], constructed cylinder-symmetrically about the horizontal beam axis with a diameter of 15 m, is 28.7 m long and weights 14 000 t. A highly uniform magnetic field of about 4 T, used to bend the charged particle tracks generated in the collisions, is produced by a superconducting solenoid, whose axis coincides with the colliding beams. A schematic view of CMS is shown in Figure 3.2 and a brief overview of the sub-detector components is given in the following. A detailed description of each element can be found in [73, 74, 75, 76, 77].

CMS is a succession of cylindrical sub-detectors through which the particles produced in the event interact. The information collected by all the sub-systems are combined to identify the incident particles and to measure their properties with a high precision. The experiment has a nearly perfect 4π hermeticity as the central barrel is closed with two endcaps perpendicular to the beam axis. From the IP located at the very centre of the detector, the sub-detectors are:

Tracker The tracking system is the innermost layer of the CMS detector. The charged particles leave electrical signals (hits) proportional to the energy lost by interacting with the material. From the hits, each particle trajectory is reconstructed and used to measure the particle charge and momentum, as well as its origin (vertex).

This detector is made of fourteen layers of finely segmented silicon pixels and silicon strips, which provide a fine-granularity and precision for the tracking of charged particles in a high particle multiplicity environment. The impact parameter resolution for high-momentum tracks is of in the order of $10\ \mu\text{m}$ and the strong magnetic field allows the track momenta to be measured at the percent precision [74]. The detector acceptance is limited to the pseudo-rapidity interval $|\eta| < 2.5$.

ECAL Surrounding the tracking system, the Electromagnetic Calorimeter (ECAL) [75] is designed to very precisely measure the energy of the electromagnetic shower generated by electrons

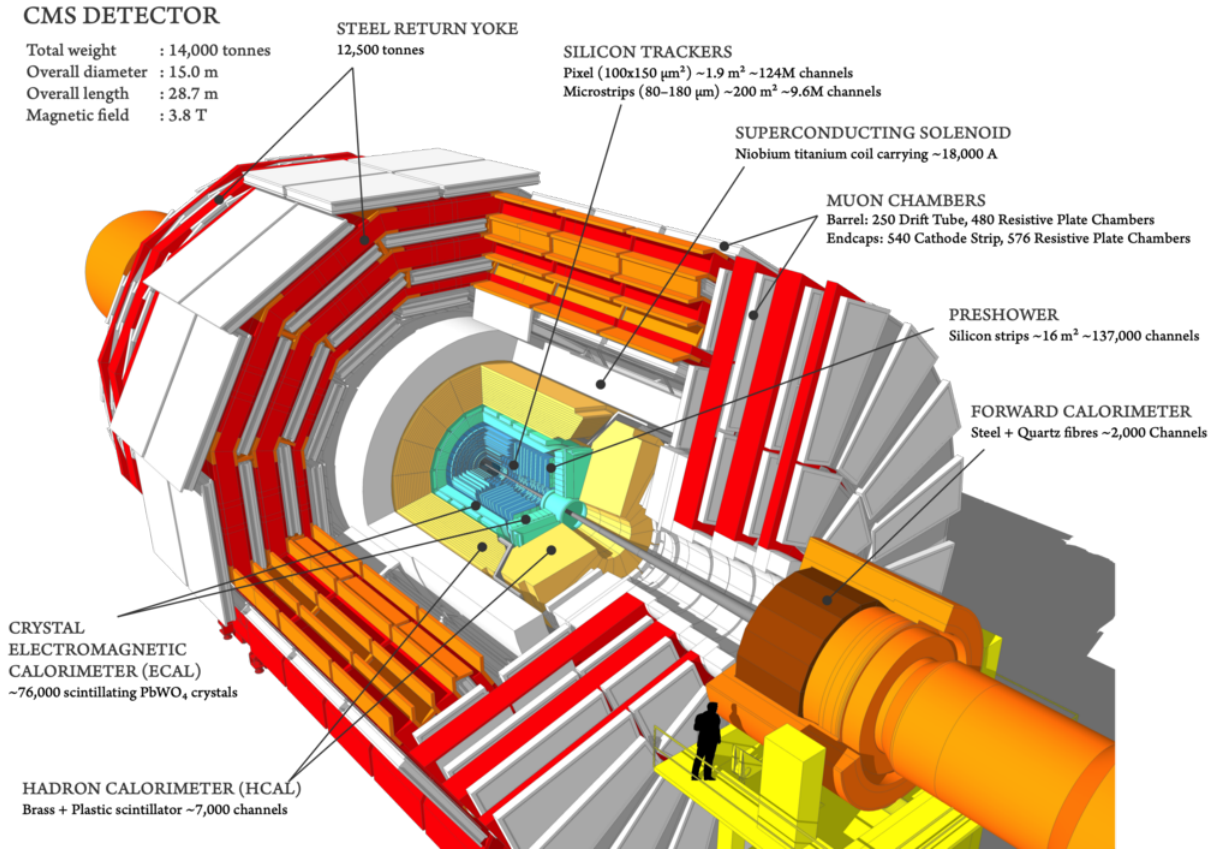


Figure 3.2 – Schematic representation of the CMS detector structure in Run II [20]

From the interaction point and moving outwards it includes: the tracking system, the electromagnetic and hadronic calorimeters, the superconducting solenoid and the muon chambers interleaved in the return yoke. On this Figure, both the barrel and the endcaps are represented.

and photons. It is an homogeneous and finely grained detector made of lead-tungstate (PbWO_4) crystals acting as both absorber and active detector material (scintillator). An electromagnetic particle passing through the crystal will produce a shower exciting the medium that emits light during its de-excitation. The energy deposited by the particle is proportional to the measured light, collected at the end of each crystal by a photodiode. The shape of an electromagnetic shower is described by:

- The Molière radius which characterises the shower width. It corresponds to the radius of a cylinder containing approximately 90% of the shower energy.
- The radiation length, X_0 , characterises the material in its power of longitudinal containment of an electromagnetic shower. It is a density-weighted depth of material into which a crossing electron reduces its initial energy E_0 to $\frac{E_0}{e}$.

The PbWO_4 crystals have a density of $8.3 \text{ g}\cdot\text{cm}^{-3}$, a short radiation length ($X_0 = 0.89 \text{ cm}$) and a small Molière radius ($R_m = 2.2 \text{ cm}$). They provide an excellent energy resolution parametrized as:

$$\frac{\sigma(E)}{E} = \frac{2.8\%}{\sqrt{E}} \oplus \frac{12.8\%}{E} \oplus 0.3\% \quad (3.4)$$

The first term is the *stochastic term* and results from the fluctuations in the development of the shower: fluctuations of the visible energy coming from nuclear effects (delayed photons from nuclear reactions, soft neutrons, binding energy contribute to a form of invisible energy), sampling fluctuations due to fluctuations of the deposited energy in the active medium (active and passive absorber layers interleaved for sampling calorimeters, such as HGCal, only), signal fluctuations from photo-electron statistics (for optical devices, such as $PbWO_4$, only). The thinner the sampling the better the resolution. The second term is the *noise term*. It is mainly due to the electronic noise of the readout chain to which a pileup noise must be added in high luminosity environments. The last term is the *constant term*. It results from various contributions such as inhomogeneities, leakages, dead channels or imperfect calibrations. At high energies (typically around 200 GeV for the CMS central barrel part of the electromagnetic calorimeter), the constant term is the dominant contribution to the resolution. In the case of hadronic showers the fluctuations in the electromagnetic shower fraction, which are non Gaussian, are a major contribution to this term. In general the hadronic component of a hadron shower produces a smaller signal than the hadronic component ($e/h > 1$). The hadron energy resolution is degraded and the response is non linear with energy. Although this contribution is energy dependent, it is often approximated by a constant term.

In front of each endcap, a pre-shower detector is used to improve the π_0 rejection and to help with the interaction-vertex identification. The ECAL detector covers the pseudo-rapidity range of $1.479 < |\eta| < 3$.

HCAL The energy of hadronic particles is measured in a brass-scintillator sampling calorimeter named Hadronic Calorimeter (HCAL) [76]. The particles reaching the HCAL are heavier than the electromagnetic particles, stopped in the ECAL, and initiate larger and deeper showers. The shape of an hadronic shower is characterised by the nuclear interaction length (λ_I), which is the mean distance travelled by a hadron before undergoing an inelastic nuclear interaction. The effective depth of the hadron detector in CMS is about 11 λ_I (1 λ_I comes from the ECAL). The original pseudo-rapidity range covered was up to $|\eta| = 3$, and was extended to $|\eta| = 5$ with an additional iron/quartz-fibre endcap calorimeter (HF). The HCAL resolution is:

$$\frac{\sigma(E)}{E} = \frac{110\%}{\sqrt{E}} \oplus 9\% \quad (3.5)$$

Solenoid magnet This magnet is large enough to host both the tracking and calorimetry systems. It provides a strong magnetic field curving the trajectory of charged particles in the silicon tracker. The charged particles momentum is very precisely derived from the curvature of the particle path. The CMS coil [78] is made of NbTi superconducting wires. It is the largest ($6.3 \times 13 \text{ m}^2$) and the most powerful superconducting solenoid ever built and it produces a uniform magnetic field in the beam direction of approximately 4 T. As the vacuum pipe accommodating the beams, the magnet is cooled down to the operating temperature of 1.9 K. A massive steel return yoke returns the magnetic flux.

Muon system The muon detector is the outermost sub-detector of CMS. Interleaved with the return yoke, various gaseous detectors perform a precise detection of muons. It is made of drift tubes in the barrel and cathode strip chambers and resistive plate chambers in the endcaps, covering the pseudo-rapidity range up to $|\eta| < 2.5$. The muons are not stopped by the calorimeters and are

identified by the ionisation of atoms, while passing through the gas volumes. The muon tracking system has a very high identification efficiency, above 95% over the whole region.

The other sub-systems such as the two-stage trigger system, which enables the data acquisition, or the luminosity telescopes, which measure the instantaneous luminosity are not described here, however, information on both of them is available in [79] and [80, 81].

3.1.2.2 HL-LHC upgrades

The CMS detector has excellent performance in terms of efficiency, resolution and background rejection, and the ultimate objective of the HL-LHC upgrade is to preserve them. Due to the high expected integrated luminosity, the two major challenges are the high radiation and PU levels.

The damages caused by an integrated luminosity of about 3 ab^{-1} will be different from a sub-detector to another [21]:

Tracker The radiation will affect the electrical properties of the silicon, resulting in lower signals from charged particles, and the PU will introduce more hits leading to mismeasured or misidentified tracks. The tracker system will be completely replaced by a high-radiation tolerant and high-granularity tracker [82], using thin planar silicon sensors segmented into very small pixels. This segmentation will improve the impact parameter resolution and the two-tracks separation. The tracking acceptance will be extended up to $|\eta| = 4$.

Calorimeters In the barrel, the PU level will introduce noise in the photo-detectors, leading to extra energy measurements. An upgrade of the electronics is therefore required [83]. In the barrel, almost the same radiation damage is expected after 3 fb^{-1} or 3 ab^{-1} . It is not the case for the forward region where 3 ab^{-1} , mainly in the innermost part as shown on Figure 3.3, will introduce a significant deterioration of the detector performance. Moreover, the PU increase will stress the background rejection capability; therefore, the forward detector will be replaced with a radiation tolerant, high granularity and timing detector. More detail of the endcap upgrade is given in Section 3.1.2.3 [65].

Muon system There are three types of upgrade of the muon detector for Phase-II: the upgrade of the existing muon system and its electronics to maintain their longevity and high-level performance, a new detector in the forward region $1.6 < |\eta| < 2.4$ for additional measurement points and the extension of the muon coverage up to $|\eta| < 3$ [84].

3.1.2.3 The High-Granularity Calorimeter

The HGCal has been chosen to replace the existing forward CMS calorimeter to cope with the harsh environment in terms of PU and radiations expected at the HL-LHC. This section gives an overview of the HGCal structure; a full description of the HGCal structure can be found in [21, 65].

The longitudinal structure of the upper half of one of the two endcaps is presented in Figure 3.4. The HGCal regroups both the electromagnetic (Endcap Calorimeter Electromagnetic (CE-E)) and hadronic (Endcap Calorimeter Hadronic (CE-H)) calorimeters. It covers the region $1.47 < |\eta| < 3.0$ and there are discussions about extending the acceptance up to 4.0. In both electromagnetic and innermost parts of the hadronic section, where high radiation levels are expected (up to $10^{16} \text{ n}_{eq}/\text{cm}^2$),

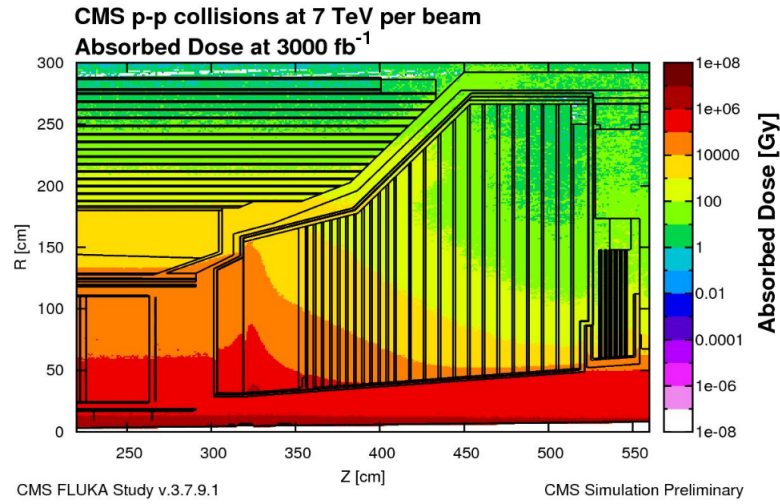


Figure 3.3 – Expected radiation dose over the current calorimetry of the CMS detector in HL-LHC conditions [21]

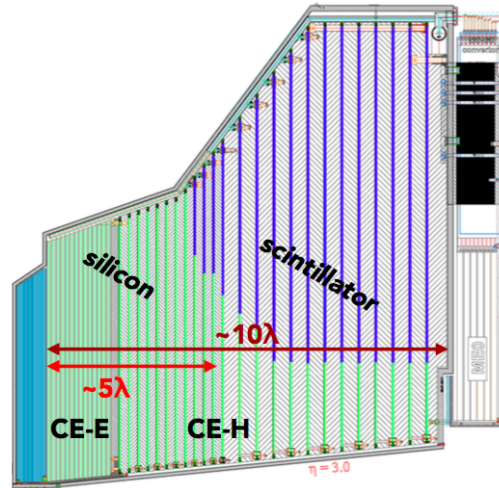


Figure 3.4 – Longitudinal upper half structure of one of the endcap calorimeters. The electromagnetic part (CE-E) is the closest to the interaction point, followed by the hadronic part (CE-H)

The silicon sensors (green) are in the high-radiation region while the scintillator tiles (blue) are used in the low-radiation region. [85]

the silicon has been chosen as active material because of its tolerance. In the outermost region of the hadronic detector, plastic scintillator tiles are used.

CE-E is a full silicon detector with a thickness of 34 cm divided in 28 sampling layers, for a total depth of about $26 X_0$ and $1.7 \lambda_I$. The silicon sensors are mounted on both sides of 14 copper plates that are interspaced by tungsten plates as an absorber material. These plates also provide the mechanical rigidity and host the cooling pipes that maintain the detector at -30 C° to limit the leakage current caused by radiations. The plates are rotated by 10 degrees with respect to the others to prevent detection losses at the limits.

CE-H is divided into 22 sampling layers, bringing the total longitudinal calorimeter depth to

1.5 m and the total calorimetry thickness to $10.7 \lambda_I$ (including CE-E). The first 8 layers of the CE-H section are fully made of silicon planes, while the other layers are hybrid planes of silicon and scintillator plastic tiles. The frontier between the silicon and the scintillator is determined by the radiation level and varies from a layer to another. Stainless steel is used as an absorber. Layouts of full-silicon and hybrid silicon-scintillator layers are shown on Figure 3.5.

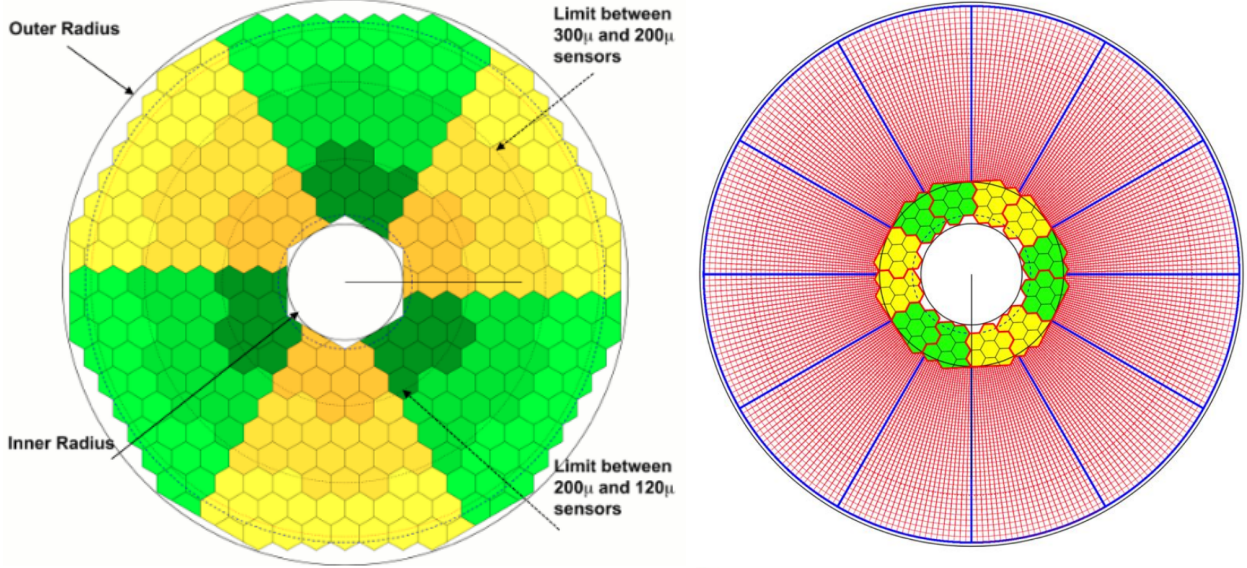


Figure 3.5 – Layout of a full silicon (left) and hybrid silicon-scintillator (right) layers of the HGCal detector

On the left, the different thickness are represented by radial changes in darkness of colour. The 60 degrees sectors (cassettes) making up each layer are shown by the alternative colours. On the right, the tiles are represented in red and the silicon hexagonal sensors in green and yellow. The 30 degrees sectors are delimited in blue. [21].

The silicon sensors are hexagonal blocks from 8" p-type silicon wafers, arranged as shown on Figure 3.5. The sensor thickness and cell size are η dependent to minimise the radiation damages and to provide a better shower separation in the high-occupancy region. The different thicknesses are 120, 200 and 300 μm . Each of the hexagonal wafers is divided in 1.18 or 0.52 cm^2 hexagonal cells for an optimal use of the surface (1.3 gain with respect to square sensors [21]). Table 3.1 gives an overview of the silicon cells properties.

Table 3.1 – Properties of the active material for full silicon layers [21]

| Thickness [μm] | 120 | 200 | 300 |
|--------------------------------------|---------------------|---------------------------|----------------------|
| Radius [cm] | $R < 70 \text{ cm}$ | $70 < R < 100 \text{ cm}$ | $100 \text{ cm} < R$ |
| cell size [cm^2] | 0.52 | 1.18 | 1.18 |
| Stochastic term of energy resolution | 24.3% | 21.4% | 19.9% |

The scintillator modules are square tiles made of plastic scintillator, varying in size from 4 to 32 cm^2 (from small to large radius), and arranged in a $r - \Phi$ grid. Their design is based on the SiPM-on-tile technology used in the CALICE AHCAL prototypes [86]. The readout is performed

by on-tile SiPM photodetectors, directly implemented on the centre of the tile, which provide an uniform response. The boundary between silicon sensor and scintillator is not fixed and is determined by the region where the integrated dose is low (≤ 3 kGy) and the fluence limited to 8×10^{13} n_{eq}/cm². This low radiation region is occupied by the scintillators and guarantees good performance of the calorimeter during the whole HGCal lifetime. As a result, the region $|\eta| \geq 2.4$ is exclusively covered by silicon sensors. Table 3.2 lists several characteristics of a layer made of an assembly of silicon sensors and scintillator tiles.

Table 3.2 – Properties of the active material for hybrid layers, with both silicon and scintillators [21]

| Material | Silicon | Silicon | Scintillator |
|--------------------------------------|-------------------|-------------------|----------------------------------|
| Thickness | 200 μm | 300 μm | 3 mm |
| Largest outer radius [cm] | R = 100 cm | R = 160 cm | R = 235 cm |
| Smallest inner radius [cm] | R = 45 cm | R = 80 cm | R = 90 cm |
| cell size [cm ²] | 1.18 | 1.18 | 2×2 to 5.5×5.5 |
| Stochastic term of energy resolution | 24.3/21.4/19.9% | | 75% |

With its 50 layers, the HGCal has a high longitudinal granularity allowing a good energy resolution, particle identification and PU rejection: the energy resolution is not as good as that of homogeneous calorimeters (such as PbWO₄) but is still good enough. Moreover, it is transversely segmented, with tiny silicon cells of about 0.52 and 1.18 cm² for a total of over 6 million channels. The fine lateral granularity will ensure a good adjacent shower separation. This high granularity in both transverse and longitudinal directions will facilitate the particle flow analysis.

The HGCal also has excellent timing performance [21] reaching 25 ps time resolution thanks to the fast response of the silicon sensors and the design of the front-end electronic. Such time resolution helps for the particle flow reconstruction: correct hit assignments between overlapping showers, identification of the selected interaction vertex and background event suppression. The timing information will significantly improve the PU rejection capability.

3.2 The Future Circular Collider project: FCC

The FCC is one of the four post-LHC projects requested by the European strategy [71]. Kicked-off in 2014 following these recommendations, a large effort has been provided by the 136 institutes (34 countries) of the international FCC collaboration, leading to the publication of a four-volume CDR [67, 24, 68, 69]. A quick presentation of this ambitious project, and in particular, FCC-ee, the energy frontier e^+e^- collider is given in the following section.

3.2.1 Overview of the project

The FCC infrastructure would be hosted in a 100 km tunnel close to CERN in the Geneva area as shown on Figure 3.6. It is an integrated project with a 100 TeV proton-proton collider (FCC-hh) as the ultimate goal and a high luminosity e^+e^- collider (FCC-ee) as a potential first step. Lepton-hadron collisions and, similarly to the LHC, heavy-ion collisions are two optional programmes with the hadron collider. This ambitious project also offers the possibility of a muon collider with colli-

sion energies from 3 TeV to 14 TeV [87].

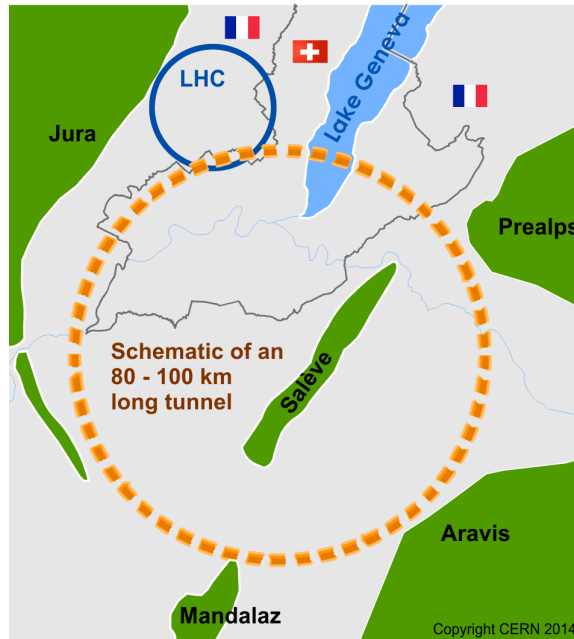


Figure 3.6 – Schematic view of the 100 km Future Circular Collider in the Geneva area [22]

The whole FCC programme has a very high physics potential in particular because of the full complementarity between the machines. A complete description of the physics opportunities is available in the CDRs but in a nutshell:

- Measurement of the electroweak gauge bosons properties and electroweak observables (m_Z , m_W , m_H , m_{top} , $\sin^2\theta_W$, R_b , $\alpha_{QED}(m_Z)$, $\alpha_s(m_Z, m_W, m_\tau)$, Higgs and top quark couplings) with unprecedented precision. These observables play a key role in testing the Standard Model or searching for small deviations from expectations through which new physics would manifest itself. Electroweak measurements are crucial elements to achieve the full potential of the precision Higgs programme.
- The FCC Higgs physics programme will extend the range and complete our understanding of the Higgs boson properties allowing to measure, for instance, the Higgs couplings to other SM particles with a sub-percent precision. With such high precisions, the Higgs boson becomes an exploration tool, providing a direct and indirect probe of the new physics and will help to characterise the nature of possible discovery.
- FCC is a door to BSM physics with direct observations of new particles thanks to the large reachable mass range. Possible candidates for Dark matter (weakly interactive massive particles) and matter-antimatter asymmetry (particles with masses below one TeV witnessing of a sufficient violent transition phase) could also be discovered.
- Probing the parton structure of the proton with unprecedented accuracy would provide high precision measurements of the strong coupling constant and the parton density functions (PDFs). These accurate measurements are an essential input for the FCC-hh precision programme and increase the sensitivity to new phenomena.

- The heavy-ion collisions at high energy and luminosity will improve the study of quark and gluon collective properties.

As a long-term goal, the FCC-hh defines the accelerator infrastructure. As shown by the layouts on Figure 3.7, the FCC-ee and FCC-hh would have a common footprint except around the two main IPs A and G for both machines. The FCC-ee asymmetric beam lines around the interaction region are introduced to limit the synchrotron radiation effect in the detector. The beam crossing angle would be equal to 30 mrad. A possible development with 4 IPs and detectors is under consideration for both machines, to increase the total integrated luminosity.

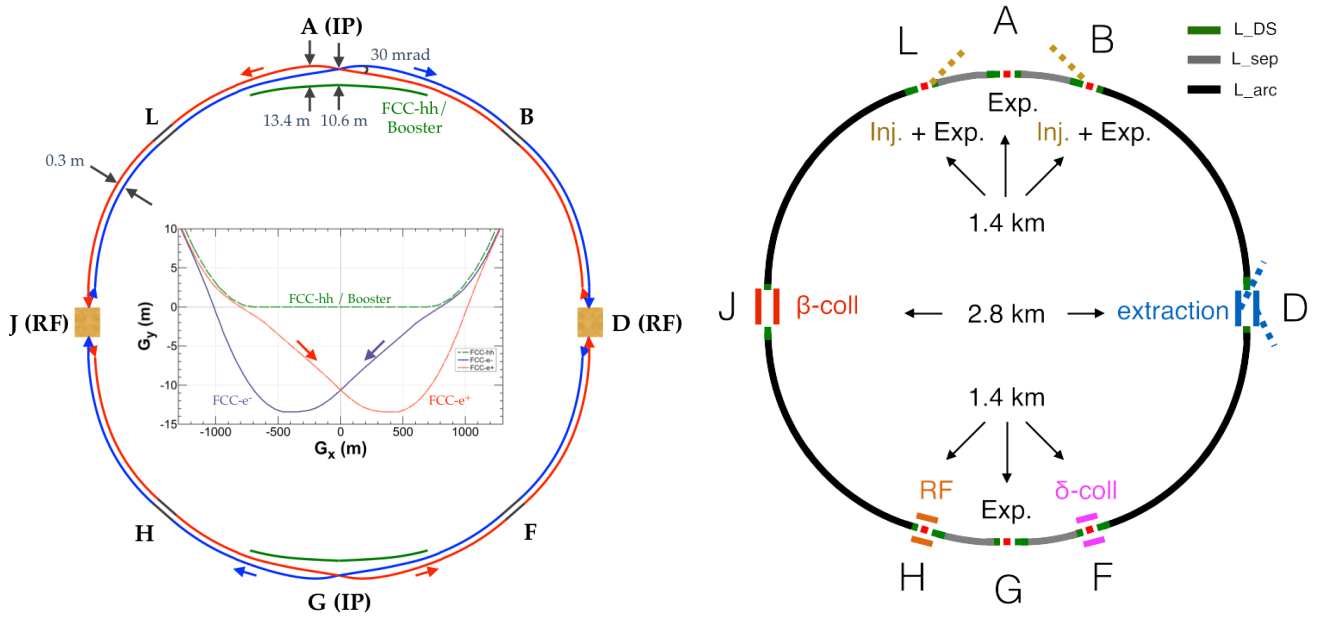


Figure 3.7 – Schematic implementation of the FCC-ee (left) and FCC-hh (right) infrastructures and a zoom on the particle trajectories in the G interaction point region at FCC-ee (middle of the left layout) [22]

The FCC-hh infrastructure can be directly used by the FCC-ee first step. The two main experiments, in A and G, will share the same cavern for both machines.

The FCC-ee step can start right after the HL-LHC exploitation. The FCC integrated project technical schedule is given in Figure 3.8. The 15-years of FCC-ee operation provide time for the R&D, technical design and production of the FCC-hh 16 T magnets.

The cost for this complete project was estimated at 28.6 billions of CHF; 17 billions (4 billions) CHF for the FCC-hh (FCC-ee) collider and injector, and 7.6 billions CHF for the common civil engineering and technical infrastructure. The 16 T magnets enabling 100 TeV hadron collisions in the 100 km ring represent 9.4 billions CHF of the FCC-hh collider cost and require a strong R&D programme. Such technology does not exist yet but very promising 14 T (possible 15 T) magnets are already achievable [88]. These first results coupled with the additional development time allocated to the hadron collider due to the multiple pre-steps, suggest a possible cost reduction.

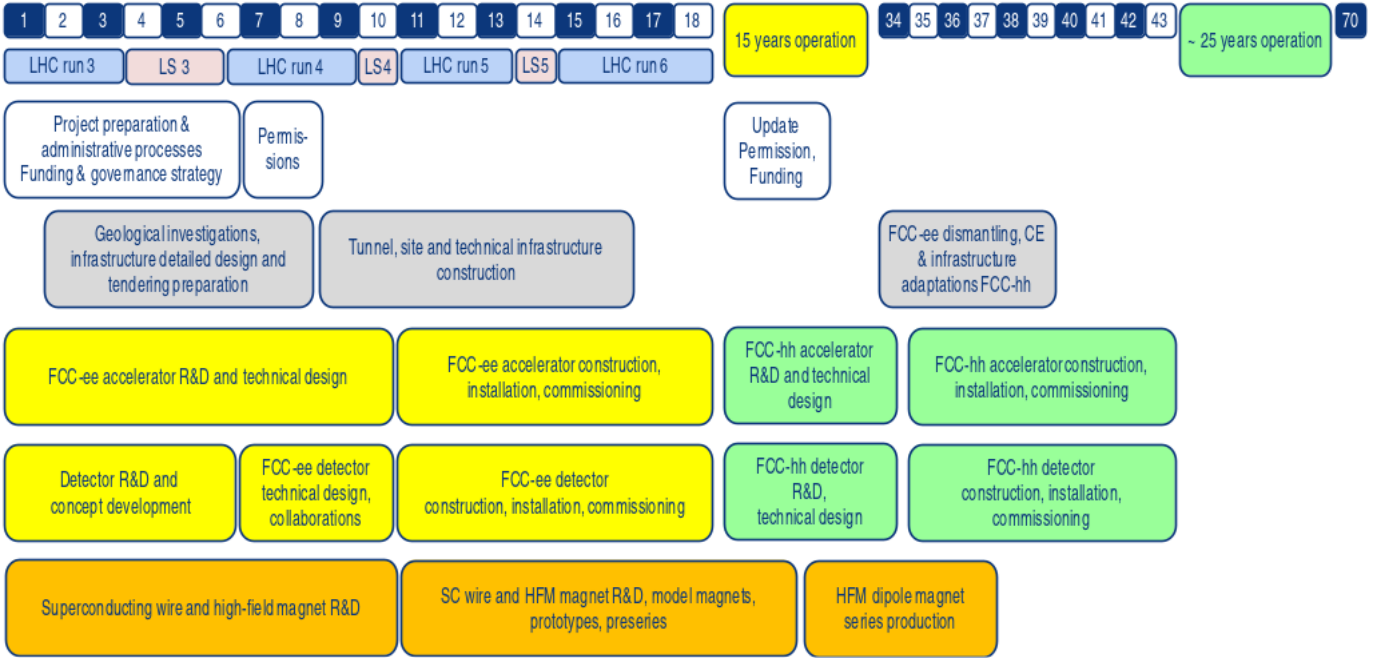


Figure 3.8 – FCC integrated project technical schedule [22]

Year 1 corresponds to the beginning of the LHC Run-III era planned to start in early 2021. Year 18 is the end of the HL-LHC phase that should take place in 2039.

3.2.2 The FCC-ee machine

The FCC-ee physics operations would start around 2040, directly after HL-LHC era. The full description of the FCC-ee programme is available in the CDR volume 2 [24]. As shown on Table 3.3, it would operate at multiple centre-of-mass energies \sqrt{s} , producing 5×10^{12} Z bosons ($\sqrt{s} \sim 91$ GeV), 10^8 WW pairs ($\sqrt{s} \sim 160$ GeV), 10^6 Higgs bosons ($\sqrt{s} \sim 240$ GeV) and over 10^6 $t\bar{t}$ pairs ($\sqrt{s} \sim 350\text{--}365$ GeV). With such statistics FCC-ee would be an electroweak, flavour and Higgs factory enabling the study of the electroweak and strong interactions with unprecedented precisions. The indepth study of the four heavy particles of the SM opens a very unique discovery potential.

As shown on Figure 3.9, the FCC-ee proposal is the electron-positron collider with the highest luminosity potential at each centre-of-mass energy, compared to the other e^+e^- projects¹. Preliminary studies with four IPs instead of two show that the luminosity would be almost doubled [67]. Then with four IPs two years at the Z pole and one year at the WW pair production threshold would be sufficient to reach the same integrated luminosity as after six years with two IPs. The saved years could be used for the study of the Higgs boson and the top observables that are statistically limited. The discovery potential of the FCC-ee project would be enhanced and a 5σ sensitivity to the Higgs self-coupling attainable.

To be able to measure the SM properties with unprecedented accuracy and increase the sensitivity of these measurements to new physics, requirements are set on the detectors and the IP inner region. The complex inner region (the Machine-Detector Interface, MDI) with a beam crossing an-

¹The circular collider, CEPC [89] and two linear colliders, International Linear Collider (ILC) [90], and Compact Linear Collider (CLIC) [91], are the other e^+e^- collider proposals. They will not be discussed.

| Working point | Z, years 1-2 | Z, later | WW | HZ | t \bar{t} | |
|--|----------------------|----------|-----------|--|---|------|
| \sqrt{s} (GeV) | 88, 91, 94 | | 157, 163 | 240 | 340-350 | 365 |
| Lumi/IP ($10^{34} \text{ cm}^{-2} \text{ s}^{-1}$) | 115 | 230 | 28 | 8.5 | 0.95 | 1.55 |
| Lumi/year (ab^{-1} , 2 IP) | 24 | 48 | 6 | 1.7 | 0.2 | 0.34 |
| Physics Goal (ab^{-1}) | 150 | | 10 | 5 | 0.2 | 1.5 |
| Run time (year) | 2 | 2 | 2 | 3 | 1 | 4 |
| Number of events | 5×10^{12} Z | | 10^8 WW | 10^6 HZ + 25k WW \rightarrow H | 10^6 t \bar{t} +200k HZ +50k WW \rightarrow H | |

Table 3.3 – Run plan for FCC-ee operations in the configuration of two interaction points. This table shows the centre-of-mass energies, instantaneous luminosities per IP and the integrated luminosity per year over the two interaction points (185 days of physics and 75% efficiency). The physics goals set the total luminosities, which in turn require the run time at each energy. The yearly integrated luminosities are given with a conservative 10% margin. Table taken from [23]

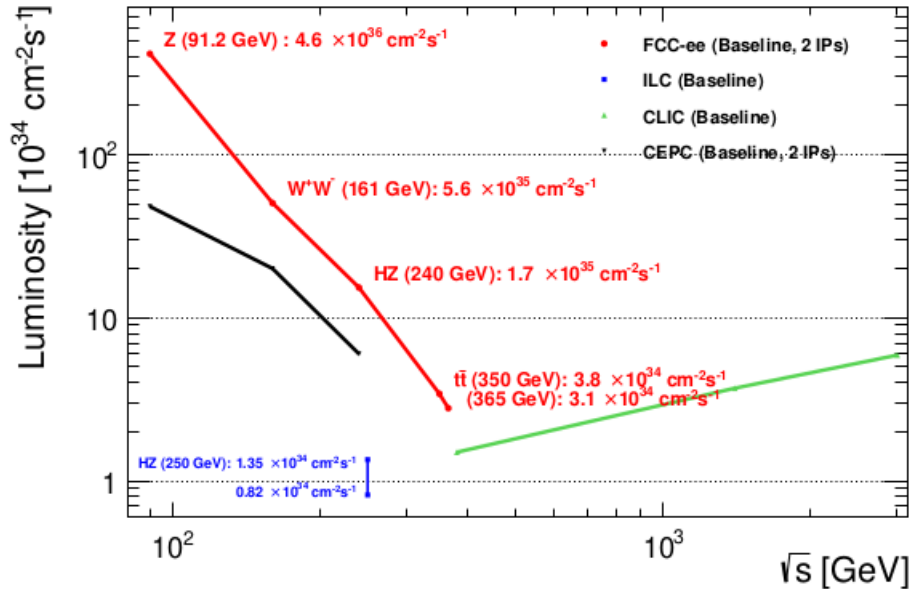


Figure 3.9 – Luminosity as function of the centre-of-mass energy for FCC-ee summed over two interaction points, compared to the estimated luminosities of the other e^+e^- collider projects [23]

The luminosities indicated for the FCC-ee project are given within a 10% safety margin.

gle of 30 mrad, the final quadrupoles, screening and compensating solenoids and the luminometers, govern the detector geometry close to the beamline and limit the magnetic field to 2T in the detector. The MDI will not be described; a detailed presentation of the MDI general requirements at FCC-ee is available in the CDR [24]. To fit the required performance, the detector subsystems must exhibit excellent heavy-flavour tagging capability, a precise particle identification, excellent tracking and PF reconstruction performance, excellent acceptance definition and state-of-the-art energy and angular resolutions for leptons, photons and jets. Three detector benchmarks have been designed, the International Detector for Electron-positron Accelerators (IDEA), the CLD and an option using Noble liquid Argon calorimeter. The study of the W mass at the FCC-ee was performed using the

CLD described in the following section.

3.2.3 The CLD

The CLD would be a multi-purpose silicon-based detector. It is based on an updated version of the CLIC detector model [92], that has been adapted to the FCC-ee specificities.

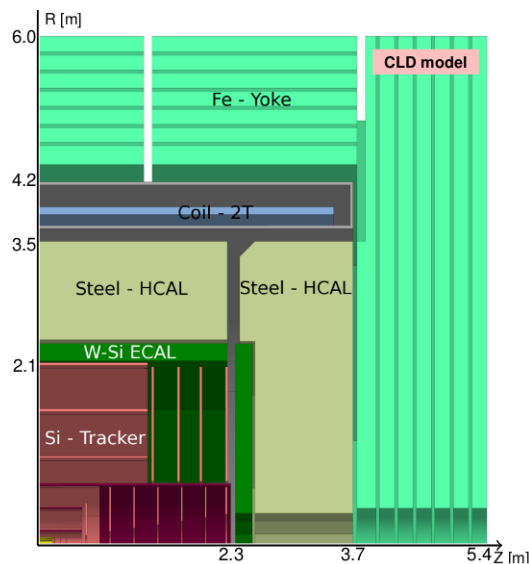


Figure 3.10 – Longitudinal top right quadrant view of the CLD detector concept [24]

The CLD has a cylindrical structure with an overall height of 12 m and overall length of 10.6 m. The longitudinal cross-section of the top right quadrant is shown on Figure 3.10. It is a succession of several cylindrical sub-detectors and from the IP the constituents are:

- A full silicon tracking system composed of a silicon vertex detector and a silicon tracker providing more than 12 hits per track.

The vertex detector is made of three double layers of silicon pixels of size $25 \times 25 \mu\text{m}^2$. The thickness of the vertex detector is $0.6\%X_0$ for each double layer in the barrel and $0.7\%X_0$ for each double disk in the forward region. The single-point resolution is $3 \mu\text{m}$. This detector is very close to the IP (17 mm) thanks to a strong beam focusing.

The tracker is a silicon pixel and microstrips detector. The inner tracker consists in three barrel layers and seven forward disks and the outer tracker completes the system with three barrel layers and four forward disks. The material budget is $11\% X_0$ ($20\% X_0$) in the barrel (forward) region. The tracker has good reconstruction performance with a single-point resolution of $5 \times 5 \mu\text{m}^2$ for the innermost disk and $7 \times 90 \mu\text{m}^2$ for all other layers.

The full tracking efficiency and momentum resolution of the central region have been studied by simulation. As shown on Figure 3.11, the tracker resolution reaches $5 \times 10^{-5} \text{ GeV}/c^{-1}$ for high momentum particles. The same study also showed that the tracking is fully efficient

for particles with transverse momentum above 1 GeV/c and falls to 96% efficiency for $p_T = 0.1$ GeV/c [93].

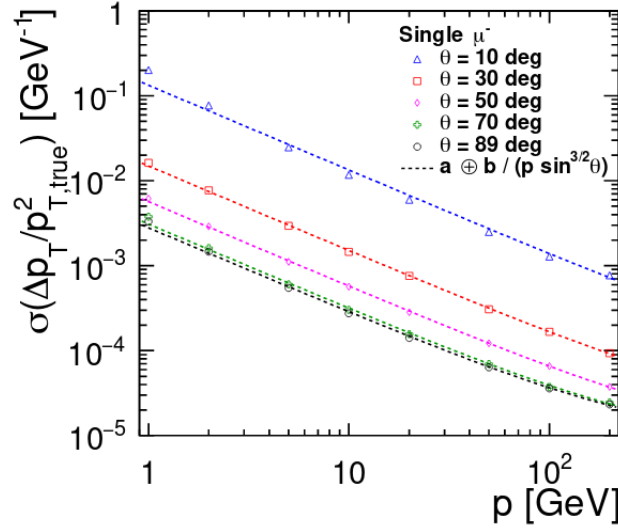


Figure 3.11 – Transverse momentum resolution of the tracker for single muons as a function of the momentum at a fixed polar angle [24]

- High granularity calorimeters made in silicon-tungsten for the ECAL and scintillator-steel for the HCAL.

The 20 cm long ECAL calorimeter is a succession of 40 identical layers segmented in 5×5 mm² cells. The total depth is about $22 X_0$ and $1 \lambda_I$. The fine segmentation is important for a good energy resolution. With 40 layers, the stochastic term is $15\%/\sqrt{E}$. By reducing the number of layers to 30 and keeping a constant depth of about $22 X_0$, the stochastic term is degraded to $17.6\%/\sqrt{E}$.

The HCAL accommodates 44 sampling layers in about 117 cm ($5.5 \lambda_I$ deep) for an overall depth of $6.5 \lambda_I$ combining ECAL and HCAL. The polystyrene scintillators are 3 mm thick with a tile size of 30×30 mm². The CALICE calorimeter design, based on the SiPM-on-tile technology [86] is also considered [94]. The expected jet-energy resolution of this calorimeter is $50\%/\sqrt{E}$.

- A superconducting solenoid providing a 2 T homogeneous magnetic field. The coil accommodates the tracking and the full calorimetry systems. The magnetic field is limited to 2 T to avoid luminosity losses and emittance blow up generated by the residual transverse fields, resulting from the 30 mrad beam crossing angle.
- A steel return yoke (1.5 thick steel) interleaved with 6 layers of resistive plate muon chambers with cells of 30×30 mm².

The following chapter presents the software that were used to simulate and reconstruct the events in the different present studies of the W mass.

Chapter 4

Events simulation and reconstruction

*"Theory provides the maps that turn an uncoordinated set of experiments
or computer simulations into a cumulative exploration."
David Goldberg*

Contents

| | | |
|------------|---|-----------|
| 4.1 | LHC and HL-LHC | 48 |
| 4.1.1 | CMSSW | 48 |
| 4.1.1.1 | Event simulation | 48 |
| 4.1.1.2 | CMS event reconstruction at LHC | 49 |
| 4.1.1.3 | CMS event reconstruction at HL-LHC | 50 |
| 4.1.1.3.1 | Event reconstruction | 50 |
| 4.1.1.3.2 | Performance of the physics objects reconstruction | 51 |
| 4.1.2 | Delphes | 52 |
| 4.2 | FCC-ee | 54 |
| 4.2.1 | Event simulation | 54 |
| 4.2.1.1 | Generator step | 54 |
| 4.2.1.2 | Detector step | 56 |
| 4.2.1.2.1 | Detector implementation | 56 |
| 4.2.1.2.2 | Particle interactions in the detector | 58 |
| 4.2.2 | Event reconstruction | 60 |

To a priori estimate the expected physics potential of an experiment and to optimise its layout, pseudo-data are generated to emulate future real data. PYTHIA [49] is the most widely used event

generator to study the physics performance of the detectors. Event generators simulate creation of particles from an e^+e^- or pp interaction (event) and their subsequent decays until they reach a stable state within the acceptance of the experiment. The 'data' output from the generators are in the form of four-momentum vectors for all the produced particles. The generator level information of particle kinematics and the decay tree are kept as the 'MC truth', which is then used to validate the various analyses. The event is then placed in a simulated detector environment, which input is the description of the detector geometry. The pseudo-data will then be reconstructed as real data would be. This chapter introduces the different simulation and reconstruction software used in the current analyses of the W boson.

4.1 LHC and HL-LHC

4.1.1 CMSSW

4.1.1.1 Event simulation

The CMS Software (CMSSW) [95, 96] is a framework based on GEANT4 [97], used to process simulation and reconstruction of the CMS detector data. Several versions (releases) are available, corresponding to different phases of CMS. The release 8 is the most advanced simulation of the current CMS experiment. All releases above 8 (from 9 to 11) correspond to the software implementations for the HL-LHC upgrade.

The CMSSW framework can be used transparently with both detector and MC data. The full detector characteristics, as described in Chapter 3, are very precisely implemented. To perform quick studies with a personal analyser or a detector component for instance, a Fast Simulation tool of each subdetector is also integrated. A Fast Simulation of the HGCal detector was absent and has been developed as presented in Chapter 5.

Real data or simulated data, are identified by their particle four-momenta. These vectors are processed by GEANT4, that contains all the geometry, material and physics processes description, for the hits simulation (*SimHits*). Using different framework modules (producers, analysers, filters), an output ROOT file is produced to be used in the analyses.

The modus operandi used to identify and reconstruct all the stable particles in the final state from the SimHits, the Particle-Flow (PF) algorithm, is described in Section 4.1.1.2. The reconstruction principle of the tracks and clusters, the basic PF elements, within the CMS detector, is explained hereafter. The details of the particle identification and reconstruction method at CMS can be found in [98]. The tracks are the trajectories of the charged particles. They are reconstructed from the hits generated in the tracking layers along the way of the charged particles, and they are subsequently grouped together to reconstruct the primary vertex. A track is reconstructed from at least three hits in total and is required to have a p_T larger than 200 MeV/c. The clustering is performed separately in ECAL and HCAL. A cell passing the thresholds of 80 MeV (barrel) and 300 MeV (endcap) for ECAL and 800 MeV for HCAL, is identified as a *seed*. A cluster is formed from a seed aggregating neighbour cells of a seed (at least one corner in common) with energy larger than two times the noise level. The energy and position of the resulting clusters are computed using a Gaussian mixture model [98], sharing a Gaussian energy deposit between the seeds of a same cluster. The neutral

particles are reconstructed as a clear signature from an isolated cluster, if no track can be associated to it, or from an energy excess, if they overlap with charged particle clusters. Once the clusters are identified, the calorimeter energy is calibrated, as explained in [98], to be as close as possible to the true particle energy.

4.1.1.2 CMS event reconstruction at LHC

The philosophy of the PF algorithm is to entirely make use of the various subdetectors information for connecting the PF elements and for reconstructing the event. Before the particle reconstruction, the association, if any, between the tracks and clusters have to be found. Each track is extrapolated from its last tracker hits to the calorimeters, at a depth corresponding to the maximum of typical electron longitudinal shower profile in the ECAL, and at one interaction length in the HCAL. A track is linked to a cluster if its extrapolated position is within the cluster area, hence if the distance between the track impact and the cluster position is smaller than the cluster radius. This link distance quantifies the quality of the link and in case of multiple association of tracks (clusters) with a single cluster (track), the smallest link distance is retained. The cluster-to-cluster link between ECAL and HCAL is established when the most granular calorimeter clusters (ECAL) are within the cluster envelope of the less granular (HCAL). As previously, when multiple HCAL clusters are associated to the same ECAL cluster, the association corresponding to the smallest distance is kept. Any track with a p_T larger than 0.5 GeV/c and a total momentum p larger than 2.5 GeV/c is extrapolated to the muon spectrometer. The extrapolated track and the spectrometer segment are matched if their absolute distance in the x direction of the detector is smaller than 3 cm or if the pull (ratio of this distance to its uncertainty) is smaller than 4 [98]. Once these PF blocks are built, the single particles as well as jets are finally reconstructed by the algorithm.

First, the muons are identified and the corresponding PF blocks are removed from the block collection. The muon momentum is taken to be the inner track momentum if its p_T is smaller than 200 MeV/c and a combination of the inner and spectrometer track momenta above.

The electrons are recognised as an energetic and well-isolated track coupled to an energetic ECAL cluster ($E_T > 4$ GeV). The four-momentum is a combination of the track and cluster energies and positions. Most electrons emit a sizeable fraction of their energy as bremsstrahlung photon as they interact with the significantly thick matter of the tracker. These photons are associated to the electron within a *supercluster*, built by collecting clusters in a small (η, ϕ) window around the electron direction. The energetic and isolated photons are identified in the same step. A photon candidate is seeded from an ECAL supercluster if the corresponding cluster has $E_T > 10$ GeV and is not linked to a track. The identified PF objects are masked against further processing.

The hadrons (charged and neutral) are identified from the jet fragmentation and hadronisation. In the tracker acceptance ($|\eta| = 2.7$), ECAL clusters which are not linked to tracks are turned into photons, as 25% of the jet energy is carried out by photons against 3% for neutral hadrons. Unassociated HCAL clusters are turned into neutral hadrons. Outside the tracker acceptance, an ECAL cluster linked to HCAL is supposed to arise from the same hadron shower and is identified as a neutral hadron while an unassociated ECAL cluster is recognised as a photon. The HCAL clusters connected to at least one track are handled in the following way. The sum of all associated track energies is noted E_{tracks} . The HCAL cluster energy is referred to as E_{HCAL} . The energies of all ECAL clusters linked to the tracks are summed and referred to as E_{ECAL} . Then, the excess of

calorimeter energy with respect to the total track momentum is computed:

$$\Delta = E_{HCAL} + E_{ECAL} - E_{tracks}. \quad (4.1)$$

If no significant excess is found, the associated clusters are identified as charged hadron and discarded from further processing. Otherwise new particles are created in addition to the charged hadron. In the case $\Delta < E_{ECAL}$, a single photon is created, which direction is that of the ECAL cluster and energy is equal to the excess. If $\Delta > E_{ECAL}$, two particles are created: a neutral hadron, which energy is equal to $\Delta - E_{ECAL}$ and the direction of the HCAL cluster, and a single photon with the energy E_{ECAL} and the direction of the ECAL cluster.

The charged hadron momentum is computed from a weighted average of the tracker and calorimeter momenta. The weights correspond to the resolution of the subdetectors. This combination ensures a smooth transition between the low energy region, dominated by tracker, and the high energy region, dominated by the calorimeters.

The particles thus created are inputs to higher-level algorithms like jet clustering or missing energy calculation.

4.1.1.3 CMS event reconstruction at HL-LHC

4.1.1.3.1 Event reconstruction The particle identification and reconstruction in the CMS detector at the HL-LHC will be done using the existing CMS PF and physics object reconstruction system, whose principle has been described in Section 4.1.1.2. Because of the high-PU expected in the HGCal, the clustering algorithm has been optimised to balance the low computational speed due to the high layer occupancy. The principle of the new clustering to be used in the HGCal is the following [99].

The HGCal has a transversal and a longitudinal segmentation and two kinds of clusters can be reconstructed: the two-dimensional clusters (*2D-clusters*) that are layer clusters and the three-dimensional clusters, *3D-cluster (so-called multicluster)*, built from consecutive 2D-clusters. The 2D-clusters are reconstructed in each HGCal layer, and local concentrations of energy are identified. For each cell, i , with energy larger than three times the noise level, an energy density is defined:

$$\rho_i = \sum \chi(d_{ij} - d_c), \quad (4.2)$$

where d_{ij} is the 2D distance between the centres of cells i and j , and d_c is an arbitrary critical distance. The function χ is defined as:

$$\chi(d_{ij} - d_c) = \begin{cases} E_j & \text{if } d_{ij} - d_c < 0, \\ 0 & \text{otherwise,} \end{cases} \quad (4.3)$$

where E_j is the energy of the j^{th} calorimeter hit, with j running over all hits on the given layer, including hit i . Basically, ρ_i is the sum of the energy of all hits that are closer to hit i than some cut off distance d_c . The density map thus obtained is used to calculate, for each hit cell, the minimum distance to another hit with higher density:

$$\delta_i = \min_{\forall j: \rho_i < \rho_j} d_{ij}. \quad (4.4)$$

Hits in a given layer are thus arranged in the $\delta - \rho$ parameter space. Most of the hits are grouped in two categories: cluster cores with large ρ but small δ and potential cluster for which both δ and ρ are large. All hits with $\delta_i > d_c$ are potential cluster centres if and only if their local density ρ_i is larger than some value ρ_c , but in any case larger than nine times the noise threshold of the cell in question. Once the cluster centres have been identified, the list of hits ordered by decreasing values of ρ_i is used to assign every hit to a cluster. The hit with the highest density in a layer is by definition the initiator of the first cluster. By assuming that a hit always belongs to the same cluster as its nearest neighbour with higher energy density, a single iteration over the ordered list of hits is sufficient to assign each and every hit above the noise threshold to one and only one cluster.

The layer clusters are then collected together into a multicluster, associating any layer cluster aligned within 2 cm of the seed direction, formed by a straight line from the detector centre to the cluster direction. The multiclusters are then used in the CMS particle flow algorithm.

As in the case of the LHC detector described in Section 4.1.1.2, the PF objects are also formed in the HGCal implementation and then fed into the PF algorithm. The *SimPFProducer* is the CMSSW producer responsible for injecting the HGCal reconstructed objects into the PF. It is mostly derived from MC truth information. In release 11.0.0.6, the clusters associated with tracks are injected as charged hadrons or electrons and their momentum is fully taken from the reconstructed tracks. The clusters that are not linked to a track are inserted as neutral hadrons or photons with a momentum taken from the MC generator. The reconstruction performance of this momentum attribution are discussed hereafter by studying the jet and missing transverse energy resolutions. Assigning only the track momentum to the charged hadrons is not the optimal choice and an alternative implementation is proposed.

4.1.1.3.2 Performance of the physics objects reconstruction The jet resolution of the HGCal, in version 11.0.0.6 of CMSSW, has been studied by generating jets (PYTHIA) of various p_T and η values without PU. As shown in red on Figure 4.1, the fully track-derived resolution (*default*) grows as p_T grows since the track resolution deteriorates with increasing momentum.

The different models tested to improve the jet resolution are also represented on this figure. The green resolution is fully derived from the calorimeter. Using the momentum of the cluster associated to a charged hadron improves the jet resolution but it still grows as p_T grows. This bad behaviour, due to the fact that the calorimeter resolution deteriorates with the momentum because of angular effects, is particularly evident at high η as shown on Figure 4.2. The clusters are built from the *Realistic Sim Clusters* collection that have been introduced to inject some realism into the HGCal MC based reconstruction described in Section 4.1.1.3. A merging mechanism, exclusively energy-based, controls via a threshold the merging of two clusters into a single cluster. From previous optimisations, it has been estimated that two clusters should be merged when they share more than 40% of their energies. This value is the default threshold into the HGCal implementation; the red and green resolution distributions were obtained with a 40% merging-threshold. In order to understand the growth with the p_T estimated from the energy of the full calorimeter-derived Realistic Sim Cluster, this condition has been released; clusters were merged if they share more than 90% of their energies. By increasing the merging-threshold, the Realistic Sim Clusters (purple) gets closer to the *perfect* HGCal reconstruction (blue). The perfect clusters are directly derived from MC truth and show an excellent resolution that is clearly impossible to reproduce in reality; they were only

used here as a reference. With a higher merging-threshold, the Realistic Sim Clusters tend to give a perfect resolution. This behaviour might be due to the fact that, merging two clusters, the cluster energy is artificially increased, giving a better resolved cluster. However, the threshold has been previously fixed to a realistic value and must be, if required, only slightly changed. Moreover, even changing the threshold parameter, the increase of the resolution is still visible at high η (Figure 4.2).

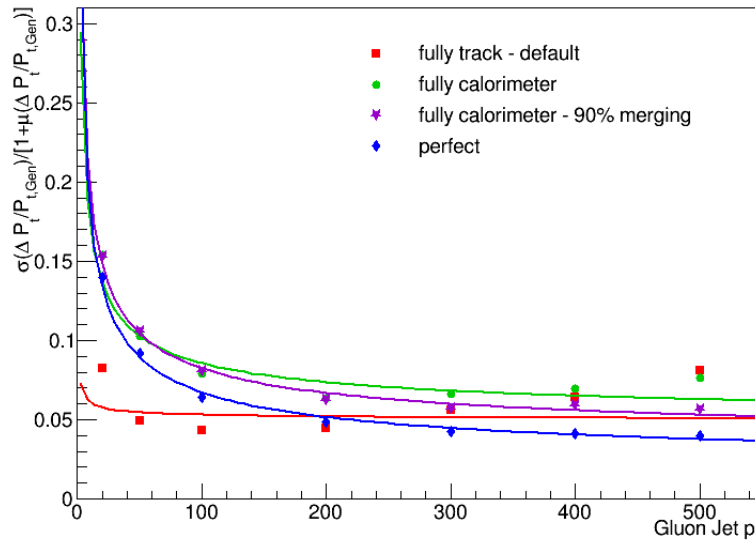


Figure 4.1 – Jet resolution as function of p_T obtained for different models of the charged hadrons momentum

These distributions were simulated with PYTHIA, without PU and for different p_T and η values. This figure shows the resolution across all the η values produced. See the text for details about the different models.

In order to benefit from both the tracker (at low energy) and the calorimeter (at high energy) resolutions, a smooth transition will be implemented to derive the most accurate charged hadron momentum. As the jet resolution depends on p_T and η , this momentum will be parametrized as a function of both parameters. The missing energy resolution will also be improved with respect to an estimate fully based on tracks. This study is not yet complete and coming results will allow to conclude on this approach.

4.1.2 Delphes

The DELPHES software [100] has a simplified approach, which allows to perform a fast and realistic simulation of the detector response, propagating MC particles through the central tracking system, calorimeters and muon chambers, immersed in a magnetic field. The DELPHES PF algorithm is inspired from the CMS one, introduced in Section 4.1.1.2. It is also based on reconstructed track and cluster collections and is extensively described in [100].

As explained in Chapter 2, the precise reconstruction of the recoil is fundamental to get an accurate measurement of the W mass. The DELPHES simulation has been used to estimate the effect of the HGCal parameters on the recoil reconstruction with respect to the present LHC detector. This study is described in Chapter 6. The HGCal granularity, resolution and efficiency had to be changed in the current CMS geometry. However, the CMS detector as implemented in CMSSW does

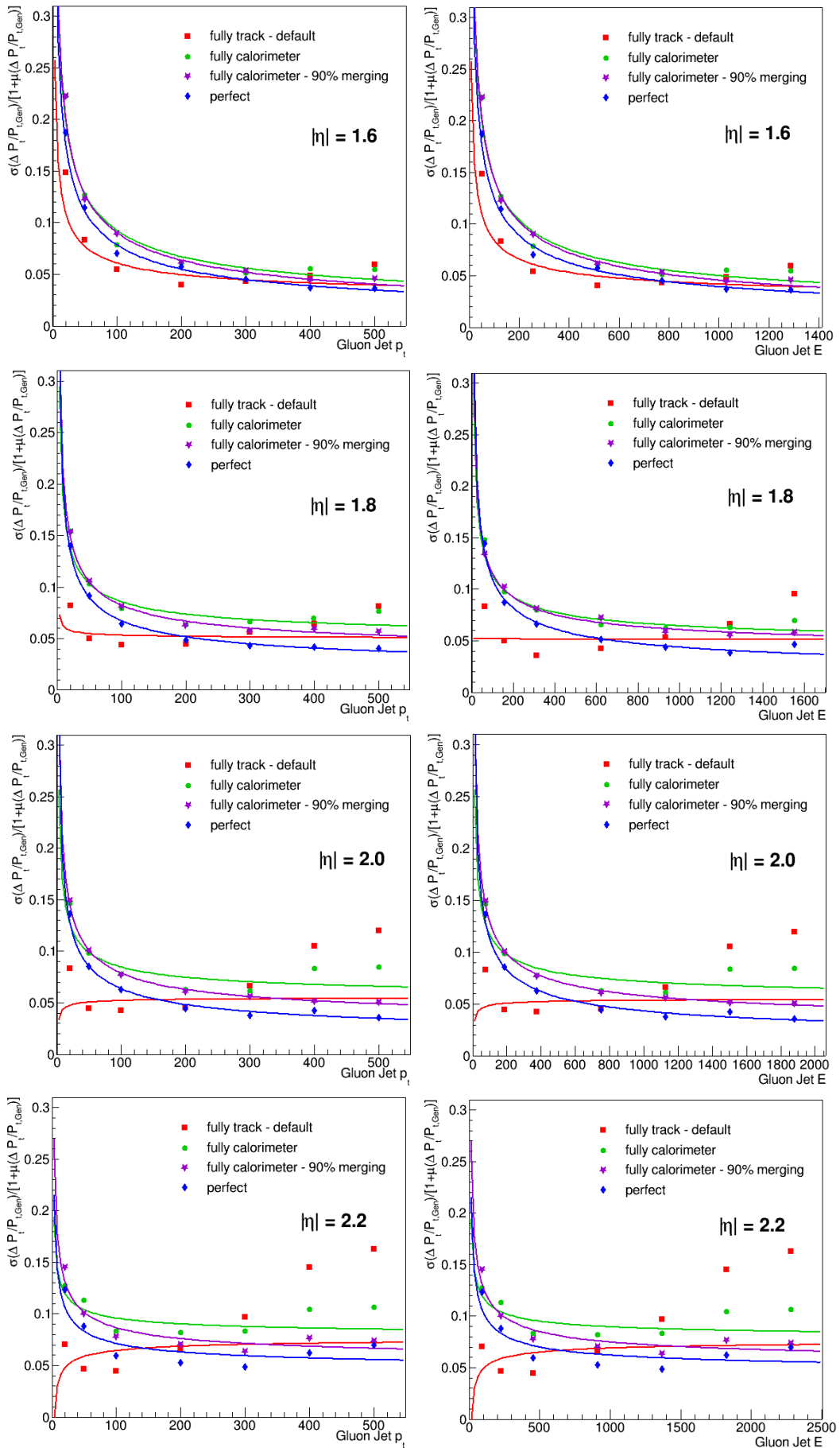


Figure 4.2 – Jet resolution as a function of p_T for different η values and computed for different models of the charged hadrons momentum

not allow these substitutions. Moreover, Machine Learning techniques has been used to improve the recoil measurement, requiring large samples, whose reconstruction with Geant4 might be time consuming. Thereby, DELPHES has been chosen to generate the HGCal-like data sets. The recoil was next reconstructed from these data with the CMSSW packages usually used with the real CMS data.

Before using the DELPHES reconstruction as input for the recoil study with HGCal, and before any HGCal-parameters implementation, the agreement of CMSSW and DELPHES simulations has to be shown. Figure 4.3 shows the p_T , η and ϕ of the lepton and the recoil reconstructed with both software. These distributions confirm that DELPHES gives an accurate reproduction of these key variables of the recoil reconstruction. Then DELPHES can be safely used to generate HGCal-like data.

4.2 FCC-ee

The physics program accessible at the FCC-ee has been presented in Chapter 3. This collider will successively span the entire energy range from the Z pole (~ 91 GeV), over the WW threshold (~ 160 GeV) and HZ production peak (~ 240 GeV) to the $t\bar{t}$ threshold (~ 350 GeV) and above. At the WW threshold and at higher energies, W pairs will be copiously produced and such huge data samples will allow for the W mass measurements with unparalleled precision.

Signal and background four-vectors, output of the event generator, are used as input to a single software, the HEPPY, which successively simulates the interaction of decay products within the detector and reconstruct their four-vectors.

4.2.1 Event simulation

4.2.1.1 Generator step

The signal $e^+e^- \rightarrow W^+W^-$, the double resonant W pair decay and the hadronisation of quarks in the final state, as well as the background were simulated with PYTHIA, version 8.24 [49]. This study of the W mass uncertainty has been done in two steps. First the statistical uncertainty expected at the different centre-of-mass energies has been evaluated. The details of this analysis are given in Chapter 7. Then, the effects of the FSI between the W decay products on the mass and width has been studied and are presented in Chapter 8.

Samples of four-fermion events ($q\bar{q}q\bar{q}$ for the hadronic channel and $q\bar{q}l\nu_l$ for the semi-leptonic channel), were generated at each of the three centre-of-mass energies: close to the W-pair production threshold (162.6 GeV) and above (240 GeV and 365 GeV). Among the radiative corrections defined in Section 2.2.3, the coulomb correction was neglected whereas the ISR, FSR and QCD corrections were integrated to the parton shower step. For the study of the statistical uncertainty, the CR and the BEC defined in Section 2.2.3.3 were not included in the hadronic samples. The mass of the W boson was set to its Particle Data Group (PDG) value, 80.385 GeV/ c^2 , and the width, computed from the SM predictions (Equation (2.13)). At the considered centre-of-mass energies, the typical maximum energy/momentum of the fermions from W decays lies in the range from 40 to 90 GeV. In this range the momentum of the electrons is better measured in the tracker than its energy

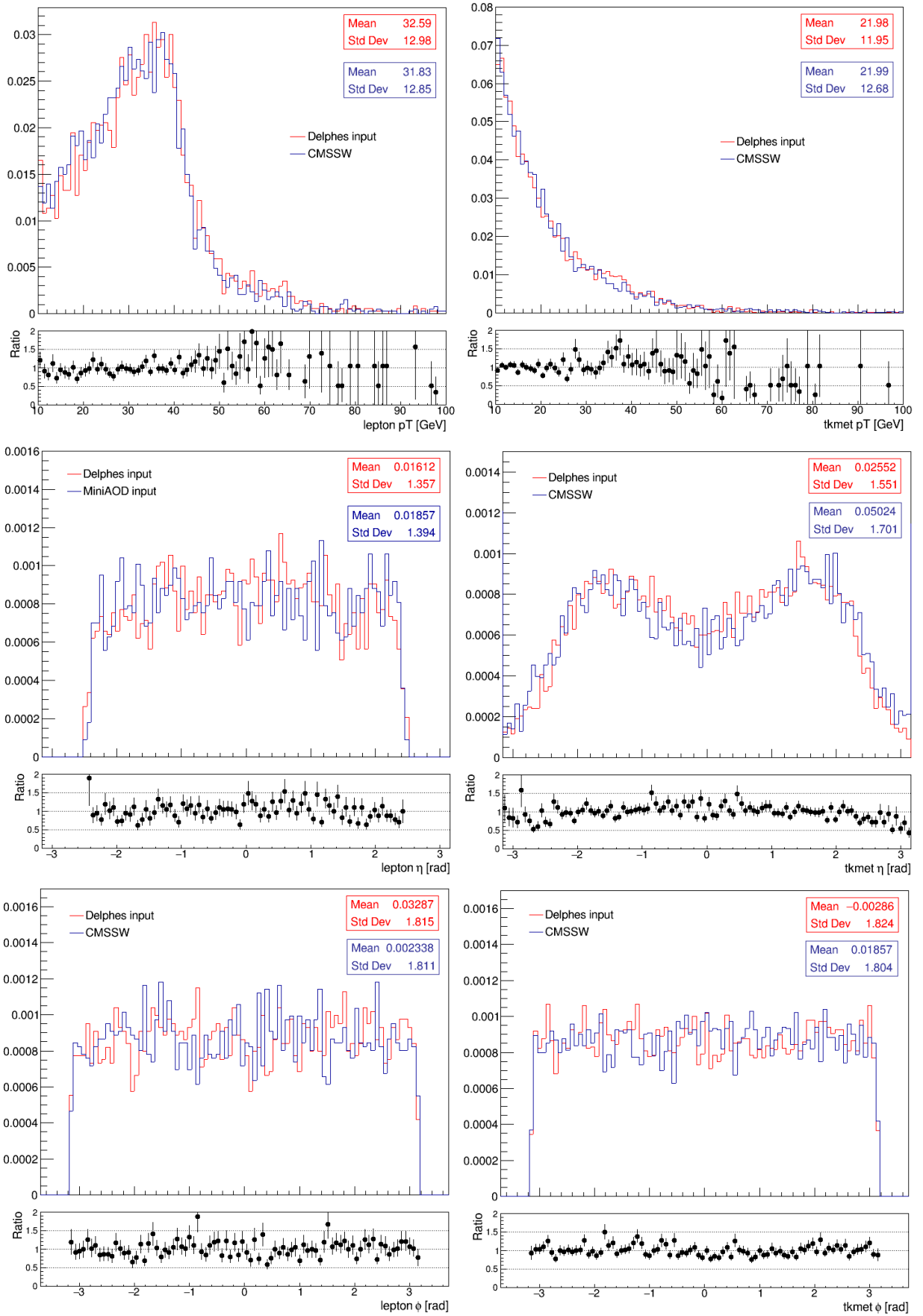


Figure 4.3 – Comparison of the lepton (left) and recoil (right) p_T , η and ϕ reconstructed using CMSSW and DELPHES

in the electromagnetic calorimeter (Table 4.2), therefore, in the semi-leptonic decay channel, only the muon decay of the leptonic part was studied, assuming then that muons and electrons will be reconstructed with the same performance. This assumption relies on the capability of associating bremsstrahlung photons to a radiating electron, which should be an easy task in the clean FCC-ee environment. Moreover the tracker being very thin, the amount of bremsstrahlung is expected to be small.

In order to estimate the statistical uncertainties on both the W mass and width measurements, additional samples were generated for the different centre-of-mass (CM) energies and both decay channels. Templates used to determine the statistical uncertainty on the W mass were generated at fixed Γ_W and for different values of the W mass: $79.385 \text{ GeV}/c^2$ and $81.385 \text{ GeV}/c^2$, whereas templates for the study of the width statistical uncertainty kept M_W fixed and varied the width to: $1.985 \text{ GeV}/c^2$ and $2.185 \text{ GeV}/c^2$.

To evaluate the impact of the FSI, samples including on one hand the CR and on the other hand the BEC were then generated. The CR was described using the two models implemented in PYTHIA for the e^+e^- collisions, SKI and SKII presented in Section 8.1. The model used for the BEC is presented in the same section.

All the background processes to the CC03 signal discussed in Section 2.2.1 were also simulated using the PYTHIA generator. At the FCC-ee, the background level is expected to be very small because of clean e^+e^- collisions. The contamination of these backgrounds on the W mass was studied for all centre-of-mass energies and the effect of these contributions is discussed in [101, 102].

4.2.1.2 Detector step

This step starts with the choice of the detector and the definition of its characteristics: geometry and performance, which will be used to define the pseudo-data from the interaction of the generated particles within the detector.

4.2.1.2.1 Detector implementation The CLD concept, a possible future detector for FCC-ee, is derived from the most recent CLIC detector model [103]. Based on the characteristic presented in Chapter 3, the detector implemented in the PAPAS fast simulation software [104] has a cylindrical structure modelled by three nested cylindrical sub-detectors centred on the beam axis: the tracking system, the ECAL and the HCAL, respectively represented in white, red and blue on Figure 4.4. The whole system is immersed in a uniform 2T magnetic field, directed along the detector axis.

The silicon tracker, the closest sub-detector to the interaction point, is defined as a cylinder with a radius of 2.15 m and a length of 4.816 m. The amount of material in the inner tracker is neglected. In the tracker, charged particles may be detected as tracks, taking into account acceptance, momentum resolution, and efficiency of this detector, i.e. the fraction of reconstructed particles with respect to the input MC particles. Their momentum is measured with an expected resolution, as given in input to PAPAS. From the study of the Silicon Detector concept for ILC (SiD) [103], the tracker is expected to be efficient down to $\theta = 10^\circ$ and the efficiency values as

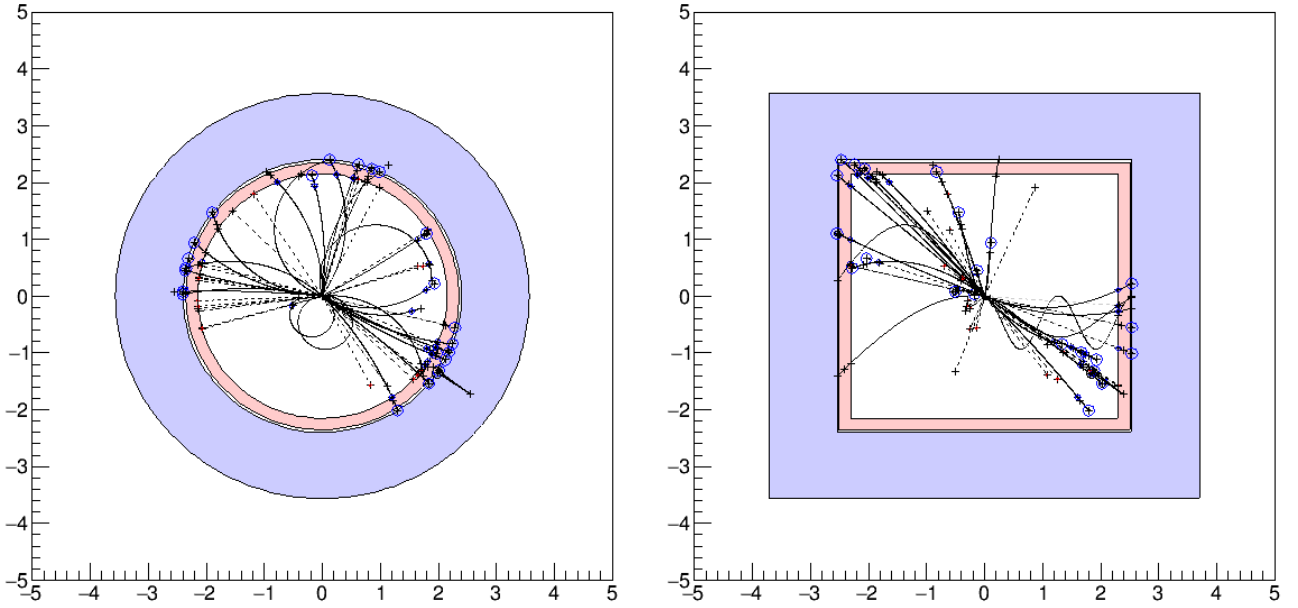


Figure 4.4 – Interaction of a $ee \rightarrow WW \rightarrow q\bar{q}q\bar{q}$ event, generated at $\sqrt{s} = 240$ GeV with PYTHIA, through the CLD detector using the PAPAN simulation

The axis are graduated in meters. The left (right) plot corresponds to the XY (YZ) projection. From the interaction point to the outside, the sub-detectors are the silicon tracker (white), ECAL (red) and HCAL (blue). The photons are drawn in black dashed lines while all other particles are in full lines. The ECAL clusters are represented in red and the HCAL clusters in blue circles whose the radius is given by the calorimeter granularity implementation, $R_{em} = 1.5$ cm and $R_{had} = 4.5$ cm for the ECAL and $R_{had} = 10$ cm for the HCAL. The interaction point position of a particle in a sub-detector is represented by a cross.

function of p_T are [93]:

$$\begin{aligned} 0.1 < p_T < 0.3 \text{ GeV}/c & \quad \epsilon = 0.9, \\ 0.3 < p_T < 1 \text{ GeV}/c & \quad \epsilon = 0.95, \\ p_T > 1 \text{ GeV}/c & \quad \epsilon = 0.99. \end{aligned} \quad (4.5)$$

As shown by Figure 3.11, the tracker transverse momentum resolution, $\sigma(\Delta p_T/p_T^2)$, is parametrized as a function of the polar angle [24] and is given by:

$$\sigma(\Delta p_T/p_T^2) = a \oplus \frac{b}{p \sin^{3/2} \theta}, \quad (4.6)$$

where parameter a is the contribution from the curvature measurement and parameter b is the multiple scattering contribution term which is constant in the barrel and increases in the forward region. Their input values to PAPAN are summarised in Table 4.1 [66].

With this parametrization, a charged particle with an angle $\theta > 10^\circ$ and a transverse momentum smaller than 100 GeV/c is reconstructed with a p_T resolution better than the percent [66].

Around the tracker, the 20.2 cm deep ECAL is defined with a radiation length, $X_0 = 0.92$ cm and an interaction length, $\lambda_I = 20.2$ cm. The interaction length of the ECAL material is used

Table 4.1 – Parameters of the transverse momentum parametrization (Eq. 4.6) in PAPAS

| $\theta(\text{deg})$ | a | b |
|----------------------|----------------------|-------|
| 10 | 5.6×10^{-5} | 0.010 |
| 30 | 1.7×10^{-5} | 0.005 |
| 50 | 1.2×10^{-5} | 0.004 |
| 70 | 1.6×10^{-5} | 0.003 |
| 89 | 2.5×10^{-5} | 0.003 |

to model early hadron showers following their path length. The energy deposits in the ECAL are modelled following the main characteristics: the acceptance, the energy resolution, the energy threshold and the calorimeter granularity. Any particle with an energy above $E_{min} = 0.2$ GeV and a rapidity smaller than $|\eta_{max}| = 2.7$ is selected. These particles are reconstructed with an energy resolution [92]:

$$\frac{\sigma_E}{E} = \frac{17\%}{\sqrt{E}} \oplus 1.1\%. \quad (4.7)$$

The granularity is defined as the distance between two clusters below which they cannot be resolved and are considered as a single cluster. The granularity of the ECAL is modelled by assigning a radius to each calorimeter cluster as a function of the type of the particle that produced the cluster, hadron or electromagnetic particle (electron or photon). The radius for an electromagnetic particle is set to $R_{em} = 1.5$ cm, i.e. roughly 5 R_M (Molière radius), into which 99% of an electromagnetic shower is contained. Most of the lateral development of an hadronic shower starting in the electromagnetic calorimeter is contained in a radius corresponding to about 5 interaction lengths, i.e. $R_{had} = 4.5$ cm.

The HCAL volume is a cylinder, 160 cm thick, defined with an interaction length $\lambda_I = 21.3$ cm. Hadrons with an energy larger than $E_{min} = 1$ GeV and with a rapidity smaller than $|\eta_{max}| = 2.9$ are retained. These hadrons are reconstructed with an energy resolution [92]:

$$\frac{\sigma_E}{E} = \frac{50\%}{\sqrt{E}} \oplus \frac{0.5 \text{ GeV}}{E} \oplus 2.5\%. \quad (4.8)$$

As for the ECAL, the HCAL granularity is modelled by assigning a radius to the hadronic cluster. The radius of hadron clusters is $R_{had} = 10$ cm which is the minimal distance, below which the perturbative jet information becomes unresolvable due to the overlap between the hadronic showers [105].

The main characteristics of the CLD detector used as input to PAPAS are gathered in Table 4.2.

4.2.1.2.2 Particle interactions in the detector From the PYTHIA generator output, only the interactions of stable particles, defined as final particles with a transverse momentum larger than 10^{-5} GeV/c and that are not neutrinos, are simulated in the CLD detector. The interaction of the particles in the detector depends on the particle type.

A simple resolution and efficiency model is applied. The lepton momentum is smeared, assuming a Gaussian probability density function, centred on the generated particles energy and a width

Table 4.2 – Main characteristics of CLD detector as implemented in PAPAS

| | | CLD | |
|---------|------------------|---|--|
| B field | | 2 T | |
| Tracker | resolution | $< 1\%$ | if $\theta > 10^\circ$ and $p_T < 100$ GeV/c |
| | efficiency | 0.9 | if $0.1 < p_T < 0.3$ GeV/c |
| | | 0.95 | if $0.3 < p_T < 1$ GeV/c |
| | | 0.99 | if $p_T > 1$ GeV/c |
| ECAL | inner radius | 2.15 m | |
| | resolution | $\frac{17\%}{\sqrt{E}} \oplus 1\%$ | |
| | acceptance | $ \eta < 2.7$ and $E > 0.2$ GeV | |
| | R_{em} | 1.5 cm | |
| | R_{had} | 4.5 cm | |
| | λ_I | 0.92 cm | |
| | X_0 | 20.2 cm | |
| HCAL | inner radius | 2.4 m | |
| | resolution | $\frac{50\%}{\sqrt{E}} \oplus \frac{0.5 \text{ GeV}}{E} \oplus 2.5\%$ | |
| | acceptance | $ \eta < 2.9$ and $E > 1$ GeV | |
| | R_{had} | 10 cm | |
| | λ_I | 21.3 cm | |

corresponding to the tracker resolution. Due to the large amount of material before the muon chambers, it has been assumed that the muon spectrometer cannot improve the resolution in the energy domain of FCC-ee [103]. Muons with $\theta > 10^\circ$ and $E > 7.5$ GeV are detected with 100% efficiency. The hadronic decay products of tau leptons in jets are simulated just like other particles.

The photons are extrapolated to the surface of the ECAL. The reconstructed ECAL cluster energy is smeared to account for the ECAL energy resolution. The reconstructed cluster position is set to the impact position of the generated particle, without any smearing.

The momentum of the charged hadrons is smeared to reflect the momentum resolution of the inner tracker. All stable hadrons, whether charged or neutrals, are extrapolated to the ECAL and HCAL front faces. The ECAL interaction length is used to randomly determine a possible showering point for the hadron along its path. If this point is located within the ECAL material, an early showering in the ECAL is assumed and two clusters are produced, one in the ECAL, the other one in the HCAL. Otherwise, only a single cluster is produced in the HCAL. In both cases, the total reconstructed calorimeter energy is obtained by smearing the generated hadron energy with the HCAL resolution. In case of early shower, the fraction of the reconstructed energy detected in the ECAL is randomly determined assuming a uniform probability distribution ranging from 0 to 0.7. Eventually the selection requirements of the ECAL (in case of an early shower) and HCAL are applied.

The tracks and clusters simulated by PAPAS are then processed and associated by a PF algorithm for an optimal reconstruction of all particles in the final state of the collision. The PF algorithm is built on the CMS model, which principle has been explained in Section 4.1.1.2. The FCC-like events are finally fully reconstructed by the HEPPY analysis framework.

4.2.2 Event reconstruction

Lepton reconstruction

The lepton candidate from the semi-leptonic final state is identified as the most energetic lepton among all reconstructed leptons. Any particle not associated to the object to which it belongs would have an impact on the reconstructed W mass. In particular FSR photons must be associated to the radiating lepton. Such photons must be closer to the lepton track rather than to any other particle or the beam axis and at least 0.4 radians away from any other track. Any photon in the event answering these conditions was identified as FSR photon and its four-momentum was combined to the lepton four-momentum.

Figure 4.5 shows the energy of the reconstructed lepton before and after the FSR association. For the comparison, the MC generated lepton energy, reconstructed without detector, is also represented. The FSR association slightly improves the lepton reconstruction.

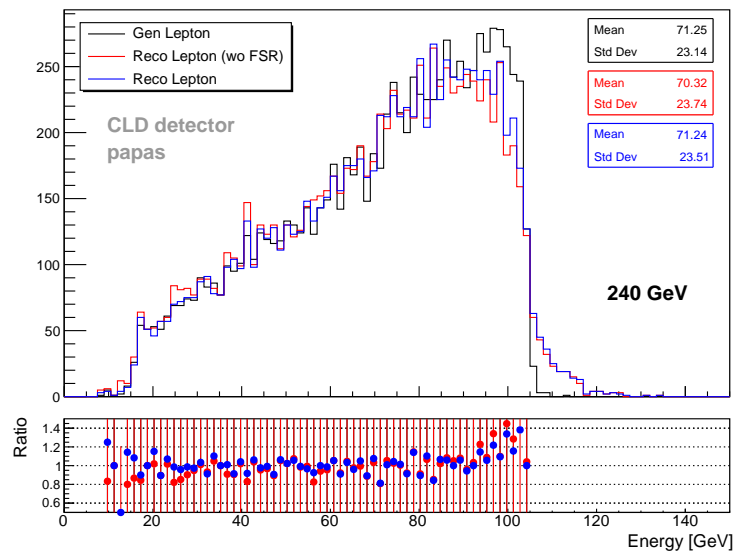


Figure 4.5 – Comparison of the lepton energy before an after FSR association
The MC generated lepton is also represented as reference.

Jet clustering

The quarks produced in the collision will form hadrons and other particles through the process of fragmentation and hadronisation. The ensemble of these objects is called a jet, since the fragments all tend to travel in the same direction, forming a narrow "jet" of particles. The particles that have not been identified as a lepton or a photon are clustered into jets using FASTJET [106, 107], a C++ package providing several implementations of jet algorithms. In the hadronic (semi-leptonic) decay channel, the event is expected to contain four (two) jets. When a fixed number of jets is required, the exclusive $ee-k_T$, also called DURHAM [60], algorithm is used.

When merging particles during the clustering procedure, there are several ways to combine the momenta. In e^+e^- collisions the E-scheme, based on energy-momentum conservation, is preferred. The DURHAM algorithm was developed and implemented for LEP studies, in replacement of the JADE algorithm [108], because of its better angular resolution and is smaller sensitivity to soft gluon radiations [60]. The implementation of both algorithms is very similar and the main difference is that DURHAM is based on the transverse momentum of a pair of tracks while JADE emphasizes its invariant mass. The distance d_{ij} between any pair of particles i and j is given by:

$$d_{ij} = 2 \min(E_i^2, E_j^2)(1 - \cos \theta_{ij}), \quad (4.9)$$

where E_i and E_j are the energy of the two particles and θ_{ij} is the angle between them. d_{ij} is computed for each possible pair of the final state and the pair for which the distance is minimal is selected. The two particles are combined and replaced by a pseudo-particle with momentum $p_{ij} = p_i + p_j$. This procedure is repeated until all the particles are clustered in the required number of jets.

The jet resolution obtained with the HEPPY reconstruction is shown on Figure 4.6. This resolution is better than the jet resolution at LEP and is due to better energy resolution of the HCAL.

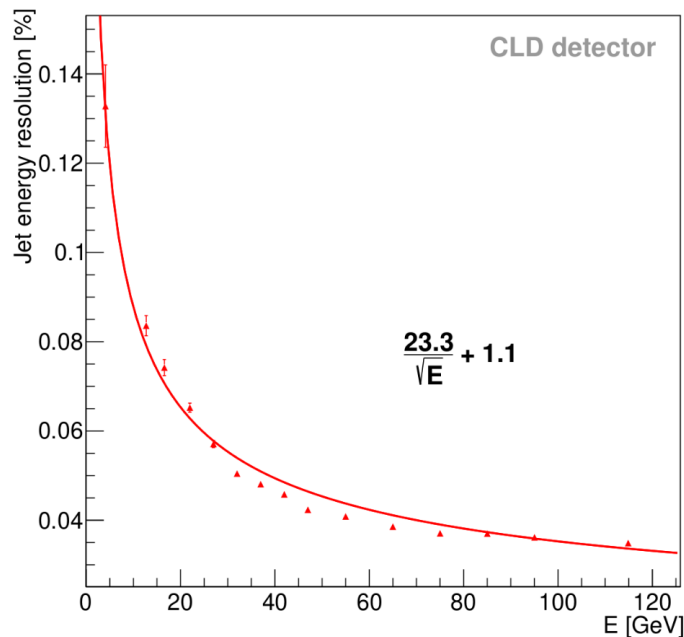


Figure 4.6 – Jet resolution of CLD simulated with HEPPY

The jet angles and energies are fundamental parameters of the kinematic fit. Figure 4.7 shows the CLD detector effect, simulated with HEPPY, on the jet energy and theta angle. The phi angle is not presented here as it is uniformly distributed into 2π . The reconstructed jets have the slight tendency to be softer and more central than generated jets.

Missing energy

In the semi-leptonic decay, a neutrino is produced in association to the lepton. This particle is undetected in the different sub-detectors and is identified as the missing energy-momentum, i.e.

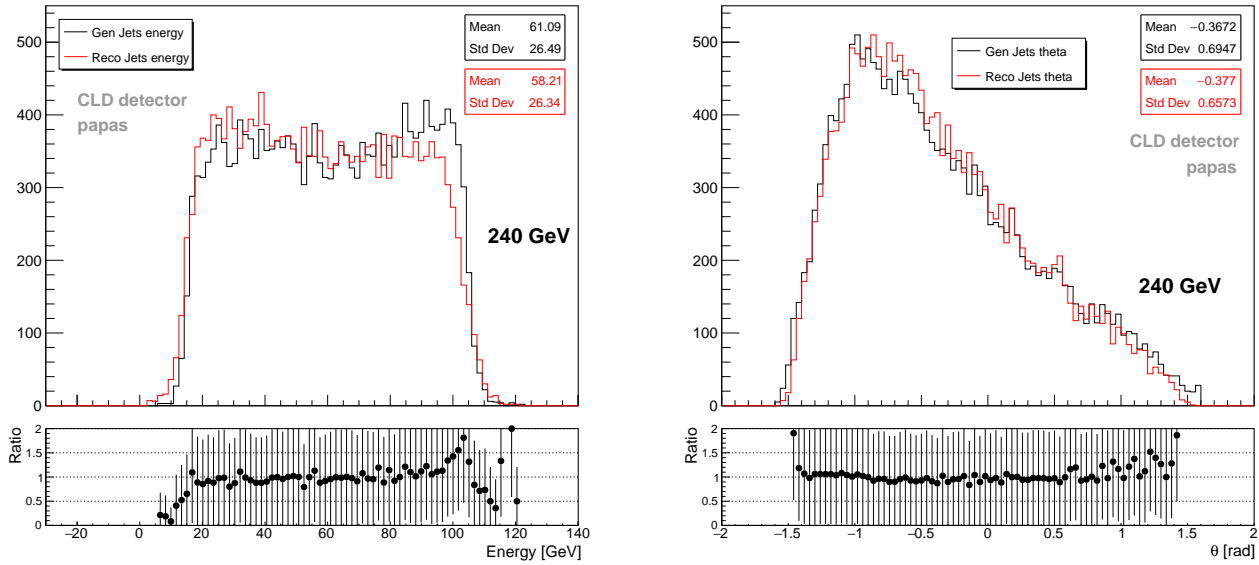


Figure 4.7 – Reconstruction of the jet energy and theta angle by the CLD detector simulated with HEPPY

the part of the energy collision that is not carried away by the detected products of the collision. The energy in the centre-of-mass in e^+e^- collisions is precisely measured. Then making use of the energy-momentum conservation, missing energy and momentum are then easily reconstructed from the difference of the energy in the centre-of-mass and the sum of the four-vectors of all detected particles.

Figure 4.8 shows the reconstructed missing energy with the CLD detector using the HEPPY fast simulation. It is compared to the generated missing energy, reconstructed as described above, without detector. The true energy carried away by the neutrino is also represented. The reconstructed energy has the tendency to be overestimated and wider than the true neutrino energy. This effect is due to reconstruction inefficiency and detector resolution.

The theoretical and experimental context of this study is now completely described. The original work of the W mass measurement at CMS, at HL-LHC and in a future experiment at the FCC-ee are presented in the following chapters.

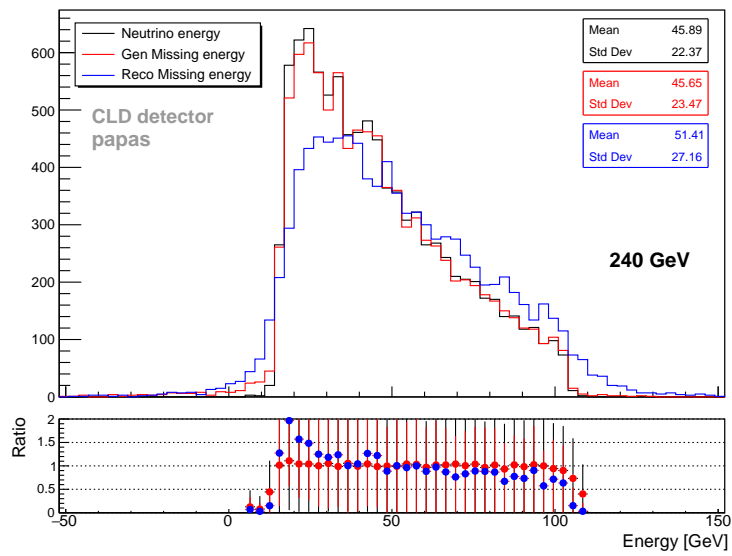


Figure 4.8 – Reconstruction of the missing energy with the CLD detector simulated with HEPPY. The neutrino momentum generated by PYTHIA is used as reference. It has never been used in the following studies.

Chapter 5

A fast simulation for the CMS HGCal Upgrade

*"The only way to go fast, is to go well."
Robert C. Martin*

Contents

| | | |
|------------|---|-----------|
| 5.1 | Geometry implementation | 66 |
| 5.1.1 | Geometry model | 66 |
| 5.1.2 | Geometry in FastSim | 67 |
| 5.2 | Particle interactions through the detector | 69 |
| 5.2.1 | Parametrisation of the electromagnetic and hadronic showers | 69 |
| 5.2.1.1 | Longitudinal profile | 69 |
| 5.2.1.1.1 | Electromagnetic showers | 69 |
| 5.2.1.1.2 | Hadronic showers | 70 |
| 5.2.1.2 | Transverse profile | 70 |
| 5.2.1.2.1 | Electromagnetic showers | 70 |
| 5.2.1.2.2 | Hadronic showers | 71 |
| 5.2.2 | Hits generation | 74 |
| 5.3 | A very fast simulation | 75 |
| 5.4 | Software validation | 77 |

The simulation of electromagnetic showers and hadronic cascades is crucial for the design and optimisation of calorimeters regarding their performance for different physics benchmarks as well

as for data analysis. High statistics and high precision experiments require a detailed simulation of the detector response to given physics processes, starting from the final state of the primary interaction and performing individual tracking of all generated particles throughout the detector. A very large number of MC events may need to be produced and the computing time for detailed simulations may become prohibitive. As the largest part of the simulation time (70%) is consumed by the tracking through the calorimeters, parametrizations for the electromagnetic and hadronic showers can considerably reduce the computing time while conserving the same level of accuracy.

The CMSSW [95] is the common Geant4-based [97] simulation and reconstruction framework for the CMS detector. The HGCal fast simulation tool (FastSim), developed as a complement to the full-scale simulation (FullSim), is presented in this chapter.

A first, simplistic version of the fast simulation was developed at the LLR Laboratory (Paris) a few years ago. This incomplete tool has been turned into a full-feature standalone software that is able to reproduce the electromagnetic and hadronic shower development through the full HGCal structure. The full geometry is built layer by layer within a single HGCal cassette (described in Chapter 3). Next, the particle interactions through the entire detector structure are simulated using electromagnetic and hadronic showers description, parametrized as defined in Section 5.2. After the combination of each hit with the corresponding cell, the electronic noise is added, making the hit energies more realistic. Section 5.3 explains how the simulation has been accelerated and is now able to reach a high generation rate using a Quadtree data structure. The fast simulation software has been validated by comparing its results with those from CMSSW, as shown in Section 5.4. This comparison shows that the FastSim is accurate enough for HGCal parameters optimisation.

5.1 Geometry implementation

5.1.1 Geometry model

The development of the FastSim has been completed during the design period of the HGCal Technical Design Report (TDR) [65]. Before the engineering decisions presented in this volume were made, the geometry of the full simulation software was frozen to its 2016 version, as described in the Technical Proposal (TP) [21]. Because CMSSW was used both as a reference and as a tool for the development of the fast simulation, the geometry in the FastSim corresponds to the 2016 design as well. Nevertheless there are very tiny differences between the TDR and the current geometry, and the fast simulation could be very easily updated. As the update to the parameters had a negligible impact on the full simulation output, the FastSim implementation and validation presented here, using the old geometry, are assumed to remain valid.

In the 2016 geometry, the detector had the same overall structure as described in Chapter 3. It was divided into an electromagnetic part (previously called Endcap Electromagnetic (EE)) and two hadronic parts (previously called Front Hadronic (FH) and Back Hadronic (BH)). Both the EE and FH layers were made of silicon plates while the BH layers were scintillator tiles. The hybrid active medium was not yet proposed at that time. The differences between the FastSim and current geometry parameters are given in Table 5.1. All the parameters which are not referenced in this table have not been changed since then and their values are given in Section 3.1.2.3.

Table 5.1 – HGCal parameters differences between the current geometry and the model used in the fast simulation (2016 geometry frozen for the TDR studies)

| Parameters | | FastSim | Current |
|---------------------------------------|--------------------------------|--------------------|-----------------------------|
| Total λ_I | | 10 | 10.7 |
| Absorber | | brass-absorber | stainless-steel |
| Silicon thicknesses [μm] | | 100; 200; 300 | 120; 200; 300 |
| Silicon cell size [cm^2] | | 0.53 and 1.05 | 0.52 and 1.18 |
| EE/CE-E | Thickness [cm] | 30 | 34 |
| | Cassettes [degrees] | 30 | 60 |
| | Silicon thickness regions [cm] | $R < 75$ | $R < 70$ |
| | | $75 < R < 120$ | $70 < R < 100$ |
| | $120 < R$ | $100 < R$ | |
| (FH+BH)/CE-H | Number of layers | 12+12 | 22 |
| | Active material | Homogeneous layers | Hybrid silicon-scintillator |
| | Silicon thickness regions [cm] | $R < 60$ | $R < 70$ |
| | | $60 < R < 100$ | $70 < R < 100$ |
| | $100 < R$ | $100 < R$ | |

5.1.2 Geometry in FastSim

The HGCal full geometry construction is initiated once, at the beginning of the simulation. To enhance the simulation performance in terms of computational speed, each layer is built within a window limited by $1.475 < \eta < 3$ and $|\phi| < \frac{\pi}{6}$, corresponding to a single HGCal cassette. Both the electromagnetic and hadronic parts of the structure are implemented. The first forty layers (EE+FH) are built with hexagonal cells while the last twelve layers (BH) are modelled with square cells. Appendix A.1 shows both silicon and scintillator layers as modelled in the FastSim. The implementation principle, a tiling of a plane with polygonal cells in the defined window, is the same for both type of cells.

The real HGCal layout of the electromagnetic and front hadronic parts are a tiling of hexagonal wafers on which small (0.53 cm^2) or large (1.18 cm^2) silicon cells are built. This configuration introduces cut cells at the wafer boundaries that are difficult to model. In CMSSW, the exact geometry is defined but for the current fast simulation, the layout has been approximated by a tiling of hexagonal cells. The three silicon thicknesses and the two cell sizes are simulated. The small and large cell regions are delimited by the smallest radius given in Table 5.1. At the limit, if the cell centre falls below this radius, the small cell is modelled. This implementation is not ideal as it introduces small losses and cell overlap areas between the two regions. The losses are compensated by the 10 degrees rotation of a layer with respect to the neighbour layers; the holes will not have the same position from one layer to another and the hit energy that could not be deposited in the "missing layer" will be stored in the next one. In the case of cell overlaps, the hit is associated with the smallest cell, where the resolution is worse, to avoid overestimation of the calorimeter performance. In the twelve last layers, the scintillator tiles are modelled with square cells of size $3 \text{ cm} \times 3 \text{ cm} \times 3 \text{ mm}$. They have the same size on the whole surface and, consequently, there are no losses nor overlaps.

In each layer, the tiling is made in the infinite plan, (\vec{u}, \vec{v}) mapped with the cells as shown on

Figure 5.1. For the silicon layers, \vec{u} coincide with the \vec{x} axis and \vec{v} is obtained by rotating \vec{u} by 60 degrees. For the BH layers, (\vec{u}, \vec{v}) corresponds to the Cartesian plan. The cells are identified with the centre coordinates (i, j) where i and j are respectively the index along the \vec{u} and \vec{v} axis.

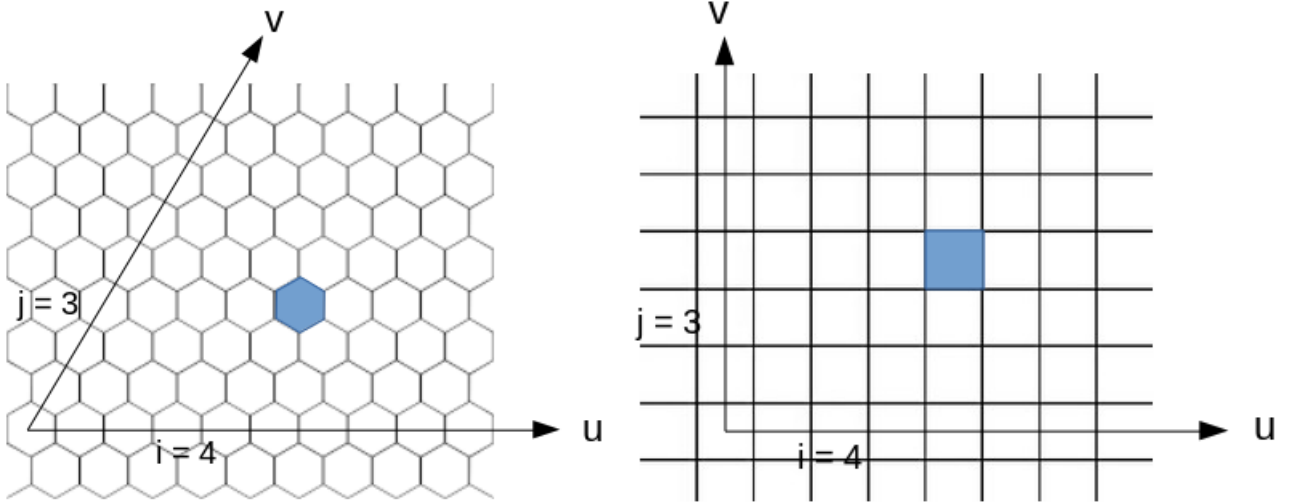


Figure 5.1 – Hexagon and square cells telling as implemented in the FastSim (i, j) are the cell centre coordinates. i is along \vec{u} corresponding to the \vec{x} axis. j is along \vec{v} , obtained by rotating the \vec{u} axis by 60 degrees in case of silicon layers (left), or coinciding with \vec{y} in case of scintillators (right). On both sketches, the cell $(4, 3)$ is identified.

This structure is built from the smallest boundary (x_0, y_0) by translation of the cell centres towards higher (x, y) until they reach the limit of either the region or the window, ϕ_{max} . The centre coordinates are first positioned with the geometric relations given hereafter and the cell vertices are then built from the centre.

Hexagonal cells

$$\begin{aligned} x &= x_0 + i \cdot a\sqrt{3} + j \cdot \frac{a\sqrt{3}}{2}, \\ y &= y_0 + j \cdot \frac{3a}{2}, \end{aligned} \quad (5.1)$$

where (x_0, y_0) corresponds to the coordinates of the cell at the origin of the first (0.53 cm^2 cells) or second (1.05 cm^2 cells) region and a is the cell side.

Square cells

$$\begin{aligned} x &= x_0 + i, \\ y &= y_0 + j. \end{aligned} \quad (5.2)$$

The software can be also used with an external geometry that defines all the cell-related dimensions (mapping coordinates, centre, orientation, vertex coordinates) in an input file. This feature is interesting to address the shortcoming of the simulation (loss, overlap, structure approximations) or to simulate particles within a more realistic geometry.

5.2 Particle interactions through the detector

5.2.1 Parametrisation of the electromagnetic and hadronic showers

The electromagnetic shower is generated by the interaction of electrons or photons with matter via a few well-known QED processes. At low energy, electrons lose their energy through collisions with atoms and molecules of the material, while photons lose it through Compton scattering and the photoelectric effect [9]. For energies larger than approximately 10 MeV, the dominant interaction processes are the electron-positron pair production (photons) and bremsstrahlung (electrons). The number of particles in the shower increases until the energy of the secondary particles reaches a critical level E_c , mainly dissipated by ionisation and excitation. The rate at which electrons lose energy by bremsstrahlung is the radiation length, X_0 . It represents the distance that an electron needs to travel to reduce its primary energy, E , to $1/E$. It is also 7/9 of the mean free path for pair production by photons [9]. The shower spread is due to multiple scatterings of electrons and positrons away from the shower axis. The transverse size of an electromagnetic shower is characterized by the Molière radius, R_M . On average, about 90% of the shower energy is contained in a cylinder of radius equals to R_M .

The hadronic shower is more complex than the electromagnetic shower and is produced via two kind of effects. The nuclear processes involved in the production of the hadronic shower produce secondary energetic particles (mainly pions), then nucleons, nucleon aggregates from spallation and nuclear fragments. Secondary energetic particles are generated and undergo further inelastic collisions until they fall below the pions production threshold. A large fraction of the produced pions are neutral mesons that decay through the electromagnetic interaction ($\pi_0 \rightarrow \gamma\gamma$) and generate their own electromagnetic shower. The longitudinal and transverse profiles of hadronic showers are both characterised by the interaction length, λ_I . On average, about 95% of the shower energy is contained in one λ_I and 6-9 λ_I in lateral and longitudinal size, respectively [9].

In a simplistic model, electromagnetic and hadronic showers are parametrized using their longitudinal and radial profiles. In the FullSim, the showers are very precisely described, as they come directly from Geant4 [97]. The shower implementation in the FastSim has thus been based on FullSim results, as explained hereafter.

5.2.1.1 Longitudinal profile

5.2.1.1.1 Electromagnetic showers The longitudinal profile of a shower can be described by a Gamma function [109]:

$$\left\langle \frac{1}{E} \frac{dE(t)}{dt} \right\rangle = \frac{(\beta t)^{\alpha-1} \beta e^{-\beta t}}{\Gamma(\alpha)}, \quad (5.3)$$

where,

$$\begin{aligned} \langle t \rangle &= \frac{\alpha}{\beta}, \\ T_{max} &= \frac{\alpha - 1}{\beta}, \end{aligned} \quad (5.4)$$

are respectively the shower depth inside the material and the shower maximum (depth at which the number of secondary particles is maximum). They are calculated from free parameters related

to the nature of the incident particle, the shape α , and the scaling β , parameters.

The Gamma profile, the energy mean and the fluctuations per layer are well known from the CMSSW full simulation. Therefore, the longitudinal shower profile in the FastSim has been set to that derived from the full simulation and the incident energy is simply shared between layers according to the mean profile distribution given by the FullSim. This approximation showed only a 5% deviation of the shower length compared to the exact parametrisation given by the Equation (5.3) [21]. The mean profile distribution of a 50 GeV electron, generated with the full simulation, is shown as an example on Figure 5.2.

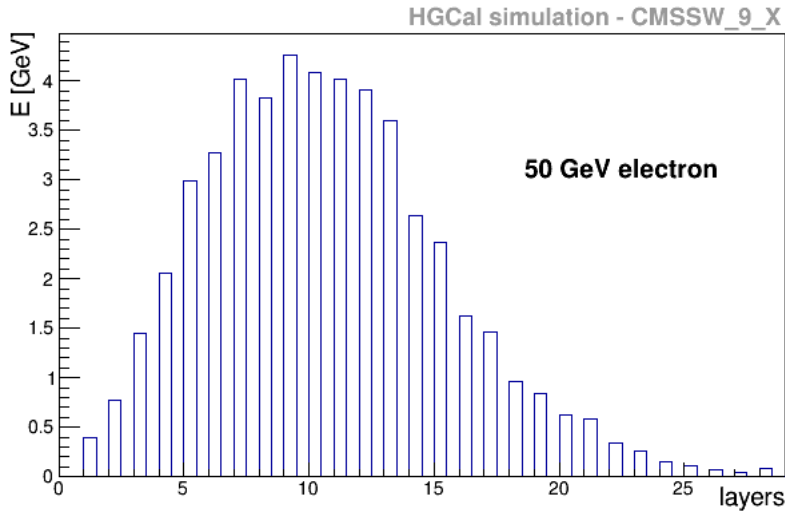


Figure 5.2 – Electromagnetic longitudinal shower profile of 50 GeV electrons in the HGCal, generated with CMSSW

5.2.1.1.2 Hadronic showers The hadronic longitudinal profile has been implemented following the same approach. The mean profile distribution of a 100 GeV pions, generated with the full simulation, is shown as an example on Figure 5.3.

5.2.1.2 Transverse profile

The transverse shower profile is decomposed into its core and halo contributions. The core corresponds to the shower maximum and vanishes with increasing shower depth. The halo is the tail of the shower, this profile distribution becomes nearly flat as the radius increases. In the following, only the parametrisation used in the fast simulation is discussed. It has been taken from the exact parametrisation defined in [109] and adapted to the HGCal study.

5.2.1.2.1 Electromagnetic showers The transverse profile of the electromagnetic shower can be written:

$$\frac{dE}{dr} = \alpha e^{-r/R_M} + \beta e^{-r/\lambda_I}, \quad (5.5)$$

where α and β are free scaling parameters, R_M is the Molière radius and λ_I is the range of low energetic photons. The first term, the shower core, is the inner part of the shower in which electrons

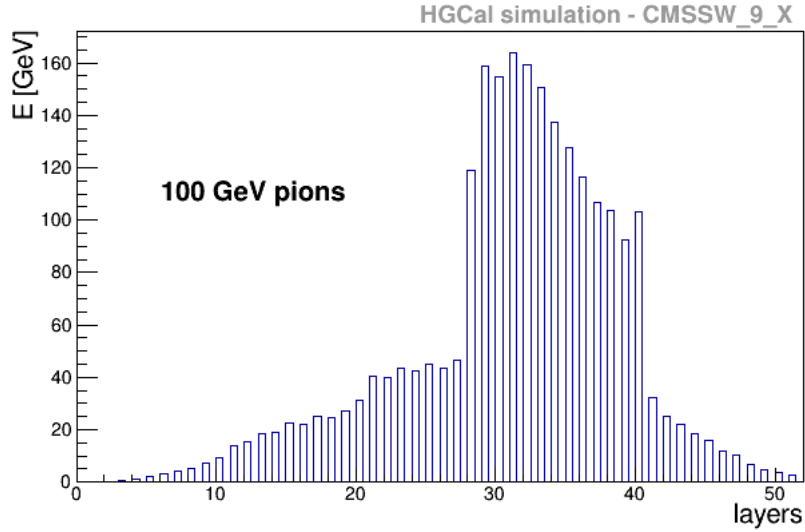


Figure 5.3 – Hadronic longitudinal shower profile of 100 GeV pions in the HGCal, generated with CMSSW

and positrons move away from the shower axis due to multiple scatterings. The second term is the contribution of the outer part of the shower, mostly corresponding to the movement of photons produced in isotropic processes (Compton scattering, photo-electric effect). In the HGCal, the shower transverse profile is well described by the exponential core [21], so the tail has been neglected in the FastSim ($\alpha = 1$ and $\beta = 0$).

The radial containment in a layer r , is defined by a second order polynomial:

$$r = \frac{1}{L_{EM}} \times (a_0 + a_1 \cdot layer + a_2 \cdot layer^2), \quad (5.6)$$

where L_{EM} is the total number of layers containing the electromagnetic shower (28 for the HGCal) and a_0 , a_1 and a_2 are parameters given by the fit of the 90% containment radius distribution in EE, as shown on Figure 5.4 [21]. This figure shows the 68% and 90% containment radius for each layer of the electromagnetic part, weighted by the fraction of the shower energy deposited in each layer. The Molière radius, expected to contain 90% of the shower energy, has been estimated around 28 mm from this distribution.

5.2.1.2.2 Hadronic showers Similarly, the hadronic radial shower profile can be parametrized with [110]:

$$\frac{\Delta E}{\Delta S} = A_{core} \cdot e^{-r/\beta_{core}} + A_{halo} \cdot e^{-r/\beta_{halo}}, \quad (5.7)$$

where $\Delta S = 2\pi r \Delta r$ is the area of the ring of width Δr at the distance r of the shower axis. A_{core} and A_{halo} are free scaling parameters and β_{core} and β_{halo} are the slope parameters ($\beta_{core} < \beta_{halo}$). β_{core} characterises the transverse shower near the shower axis and is related to the angular distribution of secondary pions from the first inelastic collisions. The halo of the hadronic shower contains all the secondary particles. These parameters are estimated by fitting the radial profile distribution as shown on Figure 5.5. The fit range is from 0 to 250 mm with a bin width of $\Delta r = 10$ mm.

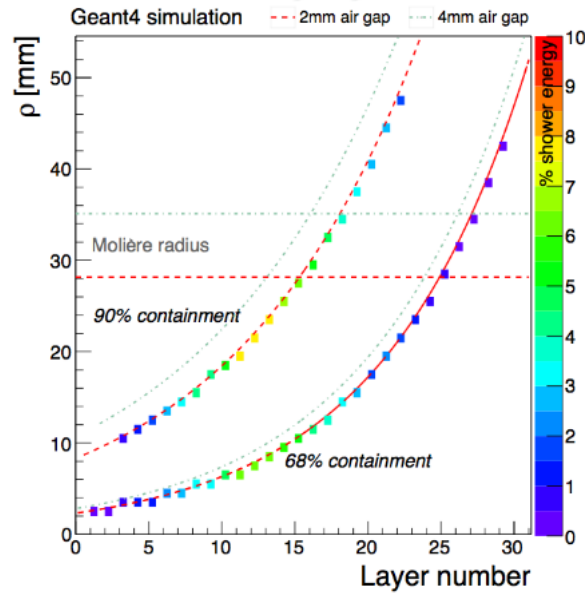


Figure 5.4 – Radius, ρ , containing 68% and 90% of the energy deposited in a silicon layer (EE) as a function of layers

This figure is taken from the Technical Proposal studies [21]. The fraction of total energy deposited in each layer is indicated by the coloured code. The polynomial coefficients of Equation (5.6) are estimated with the fit of the 90% containment: $a_0 = 8.93$, $a_1 = 0.046$, $a_2 = 0.0181$.

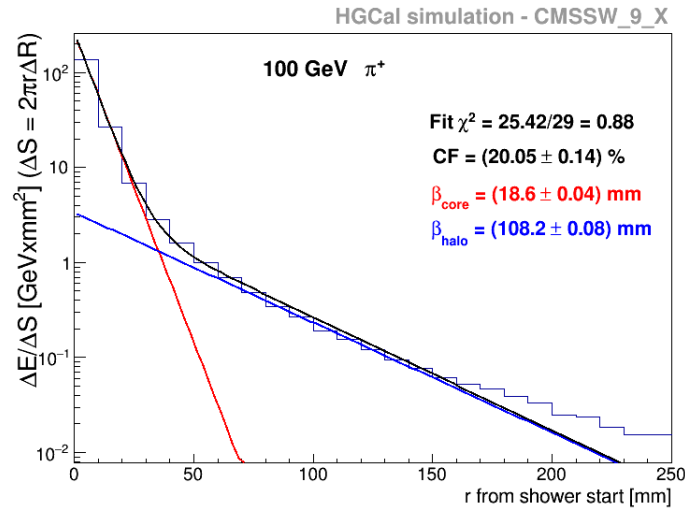


Figure 5.5 – Fit of the radial profile of a shower initiated by 100 GeV pions in the HGCal. *Fit of the core (red) and halo (blue) components for the hadronic shower parametrisation. The fitted values and the CF (see text for details) are indicated on the figure. This distribution was obtained with the release 9 of CMSSW.*

The fitted core and halo parameters for 100 GeV pions are written on Figure 5.5. The scale parameters A_{core} and A_{halo} are also estimated from this fit, computing the fractional contribution of the core, called core fraction (CF), to the total shower energy. CF is calculated as the ratio of the integral under the core component, represented by the red curve in Figure 5.5, to the total shower energy.

In order to estimate the variation of these parameters with the incident energy, the same fit has been done with 40 GeV pions. The fitted radial profile is available in Appendix A.1. The comparison of these two fits shows that β_{halo} has no energy dependence while β_{core} decreases from 23.8 mm at 40 GeV to 18.6 mm at 100 GeV. At small energies, the estimated β_{core} is close to R_M (~ 28 mm), which is compatible with the electromagnetic nature (π_0) of the beginning of the shower. The electromagnetic fraction increases as $\ln(E)$, which explains why the slope of the core decreases with the energy. The core fraction varies from $\sim 17\%$ to $\sim 20\%$ in the studied energy range. These observations are in agreement with the conclusions obtained in the study of the hadron shower decomposition in CALICE calorimeters [110, 111].

As for the electromagnetic shower, the radial containment r , in a single layer is defined by a second order polynomial function:

$$r = \frac{1}{L_{Had}} \times (a_0 + a_1 \cdot layer + a_2 \cdot layer^2), \quad (5.8)$$

where L_{Had} is the number of layers containing the hadronic shower (the full 52 layers of the HGCal for the hadronic shower), and a_0 , a_1 and a_2 are parameters given by the fit of the 95% containment radius distribution in the HGCal. Figure 5.6, shows the 68% and 95% containment radius in the HGCal, weighted by the fraction of the shower energy deposited in each layer. 95% of the shower energy, are expected to be contained in about 165 mm.

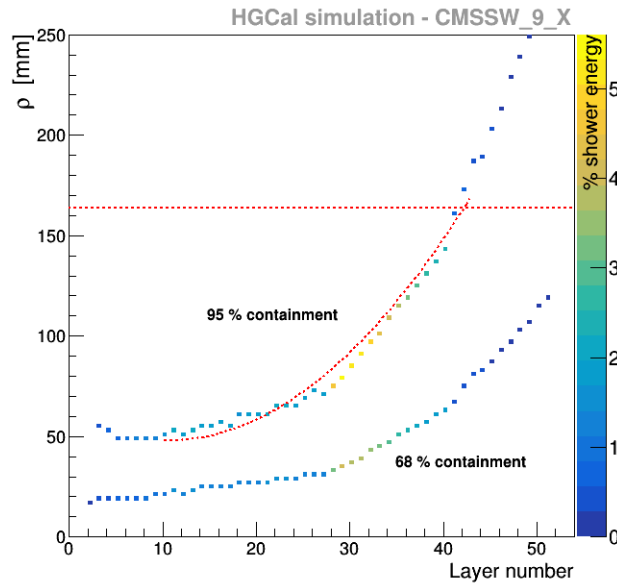


Figure 5.6 – Radius, ρ , containing 68% and 95% of the energy deposited by the hadronic shower in the HGCal

These distributions have been generated using the CMSSW full simulation. The fraction of total energy deposited in each layer is indicated by the coloured code. The dotted red line shows the 95% containment of the shower energy. The polynomial coefficients of the Equation (5.8) have been estimated by fitting the 95% containment from layer 10 to 40 (the pion is MIP-like deposit in other layers): $a_0 = 60.2$, $a_1 = -2.37$, $a_2 = 0.114$.

5.2.2 Hits generation

The calorimeter energy resolution is degraded by the fluctuations related to the physical development of the shower:

$$\frac{\sigma_E}{E} = \frac{a}{\sqrt{E}} \oplus \frac{b}{E} \oplus c \quad (5.9)$$

where a , b , c correspond to the stochastic term, the noise term and the constant term, respectively. All these contributions have been explained in Section 3.1.2.

The stochastic term

In the example shown in Figure 5.7, the energy resolution for 100 GeV pions is dominated by the sampling fluctuations.

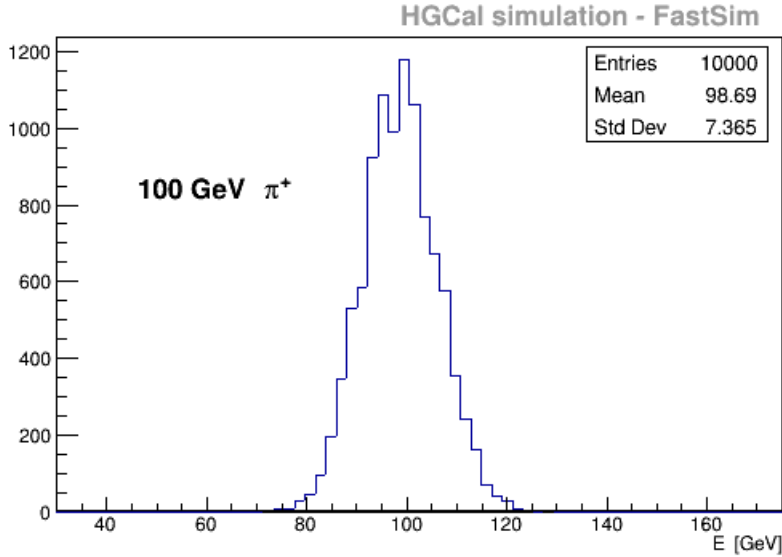


Figure 5.7 – Energy fluctuations of 100 GeV pions in the HGCal

This energy distribution is the reconstructed energy of a pion with incident energy 100 GeV after passing through the HGCal. The fluctuations in the measured energy are largely dominated by the sampling fluctuation. This distribution is a result of the HGCal fast simulation in which the sampling fluctuations are modelled as explained here.

The sampling fluctuations implementation in the fast simulation is the following. The number of hits N of fixed energy e follows a Poisson distribution. Identifying:

$$E = Ne, \quad (5.10)$$

where E is the incident energy, the energy of each spot in a layer is:

$$e = a^2. \quad (5.11)$$

The stochastic terms used in the FastSim are given in Tables 3.1 and 3.2. In this simulation, if the fluctuations are not enabled, a fixed number of hits per GeV, N , of energy E/N can be used.

In both cases, the number of hits per layer is weighted by the mean layer energy profile given by the longitudinal shower profile. The number of spots per layer is computed as:

$$\text{hits per layer} = \text{Poisson} \left(\frac{E \times \text{LayerWeight}}{e} \right). \quad (5.12)$$

Electronic noise implementation

In the HGCal the noise term is η and layer dependent. In the hybrid layers section it varies in a small range (assuming good quality electronics). In scintillators, the signal is collected in the form of light and read out by photosensitive captors, small levels of noise can be achieved. In order to add a realistic level of noise through all the HGCal structure, the noise contribution is directly taken from the same file used to add the noise contribution to the hits produced by Geant4 in the full simulation. This noise estimate is based on a study of the signal-to-noise ratio after a lifetime exposure (3000 fb^{-1}) [21].

To maintain the good software timing performance of the simulation, the noise is added only in the cells containing the signal.

Constant term

The constant term has been neglected in this simulation.

The final energy of the hit is the sum of the spot energy e and the computed noise as previously explained.

The hits are then associated with the closest cell based on its distance with the cell centre. The matching is done searching the corresponding cell by scanning all the list of cells built as explained in Section 5.1. This technique is not optimal and the following section presents an improved hit-cell pairing algorithm, that allows for a high generation rate.

5.3 A very fast simulation

In the initial implementation, only the electromagnetic shower was simulated in a single layer of the EE part. With this new version, the hit positions of the electromagnetic and hadronic showers have to be compared with a list that contains the cells of all 52 layers. Iterating on this huge list for each hit exhibited a poor performance which made the software unusable.

This new hit-cell association algorithm is based on a Quadtree [112, 113] data structure. It is used to efficiently store points in a two-dimensional space. In the fast simulation, the cells are identified with their centre coordinates ; therefore the Quadtree can be used to store them within the simulated window. The cell storage and the hit-cell association, illustrated by Figure 5.8, are explained using the hexagonal cells as an example, but the principle is the same with square cells.

The plane is first divided into four rectangles (nodes) which are themselves recursively subdivided into four children until a defined depth, $n = 3$ on Figure 5.8. As explained in Section 5.1, the observation window is not a rectangle but it corresponds to a HGCal cassette ($1.475 < |\eta| < 3$ and $|\phi| < \frac{\pi}{6}$). The first step is to determine the initial rectangle dimension (dotted rectangle), which is approximated by the cells with the smallest, $cell_{min} = (x_{min}, y_{min})$, and the largest, $cell_{max} = (x_{max},$

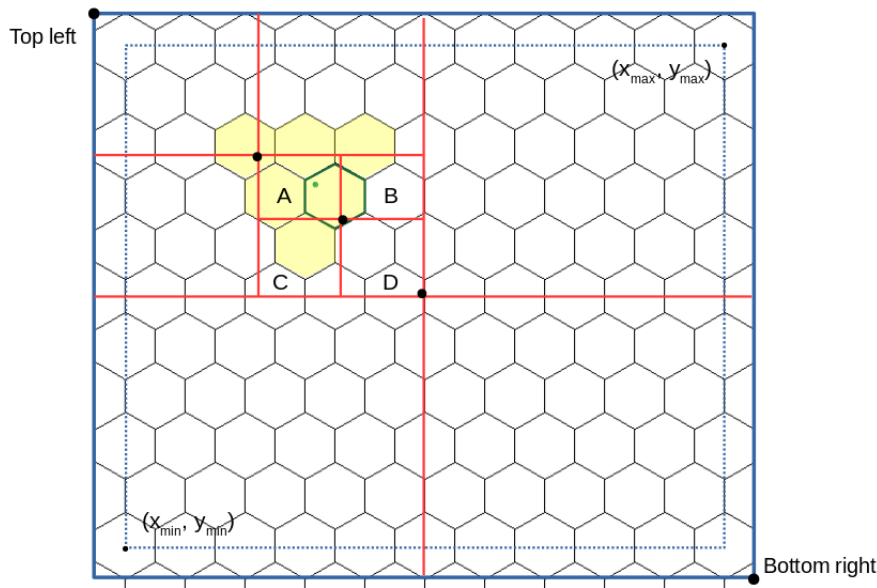


Figure 5.8 – Principle of the Quadtree data structure applied on the hexagon geometry in the fast simulation

A rectangle is approximated using the cell centres (blue dotted rectangle) and extended to the real rectangle (blue plain rectangle). This plan is then recursively subdivided until a given level of subdivision of the Quadtree, fixed to three on this figure. The cells are added to each leaf based on their location. Each hit (for example the green dot) is compared to the list of cells contained in the same leaf (yellow cells). The hit is matched to the cell minimising the distance between itself and the cell centre. See the text for details.

y_{max}), coordinates. As these points correspond to cell centres, the real rectangle (plain rectangle) is found by adding a margin to reach the cell borders; all the cells are then contained in the rectangle.

Each node is defined by its top left and bottom right corner coordinates. The last node of depth n has no children and is called leaf (A, B, C and D on Figure 5.8). The cells are recursively distributed throughout the structure and stored in the corresponding leaf based on their locations. At the end of the association process, each leaf contains a list of cells. Once the tree structure is built, each hit is matched to the corresponding leaf by using its coordinates and the hit-cell association is done comparing it with all the cells contained in the leaf. As shown on Figure 5.8, each leaf only contains a fraction of the initial cell list (yellow hexagons) and this iteration is very fast. The average number of cells by leaf can be adjusted by changing the depth of the Quadtree.

As shown on Figure 5.9, a wrong association can occur if the hit and its cell belong to different leaves; this situation is possible if the cell distribution in the Quadtree is based on its centre coordinates. To prevent this situation, a square is defined around each cell, which was added to the leaves containing at least one corner of this square.

This geographical discrimination data structure is very efficient compared to a simple list, allowing searches in $\mathcal{O}(\log n)$ time against $\mathcal{O}(n)$ respectively. By using this approach, the fast simulation reaches a 2.6 kHz generation rate. Some run time measurements are given in Table 5.2. The geometry display time is just given for indication as it is not used in normal simulation.

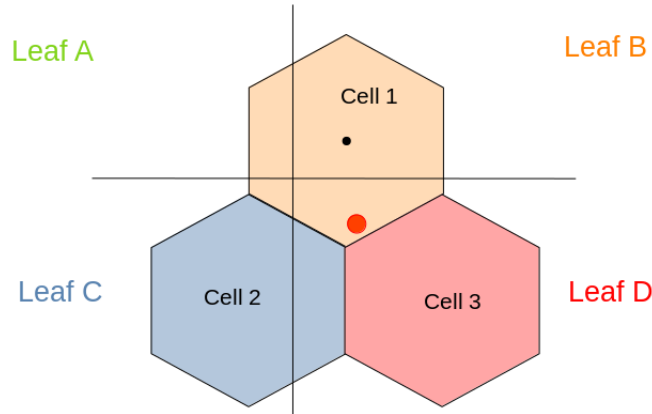


Figure 5.9 – Wrong hit and cell distribution within Quadtree leaves

On this figure, the cells are added to the leaf based on the cell centre coordinates. Each cell is added in only one leaf. The hit is added to its nearest cell in Leaf D, while it in fact belongs to Leaf B. If the cell is defined in a square and added to the leaves containing at least one corner of this square, the cell 1 belongs to leaves A, B, C and D and the hit is correctly assigned.

Table 5.2 – Fast simulation run time (seconds)

| | | | | | |
|---------------------|--------------------|------|--------|---------|-----------|
| Geometry simulation | Without display | 17 | | | |
| | Silicon layer | 25 | | | |
| | Scintillator layer | 40 | | | |
| Event generation | Nb. event | 1000 | 10 000 | 100 000 | 1 000 000 |
| | 1 particle | 2 | 15 | 35 | 380 |
| | 2 particles | 3 | 20 | 70 | 725 |

5.4 Software validation

The fast simulation software has been validated by comparing the distributions with those from the full simulation. The comparison of the longitudinal and transverse profiles of the shower as well as the energy distribution for electrons, photons, pions are respectively shown on Figure 5.10, Figure 5.11 and Figure 5.12.

These distributions show a sufficient agreement between the CMSSW and the fast simulation of the HGCal if the objective is to optimise the detector parameters. It confirms the accuracy of the software. The electromagnetic shower is well described by the FastSim. The hadronic shower is hard to model, nevertheless the shower implemented in the fast simulation, based on full simulation results, is roughly reproduced. However, the FastSim does not take into account the large fluctuations of the visible energy and of the electromagnetic fraction. This is why the energy distribution from the fast simulation nicely peaks around 100 GeV while the width of the FullSim distribution is much larger (about 3 times).

The validation has been done with particles generated at fixed η , ϕ and energy without PU. However, it is possible to use the fast simulation with incident parameter variations or to shoot several particles at the same time. Only fixed energy electron, photon and pion are currently avail-

able in the fast simulation and the PU has not been studied. Other particles or PU can be easily added and the main parameters to adapt are the mean energy profile as well as the core and halo parameters of the radial profile. For now, they can be changed using the fitting procedure described in Section 5.2.1. However, it could be worthwhile to implement a better description of the shower. In particular introducing visible energy fluctuations and electromagnetic fraction into the hadronic shower description for example, that have small impact on the pic position but large effect on the width.

As explained in Section 5.1.1, the geometry has been updated since its 2016 version, which is used in FastSim. The new geometry has not been tested here. As it shows a negligible impact on the FullSim distributions, the results presented in this chapter are assumed to be still valid. Nevertheless, the geometrical parameters can be easily changed if needed.

The fast simulation of the HGCal is a standalone and accurate complementary tool to the full CMSSW simulation. The geometry, granularity and detector materials are easily adaptable, which makes a fast, flexible and easy to use tool, able to emulate both the electromagnetic and hadronic shower developments in the HGCal. It can be used either with the last HGCal design or to make quick tests on the HGCal parameters. All these characteristics make it a powerful optimisation tool.

Possible further developments could be added to make it a more complete tool. For instance, the approach of the showers development is simple and some physics elements, such as the electromagnetic field, are not simulated. The longitudinal shower implementation could be improved to become energy dependent, using a parametrization given by Equation (5.4). The hadronic shower is only a rough estimation and could be enhanced to describe as closely as possible the real development. Ultimately, the profile of other particles and the PU are also interesting complements to consider.

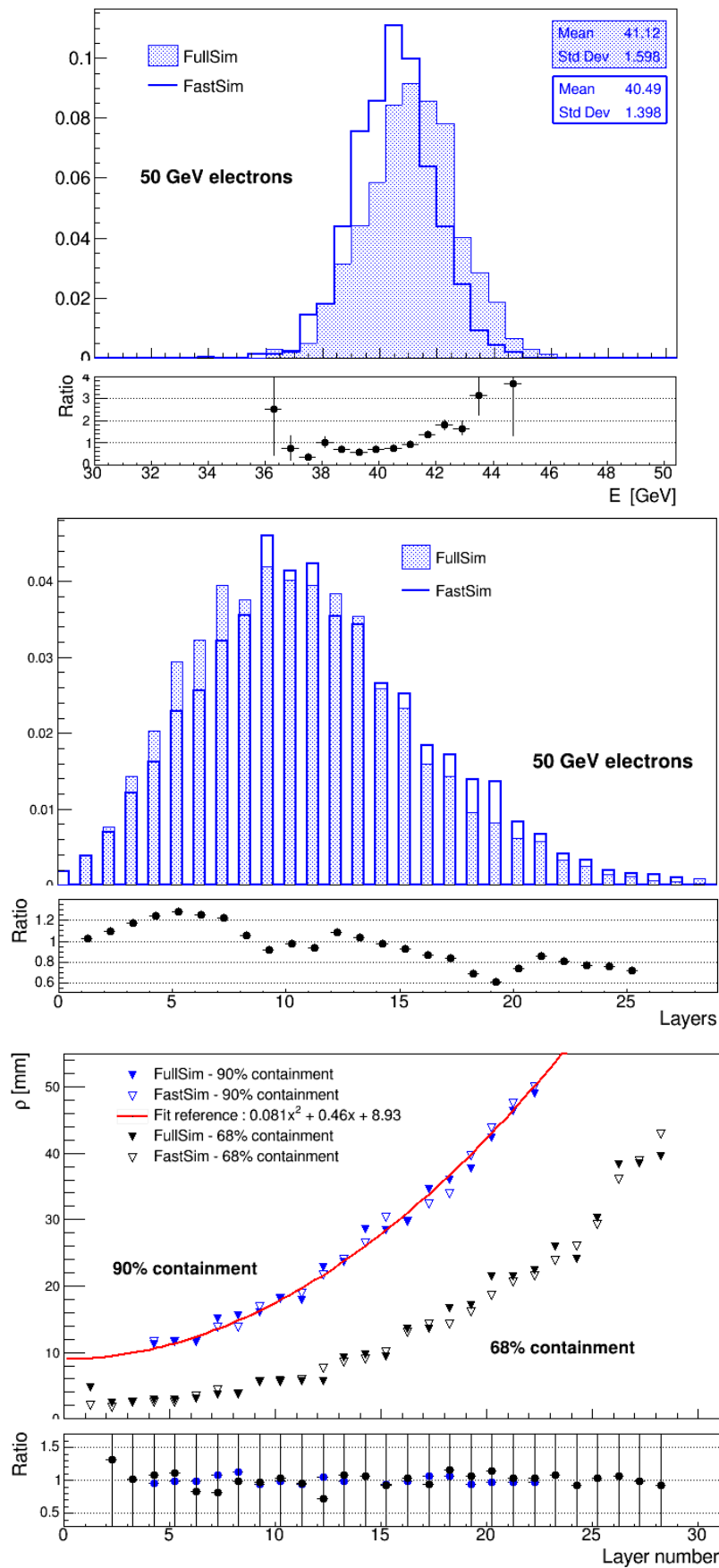


Figure 5.10 – Comparison of the distributions from the fast simulation to CMSSW results for 50 GeV electrons

*Top: reconstructed energy of the particle.
 Middle: mean profile distribution in layers.
 Bottom: 68% and 90% containment radius.*

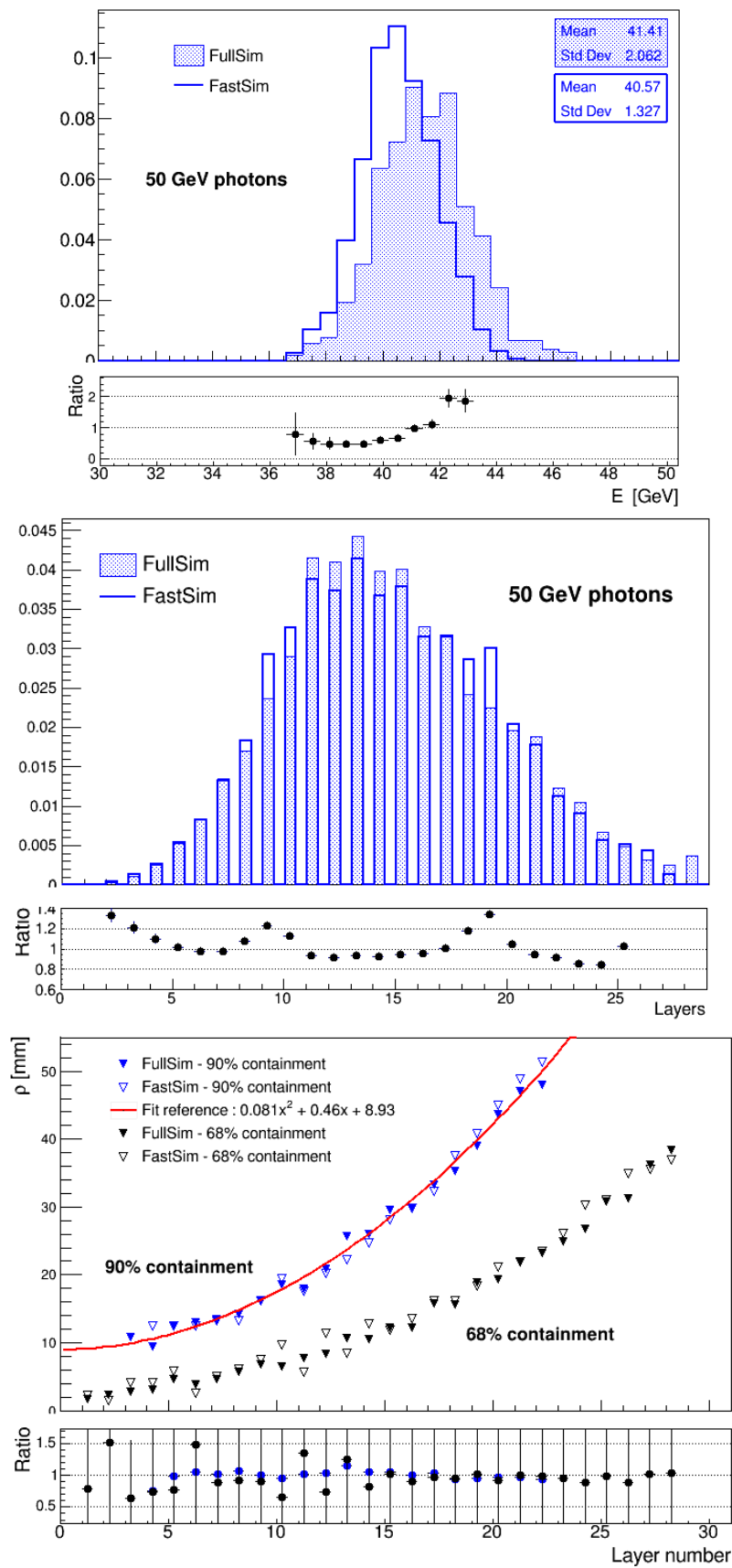


Figure 5.11 – Comparison of the distributions from the fast simulation to CMSSW results for 50 GeV photons

*Top: reconstructed energy of the particle.
 Middle: mean profile distribution in layers.
 Bottom: 68% and 90% shower containment radius.*

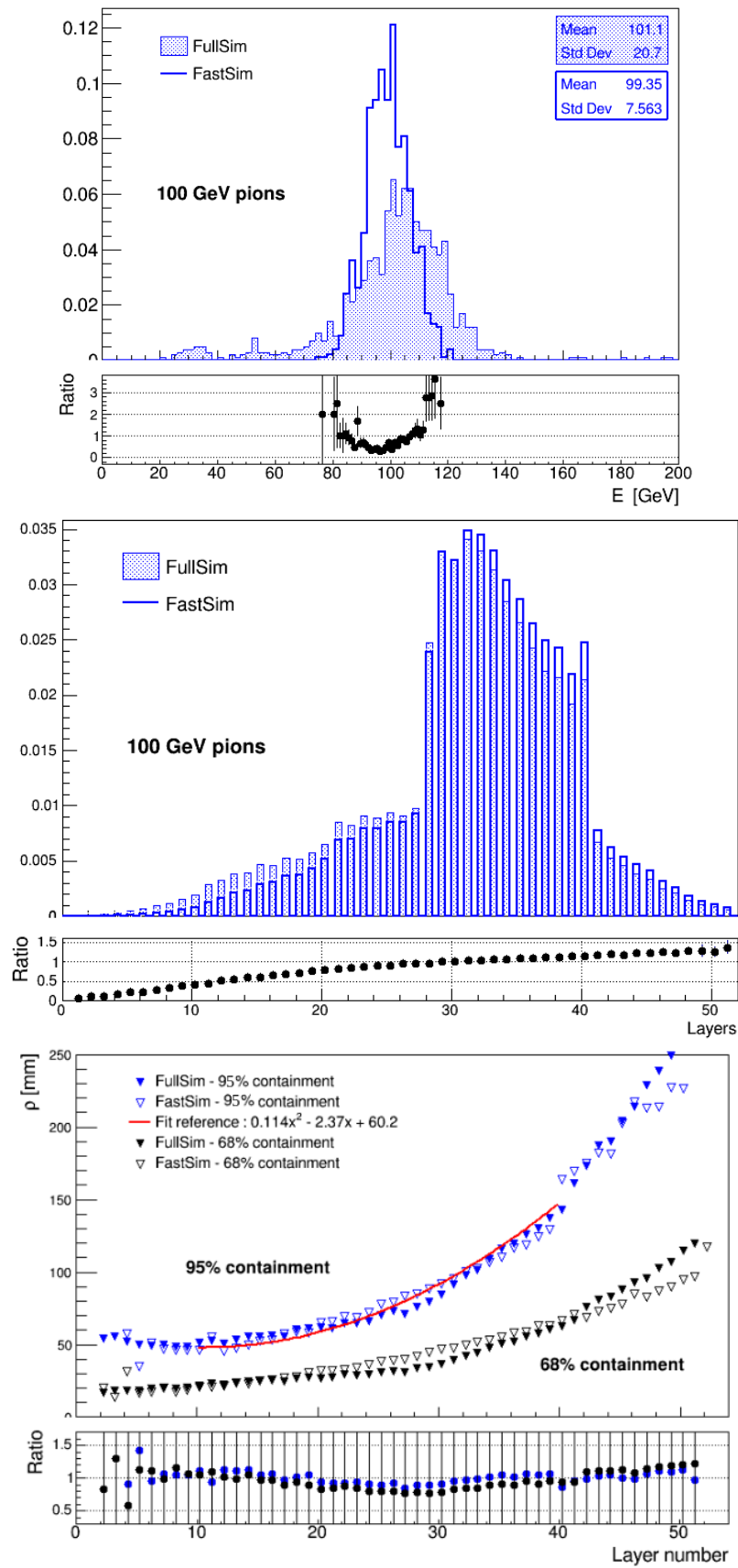


Figure 5.12 – Comparison of the distributions from the fast simulation to CMSSW results for 100 GeV pions

*Top: reconstructed energy of the particle.
 Middle: mean profile distribution in layers.
 Bottom: 68% and 90% shower containment radius.*

Chapter 6

W mass measurement at the HL-LHC with CMS

"An experiment is a question which science poses to Nature, and a measurement is the recording of Nature's answer."
Max Planck

Contents

| | | |
|------------|---|-----------|
| 6.1 | Recoil definitions | 84 |
| 6.1.1 | Traditional definitions | 84 |
| 6.1.2 | Recoil resolution | 85 |
| 6.1.3 | Improvement of the recoil definition | 86 |
| 6.1.3.1 | Principle | 87 |
| 6.1.3.2 | Regression targets | 88 |
| 6.1.3.3 | Quantile regression | 90 |
| 6.1.3.4 | Corrections | 91 |
| 6.2 | Recoil study | 91 |
| 6.2.1 | Input variables | 91 |
| 6.2.2 | Comparison of the estimators | 94 |
| 6.3 | Effect of the HGCal parameters on the W mass | 96 |

In hadron collisions, only the leptonic decay of the W is clear enough to compute the mass of the W boson. It is produced in the process:

$$pp \rightarrow W + X \quad \text{with} \quad W \rightarrow l\nu.$$

X is the hadronic recoil of the collision, resulting from the hadronisation of the proton remnants and of the gluon initial state radiation. It is reconstructed from all particles produced in the collision but the lepton.

The W mass can be measured from the lepton and neutrino transverse momentum, p_T^l and p_T^ν , as well as the transverse mass, m_T . The first two observables are most sensitive to the W transverse momentum spectrum, p_T^W , which is very difficult to predict from theory. The transverse mass is less theory dependent but more difficult experimentally, as the recoil transverse momentum is used in the computation of m_T . Given the present state of the art of the present theoretical calculations, M_T is expected to provide the smaller combined error (experimental and theoretical uncertainty). Hence an accurate W mass measurement directly relies on a precise measurement of the recoil. See Chapter 2 for more details.

The systematic uncertainty on the recoil directly depends on the recoil definition model, the detector effect and the PF algorithm used for the reconstruction. This chapter first treats about the recoil definition and proposes a method to improve its definition, further exploiting the full information collected by the detector. In the last section, the effects of the HGCal parameters on the recoil reconstruction at HL-LHC, and therefore the ability to precisely measure the W mass with the upgraded CMS detector, are estimated.

6.1 Recoil definitions

6.1.1 Traditional definitions

The recoil corresponds to the underlying event of the collision. At the generator level, i.e. without detector or PU effects, its transverse momentum, \vec{h} , is equal and opposite to the momentum of the W boson, p_T^W . From the information collected by the detector, \vec{h} is defined as the vectorial sum of the transverse momenta of all the reconstructed particles in the detector acceptance excluding the lepton. The transverse component of the recoil then satisfies:

$$\vec{h} = \sum_{i \neq l, \nu} p_T^{(i)} = -p_T^W. \quad (6.1)$$

The experimental definition of the recoil is not trivial because it is a non-local object arising from particles with different p_T and distributed throughout the detector, i.e. involving information from both the calorimeters and tracking systems, limited by the detector acceptance and subject to PU. The recoil is therefore treated as a 2D object which lies in the transverse plane and thus the two components are the magnitude, h , and the direction, ϕ .

Once the lepton is discarded, the remaining particles are either from the PU or from the primary vertex (PV), identified as the vertex with the highest p_T scalar sum. That gives rise to several possible state-of-the-art experimental definitions of the 2D vector quantity. The most common alternative is either the *particle flow recoil*, \vec{h}_{PF} or the *track recoil*, \vec{h}_{TK} .

\vec{h}_{PF} , is reconstructed from the vectorial sum of the transverse momenta of all the PF candidates. At the generator level, as the PF particles exclusively originate from the PV, in the absence of PU and detector effects, the W hadronic recoil is perfectly reconstructed by the PF algorithm. When

taking into account the detector acceptance and resolution, and the PU contamination, the tracks originating from the primary vertex can still be attached to it with a great efficiency, but neutral particles are more difficult to associate to the right vertex. Solutions exist for this [114] but have not yet been implemented in CMSSW. Even if it uses the information of all reconstructed particles, the performance of the particle flow recoil is limited by the PU contamination, as shown on Figure 6.1. This PU dependence is expected to be reduced, but not eliminated, with the CMS upgrade for HL-LHC, thanks to more granular sub-detectors and HGCal timing ability.

\vec{h}_{TK} is a recoil vector reconstructed from the sum of all the transverse momenta of tracks coming from the PV. If the W boson is generated with a high transverse momentum, the reconstructed recoil momentum is expected to be correctly oriented. At small p_T^W , the low p_T particles are uniformly distributed in the detector and then the recoil magnitude might be overestimated with a poor direction resolution. Although \vec{h}_{TK} contains only 40% of the true recoil, this definition exhibits good data-MC agreement and is insensitive to PU contamination due to an accurate charged particles to vertices association, as shown on Figure 6.1. This characteristic is expected to be conserved in the high PU environment of the HL-LHC thanks to the high granularity planned by the tracker update [21]. A good data-MC agreement is particularly important as the W mass is usually measured by comparing the experimental distributions with similar ones obtained with a MC simulation.

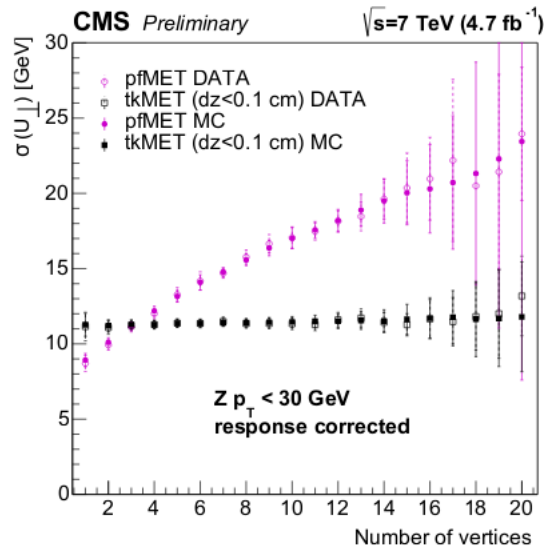


Figure 6.1 – Resolution of the transverse momentum of the recoil from Z events as function of the number of vertices for particle-flow and track recoil definitions for simulated data and data samples [25]

The W events behave the same way than the Z events shown on this figure.

6.1.2 Recoil resolution

The resolution of the recoil is defined as:

$$\Delta\vec{h} = \vec{h}_{measured} - \vec{h}_{true}, \quad (6.2)$$

where $\vec{h}_{measured}$ is the experimental reconstruction of the recoil and \vec{h}_{true} is the generator level recoil. Figure 6.2 shows the distributions of the resolution of the track recoil in x-y transverse plane of the

detector (left) and in the coordinate system parallel and perpendicular to the true recoil (right). In the first case the resolution is almost homogeneous whereas the reconstructed momentum of particles coming from the W vertex has different variation for parallel and orthogonal components. This difference underlines a dependence of the reference frame of both the recoil and its resolution.

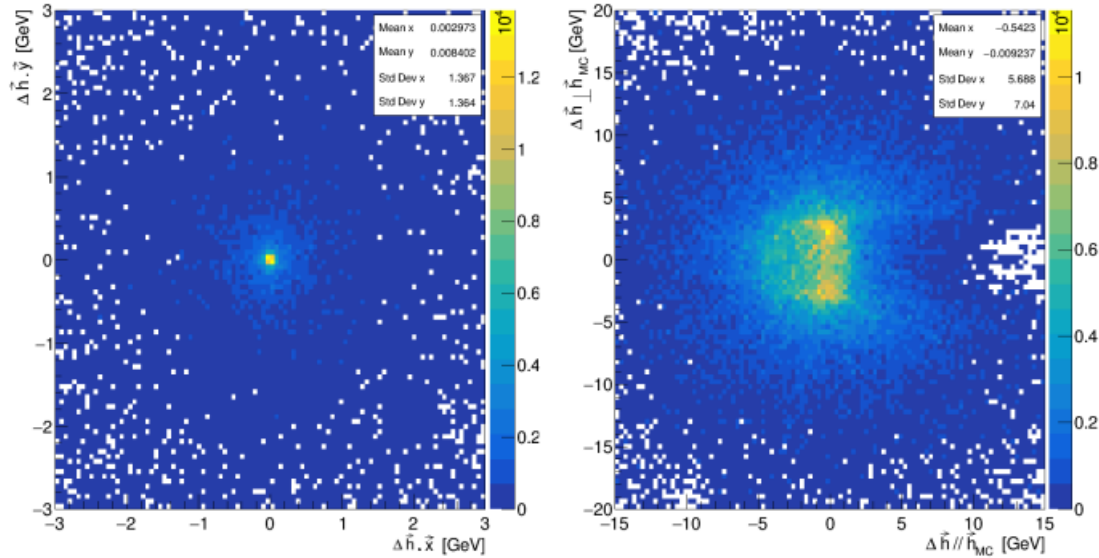


Figure 6.2 – Distribution of the track recoil resolution of $W \rightarrow l\nu$ events represented in two reference frames

Left: CMS frame (x - y axis of the detector). Right: true recoil direction (W boson flight direction).

In order to be frame-independent, an other way to estimate the recoil resolution is using the distribution of $|\Delta \vec{h}|$. Figure 6.3 shows the distributions of this quantity for the track and particle-flow recoil definitions.

Hence two main effects affect the measurement of the scale and the direction of the recoil: the acceptance and the pile-up. As discussed above the effect of the pile-up can be well mitigated by using tracks only. However this has two consequences: a tightening of the acceptance to the tracker region and a loss of response as the neutral component is missing. A tighter acceptance is harmless as long as the neutrino is emitted centrally since most of the recoil information is contained in particles centrally emitted. In that case the correlation between the recoil p_T and direction with the true p_T is preserved, but at low W p_T , there is a loss of correlation. In addition the resolution is affected by the use of tracks only and the choice of the system of coordinates. A regression of the recoil can partially recover these effects by using global event features such as the number of reconstructed tracks at a given energy or the shape of variables including parameters describing the geometrical shape of the particles in the detector. A new estimator, allowing to improve the experimental definition of the recoil by optimising, as much as possible, the recoil features is presented in the following.

6.1.3 Improvement of the recoil definition

The objective is to find the best estimator of the true recoil, y , starting from an input vector, x , containing all the experimentally measured features of the recoil. The function mapping these

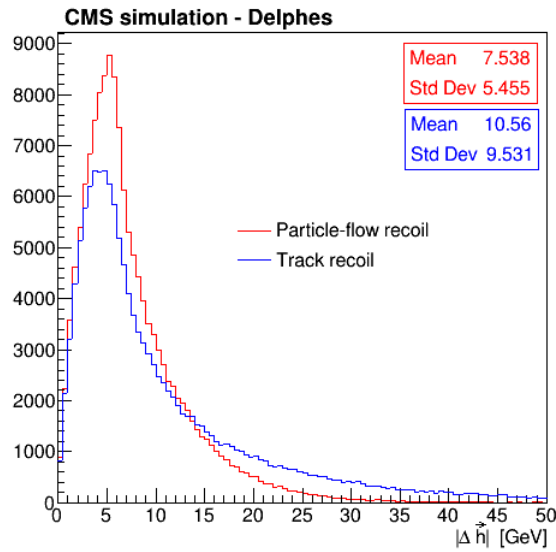


Figure 6.3 – Recoil resolution of $W \rightarrow l\nu$ events estimated with $|\Delta\vec{h}|$ and reconstructed with track and particle-flow recoil definitions

features to the recoil is defined as:

$$y = f(x). \quad (6.3)$$

This function is unknown and can be analytically computed for only a limited number of features. For example, during the W mass measurement in ATLAS, $f(x)$ was computed for only two features [19]. However, learning the exact expression of the function f per se is useless. The aim is to optimise it to predict the best reconstructed recoil from many input features. This optimisation is done event-by-event using a multivariate quantile regression [115, 116, 117] based on a deep dense neural network (DNN) [118].

6.1.3.1 Principle

The architecture of a DNN is illustrated on Figure 6.4. A DNN builds a non-linear function from a large set of input parameters. They are trained in the network architecture made of blocks, so-called *neurons*, in order to minimise a function, so-called *loss function*. The output (target) returns the best estimator of the regressed parameter.

The neurons are organised on layers with a hierarchical order. The neurons of the different layers are connected between them (dense network): the output of every neuron is given as input to every neuron of the next layer. Each neuron performs linear operation. Figure 6.4 (right), shows the sketch of the workflow of a neuron. The input parameters, x_i , are weighted by free parameters, w_i ($b = w_0$ is the bias), allowing to give different impacts to the inputs. They are then summed up before being activated by a function f to transform the weighted sum into a non-linear function. The weights and biases depend on the neuron and are chosen during the training.

In this study four hidden layers were used and the Leaky Rectified Linear Unit (LReLU) function [119] was used as activation function.

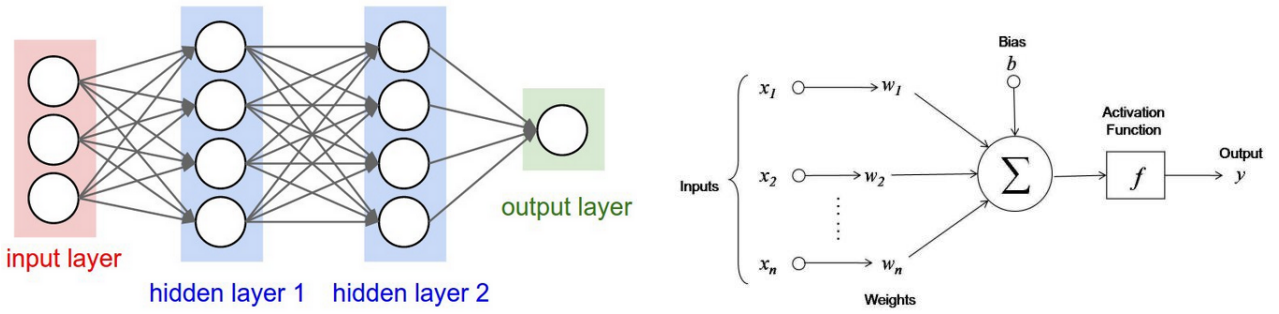


Figure 6.4 – Scheme of a deep dense neural network

Left: Example of a deep dense neural network with four layers, three input parameters and one output. The inputs are all connected to the neurons (dense network) in which linear combinations of the inputs are performed. Right: structure of a single node (neuron) in neural network. The inputs, x_i , are multiplied by the weights (w_i) and then summed up with a bias b . Next, an activation function f is applied producing the output y of the neuron. The output of each neuron is given as input to each neuron of the next layer.

6.1.3.2 Regression targets

In the present study, the recoil, is expected to be predicted by the multivariate regression. However, it is a 2D vector and then a 2D multivariate regression is needed to estimate its two components. This has been done by defining two targets, one per component, and training two multivariate regressions. Furthermore, in order to more easily assess the recoil estimator, i.e. to facilitate the DNN training thanks to simpler architecture and faster convergence, it is better to search for variables with the sharpest single-peaky shape that do not change significantly from an event to another. Therefore, instead of fitting directly the recoil magnitude and direction, corrections to these parameters have been used as targets of the regression. Several correction parametrizations are possible [120] and the only consequence of a bad choice will result in sub-optimal recoil definition.

Having defined an estimator of the recoil, either \vec{h}_{TK} or \vec{h}_{PF} , corrections for their scales and directions can be estimated on an event-by-event basis. Figure 6.5 illustrates these corrections based on the track recoil definition. These corrections:

$$e_1 = \frac{|h_{true}|}{|h_{TK}|}, \quad (6.4)$$

$$e_2 = \phi_{true} - \phi_{TK},$$

are a scale factor of the magnitude and the azimuthal angle correction by which the recoil is to be rotated to transform it into the true one. It has been found that e_1 has a regular asymmetric shape with a boundary at zero [120] and that this behaviour can be corrected by applying a logarithmic transformation. The correction coefficients used as target of this regression are then $\ln(e_1)$ and e_2 . Their distributions using the track recoil definition are shown on Figure 6.6.

The track recoil better measures the direction than the particle-flow recoil that is expected to be more complicated to correct with respect to the magnitude. Moreover, the track definition depends on less parameters than the particle flow (missing neutral objects, PU-vertices dependence) and is then more accurately modelled. For these reasons, the track-based recoil is used as a baseline for defining the corrections.

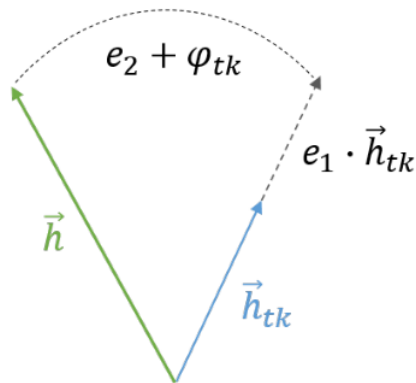


Figure 6.5 – Definition of the magnitude and azimuthal angle correction coefficients, $e_{1,2}$. On this figure, the corrections $e_{1,2}$ are shown using the track recoil definition (TK). \vec{h}_{MC} is the true value of the recoil [121]

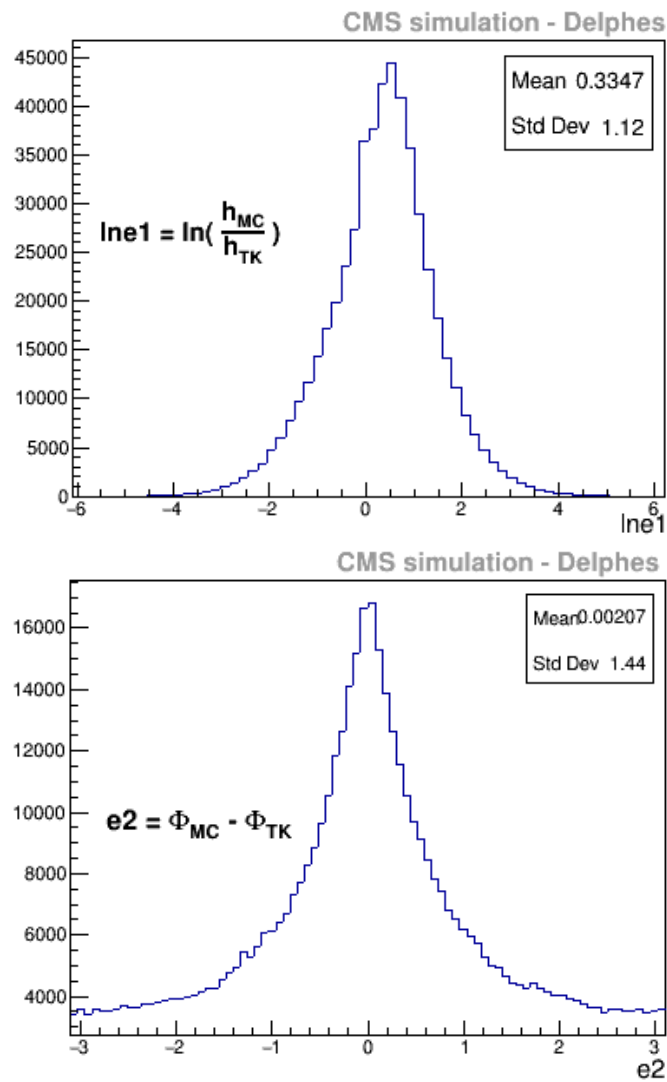


Figure 6.6 – Recoil correction coefficient distributions using the track definition

6.1.3.3 Quantile regression

To obtain a precise description of the correction parameters, the particular case of the multivariate quantile regression was used [115, 117]. In a standard linear regression, whose principle is described in Section 6.1.3.1, the targets are predicted event-by-event from the input features. The distribution of the corrections are assumed Gaussian-like (centred and symmetric) and this provides only a partial view of the relationship between the recoil features and the outcome variables. In case of experimental data, one needs more robust estimator against outliers in the input measurements. The *quantile regression* allows to obtain a more comprehensive analysis of the relationship between the input variables and gives a more precise prediction of the corrections.

In the quantile regression of a target, the DNN is executed in three steps. A first regression allows to estimate the median (peak) of the correction, and the two other steps give access to the statistical dispersion of the correction at selected quantiles. In this study, the adopted quantiles were $q_1 = 16\%$ and $q_2 = 84\%$ corresponding to a 1σ deviation. The regression targets were trained iteratively. After finishing the training of the peak and the two quantiles of $\ln(e_1)$, the internal parameters of the network were frozen and the predictions of the peak and quantiles of e_2 were started. This approach is based on previous studies and optimisations of these parameters analysis [120].

At each step of the regression, a quantile loss is minimised, predicting a certain quantile. The quantile loss function is given by [122]:

$$\rho_q(e) = \begin{cases} eq & \text{if } e > 0, \\ (q-1)e & \text{otherwise,} \end{cases} \quad (6.5)$$

where q is the quantile ($0 < q < 1$) and $e = y - f(x)$ is the residual, difference between $f(x)$, the predicted value and y the estimated target for a corresponding set of features x . Comparatively to the least-square estimate that minimises the sum of the squared error terms, the quantile regression minimises a weighted sum of the positive and negative error terms.

A large dataset of Monte Carlo events was used to train the neural network. The learning from one single event at a time can be unstable and even slow, in case of large datasets. Hence, the dataset was divided into small groups of data (batches) successively feeding the neural network to average the error over multiple events and get a faster evaluation of the relationship between the input variables and the regressed targets, $\ln(e_1)$ and e_2 . The training sample was divided into 1024 batches. When the entire dataset has gone through the network (Epoch), the neuron parameters are updated, and the loss function evaluated. In order to minimise the loss function, the algorithm learns from multiple presentations of the dataset. The number of Epochs was set to 50 for each single training, corresponding to the peak and the two quantiles of the two targets. Such a number of Epochs was sufficient to obtain stable results, as seen on Figure 6.7, showing the evolution of the training and validation loss functions as a function of the training Epoch. Each distinct part corresponds to a single training. The three first (last) parts are respectively related to the peak and quantiles, q_1 and q_2 of the recoil scale (the recoil direction). The overlap of the training and validation losses confirms the accurate prediction of the targets.

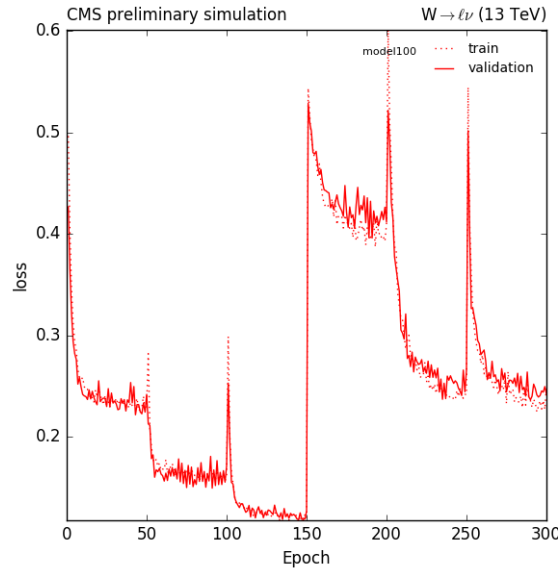


Figure 6.7 – Evolution of the loss function of the quantile regression of the recoil components as a function of Epoch

The peaks in the loss function correspond to a change in the regressed parameter. They are respectively related to the peak, q_1 and q_2 of $\ln(e_1)$ and to the peak, q_1 and q_2 of e_2 . For each target, the training and validation loss functions overlap indicating a sufficient Epoch and batch sizes.

6.1.3.4 Corrections

Peak-based correction For a first evaluation of the corrections, μ_i with i identifies $\ln(e_1)$ or e_2 , to apply on the recoil components, only the median, μ_{50} ($q = 50\%$), was used. Eventually, the estimated recoil components were computed with:

$$\begin{aligned} h^{pT} &= h_{TK}^{pT} \times \exp(\mu_{50, \ln(e_1)}), \\ h^\phi &= h_{TK}^\phi + \mu_{50, e_2}. \end{aligned} \tag{6.6}$$

PDF-based correction Both $\ln(e_1)$ and e_2 have an approximate Gaussian distribution and, for a more precise study, the corrections can be computed combining all the information given by the quantile regression. Instead of using only the mean as the estimator for one event, one could also get a likelihood distribution, by re-distributing the recoil with a Gaussian function with μ_{50} as the mean and the average of the two quantiles as the width.

The Keras library [123], a PYTHON wrapper of the TensorFlow library [124], was used. The results are presented in the next section, after a quick discussion of the chosen input variables.

6.2 Recoil study

6.2.1 Input variables

The selected input variables used in the regression were chosen in order to describe the recoil as accurately as possible. The features characterise the recoil magnitude, its composition in terms of

particles and its geometrical shape.

Although the track-based recoil definition is used to compute the corrections to apply on the recoil, the variables in input of the regression make use of some global event characteristics and properties of various recoil estimators:

- the charged tracks from the PV, \vec{h}_{TK} , as previously defined;
- all the neutral particle-flow candidates, \vec{h}_{NT} ;
- all the charged tracks that are not from the PV, \vec{h}_{NPV} ;
- the sum of the neutral and the non-PV particles, \vec{h}_{NTNPV} ;
- all the particle-flow candidates, \vec{h}_{PF} , as previously defined.
- PUPPI-based recoil estimator. PUPPI, for Pile-Up Per Particle Identification, is a particle flow algorithm developed to mitigate the pile-up [125].

If there is no PU, the NPV recoil is null and the $NTNPV$ recoil is identical to the NT one.

Table 6.1 gives the non exhaustive list of the inputs chosen in the current regression, with and without PU. Any additional variable, which would be irrelevant in this study, would not have a negative impact on the recoil reconstruction. The only negative effect would be on the training performance because the higher the number of dimension of the input vector, the bigger the statistical sample and the bigger the computational time.

In this list the magnitude and the azimuthal angle of the recoil are very important features. The sphericity is also an important characteristic that describes the shape of the recoil. In the transverse plane it is defined as the ratio between the vectorial sum and the scalar sum of the transverse momenta. The sphericity is close to 0 if the particles that form the recoil are close to each other, and close to 1 if they are uniformly distributed over the whole solid angle.

In a first step, the study of the decay $W \rightarrow l\nu$ produced at 13 TeV in the CMS detector phase I (without HGCal) was done without including PU. Figure 6.8 shows the effect of the regression on the track-based recoil using the peak-based correction only. Figures 6.8a and 6.8b show the improvement of the recoil components. Figure 6.8c shows the bias between the recoil magnitude and the true recoil magnitude. Figure 6.8d shows the recoil resolution. The quantile regression, even using the median in the correction only, well improved the recoil reconstruction.

Table 6.1 – Input features of the DNN estimating the correction on the recoil components

| Variables | Description | 0PU | 200 PU |
|---------------------------------|---|--------------------|--------|
| N_{vert} | Number of reconstructed vertex | ✓ ($N_{vert}=1$) | ✓ |
| N_{jets} | Number of reconstructed jets | ✓ | ✓ |
| N_{tracks} | Track multiplicity | ✓ | ✓ |
| ρ | FASTJET's median energy density | ✓ | ✓ |
| vx, vy, vz | Coordinates of the reconstructed vertex | | ✓ |
| $min\Delta z$ | Distance in z to the closest primary vertex | | ✓ |
| TK $\{\vec{h}, \phi, S, h\}$ | Transverse momentum, azimuthal angle, sphericity, and magnitude of track-based recoil | ✓ | ✓ |
| PF $\{\vec{h}, \phi, S, h\}$ | Transverse momentum, azimuthal angle, sphericity, and magnitude of particle-flow-based recoil | ✓ | ✓ |
| NPV $\{\vec{h}, \phi, S, h\}$ | Transverse momentum, azimuthal angle, sphericity, and magnitude of non-PV-based recoil | | ✓ |
| NT $\{\vec{h}, \phi, S, h\}$ | Transverse momentum, azimuthal angle, sphericity, and magnitude of neutral-particles-based recoil | ✓ | ✓ |
| NTNPV $\{\vec{h}, \phi, S, h\}$ | Transverse momentum, azimuthal angle, multiplicity and magnitude of neutral and non-PV-based recoil | Identical to NT | ✓ |
| PUPPI $\{\vec{h}, \phi, S, h\}$ | Transverse momentum, azimuthal angle, multiplicity and magnitude of neutral and non-PV-based recoil | | ✓ |
| lne1, e2 | Scale-angle correction coefficients for TK recoil | ✓ | ✓ |

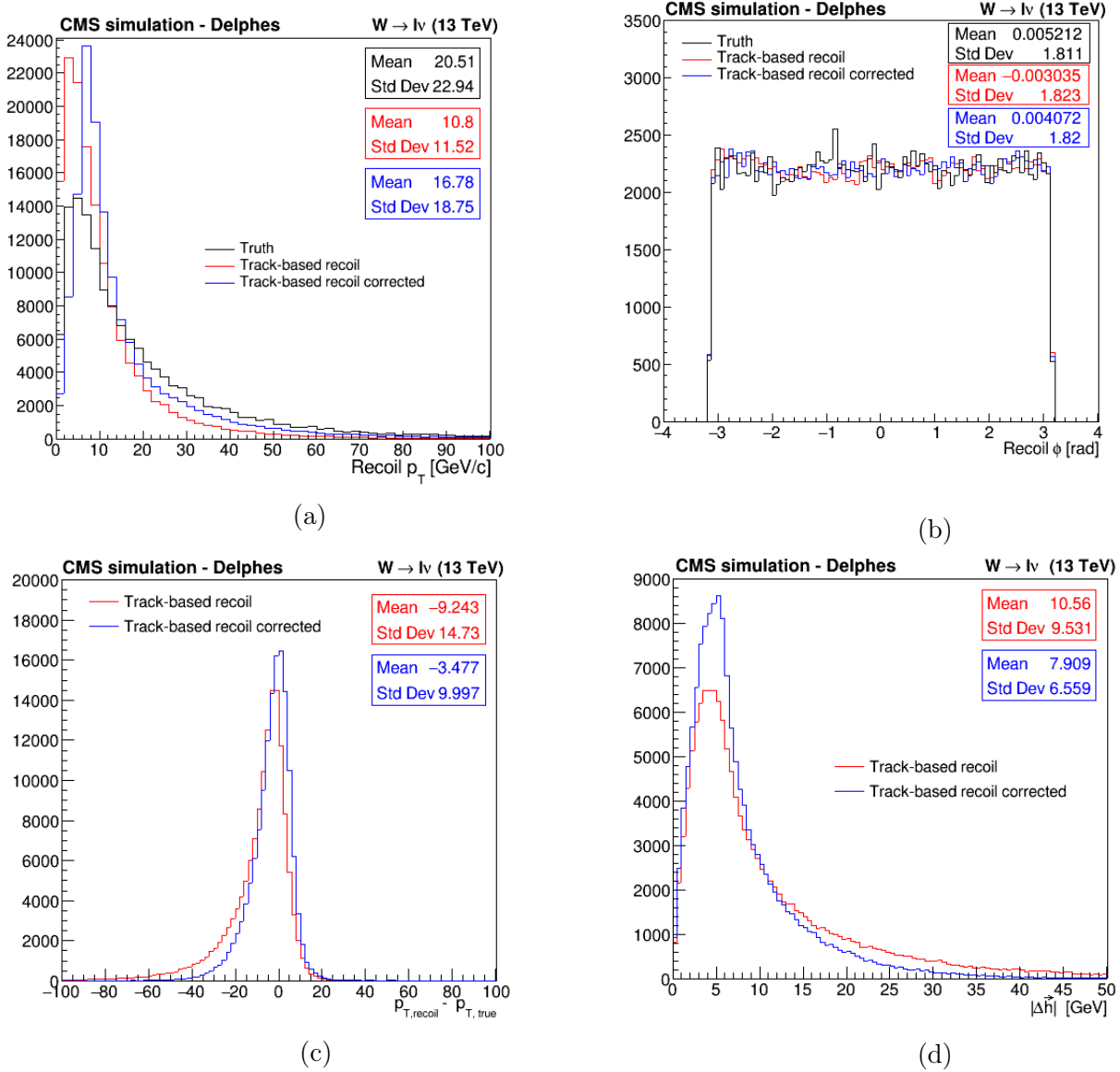


Figure 6.8 – Correction of the track-based recoil using multivariate quantile regression

Figures (a) and (b) show the improvement of the recoil components. Figure (c) shows the bias between the recoil magnitude and the true recoil magnitude. Figure (d) shows the improvement of the recoil resolution. These results were obtained with $PU = 0$. The recoil was corrected only using the median of $\ln(e_1)$ and e_2 .

6.2.2 Comparison of the estimators

The reconstruction of the recoil at 13 TeV in the CMS detector upgraded for the HL-LHC without including the HGCal was studied without PU and at 200 PU. Figure 6.9 shows the recoil scale and direction estimated with the multivariate quantile regression and corrected using the peak-based and PDF-based estimators. The distribution of the recoil direction is uniform for all estimators in the $[-\pi, \pi]$ range. Both corrections describe well the recoil scale for W - $p_T > 20$ GeV/c. Below 20 GeV/c, the Gaussian correction seems to give a better description.

The direct comparison between the different models is not straightforward. The distributions on

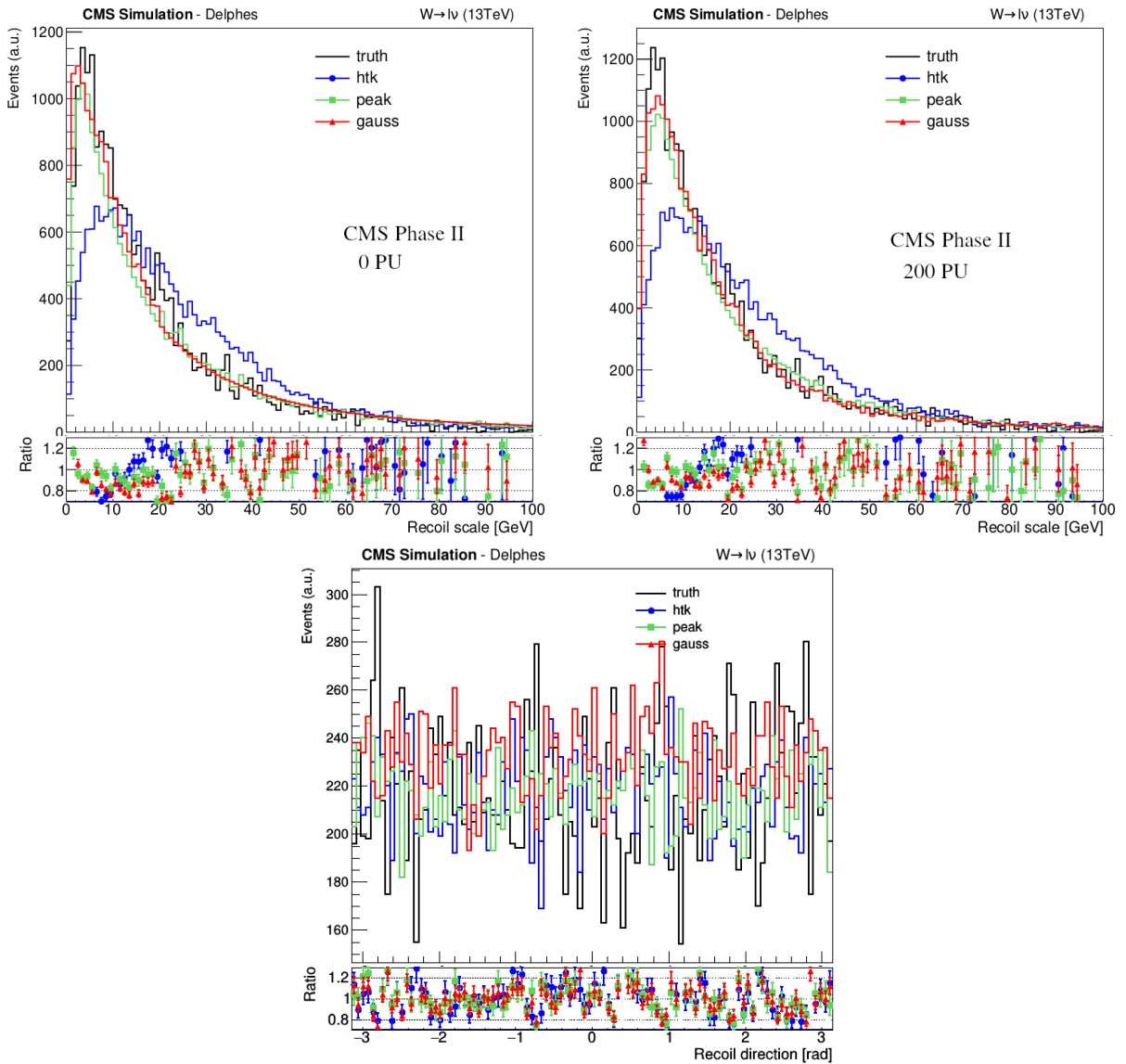


Figure 6.9 – Recoil scale and direction at 13 TeV at CMS for the Phase II reconstructed from a multivariate quantile regression using different estimators

The recoil direction is uniform between $[-\pi, \pi]$ for all estimators, it is shown at 200 PU only.

the Figure 6.9 do not depict how much the event-by-event bias and resolution differ in each model. Moreover, the peak-based correction provides a peak-only estimation while the PDF-based also considers the tails. Figure 6.10 displays how the event-by-event resolution and bias distributions with and without PU evolve as a function of the scale for the different corrections. The PDF-correction significantly improves the resolution and tends to reduce the bias at low p_T . It is interesting to note that the bias using the peak-based and the PDF-based corrections is very similar, indicating that the effect of the tails is small. Figure 6.11 shows analogous distributions as a function of the direction. The event-by-event resolution is largely improved using the Gaussian estimator at 0 PU and also yields to a better resolution at 200 PU. That indicates that the tails are crucial for the resolution of the direction. That is however not the case for the bias that remains uniform for the different models.

Despite a lack of statistics at high p_T , the comparison between the different models shows that the PDF-based correction tends to slightly improve the bias with respect to the peak-based correction while the resolution is significantly improved for both recoil components. The PDF-redistributed events model was then used to estimate the effect of the HGCal parameters.

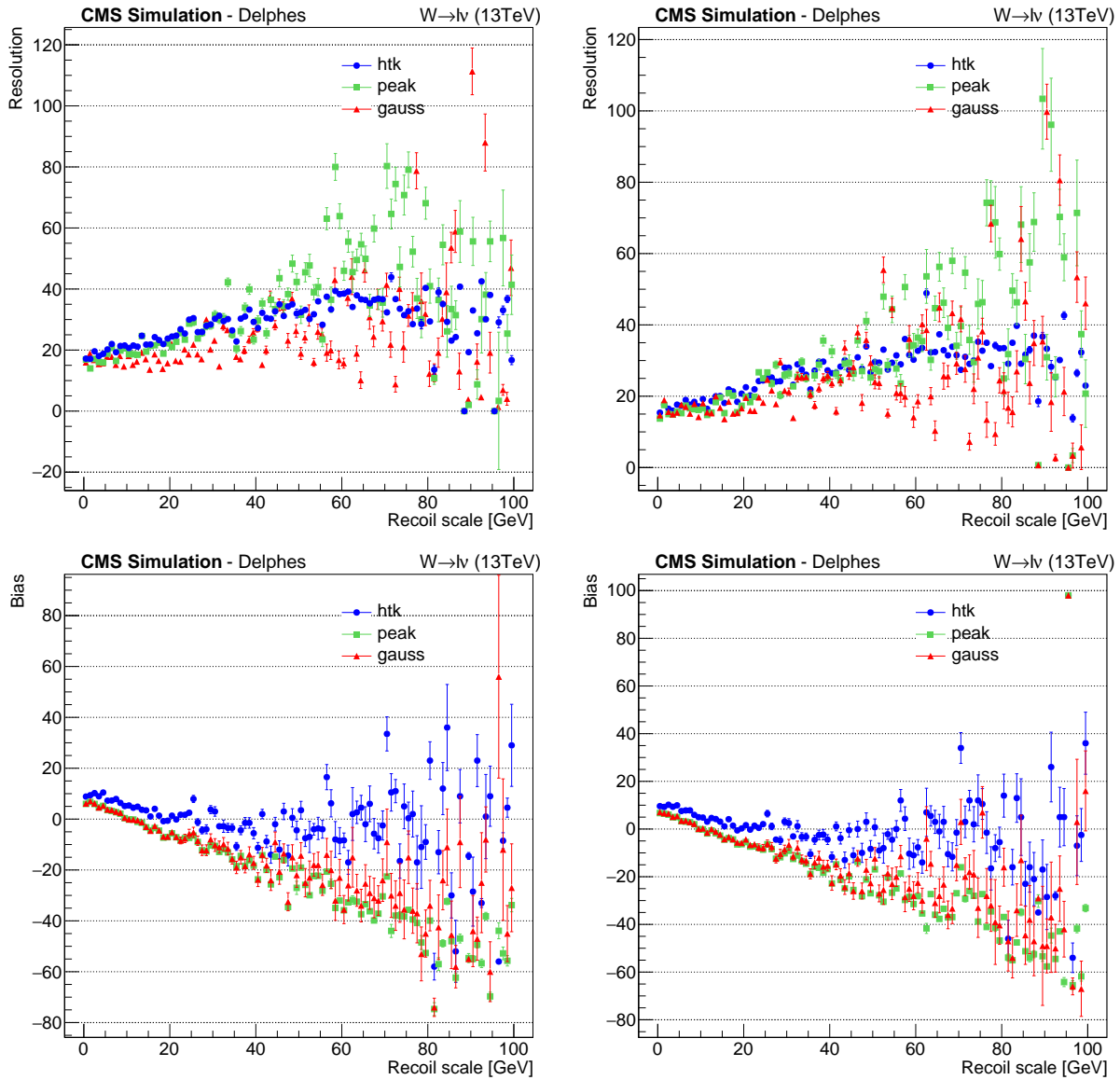


Figure 6.10 – Event-by-event resolution and bias variation as a function of the recoil scale reconstructed with different models without PU (left) and with 200 PU (right)

6.3 Effect of the HGCal parameters on the W mass

In this section, the effect of the acceptance, resolution and granularity of the HGCal on the recoil resolution with and without PU, is estimated.

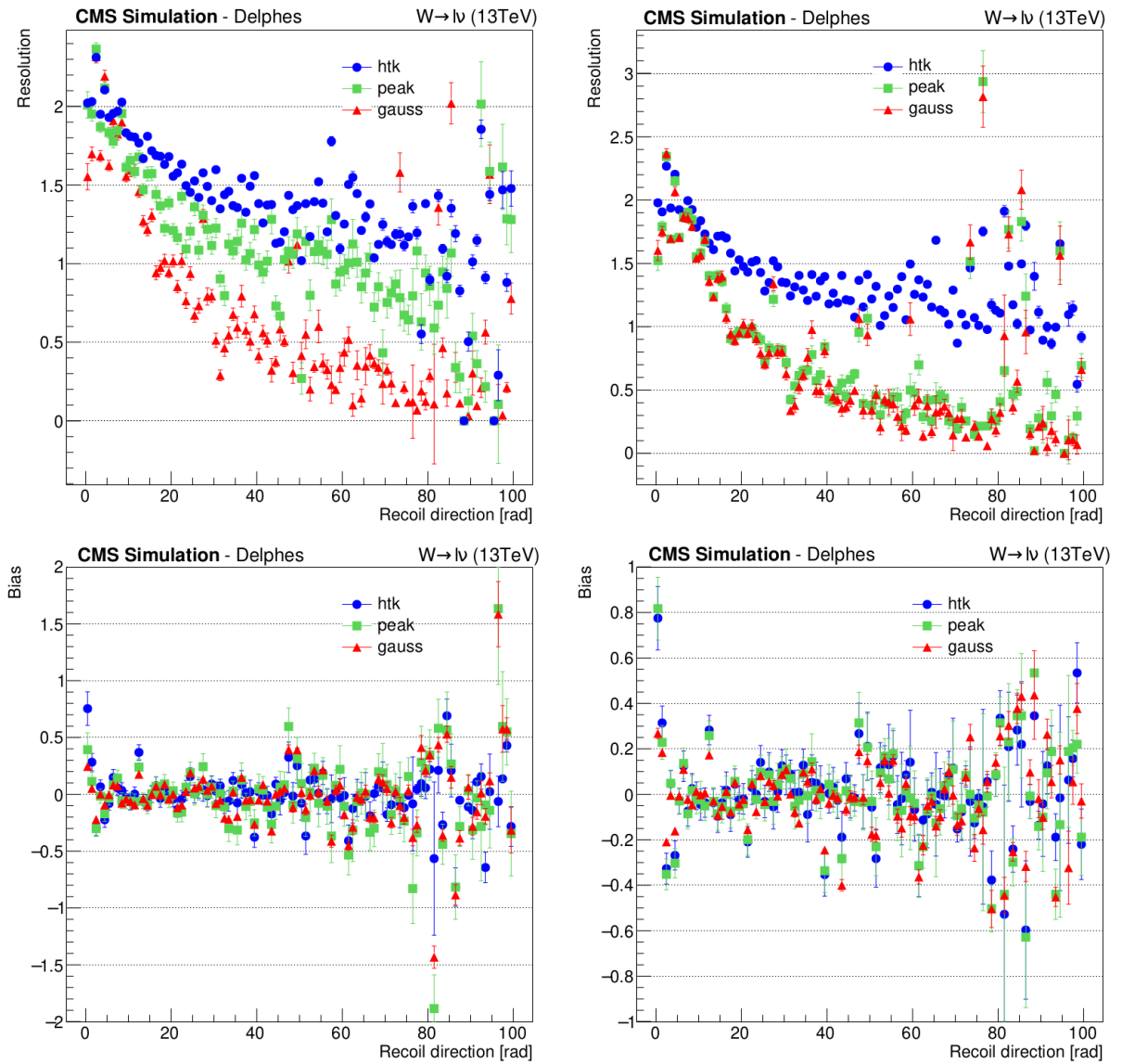


Figure 6.11 – Event-by-event resolution and bias variation as a function of the recoil direction reconstructed with different models without PU (left) and with 200 PU (right)

The HGCal parameters have been designed and optimised in previous studies [65], the 2019 geometry and parameters were then used in this study. The granularity of the cells was fixed to $\Delta\Phi = 1^\circ$ for all the HGCal layers. The energy resolution for the endcap ($1.5 < |\eta| < 3.0$) was taken from Figure 6.12 [21].

Figure 6.13 shows the effect of these parameters on the recoil scale with and without PU. The recoil scale is improved with the HGCal, even at high PU level. The possible extension of the HGCal resolution to $|\eta| = 4.0$ was also tested, and extending the acceptance gives a better reconstruction at small p_T .

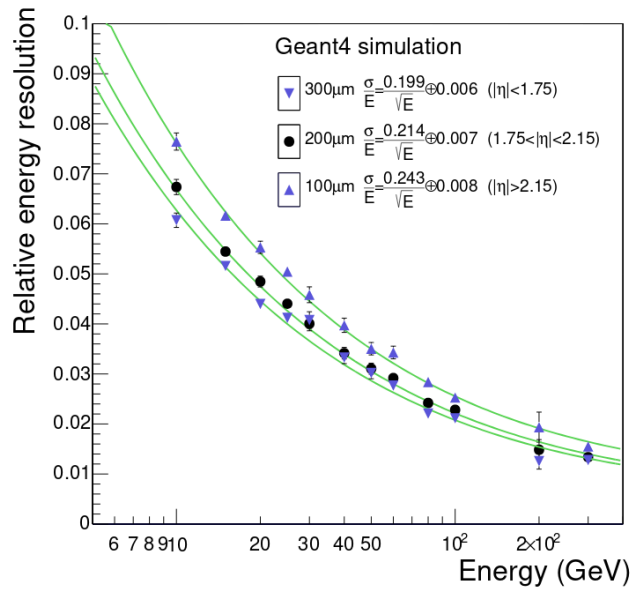


Figure 6.12 – Energy resolution as a function of energy from a standalone simulation of incident electrons on an HGCal [21]

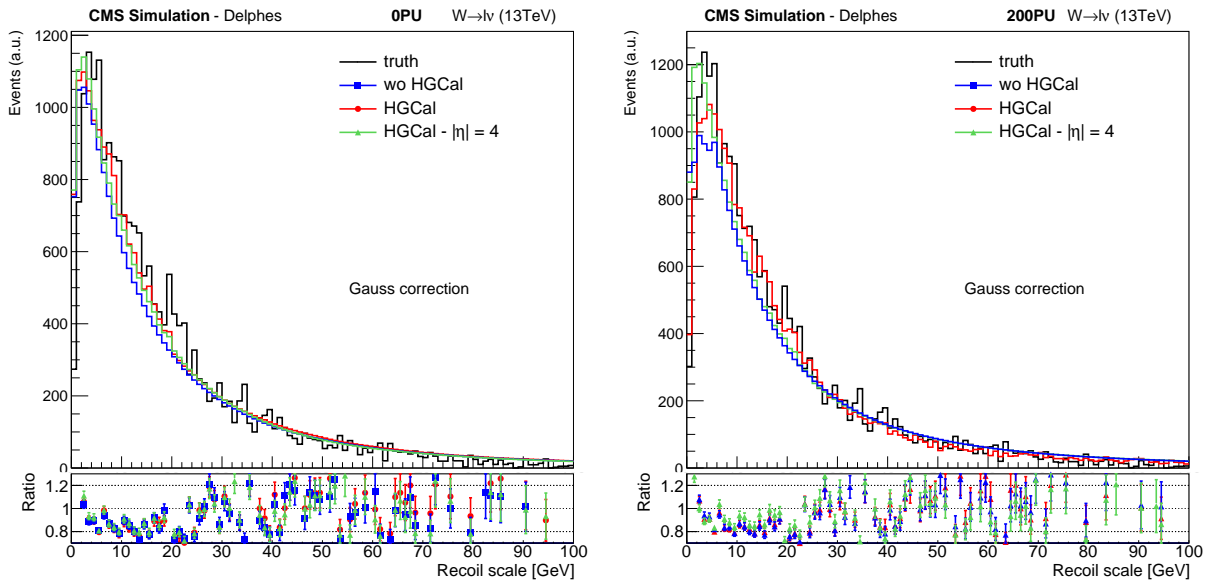


Figure 6.13 – Effect of the HGCal parameters on the recoil scale at 0 PU (left) and 200 PU (right)

To conclude on the effect of the HGCal parameters on the recoil resolution, the average bias and resolution were compared with and without PU for each estimation model. The results are shown on Figure 6.14, left for the recoil scale and right for the direction. Taking the effect of the tails into consideration leads to the smallest bias and the best resolution at 0 PU and 200 PU. This study shows that the recoil reconstruction could be improved by the HGCal, and more particularly by extending its acceptance up to $|\eta| = 4.0$.

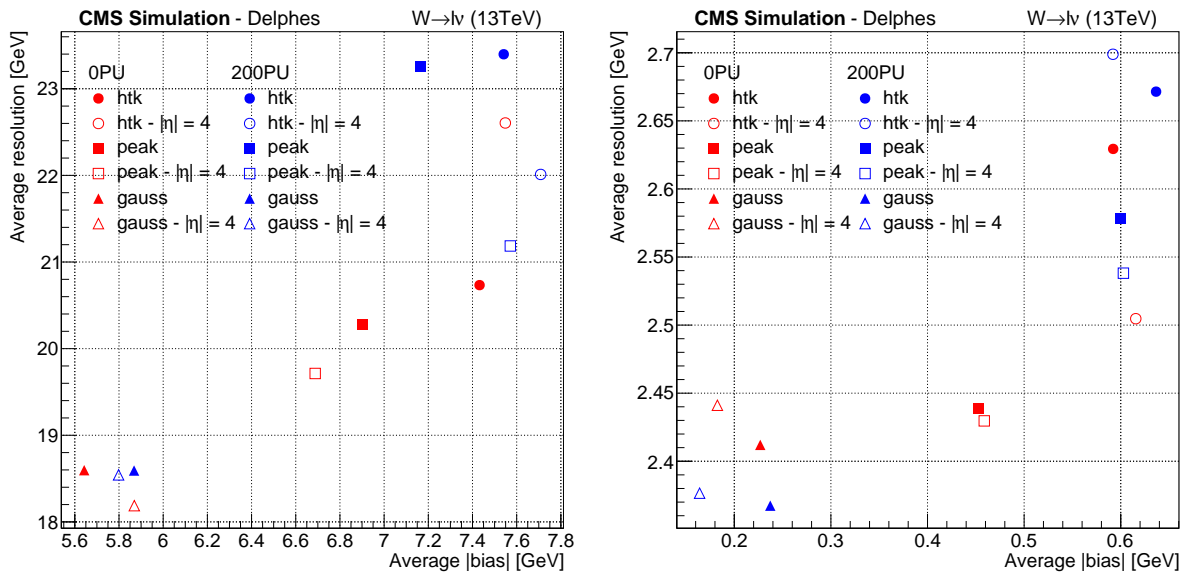


Figure 6.14 – Average bias and resolution for the estimated recoil scale (left) and direction (right) on an event-by-event basis

Chapter 7

W mass measurement at FCC-ee

"Experimental confirmation of a prediction is merely a measurement. An experiment disproving a prediction is a discovery"
Enrico Fermi

Contents

| | | |
|------------|---|------------|
| 7.1 | Kinematic reconstruction methods | 102 |
| 7.1.1 | Kinematic rescaling | 102 |
| 7.1.2 | Kinematic fit | 103 |
| 7.1.2.1 | Principle | 103 |
| 7.1.2.2 | Object parametrization | 106 |
| 7.1.2.3 | Correlation matrix | 107 |
| 7.1.2.4 | Constraints | 109 |
| 7.1.2.5 | Fit goodness | 110 |
| 7.1.2.6 | Analogy between the kinematic fit and the kinematic rescaling | 112 |
| 7.2 | Principle of the statistical uncertainty evaluation | 112 |
| 7.3 | Hadronic channel | 115 |
| 7.3.1 | Jets pairing | 115 |
| 7.3.2 | ISR and beamstrahlung treatment | 116 |
| 7.3.2.1 | Photon parametrization | 118 |
| 7.3.2.2 | ISR treatment evaluation | 118 |
| 7.3.3 | Mass and width extraction | 119 |
| 7.4 | Semi leptonic channel | 120 |
| 7.4.1 | Mass and width extraction | 121 |

7.5 Discussions 123

At the vicinity of the threshold, the dependence of the W-pair production cross-section on the W mass is large and can be used to measure M_W . At higher centre-of-mass energies, this dependence is much weaker. Nevertheless the huge statistical sample available not only at the W-pair threshold but also at the ZH cross-section maximum and $t\bar{t}$ threshold, allows a direct reconstruction of the W mass from the decay products of the two Ws with a remarkably small statistical uncertainty.

The invariant mass, m_{inv} , of each W can be calculated from the energies and momenta of its measured decay products, E_i and P_i :

$$m_{inv} = \sqrt{(E_1 + E_2)^2 - (P_1 + P_2)^2}. \quad (7.1)$$

If the energies and momenta were measured with an infinite accuracy, the width of the invariant mass distribution would be the natural width of the W boson. However leptons and hadron-jets are measured with a limited resolution: $\sim 17\%/\sqrt{E}$ for leptons and $\sim 50\%/\sqrt{E}$ for jets (Table 4.2) that smears the invariant mass distribution, which in addition is diluted due to the different pairing combinations in the fully hadronic channel.

Significant improvement on the resolution can be achieved using jet four-momenta rescaling (Section 7.1.2) to correct for the detector resolution, and constrained kinematic fit. The mathematical principle of this latter technique, applied to the current study of the W mass reconstruction, is described in Section 7.1.1.

The technique used to evaluate the mass and width statistical uncertainties is presented in Section 7.2. Finally, the reconstructed invariant mass distributions and the estimation of the statistical uncertainties on mass and width, using the different reconstruction methods at \sqrt{s} equals 162.6 GeV, 240 GeV and 365 GeV, are compared in Section 7.3 for the hadronic decay channel and Section 7.4 for the semi-leptonic final state [62, 126, 127].

7.1 Kinematic reconstruction methods

7.1.1 Kinematic rescaling

Angles are usually better measured than energies and momenta, and thus the velocity $\vec{\beta}_i = \vec{p}_i/E_i$ can be fixed to its measured value, as many systematic effects cancel in this ratio. In lepton collisions the centre-of-mass energy, \sqrt{s} , is measured with an extreme accuracy and the constraint of four-momentum conservation can be used to improve the invariant-mass resolution by rescaling the measured four-momenta:

$$\sum_{i=0}^4 E_i = \sqrt{s} \quad \text{and} \quad \sum_{i=0}^4 \vec{p}_i = \vec{0}, \quad (7.2)$$

where (E_i, \vec{p}_i) is the four-momentum of the jet i ($i = 1, 2, 3, 4$).

When the momentum is expressed as $\vec{p}_i = \vec{\beta}_i E_i$, the Equation (7.2) can be written as:

$$\begin{pmatrix} 1 & 1 & 1 & 1 \\ \beta_{x,1} & \beta_{x,2} & \beta_{x,3} & \beta_{x,4} \\ \beta_{y,1} & \beta_{y,2} & \beta_{y,3} & \beta_{y,4} \\ \beta_{z,1} & \beta_{z,2} & \beta_{z,3} & \beta_{z,4} \end{pmatrix} \begin{pmatrix} E_1 \\ E_2 \\ E_3 \\ E_4 \end{pmatrix} = \begin{pmatrix} \sqrt{s} \\ 0 \\ 0 \\ 0 \end{pmatrix}, \quad (7.3)$$

where $\beta_{x,y,z;i}$, are the projections of the velocity for the measured jet i on axes x, y, z , and E_j , the energies of the rescaled jets, solution of the system (7.3).

Each jet momentum is then rescaled by a factor α defined by the Equation (7.4):

$$\alpha = \frac{E_j}{E_i}. \quad (7.4)$$

The two W rescaled invariant masses are finally calculated from Equation (7.1) by replacing the measured four-momenta by the rescaled ones.

The major drawback of fixing the velocity to its measured value is that the system (7.3) may have unphysical solutions:

- The velocity matrix may be singular if two jets have equal directions and velocities or if there is a null linear combination of the four-jet momenta. The system is finally left undetermined and the event is discarded.
- More frequently, the solution may give at least one zero or negative energy in case of bad jet reconstruction or high energy losses by ISR. Such events are discarded by requiring all computed energies to be strictly positive.

Because the neutrino momentum is already computed by energy-momentum conservation, this method cannot be used in the semi-leptonic channel. The W mass is more effectively reconstructed by the constrained kinematic fit, usable in both hadronic and semi-leptonic channels. The analogy between the kinematic rescaling and the kinematic fit techniques is discussed in Section 7.1.2.6.

7.1.2 Kinematic fit

7.1.2.1 Principle

The constrained kinematic fit, based on the Least Squares principle, is an iterative process in which a set of measured parameters is varied within their uncertainties until a set of new values is found that minimises an estimator of consistency and satisfies a set of constraints.

For each event, the fit inputs are:

- A vector of n measured parameters ¹, $\mathbf{y} = (y_1, \dots, y_n)$, which are the measured values of the four-momentum components of the jets and/or leptons, $\mathbf{p}_M = (E_M, p_{x,M}, p_{y,M}, p_{z,M})$;
- A vector of p unmeasured parameters, $\mathbf{a} = (a_1, \dots, a_p)$, which are the unmeasured values of the four-momentum components of the neutrino in the semi-leptonic final states. For the fully-hadronic channel, $p = 0$;

¹To lighten the notation, all vectors will be written in bold from this point.

- A covariance matrix, V , containing the uncertainties over the measured parameters. V is a square matrix of dimension $n \times n$;
- $m \geq 0$ constraints, expressed as function of the measured and unmeasured parameters, i.e. $f_m(\mathbf{y}, \mathbf{a}) = 0$. The constraints are the four-momentum conservation. An additional constraint may be the equality of the two W masses.

The fit outputs are two vectors \mathbf{y}' and \mathbf{a}' , n measured and p unmeasured parameters respectively, which are the corrected values of the input parameters, that satisfy the constraints.

According to the Least Squares principle, the best estimates of the output \mathbf{y}' are those values that minimise:

$$\chi^2 = \Delta \mathbf{y}^T V^{-1} \Delta \mathbf{y}, \quad (7.5)$$

with $\Delta \mathbf{y} = \mathbf{y}' - \mathbf{y}$, under the constraints:

$$f_m(\mathbf{y}, \mathbf{a}) = 0. \quad (7.6)$$

The method of Lagrange Multipliers [128], λ , widely used in mathematical optimisation, is a strategy for finding the local maxima and minima of a function subject to equality constraints. The above two conditions may be rewritten:

$$L = \Delta \mathbf{y}^T V^{-1} \Delta \mathbf{y} + 2 \sum_{i=1}^4 \lambda_i f_i(\mathbf{y}, \mathbf{a}). \quad (7.7)$$

The factor 2 is arbitrary and this value was chosen to simplify the algebra.

Equation (7.7) is minimised when the derivatives with respect to all parameters are set to 0. If the functions f_m are linear, the solution is found in one step, otherwise the solution has to be found iteratively. At each step, the parameters are iteratively refined by successive approximations:

$$\mathbf{y}^{N+1} = \mathbf{y}^N + \Delta \mathbf{y} \quad \text{and} \quad \mathbf{a}^{N+1} = \mathbf{a}^N + \Delta \mathbf{a}, \quad (7.8)$$

where N is the iteration number and $(\Delta \mathbf{y}, \Delta \mathbf{a})$ the couple of corrections. At each step, each constraint function, k , may be approximated locally by its Taylor series expansion about $(\mathbf{y}^N, \mathbf{a}^N)$. The expansion to first order is linear:

$$f_k(\mathbf{y}^{N+1}, \mathbf{a}^{N+1}) \sim f_k(\mathbf{y}^N, \mathbf{a}^N) + \sum_{i=1}^n \frac{\partial f_k}{\partial y_i} (\mathbf{y}^{N+1} - \mathbf{y}^N) + \sum_{j=1}^p \frac{\partial f_k}{\partial a_j} (\mathbf{a}^{N+1} - \mathbf{a}^N) \sim 0, \quad (7.9)$$

or,

$$f_k(\mathbf{y}^{N+1}, \mathbf{a}^{N+1}) \sim f_k(\mathbf{y}^N, \mathbf{a}^N) + \sum_{i=1}^n \frac{\partial f_k}{\partial y_i} (\Delta \mathbf{y}^{N+1} - \Delta \mathbf{y}^N) + \sum_{j=1}^p \frac{\partial f_k}{\partial a_j} (\Delta \mathbf{a}^{N+1} - \Delta \mathbf{a}^N) \sim 0, \quad (7.10)$$

where,

$$\Delta \mathbf{y}^N = \mathbf{y}^N - \mathbf{y} \quad \text{and} \quad \Delta \mathbf{a}^N = \mathbf{a}^N - \mathbf{a}. \quad (7.11)$$

The derivatives are computed at the $(\mathbf{y}^N, \mathbf{a}^N)$ iteration and using the matrix notation, the Equation (7.9) becomes:

$$\mathbf{f}^N + A(\Delta\mathbf{a}^{N+1} - \Delta\mathbf{a}^N) + B(\Delta\mathbf{y}^{N+1} - \Delta\mathbf{y}^N) \sim 0, \quad (7.12)$$

or

$$A\Delta\mathbf{a}^{N+1} + B\Delta\mathbf{y}^{N+1} - \mathbf{c} = 0 \quad \text{with} \quad \mathbf{c} = A\Delta\mathbf{a}^N + B\Delta\mathbf{y}^N - \mathbf{f}^N. \quad (7.13)$$

With \mathbf{c} a constant vector depending on quantities computed in iteration N . The matrices A and B , are the derivatives of the constraints according to the parameters \mathbf{a} and \mathbf{y} , defined as:

$$A = \frac{\partial \mathbf{f}}{\partial \mathbf{a}} \quad \text{and} \quad B = \frac{\partial \mathbf{f}}{\partial \mathbf{y}}. \quad (7.14)$$

With the matrix notation, the Equation (7.7) can be simplified:

$$L = \Delta\mathbf{y}^T V^{-1} \Delta\mathbf{y} + 2\lambda^T (A\Delta\mathbf{a} + B\Delta\mathbf{y} - \mathbf{c}), \quad (7.15)$$

which is minimal if:

$$\begin{aligned} \frac{\partial L}{\partial \mathbf{y}} &= V^{-1} \Delta\mathbf{y} + B^T \lambda = 0, \\ \frac{\partial L}{\partial \mathbf{a}} &= A^T \lambda = 0, \\ \frac{\partial L}{\partial \lambda} &= B\Delta\mathbf{y} + A\Delta\mathbf{a} - \mathbf{c} = 0. \end{aligned} \quad (7.16)$$

Hence, the extremum of the Equation (7.7) can be found resolving the matrices system:

$$\begin{pmatrix} V^{-1} & 0 & B^T \\ 0 & 0 & A^T \\ B & A & 0 \end{pmatrix} \begin{pmatrix} \Delta\mathbf{y} \\ \Delta\mathbf{a} \\ \lambda \end{pmatrix} = \begin{pmatrix} 0 \\ 0 \\ \mathbf{c} \end{pmatrix}, \quad (7.17)$$

The full matrices expression and the resolution of the system (7.17) can be found in [61]. The solution $(\Delta\mathbf{y}, \Delta\mathbf{a}, \lambda)$ is computed for each iteration and the linearisation is repeated until user-defined convergence criteria are fulfilled. The convergence criteria require that, first the χ^2 has reached a local minimum and varies by a given small value ϵ_χ between two consecutive iterations, and second the constraints are fulfilled and the sum of all constraints does not exceed a value ϵ_F . The complete convergence criteria are thus:

$$\begin{aligned} |\chi^2(\mathbf{y}^{N+1}) - \chi^2(\mathbf{y}^N)| &< \epsilon_\chi, \\ \sum_{k=1}^m |f_k(\mathbf{a}^{N+1}, \mathbf{y}^{N+1})| &< \epsilon_f. \end{aligned} \quad (7.18)$$

In this kinematic fit implementation, the convergence criteria have been set to $\epsilon_\chi = 5.10^{-2}$ and $\epsilon_F = 1.10^{-2}$. For all fitted event, an upper limit to the number of iterations was set to 10000 to stop the iterations if the convergence criteria are never fulfilled. These values have been optimised to ensure that the fit convergence is found whilst not spending too many iterations if the event never matched the hypothesis. The divergent events are rejected.

The resolution of the problem is based on the computation of the derivatives of the constraints defined in Equation (7.14). Usually, the constraints directly depend on the objects four-vector, $\mathbf{P} =$

(E, \mathbf{p}) , which are themselves parametrized as function of the measured/unmeasured parameters. Then,

$$\partial \mathbf{f} / \partial \mathbf{y} = \partial \mathbf{f} / \partial \mathbf{P} \cdot \partial \mathbf{P} / \partial \mathbf{y} \quad \text{and} \quad \partial \mathbf{f} / \partial \mathbf{a} = \partial \mathbf{f} / \partial \mathbf{P} \cdot \partial \mathbf{P} / \partial \mathbf{a}. \quad (7.19)$$

The different objects used in the present kinematic fit of the W mass, the parametrization of the measured/unmeasured objects, the covariance matrix and the constraints for both hadronic and semi-leptonic channels, are detailed in the following.

7.1.2.2 Object parametrization

The objects used in this fit are only jets in the purely hadronic channel, and also lepton and missing energy in the semi-leptonic channel. Their four-momenta are expressed as a function of parameters that will be tuned to satisfy the constraints. Several parametrizations are possible for the same object, depending on the fitting variables. The jet, lepton and missing momentum parametrizations used in the present study are presented in the following. In addition, a dedicated object for treating ISR and beamstrahlung photons, mainly escaping along the beam pipe, is discussed in Section 7.3.2.

Jets parametrization The jet four-vectors are parametrized with four measured parameters: the rescaling coefficient, α , already defined in Equation (7.4), the polar and azimuthal angles of the jet, θ and ϕ , and the jet velocity, $\beta = p/E$ as defined in Section 7.1.1. However, as the velocity, which can also be written as $\beta = v/c$, cannot exceed 1, it is more convenient to work in terms of rapidity x . When comparing the Lorentz transformations in terms of velocity and rapidity, the following relation is obtained between them:

$$\beta\gamma = \sinh(x), \quad (7.20)$$

where γ is the Lorentz factor, and $x \in [0, \infty]$. x can be written:

$$x = \log(\beta\gamma) = \log\left(\frac{p}{m}\right), \quad (7.21)$$

and the velocity expression becomes:

$$v(x) = \frac{p}{E} = \frac{m_0 p}{m_0 E_0} = \frac{m_0}{E_0} e^x, \quad (7.22)$$

where E_0 and m_0 are respectively the measured jet energy and mass.

Finally, the jet four-vectors parametrization in the kinematic fit is:

$$\begin{aligned} p_x &= \alpha m_0 e^x \sin \theta \cos \phi, \\ p_y &= \alpha m_0 e^x \sin \theta \sin \phi, \\ p_z &= \alpha m_0 e^x \cos \theta, \\ E &= \alpha m_0 \sqrt{e^{2x} + 1}. \end{aligned} \quad (7.23)$$

Lepton parametrization The lepton four-vector is parametrized with a single measured quantity. As the lepton direction is perfectly reconstructed, only the energy is varied within its uncertainty. The lepton four-vector parametrization is similar to the jet one. With E the fitted parameter, the lepton momentum is:

$$p = \sqrt{E^2 - m_0^2}, \quad (7.24)$$

with m_0 the measured lepton mass. From this definition, with θ_0 and ϕ_0 the measured lepton angles, the lepton four-momentum parametrization is given by:

$$\begin{aligned} p_x &= p \sin \theta_0 \cos \phi_0, \\ p_y &= p \sin \theta_0 \sin \phi_0, \\ p_z &= p \cos \theta_0, \\ E &= E. \end{aligned} \tag{7.25}$$

In the following study of the semi-leptonic channel only the muon decay has been studied but for the electron decay the same parametrization might be used.

Missing energy parametrization The neutrino is not detected and its momentum is associated with the missing momentum, computed by energy-momentum conservation. Therefore, the neutrino is introduced into the kinematic fit as an unmeasured object and its four-momentum parametrization depends on three unmeasured parameters, the missing energy and the missing direction, the angles θ and ϕ , and is defined as:

$$\begin{aligned} p_x &= E \sin \theta \cos \phi, \\ p_y &= E \sin \theta \sin \phi, \\ p_z &= E \cos \theta, \\ E &= E. \end{aligned} \tag{7.26}$$

7.1.2.3 Correlation matrix

The correlation matrix V , takes part in the χ^2 expression of the fit. It contains all information about uncertainties of the measured parameters, on-diagonal terms, and their correlations, off-diagonal terms.

Diagonal terms The diagonal contains the resolutions of the measured parameters, $V_i = \sigma_i^2$. As presented in Section 7.1.2.2, the fitted parameters used in the hadronic and semi-leptonic channels are the α , θ , ϕ and $x = \log(\beta\gamma)$ of the jets and the lepton energy, E , respectively. Their uncertainties are determined fitting the distributions of the difference between the reconstructed and MC objects, built directly from the generated MC particles without extrapolation into the detector. Thus:

- σ_α is the width of the $(E_{recojet} - E_{parton})/E_{parton}$ distribution;
- σ_θ is the width of the $\theta_{genjet} - \theta_{recojet}$ distribution;
- σ_ϕ is the width of the $\phi_{genjet} - \phi_{recojet}$ distribution;
- σ_x is the width of the $\log(p/E)_{genjet} - \log(p/E)_{recojet}$ distribution;
- σ_E is the width of the $E_{genlepton} - E_{recolepton}$,

where the *parton* is the quark that has generated the jet, the *recojet(genjet)* corresponds to the jet clustered with the reconstructed(generated) particles and the *recolepton(genlepton)* is the reconstructed(generated) lepton.

As the measured parameters are independent the distributions are assumed to be normal. In reality they are rarely perfectly Gaussian and have non-Gaussian, possibly asymmetric, tails on each side of the peak. To estimate the parameter uncertainties, the distributions were fitted with a double-sided Crystal-Ball [129]. The Gaussian core is parametrized by its mean μ , and its width σ , while each tail i is defined by a power-law of degree n_i and with a_i the value setting the transition between the Gaussian and the tail function. With t the fitted parameter, the expression of the function used to fit the parameter distribution is:

$$\begin{aligned}
 & e^{-\left(\frac{t-\mu}{2\sigma}\right)^2} && \text{if } -a_1 \leq \frac{t-\mu}{\sigma} \leq a_2, \\
 & e^{-a_1^2/2} \left[\frac{a_1}{n_1} \left(\frac{n_1}{a_1} - a_1 - \frac{t-\mu}{\sigma} \right) \right]^{-n_1} && \text{if } \frac{t-\mu}{\sigma} < -a_1, \\
 & e^{-a_2^2/2} \left[\frac{a_2}{n_2} \left(\frac{n_2}{a_2} - a_2 + \frac{t-\mu}{\sigma} \right) \right]^{-n_2} && \text{if } \frac{t-\mu}{\sigma} > a_2.
 \end{aligned} \tag{7.27}$$

The tail parameters, a and n , are very strongly correlated, so n is usually fixed whereas a is left free. Examples of the jet parameters fitted distributions obtained in the hadronic channel at $\sqrt{s} = 162.6$ GeV are shown in Figure 7.1.

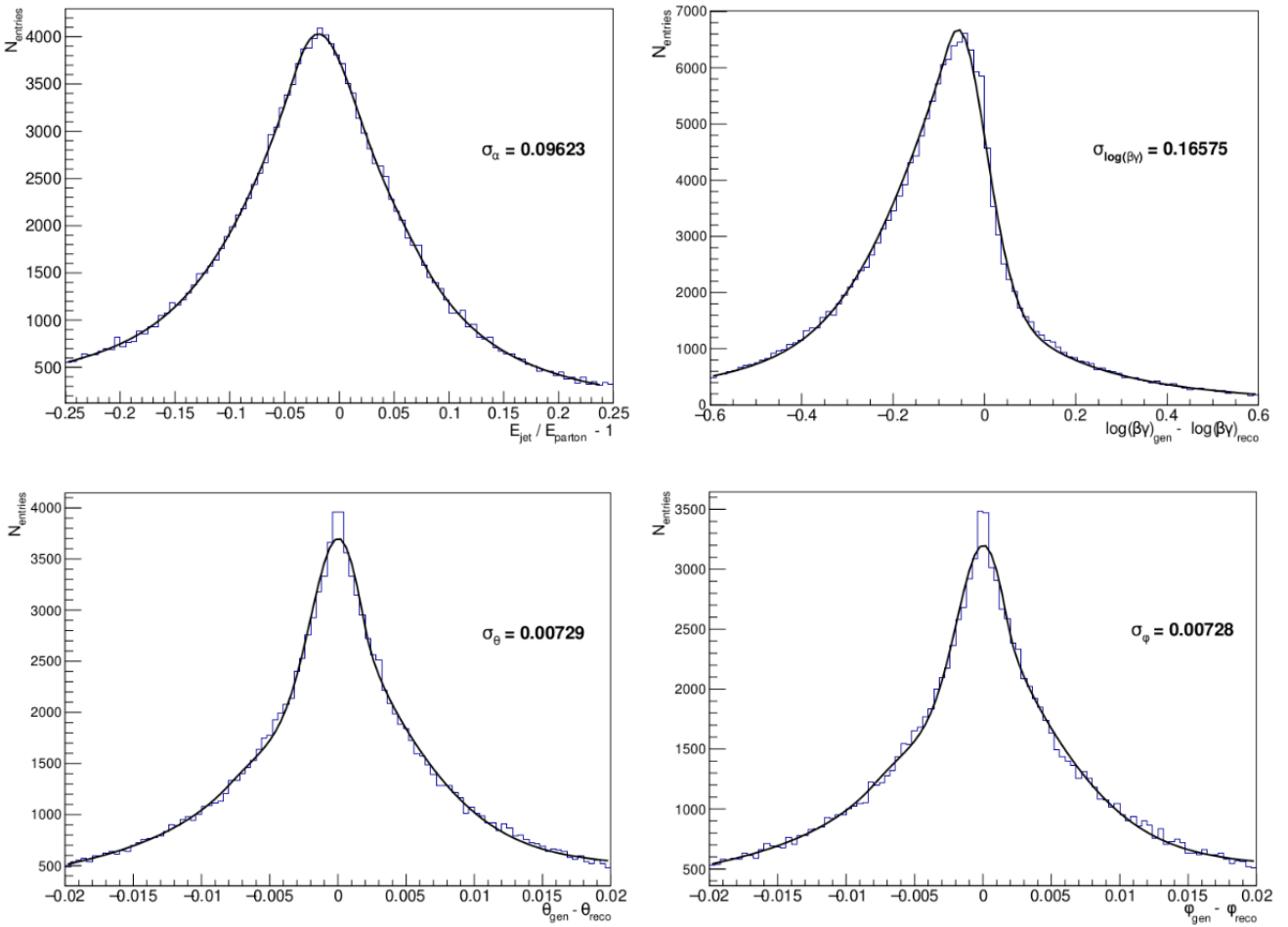


Figure 7.1 – Double-sided Crystal-Ball fit of the parameters distributions to determine the diagonal terms of the covariance matrix of the kinematic fit in the hadronic channel at $\sqrt{s} = 162.6$ GeV

Off-diagonal terms The off-diagonal terms correspond to the correlations between the parameters, $V_{ij} = \rho_{ij}\sigma_i\sigma_j$, where $\rho_{ij} = \rho_{ji}$ is the correlation coefficient ($i \neq j$). In this study, the parameters are assumed independent and the correlation matrix is reduced to a covariance matrix ; therefore the off-diagonal terms were set to zero. To confirm this conjecture, the correlations between parameters have been drawn and the distributions in the hadronic channel for $\sqrt{s}= 162.6$ GeV, are shown in Appendix B.3.

7.1.2.4 Constraints

A constraint is a function depending on the physical quantities of the fitted objects. It tends to zero in case of fit convergence, i.e. if it is fulfilled.

In e^+e^- collisions, four constraints based on the energy-momentum conservation law are typically used. This conservation principle has already been discussed in Section 7.1.1. The difference between the number of constraints and the number of unmeasured parameters, $m - p$, is the number of degrees of freedom, ndf , used to label the fit.

Imposing only the energy-momentum conservation corresponds to a four-constraints fit (4C) in the case of the fully hadronic decay channel, and to a one-constraint fit (1C) in the semi-leptonic channel because the neutrino momentum computed by energy-momentum conservation removes three degrees of freedom from the fit. In this case, two fitted W masses are reconstructed per event, one per generated W boson. For a better measurement of the W mass resolution, an additional constraint can be included, forcing the two reconstructed W masses to be equal. This additional mass equality constraint leads to a five-constraints fit (5C) in the hadronic channel and to a two-constraints fit (2C) in the semi-leptonic channel. Only one W mass per event is then reconstructed by the fit.

Taking into account all of these constraints, the matrix of the constraints is implemented in the kinematic fit as:

$$\mathbf{f}(\mathbf{y}, \mathbf{a}) = \begin{pmatrix} \sum p_x - p_{x,const} \\ \sum p_y - p_{y,const} \\ \sum p_z - p_{z,const} \\ \sum E - E_{const} \\ M_1 - M_2 \end{pmatrix} = \begin{pmatrix} \sum p_x \\ \sum p_y \\ \sum p_z \\ \sum E - \sqrt{s} \\ \sqrt{E_1^2 - \mathbf{p}_1^2} - \sqrt{E_2^2 - \mathbf{p}_2^2} \end{pmatrix} = 0. \quad (7.28)$$

Moreover, there might be additional contributions from 'soft' constraints, e.g. requirement for invariant masses equality within the W boson width. These kinds of constraints have not been handled in the current implementation and the width of the W boson has been neglected in the whole study.

Once the kinematic fit is performed with the previously defined components, the accuracy of the fit results has to be tested. The kinematic fit goodness is based on the distribution of two quality parameters, the pull distribution, which attests the quality of the covariance matrix, and the χ^2 probability distribution certifying the quality of the fit itself.

7.1.2.5 Fit goodness

Probability The entire kinematic fit procedure is developed to minimise the χ^2 . Hence, the fit quality is directly evaluated with a statistical significance estimator called p-value, $P(\chi^2)$, which gives the probability that, in a fitted event, the χ^2 fitted value be greater than or equal to the ideal χ^2 . This probability can be expressed as:

$$P(\chi^2) = \int_{\chi^2}^{\infty} f(x) dx. \quad (7.29)$$

The function $f(\chi^2)$ is the χ^2 probability density function for a given number of degrees of freedom, ndf , which can be written [130]:

$$f(\chi^2) = \frac{1}{\Gamma(\lambda)2^\lambda} (\chi^2)^{\lambda-1} e^{-\frac{1}{2}\chi^2} \quad \text{with} \quad \lambda = \frac{ndf}{2}, \quad (7.30)$$

where Γ is the Gamma function.

In the ideal case, the χ^2 probability density is uniformly distributed from zero to one. In reality, there is often a peak at low probability because some events are forced to satisfy the kinematic constraints they are not compatible with. Figure 7.2 shows for instance the p-value distribution obtained with the 4C kinematic fit of hadronic events at $\sqrt{s} = 162.6$ GeV.

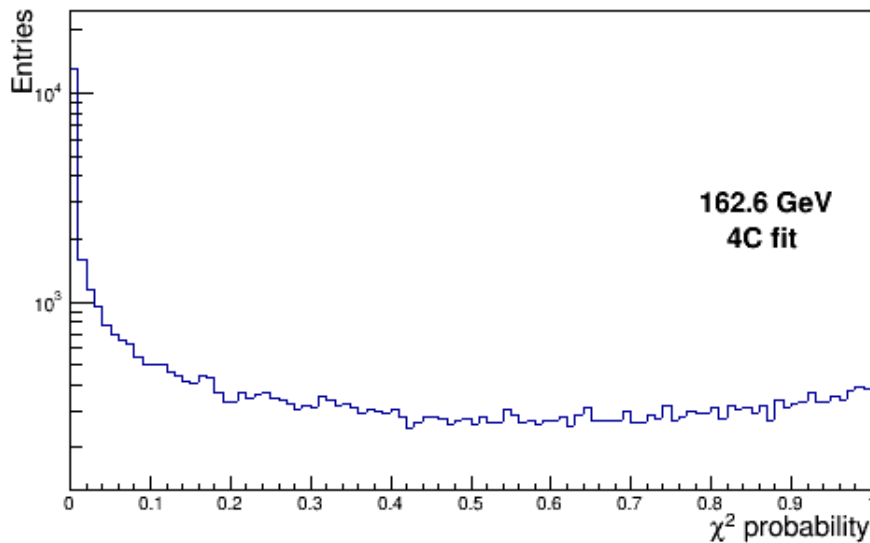


Figure 7.2 – Distribution of the χ^2 probability of the 4C kinematic fit at $\sqrt{s} = 162.6$ GeV

The distribution is rather flat between 0.2 and 1 and has a peak around zero. These low probability events are the results of bad reconstruction of the jets (overlapping, bad clustering), bad jets association in the W mass reconstruction, lost particles due to the detector resolution and/or emission of ISR. These events will be in the tails of the W mass distributions and will impact the mass resolution. They are also responsible for the non-Gaussian tails of the measured quantities distributions shown on Figure 7.1 and can introduce small correlations between the fitted parameters.

To reduce the effect of these events, an additional treatment, discussed in Section 7.3.2, has been implemented in the hadronic channel to treat the case of the events with ISR. Moreover, in both channels, events with a probability below 3% have been rejected. The comparison of the W mass distributions with and without this cut are shown in Appendix B.4.

Pull The second test on the kinematic fit accuracy concerns the covariance matrix quality. The covariance matrix consistency is provided by the pull distributions which give information about the systematic uncertainty on measured parameters and check if the input resolutions are reasonable.

The pull of a variable is its residual, difference between its measured and fitted values, normalised by the standard deviation of this residual. With $y_{meas,i}$ and $y_{fit,i}$ the measured and fitted values of a parameter i and $\sigma_{meas,i}$ and $\sigma_{fit,i}$ the corresponding uncertainties, the pull of parameter i is defined as:

$$\text{pull}_i = \frac{y_{i,meas} - y_{i,fit}}{\sqrt{\sigma_{i,meas}^2 - \sigma_{i,fit}^2}}. \quad (7.31)$$

If the covariance matrix uncertainty is correctly estimated, the pull has a Gaussian shape centred on zero and a unit standard deviation. A systematic error on one of the parameter introduces a shift or an asymmetry. In case of underestimation (overestimation) of the uncertainty of a given parameter, the standard deviation of the corresponding pull will be larger (smaller) than one. For example, the pull distributions of all 4C-fitted parameters at $\sqrt{s} = 162.6$ GeV in the hadronic decay channel are shown on Figure 7.3.

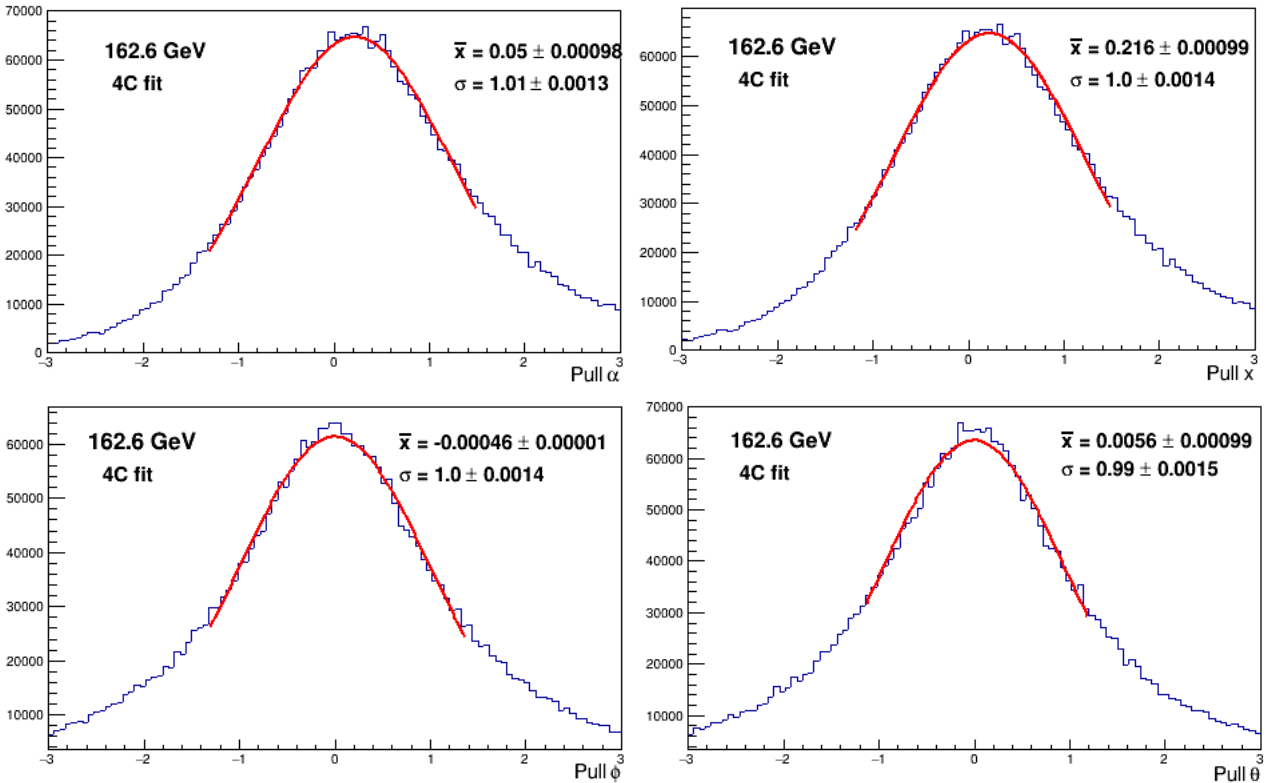


Figure 7.3 – Pull distributions of the parameters of the 4C kinematic fit at $\sqrt{s} = 162.6$ GeV in the hadronic channel, fitted with a Gaussian distribution

A good agreement with the standardised Gaussian distributions is observed. The small bias of the mean of the velocity can be attributed to a systematic misestimation of the $\log(\beta\gamma)$ uncertainty. It can be explained by the asymmetric distribution of this parameter shown on Figure 7.1. A tiny bias is also visible on the rescaling coefficient pull distribution. The angular pull distributions are unaffected by systematic errors since the direction of the fit objects inside the detector is accurately measured.

In the semi-leptonic channel, the pull of the lepton energy has shown a perfect agreement with the Gaussian fit as well, resulting from a high precision measurement of this parameter.

The non-Gaussian tails observed are mainly events with a low fit probability. These tails are consequently reduced when the probability cut ($P > 0.03$) is introduced, as shown in Appendix B.4. Regarding the width variation of the pull distributions with the centre-of-mass energy, the broadening is higher at low energy. This could be due to the decreasing number of wrong particles assignments between jets from different W: the particles coming from different W decays are moved away when the energy increases, reducing the inter-W particle mix.

7.1.2.6 Analogy between the kinematic fit and the kinematic rescaling

In the hadronic channel, the kinematic rescaling, as described in Section 7.1.1, is a particular case of the 4C kinematic fit. Indeed, the kinematic rescaling is equivalent to a kinematic fit with the rescaling coefficient, α , as a single parameter, and with the energy-momentum conservation constraints. Then the Equation (7.7) is linear and the result of the kinematic fit is found in one step. Although the 4C kinematic fit is expected to give slightly better results than the kinematic rescaling, the agreement between the two approaches validates the implementation of the method of Lagrange multipliers for the kinematic fit.

Figure 7.4 shows the distributions of the smaller and the larger of the two W masses, at $\sqrt{s}=162.6$ GeV with the kinematic rescaling and the 4C kinematic fit. The kinematic fit algorithm can then be safely used with larger sets of input parameters and additional constraint(s).

The full flowchart and the main steps of this algorithm are available in Appendix B.2. The W mass has been reconstructed at 162.6 GeV, 240 GeV and 365 GeV, using the different techniques defined above and for both the hadronic and semi-leptonic decay channels. The comparison of the reconstructed distributions is presented in Sections 7.3 and 7.4.

7.2 Principle of the statistical uncertainty evaluation

The expected statistical uncertainty on the W mass, σ_{M_W} , was estimated with a binned maximum likelihood fit of the reconstructed W mass distributions, using templates generated for different nominal mass values as described in Section 4.2.1. A similar procedure was followed to evaluate the width statistical uncertainty. Unlike what is usually done, the mass and width statistical uncertainties were independently estimated considering that the mass and width are uncorrelated. For a simultaneous determination, a 2D likelihood fit would be needed, which can be reduced to two 1D fits using this approximation.

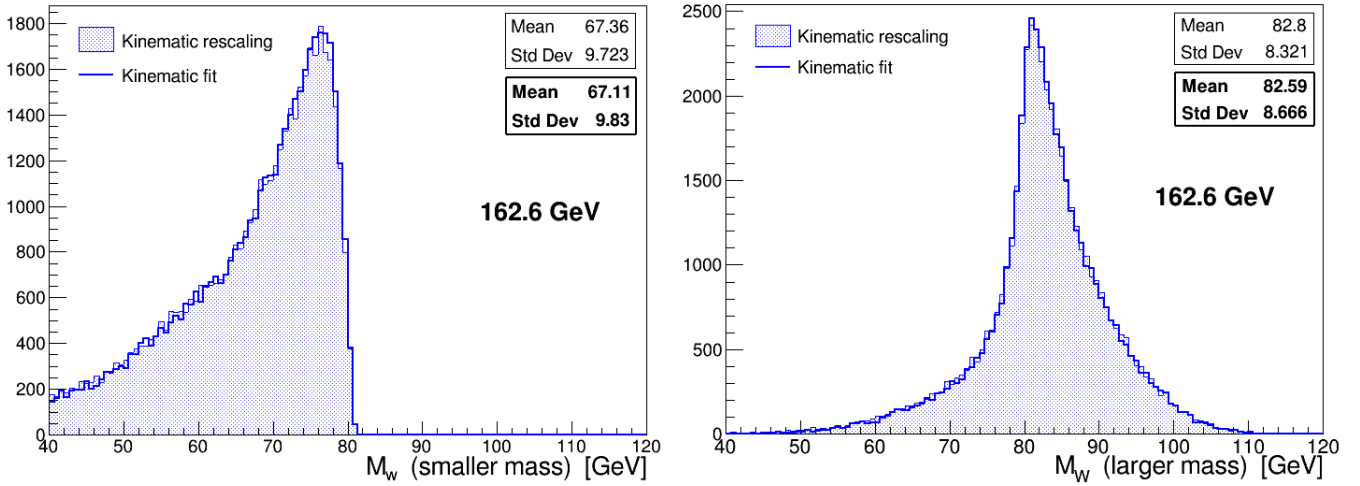


Figure 7.4 – Analogy between the kinematic rescaling and kinematic fit (4C) methods for the W masses reconstruction

The principle of the method used for the W mass statistical uncertainty evaluation is detailed in the following.

First, a statistical uncertainty per reconstructed mass is evaluated with:

$$\sigma_M = \sqrt{\frac{FOM}{N}}, \quad (7.32)$$

where N is the number of events and the FOM is the Figure Of Merit of the templates. The distributions of the smaller and larger reconstructed W masses in the hadronic channel obtained with the templates $M_W \pm 1 \text{ GeV}/c^2$, at $\sqrt{s} = 162.6 \text{ GeV}$ in the hadronic channel are represented on Figure 7.5.

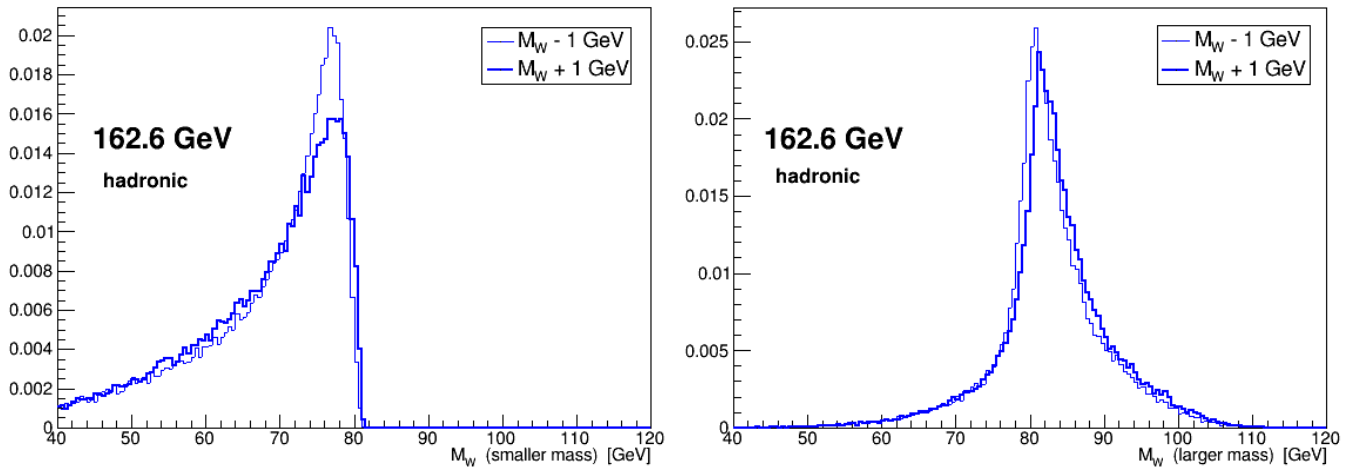


Figure 7.5 – W mass reconstructions for extreme templates ($M_W = 80.385 \pm 1 \text{ GeV}/c^2$) For both smaller and larger masses, the W mass distributions correspond to the reconstruction of templates generated with $M_W = 79.385 \text{ GeV}/c^2$ and $M_W = 81.385 \text{ GeV}/c^2$ as nominal values.

Defining:

- N_{i1} the bin content of the i-th bin for the distribution $M_W + 1 \text{ GeV}/c^2$;
- N_{i2} the bin content of the i-th bin for the distribution $M_W - 1 \text{ GeV}/c^2$;
- $sN_i = N_{i1} + N_{i2}$, the sum at the i-th bin ;
- $dN_i = N_{i1} - N_{i2}$, the difference at the i-th bin,

the Figure Of Merit (FOM) expression is:

$$\text{FOM} = DM \frac{\sum_j sN_j}{\sum_j (dN_j^2 / sN_j)}, \quad (7.33)$$

where j runs over the number of bins and DM is the template parameter variation ($DM = 2$ for the W mass templates). The full demonstration of this FOM expression is available in Appendix B.1.

The expected uncertainty is obtained by combination of the statistical uncertainties, computed for the smaller and larger masses. Two reconstructed masses in the same event are correlated and calling V_m the correlation matrix, the combined statistical uncertainty can be defined as [131]:

$$\sigma_M^2 = \sum_{ij} w_i w_j (V_m)_{ij} \quad \text{with} \quad w_i = \left(\sum_{j,k} (V_m^{-1})_{jk} \right)^{-1} \sum_j (V_m^{-1})_{ij}. \quad (7.34)$$

From this definition, with σ_1 and σ_2 the uncertainties of the smaller and the larger masses and ρ their correlation coefficient, their combined uncertainty, σ_M^2 , can be written:

$$\sigma_M^2 = (1 - \rho^2) \frac{\sigma_1^2 \sigma_2^2}{\sigma_1^2 + \sigma_2^2 - 2\rho\sigma_1\sigma_2}. \quad (7.35)$$

In the case of W mass equality constraint, only one mass per event is reconstructed. Therefore the expected statistical uncertainty is directly given by the Equation (7.32).

To give an estimation of the expected statistical uncertainty on W mass at FCC-ee, the combined uncertainty have to be converted to the full FCC-ee luminosity. The number of W-pairs, computed with $L_{int} \times \sigma_{WW}$ where L_{int} and σ_{WW} are respectively the integrated luminosity and the W-pairs production cross-section, expected at FCC-ee for the different centre-of-mass energies are gathered in Table 7.1.

Table 7.1 – Integrated luminosity L_{int} , W-pair production cross-section σ_{WW} and number of W pairs ($N_{WW} = L_{int} \times \sigma_{WW}$) expected at FCC-ee for different centre-of-mass energies

| \sqrt{s} GeV | 162.6 | 240 | 365 |
|-------------------------------|-------|-------|-------|
| L_{int} [ab^{-1}] | 12 | 5 | 1.7 |
| σ_{WW} [pb] | 5.11 | 16.73 | 11.46 |
| Number of W pairs [Millions] | 61.3 | 83.7 | 19.5 |
| $R_{Full Lumi}$ hadronic | 0.052 | 0.036 | 0.075 |
| $R_{Full Lumi}$ semi-leptonic | 0.035 | 0.025 | 0.05 |

The full luminosity uncertainties are then computed:

$$\sigma_{Full\ Lumi} = \sigma_M \times R_{Full\ Lumi}, \quad (7.36)$$

where σ_M is the combined statistical uncertainty and:

$$R_{Full\ Lumi} = \sqrt{\frac{N_{simulated}}{N_{expected}}}, \quad N_{expected} = N_{WW} \times Br. \quad (7.37)$$

$N_{simulated}$ is the number of MC simulated events and $N_{expected}$ is the expected number of hadronic or semi-leptonic events at a given luminosity. The corresponding branching ratio, Br , is selected among the channel branching ratios defined in Section 2.2.2. In this study, only the muon decays have been considered in the semi-leptonic channel, hence the corresponding branching ratio is reduced to $Br_{SL,\mu} = 0.146$. The multiplicative ratios, defined in Equation (7.37), to convert the computed statistical uncertainty into full luminosity uncertainty for different centre-of-mass energies are given in the last two lines of the Table 7.1.

In this study 50000 events have been simulated in each decay channel. However, several events are removed by the different steps of the reconstruction (light jets, divergent fitted events, cuts) and only a part is effectively used in the W mass reconstruction. The efficiency coefficient:

$$\epsilon = \frac{N_{real}}{N_{simulated}}, \quad (7.38)$$

where N_{real} is the real number of events used to reconstruct the invariant mass, is then introduced.

Finally the W mass statistical uncertainty expected with the full luminosity of FCC-ee is computed with:

$$\sigma_{Full\ Lumi} = \sigma_M \times R_{Full\ Lumi} \times \sqrt{\epsilon}. \quad (7.39)$$

The same technique was used for all the W mass reconstruction techniques. The evaluated statistical uncertainties on the W mass and width for the full FCC-ee luminosity at the different centre-of-mass energies are presented in Sections 7.3 and 7.4 for the hadronic and semi-leptonic decays respectively.

7.3 Hadronic channel

Each boson decays into two jets and before proceeding to the W mass reconstruction, the four jets have to be paired together. The pairing method is explained in Section 7.3.1. Section 7.3.2, presents an additional treatment in the kinematic fit to improve the resolution loss introduced by the emission of ISR or beamstrahlung photons. The last part gives the reconstruction and the statistical uncertainties obtained in this channel.

7.3.1 Jets pairing

The four jets are paired into di-jets, by associating those coming from the decay of the same W boson. Only three different jet combinations of the four jets are possible. Several approaches with variable pairing efficiency exist to find the adequate pairing [5, 132]. As the W mass is known with

high accuracy, the jets pairing was done by minimising the difference between the reconstructed invariant masses and the reference W mass, with Equation (7.40).

$$\chi^2 = (m_1 - m_W)^2 + (m_2 - m_W)^2 \quad (7.40)$$

m_1 and m_2 are the two reconstructed masses for the tested pair and m_W the reference mass of the W boson, set to 80.385 GeV/c²². The efficiencies of this pairing method for the different centre-of-mass energies are summarised in Table 7.2. At threshold, this method has an efficiency similar to that found at LEP (around 70%) using other pairing techniques [132]. Above threshold, the jets are boosted and jets from different Ws are better separated. Therefore, the pairing is more efficient and the selection efficiency increases with the energy. The wrongly paired events for the different energies is also visible on Figure 7.6, showing the distribution of the masses computed with the good and the wrong paired jets. The wrongly paired events are distributed in the same range of the correct jets combination.

Table 7.2 – Efficiency of the χ^2 pairing for the various centre-of-mass energies

| \sqrt{s} GeV | Efficiency |
|----------------|------------|
| 162.6 | 76.9 % |
| 240 | 81.5 % |
| 365 | 88.6 % |

In the kinematic fit reconstruction, a pairing technique is to repeat the fit for all different jet permutations and keep the pairing yielding the highest fit probability [133]. This method requires a lot of CPU time and, in this analysis, gives a similar pairing efficiency as using the χ^2 minimisation. Moreover, the wrongly paired events are in majority at low values of the kinematic fit probability, as shown by Figure 7.7, which compares the probability distributions for good and bad pairings at 162.6 GeV. Increasing the energy in the centre-of-mass shifts them towards zero ; they are all below 0.1% at 365 GeV. Hence at all energies, the wrongly paired jets are widely or completely removed by the cut on probability in the kinematic fit ($P > 3\%$).

In conclusion, the χ^2 pairing has then been used in the whole study. Choosing this pairing technique in the kinematic fit also ensures a comparison of the exactly same events for all methods of the W mass reconstruction used in this study.

In case of hard gluon emission, the decay of the W boson can contain a hard third jet, leading to a five jets final state. Forcing the event into four jets could then introduce a misclustering. During the LEP studies, a separated class of five-jet events was studied in terms of possible 2+3 jet subdivisions [5]. This treatment was not reproduced in this study, considering that these kind of events can easily be removed by applying a cut on the kinematic fit χ^2 probability.

7.3.2 ISR and beamstrahlung treatment

ISR is the higher-order QED effect through which the photons are emitted before the beams collide. Beamstrahlung is caused by the electrical fields of the bunches interacting with each other.

²This study has mainly been done before the ATLAS measurement of the W mass that shifted the world average (PDG W mass) to 80.375 GeV.

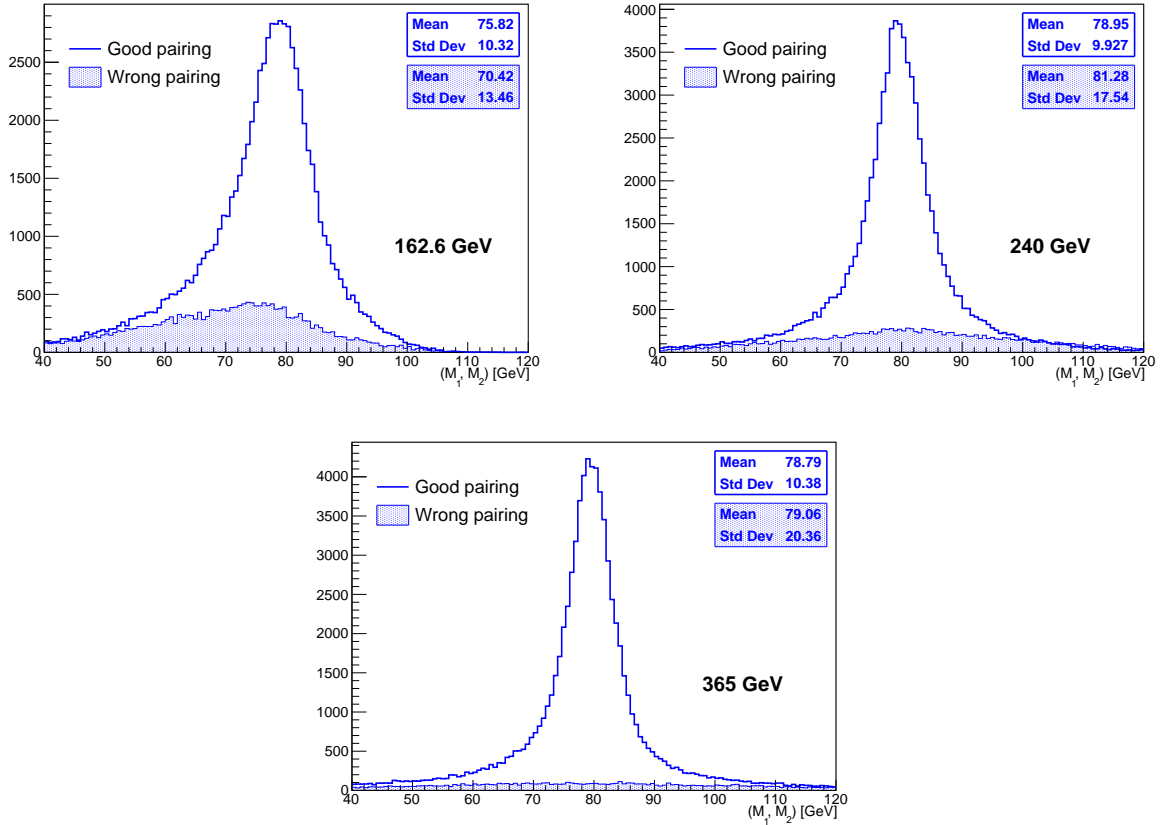


Figure 7.6 – Distribution of the W mass for good and wrongly-paired jets at various energies *Empty histograms show the W mass for the good jet pairing while the full histograms show the bad pairings. The masses were reconstructed with the direct reconstruction method.*

Electrons in one bunch are deflected by the field of the other bunch and emit photons. At LEP, the losses due to these radiations were relatively small but they might become stronger at FCC-ee because of higher beam energy and luminosity. Radiated photons, from ISR or beamstrahlung, are mostly collinear to the beam pipe and could escape undetected from the detector. They introduce a challenge for the kinematic fit in which the energy and (longitudinal) momentum constraints will fail with the unknown amount of missing energy.

The ISR photon that entered into the detector was considered as a W final product and took part to the jet clustering. For the lost photons, a method was developed by the ILC collaboration to take care of the photon radiation in the kinematic fit and to obtain a significant better mass resolution [134, 135]. This method is only focused on the treatment of ISR because it represents the main source of highly energetic photons. The maximum energy that can carry away an ISR photon, given by the Equation (7.41), is proportional to the energy in the centre-of-mass, \sqrt{s} [136].

$$E_{max} = \frac{\sqrt{s}}{2} \left(1 - \frac{M_W^2}{s} \right) \quad (7.41)$$

The approach is to model all the emitted photons as a single photon, with a momentum equal to the sum of all their momenta. It is treated as a measured object with the energy spectrum corresponding to the ISR spectrum.

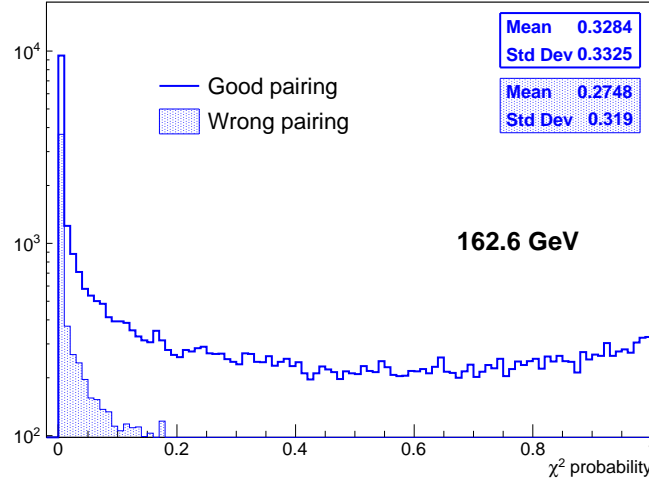


Figure 7.7 – Kinematic fit probability distribution for good and bad jets pairings at 162.6 GeV. *At threshold, the wrongly paired events are at lower values of the probability distribution. They are shifted towards zero when the energy increases. They are rejected with the probability cut ($P > 3\%$).*

7.3.2.1 Photon parametrization

Considering that ISR and beamstrahlung photons escape at small angles along the beam axis, the modelled photon transverse momentum is set to zero. Thus, $E_\gamma = |p_{z,\gamma}|$ and the longitudinal momentum, $p_{z,\gamma}$, is the only free parameter.

The distribution of the radiated photons does not follow a Gaussian distribution, ISR and beamstrahlung are both characterised by a power law [46], and the photon cannot be directly included in the χ^2 function as it was done for the previous objects. Therefore, the photon momentum is parametrized as a function of a parameter y following a Gaussian distribution with mean zero and a unit standard deviation. The expression of $p_{z,\gamma}$ as a function of y is [134]:

$$p_{z,\gamma}(y) = \text{sign}(y)E_{max} \left[\text{erf} \left(\frac{|y|}{\sqrt{2}} \right) \right]^{1/b}, \quad (7.42)$$

where E_{max} is defined in Equation (7.41), sign is the function sign, erf is the error function and b as defined in Equation (2.9). The full computation details and the validation of this technique can be found in [134].

7.3.2.2 ISR treatment evaluation

Events with radiated photons have a low fit probability. The kinematic fit without ISR treatment, as described in Section 7.1.2, was first processed for all events and repeated introducing the measured photon object, for each event with a fit probability smaller than 3%. The ISR treatment procedure is represented on the flowchart of the algorithm available in Appendix B.2.

The first indicator of performance of the ISR treatment is the comparison between the fitted photon energy and the ISR energy generated by MC. The comparison is shown on Figure 7.8 for all

energies. At threshold, the fitted ISR photon energy is almost perfectly reconstructed while it is a bit overestimated above. This is because the losses introduced by the detector resolution increase with the energy and they are attributed to the missing transverse momentum carried out by the radiative photons. Nevertheless, one can conclude from this plot that the photon reconstruction is acceptable.

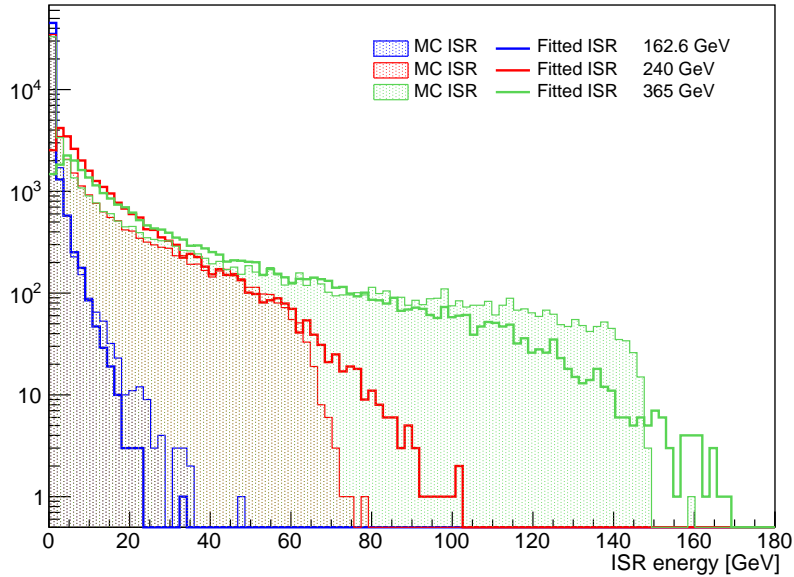


Figure 7.8 – Fitted radiated photon energy compared to the MC simulated one for different centre-of-mass energies

An other important performance indicator of the ISR treatment is the fraction of good fits recovered from the low probabilities. The right plot of Figure 7.9 shows the distribution of the fit probability with and without the ISR treatment at 365 GeV, where the photon energy is the most important. Approximately half of the events with a probability smaller than 0.1 were retrieved and scattered along all the probability range. As a final check, the 5C invariant di-jet masses, with and without the ISR treatment, are shown on the left part of Figure 7.9. The comparison demonstrates the gain in resolution achieved adding the photon parametrization.

Besides radiated photons treated as a single photon, this method leads to a significant improvement on the W mass resolution. Moreover, the photon parametrization derived from the ISR momentum spectrum, Equation (7.42), also works quite well in presence of beamstrahlung, at least for the level expected at FCC-ee.

7.3.3 Mass and width extraction

Figure 7.10 shows the smaller and the larger di-jet invariant masses reconstructed at 162.6 GeV, 240 GeV and 365 GeV using the different reconstruction techniques described at the beginning of this chapter and compared with the raw mass. In the case of 5C kinematic fit, only one mass is reconstructed per event and the same distribution is represented for the smaller and larger di-jet masses. At threshold, the smaller di-jet mass is off-shell, hence the 5C kinematic fit has not been

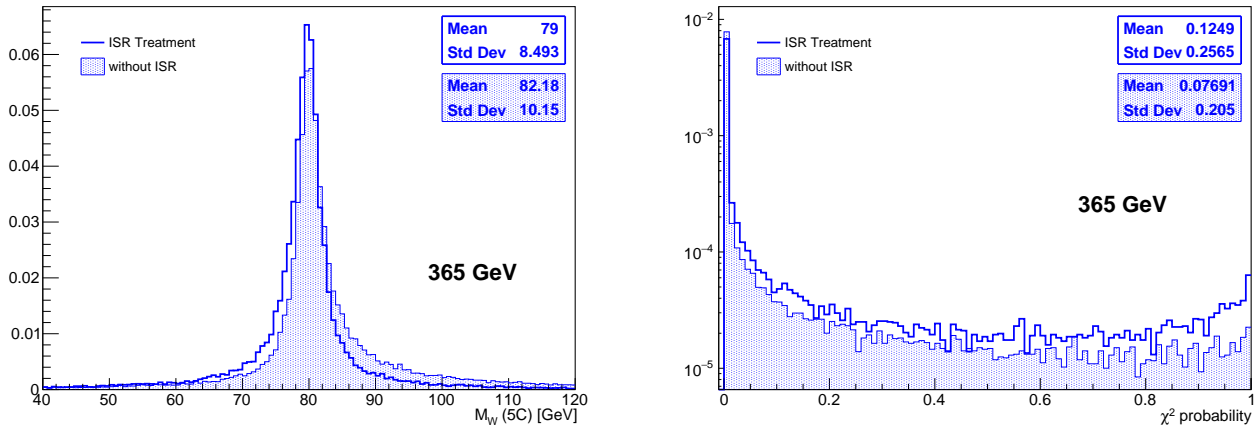


Figure 7.9 – Effect ISR treatment at 365 GeV

Left: Reconstructed mass (5C fit) at 365 GeV with and without ISR treatment.

Right: Kinematic fit probability at 365 GeV with and without ISR treatment

used because imposing an equal-mass constraint leads to an implicit averaging of the two di-jet masses in each event, which is consequently smaller than the on-shell mass.

Except at threshold, where the 4C rescaling gives distributions similar to those of the raw mass, at other energies the jet momenta rescaling technique gives a good first resolution improvement. At all energies, the kinematic fits, leading to a clear peak around 80 GeV, give the best reconstruction and the best correction to the jets resolution. The peak is shifted towards the PDG W mass value while the mass resolution is improved by 3% at threshold, 15% at 240 GeV and 20% at 365 GeV when comparing the raw mass and the 4C(5C) fit at threshold (above).

The expected statistical uncertainties on the W boson mass and width have been independently estimated, with the method described in Section 7.2. The uncertainties, for the full luminosity at FCC-ee, on both mass and width are gathered in Table 7.3. At threshold, the statistical uncertainties have been estimated using the on-shell mass only. The smallest statistical uncertainties on the W mass and width are obtained by the kinematic fit reconstruction, where the statistical accuracy is at the MeV level at threshold and better than 500 keV at higher energies. The results are presented for a luminosity corresponding to two IPs.

7.4 Semi leptonic channel

The study of the semi-leptonic decay channel has been limited to the $WW \rightarrow qq\mu\nu$ events assuming that muons and electrons will be reconstructed with the same performance (see Chapter 4 for details).

In this channel, one W decays into hadron jets while the other one decays into a muon and its neutrino, identified as the missing energy. Compared to the fully hadronic channel, this decay is easier to study because the two jets are automatically paired together (perfect pairing) and the lepton is reconstructed with a good resolution. However, the main drawback of this channel is the

Table 7.3 – Expected statistical uncertainties on the W boson mass and width for the hadronic decay channel at FCCee (full luminosity with 2 IPs) with the CLD detector for different centre-of-mass energies and different reconstruction methods

| \sqrt{s} GeV | σ_{M_W} MeV/c ² | | | σ_{Γ_W} MeV/c ² | | |
|--------------------------|-----------------------------------|-------------|-------------|--|-------------|-------------|
| | 162.6 | 240 | 365 | 162.6 | 240 | 365 |
| Luminosity (ab^{-1}) | 12 | 5 | 1.7 | 12 | 5 | 1.7 |
| Raw Mass | 1.66 | 0.49 | 0.97 | 1.44 | 1.10 | 1.71 |
| 4C rescaling | 1.72 | 0.36 | 0.73 | 1.53 | 0.77 | 1.48 |
| 4C fit | 1.14 | 0.28 | 0.5 | 1.1 | 0.58 | 0.95 |
| 5C fit | | 0.21 | 0.44 | | 0.47 | 1.02 |

bad resolution of the reconstructed leptonic mass introduced by the missing momentum dependence to any energy loss sources: photon radiations, detector resolution or presence of other neutrinos in the hadronisation phase. This resolution loss increases with the energy in the centre-of-mass because the particles are more rejected towards the beam axis at high energy, into regions where the detector resolution is getting worse. This effect is visible on the raw leptonic mass distributions shown on Figure 7.11. Finally, the ISR treatment applied in the hadronic channel, and described in Section 7.3.2, cannot be used in the semi-leptonic decay channel because the energy-momentum conservation is already used to compute the neutrino momentum.

7.4.1 Mass and width extraction

The hadronic and leptonic masses of the semi-leptonic decay have been reconstructed at 162.6 GeV, 240 GeV and 365 GeV using the estimators described at the beginning of this chapter. However, unlike the hadronic decay, the jets momenta rescaling described in Section 7.1.1 has not been used. The 1C and 2C kinematic fit reconstructions were then compared to the raw mass only. The invariant masses are shown on Figure 7.11. In case of 2C kinematic fit, only one mass is reconstructed per event and the same distribution is represented for the leptonic and the hadronic masses. The W mass equality is not forced at threshold energy because of the off-shell mass of one of the two Ws. In the hadronic channel, the off-shell mass was the smaller di-jet mass, which can be either the hadronic mass or the leptonic mass in this channel. In order to work with the on-shell mass only, the larger of the two reconstructed masses has been kept per event.

The kinematic fit gives the best W mass reconstruction at all energies with a huge mass resolution improvement in the case of the leptonic mass, of about 30% at 162.6 GeV, 40% at 240 GeV and 48% at 365 GeV with respect to the raw mass. The jets resolution is also corrected by the constrained fit and reaches resolution improvement of about 5% at 162.6 GeV, 10% at 240 GeV and 12% at 365 GeV compared to the raw mass.

The W mass and width statistical uncertainties have been independently estimated at the different centre-of-mass energies using the FOM method presented in Section 7.2. The resulting uncertainties, for the full luminosity at the FCC-ee, are presented in Table 7.4. The best statistical accuracy on the W mass is obtained using the kinematic fit, 1C at threshold and 2C above. For the width the smallest statistical uncertainty is always given by the 1C fit. As for the hadronic decay channel, the statistical accuracies were computed for luminosities given by two IPs.

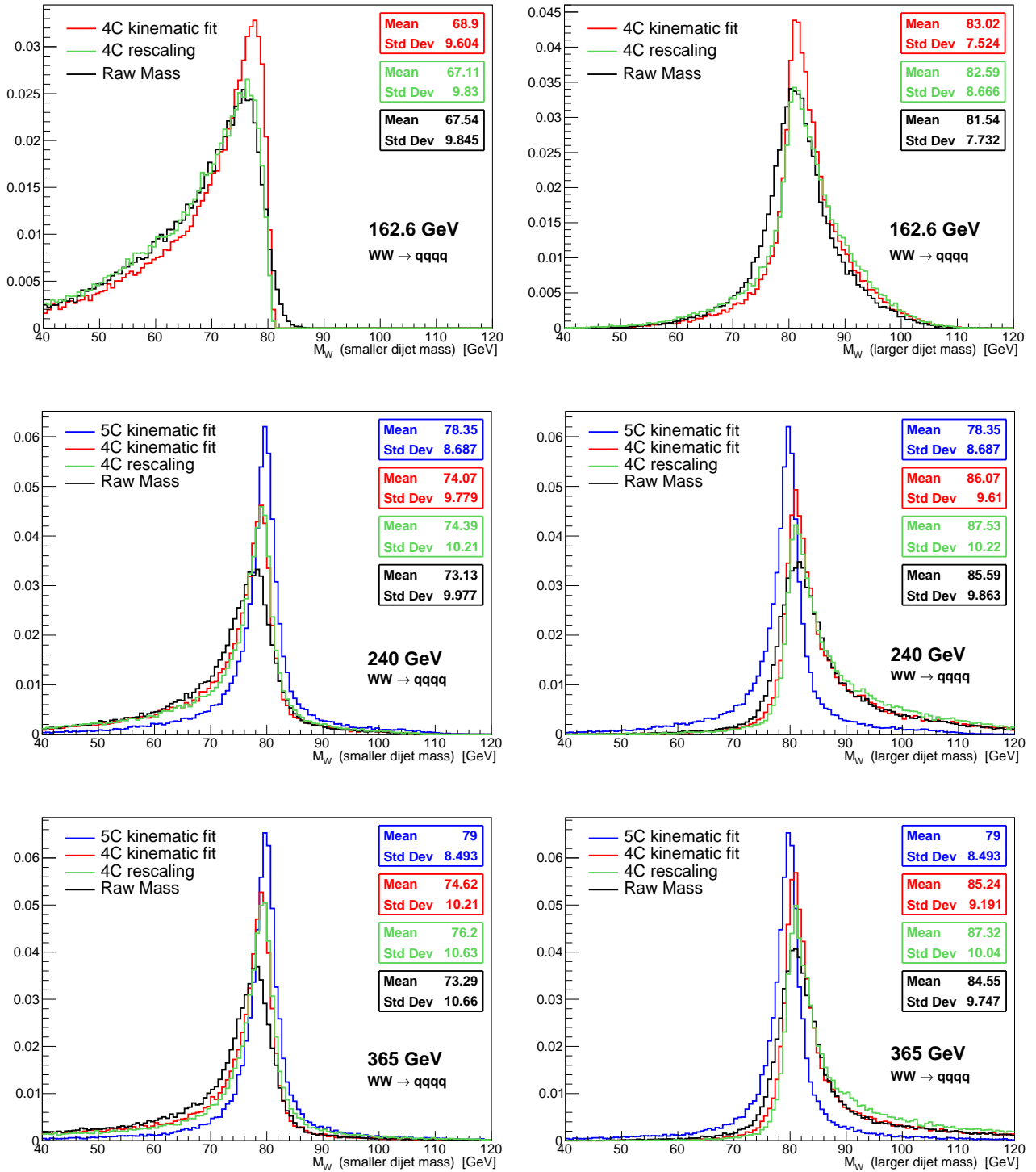


Figure 7.10 – Invariant mass distributions of the smaller (left) and the larger (right) di-jet mass of the hadronic decay channel for different centre-of-mass energies and different reconstruction techniques. The W mass has been reconstructed with the raw data (Raw Mass), with the kinematic rescaling method (4C kinematic rescaling), with the kinematic fit technique constrained by energy-momentum conservation (4C kinematic fit) and by adding the W masses equality constraint (5C kinematic fit). The distributions have been normalised to unity.

Table 7.4 – Expected statistical uncertainties on the W boson mass and width for the semi-leptonic decay channel at FCC-ee (full luminosity with 2 IPs) with the CLD detector for different centre-of-mass energies and different reconstruction methods

| \sqrt{s} GeV | σ_{M_W} MeV/c ² | | | σ_{Γ_W} MeV/c ² | | |
|--------------------------|-----------------------------------|-------------|-------------|--|-------------|-------------|
| | 162.6 | 240 | 365 | 162.6 | 240 | 365 |
| Luminosity (ab^{-1}) | 12 | 5 | 1.7 | 12 | 5 | 1.7 |
| Raw Mass | 0.42 | 0.49 | 1.19 | 0.39 | 0.87 | 1.94 |
| 1C fit | 0.26 | 0.33 | 0.78 | 0.35 | 0.59 | 1.36 |
| 2C fit | | 0.31 | 0.75 | | 0.68 | 1.56 |

7.5 Discussions

The results obtained in both hadronic and semi-leptonic channels demonstrate that the precise measurement of the W mass and width using the direct reconstruction is achievable at all energies at the FCC-ee. One clearly sees the improvement of the W mass resolution going from the raw mass to the fitted mass. The kinematic fit 1C/4C at threshold and adding the W mass equality constraint above, provides a good estimator of the W mass.

The FOM technique used for the statistical uncertainty evaluation yields a high statistical accuracy at all energies. There exists several other methods to extract the W mass and width as well as their statistical uncertainties [5]. One of them is the extraction by fitting the reconstructed 2C/5C invariant mass distribution with a Breit-Wigner function [137]. To account for the non-Gaussian tails of the W mass distribution, a more sophisticated method consists of fitting with the convolution of a Breit-Wigner and a double Crystal-Ball. This latter fit has been applied on the best W mass reconstruction at various centre-of-mass energies in both channels. They show an agreement between the fitted statistical uncertainties and the computed values, allowing the validation of the FOM technique.

As described in Section 2.3.2, the W mass and width can also be precisely measured from the W pair production cross-section with a threshold scan. At LEP, the statistical accuracy of the W mass was 210 MeV/c² for 10 pb^{-1} . The full description of the measurement using this technique at FCC-ee is described in [51]. If only the W mass is extracted, it has been found that the optimal data taking point is 161.4 GeV and the estimated statistical uncertainty on the W mass is 0.23 MeV/c². If the mass and width are simultaneously determined, the optimal configuration is $E_1 = 157.1$ GeV, $E_2 = 162.6$ GeV, $f = 0.4$ (luminosity fraction delivered at E_1). The statistical uncertainties are then 0.4 MeV/c² on the mass and 1.2 MeV/c² on the width. These accuracies have to be compared to $\sigma_{M_W} = 1.14$ MeV/c² and $\sigma_{\Gamma_W} = 1.1$ MeV/c² for the hadronic channel as well as $\sigma_{M_W} = 0.26$ MeV/c² and $\sigma_{\Gamma_W} = 0.35$ MeV/c² for the semi-leptonic decay. As expected the threshold scan gives better statistical uncertainty on the W mass than the direct measurement. The difference in the semi-leptonic channel with the muon decay is rather small but the threshold scan still gives the smallest uncertainty.

At threshold, the beam energy is measured by resonant depolarisation [138]. At lepton colliders, the electrons get transversally polarised, i.e. their spin tends to align with the magnetic field, B. The resonant depolarisation technique is based on the fact that the spin precession frequency around

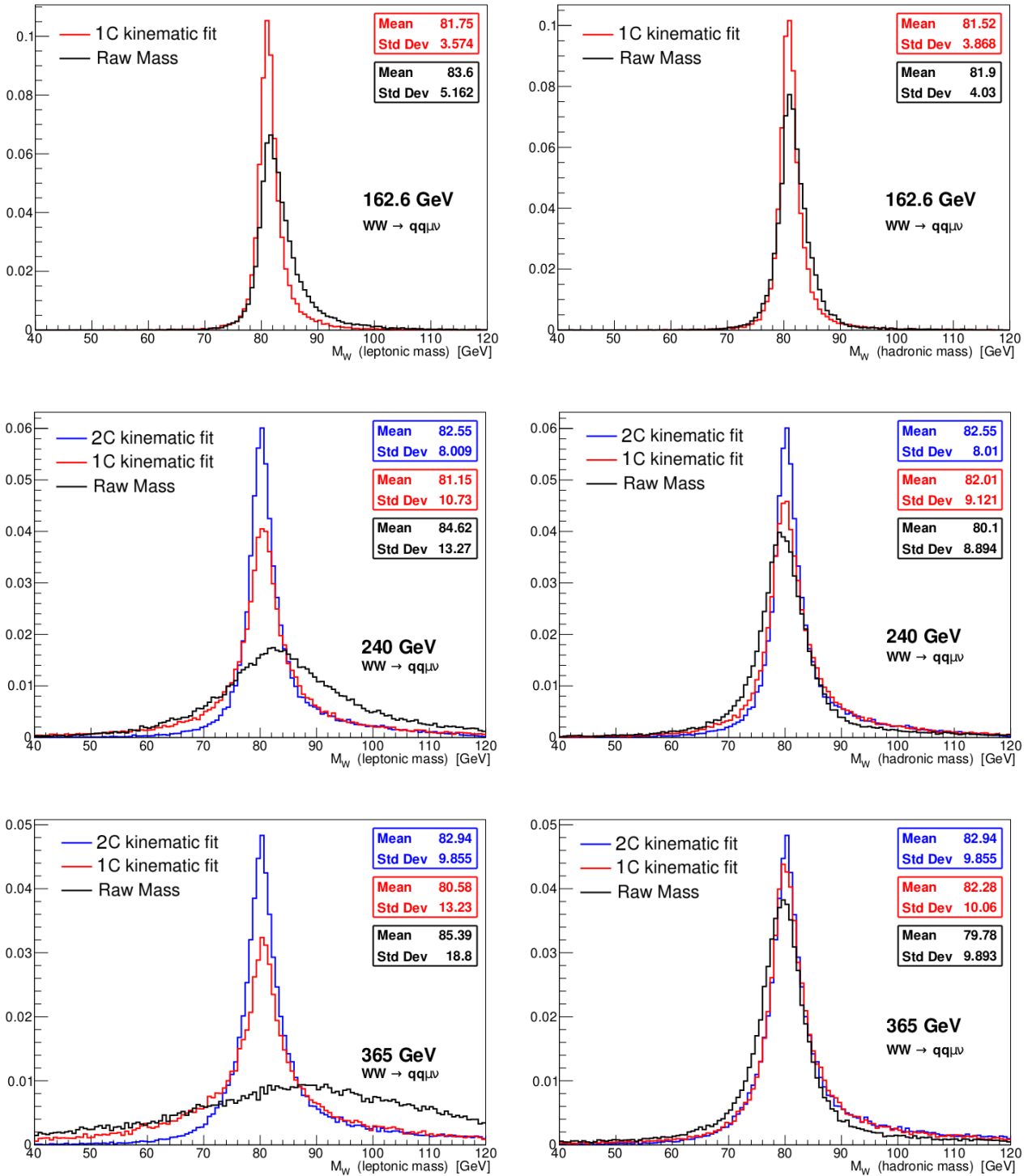


Figure 7.11 – Invariant mass distributions of the W mass for the W leptonic decays (left) and for the W hadronic decays (right) in the semi-leptonic decay channel for different centre-of-mass energies and different reconstruction techniques

The W mass has been reconstructed with the raw data (Raw Mass), with the kinematic fit constrained by energy-momentum conservation (1C kinematic fit) and by adding the W mass equality constraint (2C kinematic fit). The distributions have been normalised to unity.

B is proportional to the beam energy. This frequency is determined by resonant depolarisation, by exciting the beam with an oscillating magnetic field produced by a vertical kicker magnet. A resonance condition occurs when the frequency of the resulting spin kick is in phase with the spin precession. The electron spins are then coherently swept away from the vertical direction, and the polarization disappears. At energies above the W pair production threshold, the level of transverse polarisation is too small and the energy calibration by resonant depolarisation is unavailable. The reached level of precision on the W mass is then an opportunity for the beam calibration. For example, the precision of the centre-of-mass energy measurement at the $t\bar{t}$ threshold (~ 350 GeV) is limited to 30 MeV. The precise knowledge of the W mass provides an alternative to this measurement, allowing a statistical precision of 5 MeV at 350 GeV and 2 MeV at 365 GeV [139, 140].

At LEP, the W mass and width measurements were limited by their statistical uncertainties. With precisions below the MeV level, it will be challenging to reduce the experimental and theoretical systematic uncertainties to the same level. The next chapter discusses about the main sources of systematic uncertainties and details the study of the systematic uncertainty introduced by the FSI in the hadronic decay channel.

Chapter 8

Study of the Final State Interactions effect

"Accurate and minute measurement seems to the non-scientific imagination, a less lofty and dignified work than looking for something new. But nearly all the grandest discoveries of science have been but the rewards of accurate measurement and patient long-continued labour in the minute sifting of numerical results."
Baron William Thomson Kelvin

Contents

| | | |
|------------|--|------------|
| 8.1 | Monte Carlo models | 128 |
| 8.1.1 | Colour Reconnection | 129 |
| 8.1.2 | Bose-Einstein Correlation | 129 |
| 8.2 | Effect on M_W | 130 |
| 8.2.1 | Systematic uncertainty | 130 |
| 8.2.2 | Effect on the statistical uncertainty | 132 |
| 8.3 | Treatment using a cone analysis | 132 |
| 8.3.1 | Cone reconstruction | 133 |
| 8.3.2 | Effect of the cone on M_W and on the statistical uncertainty | 134 |
| 8.3.3 | Final State Interactions effect on the W mass with a cone | 134 |

At LEP, the W mass and width measurements in hadronic and semi-leptonic channels were statistically limited, as shown on Table 8.1 [5]. As demonstrated in Chapter 7, the statistical precision expected on these observables at FCC-ee is below the MeV level at all working points. Thus systematic uncertainties must be precisely addressed and reduced to match the statistical uncertainties.

The hadronisation and detector effects will be better controlled at the FCC-ee as a result of more efficient detectors (higher granularity allowing better particle-flow (PF) performance and particle identification) and larger datasets. The beam related effects, as beam energy spread and beamstrahlung, are expected to be well measurable at FCC-ee energies [139]. The detector granularity and resolution, the simulation and analysis efficiency [23] and the small background level resulting in a clean environment, will be sufficient to reduce the sources of systematic uncertainties referred as 'Other' in Table 8.1. However, the systematic uncertainty introduced by the final state interactions will not be reduced at the level of the statistical precision. These interferences, already discussed in Chapter 2, are decomposed in two effects: the Colour Reconnection, CR, and the Bose-Einstein Correlations, BEC, and contribute to the largest systematic uncertainty on the W mass.

Performing the most accurate measurement of the W boson mass and width in the hadronic decay channel strongly relies on the reduction of this uncertainty. A treatment to decrease the sensitivity of M_W to the QCD interference effects at all energies is presented in this chapter [126, 127, 51].

| Source | Systematic Uncertainty in MeV | | | |
|---------------------------------------|-------------------------------|--------------------|----------|---------------|
| | on m_W | | | on Γ_W |
| | $q\bar{q}l\nu_\ell$ | $q\bar{q}q\bar{q}$ | Combined | |
| ISR/FSR | 8 | 5 | 7 | 6 |
| Hadronisation | 13 | 19 | 14 | 40 |
| Detector effects | 10 | 8 | 9 | 23 |
| LEP energy | 9 | 9 | 9 | 5 |
| Colour reconnection | – | 35 | 8 | 27 |
| Bose-Einstein Correlations | – | 7 | 2 | 3 |
| Other | 3 | 10 | 3 | 12 |
| Total systematic | 21 | 44 | 22 | 55 |
| Statistical | 30 | 40 | 25 | 63 |
| Statistical in absence of systematics | 30 | 31 | 22 | 48 |
| Total | 36 | 59 | 34 | 83 |

Table 8.1 – Statistical and systematic uncertainties on the W mass and width in the hadronic and semi-leptonic channels for the combined LEP2 results obtained with the direct reconstruction method

In the hadronic channel, the largest source of systematic uncertainty is introduced by the FSI (Colour Reconnection and Bose-Einstein Correlations). The 'Other' source refers to uncorrelated uncertainties between experiments: simulation statistics, event selection, background estimation, fitting method and four-fermion treatment.[5]

8.1 Monte Carlo models

The hadronic effects on M_W mentioned above were well-observed in previous experiments [8, 5, 141] and well-described by the theory [142, 143, 58, 59]. Several phenomenological models have been

developed and implemented in MC programs to describe the CR and BEC. The philosophies of the toy models implemented in PYTHIA [49], the event generator used in the context of this work, are described hereafter. For the BEC study, one model, fitting all kinds of collisions, is implemented. For CR, only the models for e^+e^- collisions are explained but a description of the models proposed for the pp collisions can be found in [56, 57, 144].

8.1.1 Colour Reconnection

In electron-positron collisions two CR models, describing the interference between the hadronic decays of the two Ws, have been implemented in PYTHIA during the W mass study at LEP2 [55]. These models, based on string hadronisation proposed by Sjöstrand and Khoze, are singlet models in which each string is a colour singlet. In each of the W decays, a colour-confinement string stretched between two decay-product partons produces a linear confinement potential. During the fragmentation process, the strings expand out from their initial decay vertex and break up into hadrons. Before the hadronisation step, a reconnection is possible if two colour fields overlap in phase time. In that case, the string originally linking the two pairs $q_1\bar{q}_2$ and $q_3\bar{q}_4$ are replaced by strings between $q_1\bar{q}_4$ and $q_3\bar{q}_2$. The two models differ within their description of the overlap.

In the SKI scenario, the strings are represented as elongated bags with a significant transverse extension and a soft internal structure. The reconnection probability is proportional to the integrated space-time overlap of the extended strings. As given by Equation (8.1), the probability for a hadronic event of being reconnected depends on a function of the amount of the spacial overlap, f , with a free parameter, k_I , controlling the overall strength of the CR. This parameter can be varied to generate samples with different fractions of reconnected events.

$$P_{reco} = 1 - \exp(-fk_I) \quad (8.1)$$

In the SKII scenario, the strings are considered as very thin cores (vortex lines) containing all the topological information. In that case, the reconnection can only take place when the cores cross each other. There is no free parameter in this model. The fraction of reconnected events is of the order of 30% at $\sqrt{s} = 162.6$ GeV. In order to get the same fraction of reconnected events in the two models, the SKII model is used to fix the parameter k_I of the SKI model to $k_I = 0.6$ (value optimised during LEP studies) such as the number of reconnected events agree at threshold. This parameter was kept fixed in the whole study.

For both models, only one reconnection is allowed per event, the one with the largest overlap volume for the SKI, the first string crossing in SKII.

8.1.2 Bose-Einstein Correlation

The PYTHIA BEC algorithm is based on a geometric approach, involving cross-talk between all pions and kaons, in such a way to cause a possible effect on the W-mass determination. If the particle production vertices have a Gaussian distribution, the enhancement in the two-particle correlation is parametrized in terms of an isotropic and exponential source, Equation (8.2), in phase-space [58].

$$f_2(Q) = 1 + \lambda \exp(-Q^2 R^2) \quad (8.2)$$

Where, R is the source size and λ the strength (or coherence parameter of the source) defined in the range $0 < \lambda < 1$. Both parameters are determined by fitting the data.

The model implemented in PYTHIA emulates the BEC by slightly shifting the momenta of all identical final-state particles. In this approach, the momenta of identical final-state particles are redistributed to reproduce the expected two-boson momentum correlations. An appropriate momentum shift is obtained as follows.

For a given pair of particles i and j , with the relative separation Q ,

$$Q_{ij}^2 = -(\vec{p}_i - \vec{p}_j)^2, \quad (8.3)$$

the model shifts Q to $Q' = Q + \Delta Q$, emulating the inclusion of the BEC effect [58, 59]. Assuming that the inclusive distribution of Q is just defined by the phase-space, then $d^3p/E \propto Q^2 dQ / \sqrt{Q^2 + 4m^2}$, and the relation between Q and Q' is given by:

$$\int_0^Q \frac{q^2 dq}{\sqrt{q^2 + 4m^2}} = \int_0^{Q'} f_2(q) \frac{q^2 dq}{\sqrt{q^2 + 4m^2}}, \quad (8.4)$$

where $f_2(Q)$ is the enhancement defined in Equation (8.2). The shift in Q can be considered as a translation of the particle momenta. But, since the invariant mass of the pair has changed, it is not possible to simultaneously conserve momentum and energy. A simple solution is to conserve the three-momentum p in the rest frame of the W , applying the same size and opposite sign shifts along the direction connecting two bosons, i.e. to pull p_i and p_j closer. As a given particle is likely to belong to several pairs, the pair-wise shifts are evaluated based on the original momentum configuration, and only afterwards the momentum is shifted to the sum of all shifts. Although the total momentum is preserved by the above procedure, the total energy is reduced by the local shift of the pair particles.

8.2 Effect on M_W

8.2.1 Systematic uncertainty

According to the theory, the W mass is shifted of the order of a few MeV due to the FSI phenomena [143]. These shifts were evaluated in the present study of the W mass at all FCC-ee energies and for the different sources of QCD effects, using samples generated with the MC models presented in Section 8.1.

The same method was used for SKI, SKII and BEC models, consisting in simulating samples of one million events each, in which a model is implemented but forcing all other stages of the simulation to be identical. In case of CR, the branching $g \rightarrow q\bar{q}$, also allowed by the shower formalism in addition to the dominant branchings $g \rightarrow qg$ and $g \rightarrow gg$, was turned off to simplify the CR toy study [142]. The whole event reconstruction and W mass analysis was repeated as previously. The events were propagated through the CLD detector using the HEPHY fast-simulation, and the DURHAM algorithm was used to cluster the particles into four jets. The best M_W reconstruction method, 4C kinematic fit at threshold and 5C above, is used to reconstruct the invariant mass. At

threshold only the on-shell mass (the larger) is kept.

For each model, the shift, δM_W , is computed event-by-event, Equation (8.5), by comparison of the mass value obtained with and without FSI.

$$\delta M_W = M_W(FSI) - M_W(noFSI). \quad (8.5)$$

If one of the two masses is not reconstructed during the process, e.g. cut in kinematic fit, the event is rejected. The shift distribution is finally fitted with a Gaussian function and the mean gives the estimation of the systematic uncertainty on the W mass. Figure 8.1 shows the shift distribution, δM_W , obtained at 240 GeV, when the CR effect is modelled using the SKI scenario.

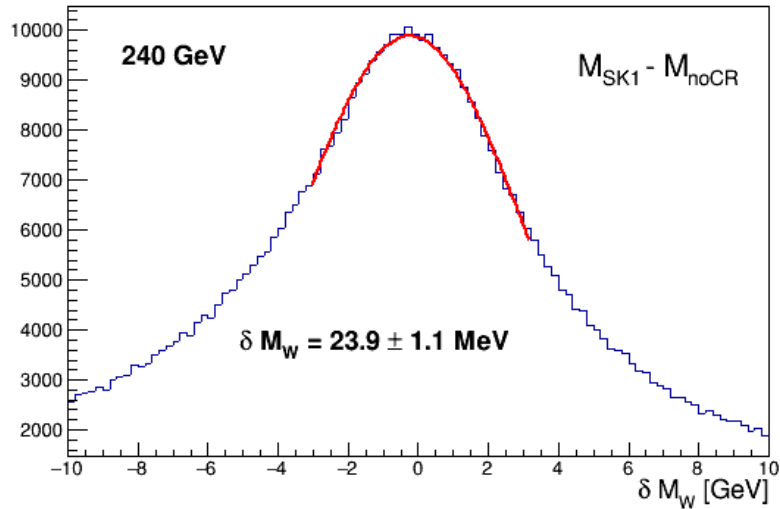


Figure 8.1 – M_W shift due to CR effect, modelled using the SKI scenario ($k_I = 0.6$) at 240 GeV

The estimated shifts on the W mass for the three models at the different centre-of-mass energies are given in Table 8.2. One million events seem sufficient for a first evaluation of the QCD effects on M_W since the statistical uncertainties are around $1 \text{ MeV}/c^2$.

The sensitivity of M_W to the FSI increases with energy. This energy dependence can be explained with two competing effects: the probability that an interconnection occurs decreases with energy, but the effect of a single reconnection becomes larger with increased energy [142].

Table 8.2 – Estimated systematic uncertainties [MeV/c^2] introduced by the CR (SKI with $k_I = 0.6$ and SKII models) and BEC in the hadronic decay channel for different centre-of-mass energies

| \sqrt{s} [GeV] | SKI | SKII | BEC |
|------------------|----------------|----------------|---------------|
| 162.6 | 14.6 ± 0.8 | 7.9 ± 0.9 | 3.1 ± 0.5 |
| 240 | 23.9 ± 1.1 | 12.1 ± 1.3 | 5.9 ± 0.6 |
| 365 | 32.2 ± 0.9 | 14.7 ± 1.0 | 9.9 ± 0.6 |

The biases due to CR are consistent with the observed mass shifts from previous studies using the same models [143, 8]. At each energy, scenario I gives a larger bias than scenario II within approximately the same uncertainty. Therefore, the mass shift depends on the model used and might

be larger than the bias estimated above. The ratio $\delta M_{W,SKI}/\delta M_{W,SK2}$ increases with the energy. It is compatible with the fact that the decrease of the reconnection probability with the energy is slower for SKII than for the SKI scenario. This phenomenon can be explained by a better separation of the vortex lines with respect to the elongated bags in case of faster motion of the Ws [142].

In the ALEPH study described in [8], the combined shifts over all centre-of-mass energies from 183 to 209 GeV, were estimated at 39 ± 2 MeV/c² and 6 ± 8 MeV/c² for the SKI and SKII models respectively. The computed values, at 162.6 GeV and 240 GeV, are then in agreement with the estimated shifts. The BEC model presented above was also used for the BEC uncertainty study in the ALEPH analysis [8]. A combined shift of 6 MeV/c² on the W mass due to this effect was evaluated. Similar conclusion can then be drawn about the BEC effect.

8.2.2 Effect on the statistical uncertainty

As demonstrated by the LEP combined uncertainties in Table 8.1, the statistical uncertainties are smaller in absence of systematic errors. Therefore, the QCD effects on the mass and width statistical uncertainties computed in Chapter 7 were also evaluated.

Table 8.3 gives the mass and width statistical uncertainties evaluated in presence of the different FSI sources used above, and computed using the FOM technique defined in Section 7.2. For the comparison, the statistical uncertainties computed without FSI, σ_{M_W} and σ_{Γ_W} , are reminded. At all energies, the interconnection effects result in an increase of the statistical uncertainties in the hadronic channel. A larger uncertainty is introduced by the SKI compared to the SKII model.

Table 8.3 – Effect of the CR (SKI with $k_I = 0.6$ and SKII models) and BEC on the W mass and width statistical uncertainties in the hadronic channel for different centre-of-mass energies and for the full FCC-ee luminosity [MeV/c²]

| \sqrt{s} [GeV] | σ_{M_W} | SKI | SKII | BEC | σ_{Γ_W} | SKI | SKII | BEC |
|------------------|----------------|-------|-------|-------|---------------------|-------|-------|-------|
| 162.6 | 1.143 | 1.179 | 1.167 | 1.172 | 1.088 | 1.158 | 1.101 | 1.122 |
| 240 | 0.215 | 0.225 | 0.218 | 0.224 | 0.474 | 0.512 | 0.489 | 0.491 |
| 365 | 0.463 | 0.478 | 0.467 | 0.471 | 1.021 | 1.345 | 1.084 | 1.173 |

To verify that all the biases observed only arise from the FSI, the different models were activated in the semi-leptonic decay channel, where no effect between the decay products of the different Ws can be present, and the same study was performed. As expected, exactly no deviation with the results presented in Section 7.4 was found.

8.3 Treatment using a cone analysis

The systematic uncertainties introduced by the FSI are expected to be the dominant uncertainties on the W mass and width in the hadronic channel at the FCC-ee. Several techniques have been developed in the LEP collaborations to reduce the sensitivity of M_W to the QCD systematics [5]. In the ALEPH collaboration, two methods, based on soft-particles rejection at the level of the jet clustering were used [8]. One of these methods consists in only using those particles that are in a

cone of opening angle R for the jet reconstruction. This study has been reproduced in the present analysis of M_W and the results are presented hereafter.

8.3.1 Cone reconstruction

All the particles of the event, forced into four jets using the DURHAM algorithm, contribute with the same weight to the jet energy and direction. In hadron collisions, other algorithms called cone algorithms, are used to cluster the jets and only the particles within a given angle around the jet-core axis contribute to the jet momentum. A similar algorithm can be used for the W-pair hadronic decays in presence of FSI. In that way the bias introduced on the mass can be reduced. This reason motivated the use of the cone algorithm in the study of FSI in ALEPH.

The particles moved by the FSI in the inter-jet region modify the jet angle. Using a cone algorithm for the reconstruction would mitigate this effect. However, the jet energies would be statistically degraded because of the rejection of low momentum particles. Hence, while using directly the cone algorithm, the jets clustered with the DURHAM algorithm were used as a starting point for the determination of the cone jets.

Every DURHAM jet is individually taken and the following steps are followed:

- The jet three-momentum defines the cone axis;
- A cone with a 0.4 radians opening angle (R), is defined around this axis;
- All particles belonging to the original jet within the cone are accepted. The momentum of each accepted particle is added to the momenta that previously passed the cone selection. This step is repeated until all the original jet particles are tested;
- The vectorial sum of the selected particle momenta, (E_{sum}, \vec{p}_{sum}) , is the new jet four-momentum;
- This jet four-momentum, is rescaled to $(E_{cone}, \vec{p}_{cone})$ by the ratio of the original jet energy to the cone jet energy, to keep the energy unchanged. Thus:

$$\begin{aligned} E_{cone} &= E_{durham}, \\ \vec{p}_{cone} &= \vec{p}_{sum} \cdot \frac{E_{durham}}{E_{sum}}. \end{aligned} \tag{8.6}$$

This algorithm corrects for the jet angles modified by the FSI while conserving the jet energies. The opening angle, $R = 0.4$ radians, was found to provide the optimal balance between the statistical and systematic uncertainties on M_W at ALEPH for centre-of-mass energies from 183 GeV to 209 GeV. The same cone was chosen for a preliminary study of the FSI systematic uncertainty on the W mass. For different cut values, the jets momentum will be changed, and consequently M_W . Therefore a more complete adjustment must be performed to determine the optimal value of the opening angle, which might differ at higher energies.

The cut on soft-particles will lose part of the information and will deteriorate the jet clustering performance. A degradation of the W mass and of the associated statistical uncertainty is then expected as shown in Section 8.3.2. However, this loss is compensated by a reduction of the FSI systematic uncertainty as presented in Section 8.3.3.

8.3.2 Effect of the cone on M_W and on the statistical uncertainty

The effect of a cone reconstruction on M_W and mass and width statistical uncertainties was first evaluated in absence of FSI. The study was performed using the cone jets, clustered using the cone algorithm described in Section 8.3.1. The results of this analysis, called cone analysis, were compared with the previous DURHAM-based analysis, called standard analysis. The comparison was done for the best reconstructed W mass only (4C on-shell mass at threshold and 5C above).

The W mass is reconstructed with the kinematic fit technique presented in Section 7.1.2, used in the very same conditions with cone and standard jets. The only difference between the two analyses is the input covariance matrix, which has to be recomputed because of the corrections of the jet directions with respect to the standard jets. Figure 8.2 shows the degradation due to the cone at the different energies. The statistical degradation is directly proportional to the information carried out by the particles left outside the cone. There was approximately a 20% resolution loss from applying a cone correction at ALEPH (between 183 and 209 GeV) [5]. From the observed distributions, one can conclude that the chosen opening angle might be a bit too large at higher energies. With $R = 0.4$ radians, the resolution loss is 2.9% at 162.6 GeV, 6.7% at 240 GeV and 16.9% at 365 GeV. This observation has to be kept in mind for the study of the reduction of the FSI systematic uncertainty: a large cone will not remove all the interconnected events and will not sufficiently reduce the systematics.

The effect of the cone jets on the mass and width statistical uncertainties was also evaluated and the comparison with the standard analysis is presented in Table 8.4. The cone increasingly degrades these uncertainties with energy. The statistical uncertainty on the W mass is degraded by a few percent at threshold and 10-15% above.

Table 8.4 – Effect of a cone ($R=0.4$ rad) reconstruction on the mass and width statistical uncertainties in the hadronic channel for different centre-of-mass energies and full FCC-ee luminosity [MeV/c^2]. No FSI were included in the simulation

| \sqrt{s} GeV | $\sigma_{M_W,stat}$ | | $\sigma_{\Gamma_W,stat}$ | |
|----------------|---------------------|-------|--------------------------|-------|
| | standard | cone | standard | cone |
| 162.6 | 1.143 | 1.181 | 1.088 | 1.089 |
| 240 | 0.215 | 0.228 | 0.474 | 0.530 |
| 365 | 0.463 | 0.564 | 1.021 | 1.214 |

8.3.3 Final State Interactions effect on the W mass with a cone

In order to evaluate the sensitivity of the different FSI sources to the cone analysis, the study explained in Section 8.2 was repeated. The results are shown hereafter and have to be compared with the standard DURHAM analysis conclusions given in this same previous section.

The study at the different centre-of-mass energies reveals a mass shift difference between the cone jet reconstruction and the standard analysis. Table 8.5 shows the reduction of the bias on the W mass due to the FSI using the cone clustering.

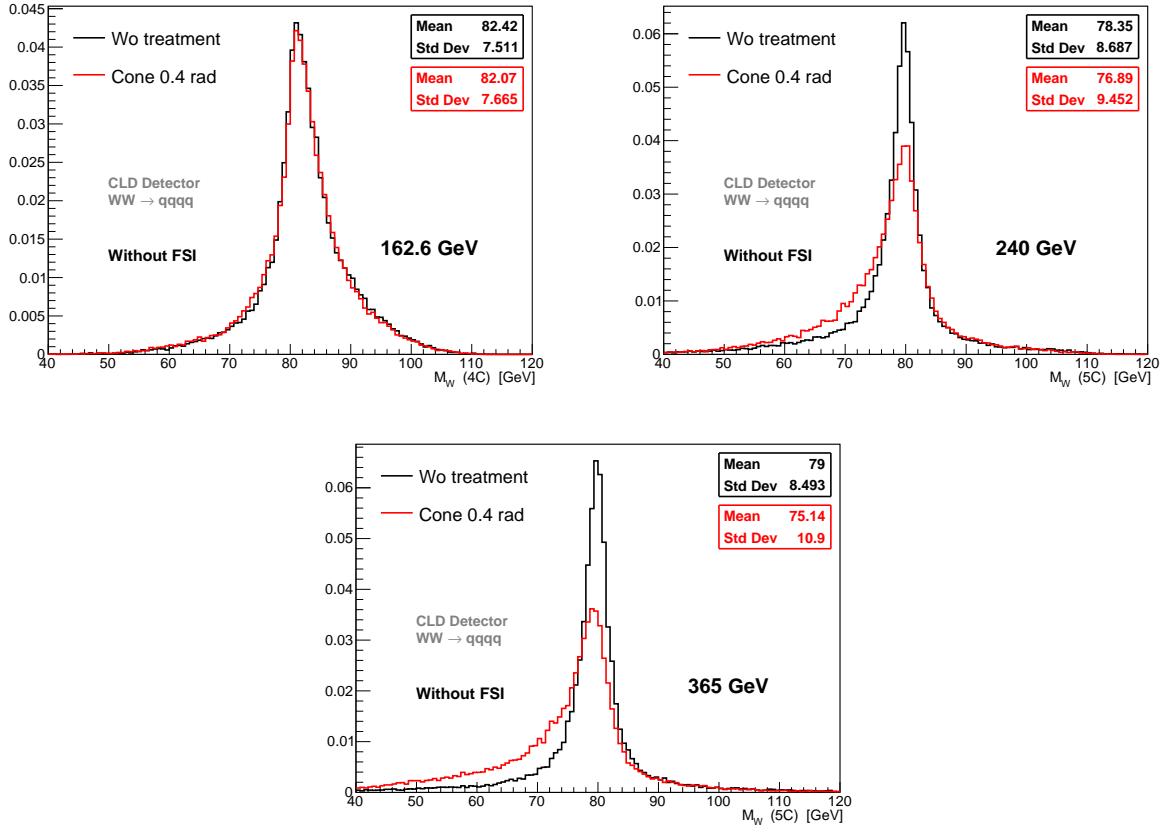


Figure 8.2 – Effect of a cone ($R=0.4$ rad) on the reconstructed mass at different energies. The distributions obtained with DURHAM (standard) jets are drawn in black, identified with the label 'wo treatment', contrasting with the jets corrected using a cone cut (in red). No FSI were included in the simulation.

Table 8.5 – Estimated systematic uncertainties [MeV/c^2] introduced by the CR (SKI with $k_I = 0.6$ and SKII models) and BEC after a cone cut ($R = 0.4$ rad) on the four jets of the hadronic decay channel for different centre-of-mass energies

| \sqrt{s} GeV | SKI | SKII | BEC |
|----------------|----------------|---------------|---------------|
| 162.6 | 7.5 ± 0.7 | 3.8 ± 0.9 | 1.8 ± 0.6 |
| 240 | 11.5 ± 0.7 | 6.0 ± 0.6 | 2.1 ± 0.5 |
| 365 | 17.5 ± 0.5 | 8.3 ± 0.8 | 5.5 ± 0.6 |

Compared to the standard analysis, the shift on M_W is smaller by about 50 % with the cone. The statistical uncertainties on these values are also reduced. In the ALEPH study detailed in [8], the cone reconstruction changed the combined shift over the eight energies, from $+56 \pm 2 \text{ MeV}/c^2$ to $+23 \pm 3 \text{ MeV}/c^2$ using the SKI scenario with $k_I = 1.0$. Extrapolating and knowing that the cone opening angle is not optimal, the estimated values obtained with the cone reconstruction are considered consistent with this previous study.

The mass and width statistical uncertainties are both affected by the cone reconstruction and the FSI effects as shown in Table 8.4 and Table 8.3. Excluding the FSI, the mass statistical uncer-

tainty is degraded by the cone by few percent at threshold, 10% at 240 GeV and 15% at 365 GeV without FSI. As confirmed by the Table 8.6, the treatment of the FSI with a cone reconstruction will add a new deterioration on σ_{M_W} and σ_{Γ_W} . Knowing that the cone should reduce the shift on M_W by approximately 50%, the additional loss on the statistical uncertainties due to the cone is considered as acceptable.

Table 8.6 – Effect of a cone ($R = 0.4$ rad) reconstruction on the mass and width statistical uncertainties [MeV/c^2] in presence of CR (SKI with $k_I = 0.6$ and SKII models) and BEC in the hadronic channel for different centre-of-mass energies and full FCC-ee luminosity

| \sqrt{s} GeV | $\sigma_{M_W,stat}$ | | | | $\sigma_{\Gamma_W,stat}$ | | | |
|----------------|---------------------|-------|-------|-------|--------------------------|-------|-------|-------|
| | no FSI | SKI | SKII | BEC | no FSI | SKI | SKII | BEC |
| 162.6 | 1.143 | 1.210 | 1.191 | 1.178 | 1.088 | 1.158 | 1.139 | 1.130 |
| 240 | 0.215 | 0.244 | 0.237 | 0.236 | 0.474 | 0.728 | 0.691 | 0.587 |
| 365 | 0.463 | 0.545 | 0.539 | 0.576 | 1.021 | 1.822 | 1.781 | 1.201 |

This study is a good first estimation of the CR and BEC effects on M_W in the hadronic channel and helped to estimate how they might be reduced in FCC-ee data. The sensitivity of the M_W to the presence of these interactions can nevertheless be reduced using a cone cut in the jet algorithm, making the measurement more robust. An other cut, called p_{cut} analysis, was studied in the ALEPH collaboration [8], consisting in rejecting all low momentum particles from the jets. In this paper, the results from both methods were found compatible, between the two cuts with a slightly better reduction of the FSI systematic uncertainty using the p_{cut} reconstruction. This additional analysis might be an interesting cross check for the present cone cut results.

This shift might be corrected for if the CR and BEC effects were precisely modelled. If the required level of accuracy is not reached in the future, these effects will likely be measured by comparing the W mass measurements in the hadronic and leptonic channels.

Conclusion and perspectives

The Standard Model of Particle Physics is a very successful theory that showed a dramatic agreement between its predictions and the experimental results. However, several theoretical issues and experimental observations suggest that the model is not complete and might only be an effective theory, the low energy approximation of a more fundamental underpinning structure. For this reason, new physics is searched both directly and indirectly through precise measurements of the model observables. Any deviation might represent a turning point in the Particle Physics field, revealing an inconsistency of the Standard Model. Currently, the prediction of the global electroweak fit and the experimental measurements are in agreement within 1σ . The mass of the W boson is an important input to the global fit and its measurement is largely dominated by both experimental and theoretical systematic uncertainties; both of them have to be reduced to the MeV-level. Future experiments, expected to produce millions of W boson decays, would allow to measure precisely the W boson properties.

Original studies towards a precise measurement of the W boson mass at HL-LHC (proton-proton collisions) and at FCC-ee (electron-positron collisions) were presented in this thesis.

Besides a high level of theoretical uncertainties, unprecedented precisions require to control both the detector and the analysis performance, whose optimisation requires an important upstream design of simulation software. Currently, the CMS endcap calorimeter upgrade for the HL-LHC, HGCal, is under study and its detailed Geant4-based simulation is under development. However, one might need for a complementary fast simulation program, in order to get quick estimations of detector parameter effects, detector response validation or production of large datasets. The implementation of a fast simulation for the HGCal was presented in Chapter 5. This tool is very flexible and can easily be tuned to reproduce the particle interactions through the entire HGCal structure. Its simplified geometry and response evaluation coupled with a Quadtree implementation, make it a high generation rate (2.6 kHz) software. It showed acceptable agreement with the full HGCal simulation and reconstruction for the physical objects that were studied. Therefore, this convenient, performing and standalone tool is waiting for being implemented in the CMS software. Presently, the tuning of the fast simulation is done using parameters derived from the detailed simulation and further improvements could be added to make it a more complete tool. For instance magnetic field or PU could be implemented as well as more complete shower parametrisation. Such simulation tool can thereafter be used to evaluate the effects of the detector on the measured objects resolution, key for accurate measurements.

In proton-proton collisions, the transverse mass is the best estimator of the W mass, thanks to its small dependence to the boson transverse momentum. This low sensitivity relies on a precise measurement of the hadronic recoil; the better the recoil is measured, the smaller is the dependence.

The recoil is a complicated physics object, estimated with a poor resolution, and both its response and resolution are degraded with increasing PU level. A precise measurement seems therefore challenging in the HL-LHC harsh environment, where the instantaneous luminosity is planned to be increased by a factor ten with respect to the LHC. However, thanks to the higher sub-detector granularity, the CMS detector is expected to reach higher performance. The recoil reconstruction at CMS was presented in Chapter 6 and the HGCal parameters are expected to have a positive effect on the recoil measurement. The precise measurement of the recoil does not only depend on detector effects but is also determined by its definition model. In order to exploit as much as possible the information collected by the detector, a multivariate quantile regression, using machine learning technique, was developed. The results obtained with this improved definition show a better reconstruction of the recoil. The logical continuation of this study would be to quantify the performance of this improvement on the transverse mass of the W boson. Moreover, additional systematic uncertainties might arise from wrong modelling of the recoil that might create discrepancies between the data and the MC simulation. Further studies could therefore evaluate the recoil definitions based on systematic uncertainties introduced on the transverse mass. An other possible development to this study is the optimisation of the DNN model by studying the effect of additional variables.

The measurement of the W boson mass in electron-positron collisions is less challenging as the background level is smaller and all the kinematics of the event is available for the reconstruction. The amount of W -pairs produced at the W threshold energy and above at the FCC-ee collider will allow the measurement of the W boson mass with unprecedented accuracy. The W mass statistical uncertainties expected at the FCC-ee were estimated in the hadronic and semi-leptonic channels at 162.6 GeV, 240 GeV and 365 GeV. The results are presented in Chapter 7. This study shows that a statistical uncertainty on the W mass below the MeV-level can be reached at the different centre-of-mass energies. Such a level of precision will turn the statistically dominated results of LEP into systematically dominated measurements at the FCC-ee. Therefore, the precise measurement of the W mass and width, depends on the reduction of the systematic uncertainties down to the level of the statistical uncertainties. Among the different sources of systematic uncertainties identified at LEP, the Final State Interaction (FSI), i.e. the Colour Reconnection and the Bose-Einstein Correlation, introduced the largest uncertainty. Chapter 8, presented a method to reduce the shift introduced on the W mass and width. It was observed that applying a cone cut with a 0.4 rad opening angle on the clustered jets could reduce this uncertainty by 50% at all centre-of-mass energies. However this cone also has an effect on the statistical uncertainty, which could be degraded by a few percent at threshold, 10% at 240 GeV and 15% at 365 GeV. Considering that the cone treatment should provide an optimal balance between the statistical and systematic uncertainties, an optimisation of the cone opening angle could be considered. Other methods, such as a cut on low-momentum particles for example, could also be studied. Finally, the W mass could be used as a benchmark for the CLD (FCC-ee detector) optimisation using the FCC software that provides a more complete simulation of this detector. The hadronic channel shows higher statistical uncertainty than the semi-leptonic channel, therefore a first step towards an optimisation could be to optimise the calorimeter granularity in order to improve the jets reconstruction.

Bibliography

- [1] S. M. Bilenky and J. Hosek. Glashow-Weinberg-Salam Theory of Electroweak interactions and the Neutral Currents. *Phys. Rept.*, 90:73–157, 1982.
- [2] F. J. Hasert et al. Observation of Neutrino Like Interactions Without Muon Or Electron in the Gargamelle Neutrino Experiment. *Phys. Lett.*, B46:138–140, 1973. [5.15(1973)].
- [3] G. Arnison et al. Experimental Observation of Isolated Large Transverse Energy Electrons with Associated Missing Energy at $s^{**}(1/2) = 540$ GeV. *Phys. Lett.*, B122:103–116, 1983. [611(1983)].
- [4] M. Banner and others. Observation of single isolated electrons of high transverse momentum in events with missing transverse energy at the CERN $\bar{p}p$ collider. *Phys. Lett. B*, 122(CERN-EP-83-25):476–485. 15 p, Feb 1983.
- [5] S. Schael et al. Electroweak Measurements in Electron-Positron Collisions at W-Boson-Pair Energies at LEP. *Phys. Rept.*, 532:119–244, 2013.
- [6] T. Aaltonen et al. Precise measurement of the W -boson mass with the CDF II detector. *Phys. Rev. Lett.*, 108:151803, 2012.
- [7] V. M. Abazov et al. Measurement of the W Boson Mass with the D0 Detector. *Phys. Rev. Lett.*, 108:151804, 2012.
- [8] S. Schael et al. Measurement of the W boson mass and width in e^+e^- collisions at LEP. *Eur. Phys. J.*, C47:309–335, 2006.
- [9] M. Tanabashi. Review of particle physics. *Phys. Rev. D*, 98:030001, Aug 2018.
- [10] M. Baak and others. The global electroweak fit at NNLO and prospects for the LHC and ILC. *Eur. Phys. J.*, C74:3046, 2014.
- [11] M. Boonekamp, S. Dittmaier, and M. Mozer. Electroweak Standard Model Physics. In Thomas Schörner-Sadenius, editor, *The Large Hadron Collider: Harvest of Run 1*, pages 95–138. 2015.
- [12] F. I. Olness. Precision QCD for LHC Physics: The nCTEQ15 PDFs. In *Proceedings, Meeting of the APS Division of Particles and Fields (DPF 2015): Ann Arbor, Michigan, USA, 4-8 Aug 2015*, 2015.
- [13] E. Reya. *Phys Rep*, 69:195, 1981.
- [14] T. Plehn. Lectures on LHC Physics. *Lect. Notes Phys.*, 844:1–193, 2012.

- [15] Studies of theoretical uncertainties on the measurement of the mass of the W boson at the LHC. Technical Report ATL-PHYS-PUB-2014-015, CERN, Geneva, Oct 2014.
- [16] D. Evelyne. *Measurement of the $e^+e^- \rightarrow W^+W^-$ Cross Section and the W-boson Spin Density Matrix at LEP*. PhD thesis, Université de Genève, 2004.
- [17] W. Beenakker et al. WW cross-sections and distributions. In *CERN Workshop on LEP2 Physics (followed by 2nd meeting, 15-16 Jun 1995 and 3rd meeting 2-3 Nov 1995) Geneva, Switzerland, February 2-3, 1995*, pages 79–139, 1996.
- [18] X. Mo, G. Li, M-Q. Ruan, and X-C. Lou. Physics cross sections and event generation of ee-annihilations at the CEPC. *Chinese Physics C*, 40(3):033001, mar 2016.
- [19] M. Aaboud et al. Measurement of the W-boson mass in pp collisions at $\sqrt{s} = 7$ TeV with the ATLAS detector. *Eur. Phys. J.*, C78(2):110, 2018. [Erratum: *Eur. Phys. J.*C78,no.11,898(2018)].
- [20] T. Sakuma and T. McCauley. Detector and event visualization with SketchUp at the CMS experiment. *Journal of Physics: Conference Series*, 513(2):022032, jun 2014.
- [21] D Contardo, M Klute, J Mans, L Silvestris, and J Butler. Technical Proposal for the Phase-II Upgrade of the CMS Detector. Technical Report CERN-LHCC-2015-010. LHCC-P-008. CMS-TDR-15-02, CMS collaboration, Geneva, Jun 2015.
- [22] D. Tommasini. 16 T magnet R&D overview. FCC week 2019, 2019.
- [23] N. Alipour Tehrani et al. FCC-ee: Your Questions Answered. In A. Blondel and P. Janot, editors, *CERN Council Open Symposium on the Update of European Strategy for Particle Physics (EPPSU) Granada, Spain, May 13-16, 2019*, 2019.
- [24] M. Benedikt and others. Future Circular Collider. Technical Report CERN-ACC-2018-0057, CERN, Geneva, Dec 2018. Published in *Eur. Phys. J.* ST.
- [25] CMS Collaboration. W-like measurement of the Z boson mass using dimuon events collected in pp collisions at $\sqrt{s} = 7$ TeV. 2016.
- [26] S. Weinberg. Conceptual foundations of the unified theory of weak and electromagnetic interactions. *Rev. Mod. Phys.*, 52:515–523, Jul 1980.
- [27] A. Salam. Gauge unification of fundamental forces. *Rev. Mod. Phys.*, 52:525–538, Jul 1980.
- [28] S. L. Glashow. Towards a unified theory: Threads in a tapestry. *Rev. Mod. Phys.*, 52:539–543, Jul 1980.
- [29] S. L. Wu and G. Zobernig. A method of three-jet analysis in ee annihilation. *Zeitschrift für Physik C Particles and Fields*, 2(2):107–110, Jun 1979.
- [30] S. Abachi et al. Observation of the top quark. *Phys. Rev. Lett.*, 74:2632–2637, 1995.
- [31] F. Reines, C. L. Cowan, F. B. Harrison, A. D. McGuire, and H. W. Kruse. Detection of the free antineutrino. *Phys. Rev. Lett.*, 117:159–173, Jan 1960.

- [32] G. Danby, J-M. Gaillard, K. Goulianos, L. M. Lederman, N. Mistry, M. Schwartz, and J. Steinberger. Observation of high-energy neutrino reactions and the existence of two kinds of neutrinos. *Phys. Rev. Lett.*, 9:36–44, Jul 1962.
- [33] S. Fukuda and others. Tau neutrinos favored over sterile neutrinos in atmospheric muon neutrino oscillations. *Phys. Rev. Lett.*, 85:3999–4003, Nov 2000.
- [34] G. Aad et al. Combined search for the Standard Model Higgs boson in pp collisions at $\sqrt{s} = 7$ TeV with the ATLAS detector. *Phys. Rev.*, D86:032003, 2012.
- [35] F. Halzen. Quarks and leptons : an introductory course in modern particle physics. 1984.
- [36] M. E. Peskin and D. V. Schroeder. *An introduction to quantum field theory*. Westview, Boulder, CO, 1995. Includes exercises.
- [37] S. Dittmaier and M. Krämer. Electroweak radiative corrections to W boson production at hadron colliders. *Phys. Rev.*, D65:073007, 2002.
- [38] S. Catani, G. Ferrera, and M. Grazzini. W Boson Production at Hadron Colliders: The Lepton Charge Asymmetry in NNLO QCD. *JHEP*, 05:006, 2010.
- [39] A. Denner and T. Sack. The W boson width. *Z. Phys.*, C46:653–663, 1990.
- [40] D. Yu. Bardin, S. Riemann, and T. Riemann. Electroweak One Loop Corrections to the Decay of the Charged Vector Boson. *Z. Phys.*, C32:121–125, 1986.
- [41] F. Jegerlehner. Vector Boson Parameters: Scheme Dependence and Theoretical Uncertainties. *Z. Phys.*, C32:425, 1986. [Erratum: *Z. Phys.*C38,519(1988)].
- [42] D. Albert, W. J. Marciano, D. Wyler, and Z. Parsa. Decays of Intermediate Vector Bosons, Radiative Corrections and QCD Jets. *Nucl. Phys.*, B166:460–492, 1980.
- [43] T. Muta, R. Najima, and S. Wakaizumi. Effects of the W-boson width in $e^+e^- \rightarrow W^+W^-$ reactions. *Modern Physics Letters A*, 01(03):203–210, 1986.
- [44] W. Beenakker and A. Denner. Standard model predictions for W pair production in electron - positron collisions. *Int. J. Mod. Phys.*, A9:4837–4920, 1994.
- [45] D. Bardin, M. Bilenky, A. Olchevski, and T. Riemann. Off-shell W-pair production in e^+e^- -annihilation. initial state radiation. *Physics Letters B*, 308(3):403 – 410, 1993.
- [46] F.A. Berends, R. Kleiss, and S. Jadach. Radiative corrections to muon pair and quark pair production in electron-positron collisions in the z_0 region. *Nuclear Physics B*, 202(1):63 – 88, 1982.
- [47] D. Bardin, W. Beenakker, and A. Denner. The coulomb singularity in off-shell W-pair production. *Physics Letters B*, 317(1):213 – 217, 1993.
- [48] St. Dittmaier, A. Huss, and C. Schwinn. Mixed QCD-electroweak $O(\alpha_s\alpha)$ corrections to Drell-Yan processes in the resonance region: pole approximation and non-factorizable corrections. *Nucl. Phys.*, B885:318–372, 2014.

- [49] T. Sjöstrand. PYTHIA 8 Status Report. (arXiv:0809.0303. LU TP 08-17. MCNET-08-09):5 p, Sep 2008.
- [50] S. Jadach and M. Skrzypek. QED challenges at FCC-ee precision measurements. *Eur. Phys. J.*, C79(9):756, 2019.
- [51] P. Azzurri, M. Béguin, and J. Gu. Di-boson physics. Writting in progress (2020).
- [52] S. Actis, M. Beneke, P. Falgari, and C. Schwinn. Dominant NNLO corrections to four-fermion production near the W -pair production threshold. *Nucl. Phys.*, B807:1–32, 2009.
- [53] M. Awramik, M. Czakon, A. Freitas, and G. Weiglein. Precise prediction for the W boson mass in the standard model. *Phys. Rev.*, D69:053006, 2004.
- [54] A. Blondel, A. Freitas, J. Gluza, T. Riemann, S. Heinemeyer, S. Jadach, and P. Janot. Theory Requirements and Possibilities for the FCC-ee and other Future High Energy and Precision Frontier Lepton Colliders. 2019.
- [55] G. Gustafson and J. Häkkinen. Colour interference and confinement effects in W -pair production. *Zeitschrift für Physik C Particles and Fields*, 64(4):659–664, Dec 1994.
- [56] J. R. Christiansen. Colour Reconnection - Models and Tests. *PoS*, EPS-HEP2015:443, 2015.
- [57] J. R. Christiansen and P. Z. Skands. String Formation Beyond Leading Colour. *JHEP*, 08:003, 2015.
- [58] L. Lönnblad and T. Sjöstrand. Bose-Einstein effects and W mass determinations. *Physics Letters B*, 351(1):293 – 301, 1995.
- [59] R. Barate and others. Bose-Einstein correlations in W -pair decays. *Physics Letters B*, 478(1):50 – 64, 2000.
- [60] S. Catani, Y. L. Dokshitzer, M. Olsson, G. Turnock, and B. R. Webber. New clustering algorithm for multi - jet cross-sections in e^+e^- annihilation. *Phys. Lett.*, B269:432–438, 1991.
- [61] J. D’Hondt, S. Lowette, O. L. Buchmuller, S. Cucciarelli, F. P. Schilling, M. Spiropulu, S. Paktinat Mehdiabadi, D. Benedetti, and L. Pape. Fitting of event topologies with external constraints in CMS. 2006.
- [62] M. Béguin. Reconstruction of the W mass and width at and above WW threshold at FCC-ee. <https://indico.cern.ch/event/577856/contributions/3420355/>, 2019.
- [63] L. Evans and P. Bryant. LHC machine. *Journal of Instrumentation*, 3(08):S08001–S08001, aug 2008.
- [64] Apollinari G., Béjar Alonso I., Brüning O., Fessia P., Lamont M., Rossi L., and Taviani L. *High-Luminosity Large Hadron Collider (HL-LHC): Technical Design Report V. 0.1*. CERN Yellow Reports: Monographs. CERN, Geneva, 2017.
- [65] CMS Collaboration. The Phase-2 Upgrade of the CMS Endcap Calorimeter. Technical Report CERN-LHCC-2017-023. CMS-TDR-019, CERN, Geneva, Nov 2017. Technical Design Report of the endcap calorimeter for the Phase-2 upgrade of the CMS experiment, in view of the HL-LHC run.

- [66] M. Benedikt and all. Future Circular Collider. Technical Report CERN-ACC-2018-0057, CERN, Geneva, Dec 2018. Submitted for publication to *Eur. Phys. J. ST*.
- [67] A. Abada and others. FCC Physics Opportunities. *Eur. Phys. J.*, C79(6):474, 2019.
- [68] M. Benedikt and others. Future Circular Collider. Technical Report CERN-ACC-2018-0058, CERN, Geneva, Dec 2018. Published in *Eur. Phys. J. ST*.
- [69] F. Zimmermann and others. Future Circular Collider. Technical Report CERN-ACC-2018-0059, CERN, Geneva, Dec 2018. Published in *Eur. Phys. J. ST*.
- [70] W. Herr and B. Muratori. Concept of luminosity. 2006.
- [71] The European Strategy for Particle Physics Update 2013. La stratégie européenne pour la physique des particules Mise à jour 2013. 16th Session of European Strategy Council. May 2013.
- [72] CMS Collaboration. CMS Physics: Technical Design Report Volume 2: Physics Performance. *J. Phys. G*, 34(CERN-LHCC-2006-021. CMS-TDR-8-2):995–1579. 669 p, 2007. revised version submitted on 2006-09-22 17:44:47.
- [73] CMS Collaboration. The CMS experiment at the CERN LHC. *Journal of Instrumentation*, 3(08):S08004–S08004, aug 2008.
- [74] V. Khachatryan et al. CMS Tracking Performance Results from early LHC Operation. *Eur. Phys. J.*, C70:1165–1192, 2010.
- [75] CMS Collaboration. *The CMS electromagnetic calorimeter project: Technical Design Report*. Technical Design Report CMS. CERN, Geneva, 1997.
- [76] Performance of CMS hadron calorimeter timing and synchronization using test beam, cosmic ray, and LHC beam data. *JINST*, 5(arXiv:0911.4877. CMS-CFT-09-018):T03013. 31 p, Nov 2009.
- [77] CMS collaboration. Performance of CMS muon reconstruction in pp collision events at $\sqrt{s} = 7\text{tev}$. *Journal of Instrumentation*, 7(10):P10002–P10002, oct 2012.
- [78] S Chatrchyan et al. Precise Mapping of the Magnetic Field in the CMS Barrel Yoke using Cosmic Rays. *JINST*, 5:T03021, 2010.
- [79] V. Khachatryan et al. The CMS trigger system. *JINST*, 12(01):P01020, 2017.
- [80] A. Kornmayer. The CMS Pixel Luminosity Telescope. Technical Report CMS-CR-2015-121, CERN, Geneva, Jun 2015.
- [81] P-J. Lujan. Performance of the Pixel Luminosity Telescope for Luminosity Measurement at CMS during Run2. Technical Report CMS-CR-2017-347, CERN, Geneva, Oct 2017.
- [82] CMS Collaboration. The Phase-2 Upgrade of the CMS Tracker. Technical Report CERN-LHCC-2017-009. CMS-TDR-014, CERN, Geneva, Jun 2017.

- [83] CMS Collaboration. The Phase-2 Upgrade of the CMS Barrel Calorimeters. Technical Report CERN-LHCC-2017-011. CMS-TDR-015, CERN, Geneva, Sep 2017. This is the final version, approved by the LHCC.
- [84] CMS Collaboration. The Phase-2 Upgrade of the CMS Muon Detectors. Technical Report CERN-LHCC-2017-012. CMS-TDR-016, CERN, Geneva, Sep 2017. This is the final version, approved by the LHCC.
- [85] A. Martelli. The CMS HGCAL detector for HL-LHC upgrade. Technical Report arXiv:1708.08234, Aug 2017. proceedings of the LHCP2017 conference, 6 pages, 8 figures.
- [86] C. Adloff et al. Construction and Commissioning of the CALICE Analog Hadron Calorimeter Prototype. *JINST*, 5:P05004, 2010.
- [87] F. Zimmermann. LHC/FCC-based muon colliders. *Journal of Physics: Conference Series*, 1067:022017, sep 2018.
- [88] M. Benedikt. Overview and status of the future circular collider study. FCC week 2019.
- [89] CEPC Conceptual Design Report: Volume 1 - Accelerator. 2018.
- [90] C. Adolphsen, M. Barone, B. Barish, K. Buesser, P. Burrows, and others. The International Linear Collider Technical Design Report - Volume 3.II: Accelerator Baseline Design. 2013.
- [91] A. Robson, P. N. Burrows, N. Catalan Lasheras, L. Linssen, M. Petric, D. Schulte, E. Sicking, S. Stapnes, and W. Wuensch. The Compact Linear e^+e^- Collider (CLIC): Accelerator and Detector. 2018.
- [92] N. Alipour Tehrani and others. CLICdet: The post-CDR CLIC detector model. Mar 2017.
- [93] O. Viazlo. Performance of the CLD detector for FCC-ee. FCC week 2019, 2019.
- [94] Author list under construction. CLD - a detector concept for FCC-ee. Draft.
- [95] CMS Collaboration. CMS simulation software - CMSSW.
- [96] S. Banerjee. CMS Simulation Software. Technical Report CMS-CR-2012-146, CERN, Geneva, Jun 2012.
- [97] S. Agostinelli et al. GEANT4: A Simulation toolkit. *Nucl. Instrum. Meth.*, A506:250–303, 2003.
- [98] A. M. Sirunyan et al. Particle-flow reconstruction and global event description with the CMS detector. *JINST*, 12(10):P10003, 2017.
- [99] S. Baffioni et al. Electron reconstruction in CMS. Technical Report CMS-NOTE-2006-040, CERN, Geneva, Feb 2006.
- [100] A. Mertens. New features in Delphes 3. *J. Phys. Conf. Ser.*, 608(1):012045, 2015.
- [101] S. Lablack. Mesure précise de la masse du boson W au futur collisionneur circulaire e^+e^- à haute énergie (FCC-ee). Master's thesis, Master 2 de Physique Subatomique - Université Claude Bernard Lyon 1, 2019.

- [102] M. Béguin. Kinematic reconstruction of the W mass and width at FCC-ee. <https://indico.ihep.ac.cn/event/9960/session/15/contribution/139/material/slides/0.pdf>, 2019.
- [103] L. Linssen, A. Miyamoto, M. Stanitzki, and H. Weerts. *Physics and Detectors at CLIC: CLIC Conceptual Design Report*. CERN Yellow Reports: Monographs. CERN, Geneva, 2012. Comments: 257 p, published as CERN Yellow Report CERN-2012-003.
- [104] C. Bernet. papas, A Fast Simulation of the Particle Flow.
- [105] Shikma Bressler, Thomas Flacke, Yevgeny Kats, Seung J. Lee, and Gilad Perez. Hadronic calorimeter shower size: Challenges and opportunities for jet substructure in the superboosted regime. *Physics Letters B*, 756:137 – 141, 2016.
- [106] M. Cacciari, G. P. Salam, and G. Soyez. FastJet user manual. *Eur. Phys. J. C*, 72(arXiv:1111.6097. CERN-PH-TH-2011-297):1896. 69 p, Nov 2011. Comments: 69 pages. FastJet 3 is available from <http://fastjet.fr/>.
- [107] M. Cacciari and G. P. Salam. Dispelling the N^3 myth for the k_t jet-finder. *Phys. Lett. B* **641**, 57, 2006.
- [108] W. Bartel, L. Becker, and others. *Z. Phys. C - Particles and Fields*, 33:23, 1986. <https://doi.org/10.1007/BF01410449>.
- [109] G. Grindhammer and S. Peters. The Parameterized simulation of electromagnetic showers in homogeneous and sampling calorimeters. In *International Conference on Monte Carlo Simulation in High-Energy and Nuclear Physics - MC 93 Tallahassee, Florida, February 22-26, 1993*, 1993.
- [110] M. and Chadeeva. Hadron shower decomposition in a highly granular calorimeter. *Journal of Physics: Conference Series*, 587:012036, feb 2015.
- [111] M Chadeeva. Parametrisation of hadron shower profiles in the CALICE Sc-Fe AHCAL. Apr 2014.
- [112] H. Samet. The quadtree and related hierarchical data structures. *ACM Comput. Surv.*, 16(2):187–260, jun 1984.
- [113] R. A. Finkel and J. L. Bentley. Quad trees a data structure for retrieval on composite keys. *Acta Inf.*, 4(1):1–9, March 1974.
- [114] E. Locci and A. Rosowsky. W mass at 8 TeV with a vintage analysis. *CMS Analysis Note*, 2019. CMS AN-2019/155.
- [115] C. F. Baum. Quantile regression. 2013.
- [116] X. Chen, W. Liu, X. Mao, and Z. Yang. Distributed high-dimensional regression under a quantile loss function, 2019.
- [117] R. Koenker and K. F. Hallock. Quantile regression. *Journal of Economic Perspectives*, 15(4):143–156, December 2001.

- [118] I. Sakshi, A. K. Goswami, S.P. Mishra, and P. Asopa. Conceptual understanding of convolutional neural network- a deep learning approach. *Procedia Computer Science*, 132:679 – 688, 2018. International Conference on Computational Intelligence and Data Science.
- [119] A. L. Maas. Rectifier nonlinearities improve neural network acoustic models. 2013.
- [120] N. Foppiani. Definition and calibration of the hadronic recoil in view of the measurement of the W boson mass with the CMS experiment, Aug 2017. Presented 20 Sep 2017.
- [121] The CMS W mass group. Measurement of the recoil of the W boson in pp collisions at $\sqrt{s} = 13$ tev. Analysis Note 2018/244, 2018.
- [122] A deep neural network for simultaneous estimation of b quark energy and resolution. Technical Report CMS-PAS-HIG-18-027, CERN, Geneva, 2019.
- [123] F. Chollet et al. Keras. <https://github.com/fchollet/keras>, 2015.
- [124] M. Abadi and others. TensorFlow: Large-scale machine learning on heterogeneous systems, 2015. Software available from tensorflow.org.
- [125] D. Bertolini, P. Harris, M. Low, and N. Tran. Pileup per particle identification. *Journal of High Energy Physics*, 2014(10), Oct 2014.
- [126] M. Béguin. Reconstruction of the W mass and width at and above WW threshold at FCC-ee. In *Proceedings of Science*, 2020. Under revision.
- [127] M Béguin. W mass measurement at fcc-ee. Writting in progress (2020), 2019.
- [128] In D. Dimitri and P Bertsekas, editors, *Constrained Optimization and Lagrange Multiplier Methods*. Academic Press, 1982.
- [129] T. Skwarnicki. *A study of the radiative CASCADE transitions between the Upsilon-Prime and Upsilon resonances*. PhD thesis, Cracow, INP, 1986.
- [130] L Demortier and L Lyons. Everything you always wanted to know about pulls. Technical Report CDF/ANAL/PUBLIC/5776, CDF, February 2002.
- [131] V. Blobel. Constrained least squares methods with correlated data and systematic uncertainties. Desy, University of Hamburg, 2010.
- [132] H. Ruiz Pérez and dir. (Institut de Física d’Altes Energies) Teubert Salabert, F. *Measurement of the W mass from the WW \rightarrow qqqq channel with the ALEPH detector*. PhD thesis, Universitat Autònoma de Barcelona, Bellaterra, 2003. Consultable des del TDX.
- [133] F. Gaede. Marlin and LCCD: Software tools for the ILC. *Nucl. Instrum. Meth.*, A559:177–180, 2006.
- [134] M. Beckmann, B. List, and J. List. Treatment of Photon Radiation in Kinematic Fits at Future e+ e- Colliders. *Nucl. Instrum. Meth.*, A624:184–191, 2010.
- [135] J. List, M. Beckmann, and B. List. Kinematic Fitting in the Presence of ISR at the ILC. In *Linear colliders. Proceedings, International Linear Collider Workshop, LCWS08, and International Linear Collider Meeting, ILC08, Chicago, USA, November 16-20, 2008*, 2009.

-
- [136] V. P. Druzhinin, L. A. Kardapoltsev, and V. A. Tayursky. The event generator for the two-photon process $e^+e^- \rightarrow e^+e^-R(J^{PC} = 0^{-+})$ in the single-tag mode. 2010.
- [137] S. Ceci, M. Hadzimehmedovic, H. Osmanović, A. Percan, and B. Zauner. Fundamental properties of resonances. *Sci. Rep.*, 7:45246, 2017.
- [138] L. Arnaudon and others. Accurate determination of the lep beam energy by resonant depolarization. *Zeitschrift für Physik C Particles and Fields*, 66(1):45–62, Mar 1995.
- [139] A. Blondel et al. Polarization and Centre-of-mass Energy Calibration at FCC-ee. 2019.
- [140] M. Koratzinos. Overview and status of CM energy uncertainties.
- [141] G. Altarelli, T. Sjostrand, and F. Zwirner, editors. *Physics at LEP2: Vol. 1*, 1996.
- [142] T. Sjostrand and V. A. Khoze. On Color rearrangement in hadronic W^+W^- events. *Z. Phys.*, C62:281–310, 1994.
- [143] T. Sjöstrand and V. A. Khoze. Does the W mass reconstruction survive QCD effects? *Phys. Rev. Lett.*, 72:28–31, Jan 1994.
- [144] S. Argyropoulos and T. Sjöstrand. Effects of color reconnection on $t\bar{t}$ final states at the LHC. *JHEP*, 11:043, 2014.

Appendix A

Complements to the HGCal fast simulation

A.1 HGCal layers implementation in the fast simulation

This appendix shows the structure of the silicon and scintillator layers of the HGCal as implemented in the fast simulation software (geometry design 2016). Details are given in Section 5.1. The shower development and the interaction of generated particles through this structure are also presented in Chapter 5.

A.2 Fit of the hadronic radial shower profile of 40 GeV pions in the HGCal

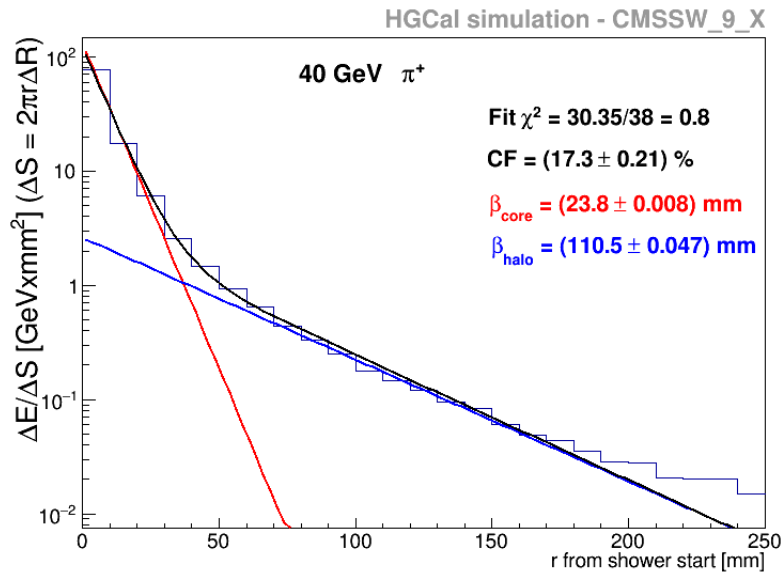


Figure A.1 – Fit of the radial profile of a shower initiated by 40 GeV pions in the HGCal. Fit of the core (red) and halo (blue) components for the hadronic shower parametrisation. The fitted values and the CF (see text for details) are indicated on the figure. This distribution was obtained with the release 9 of CMSSW.

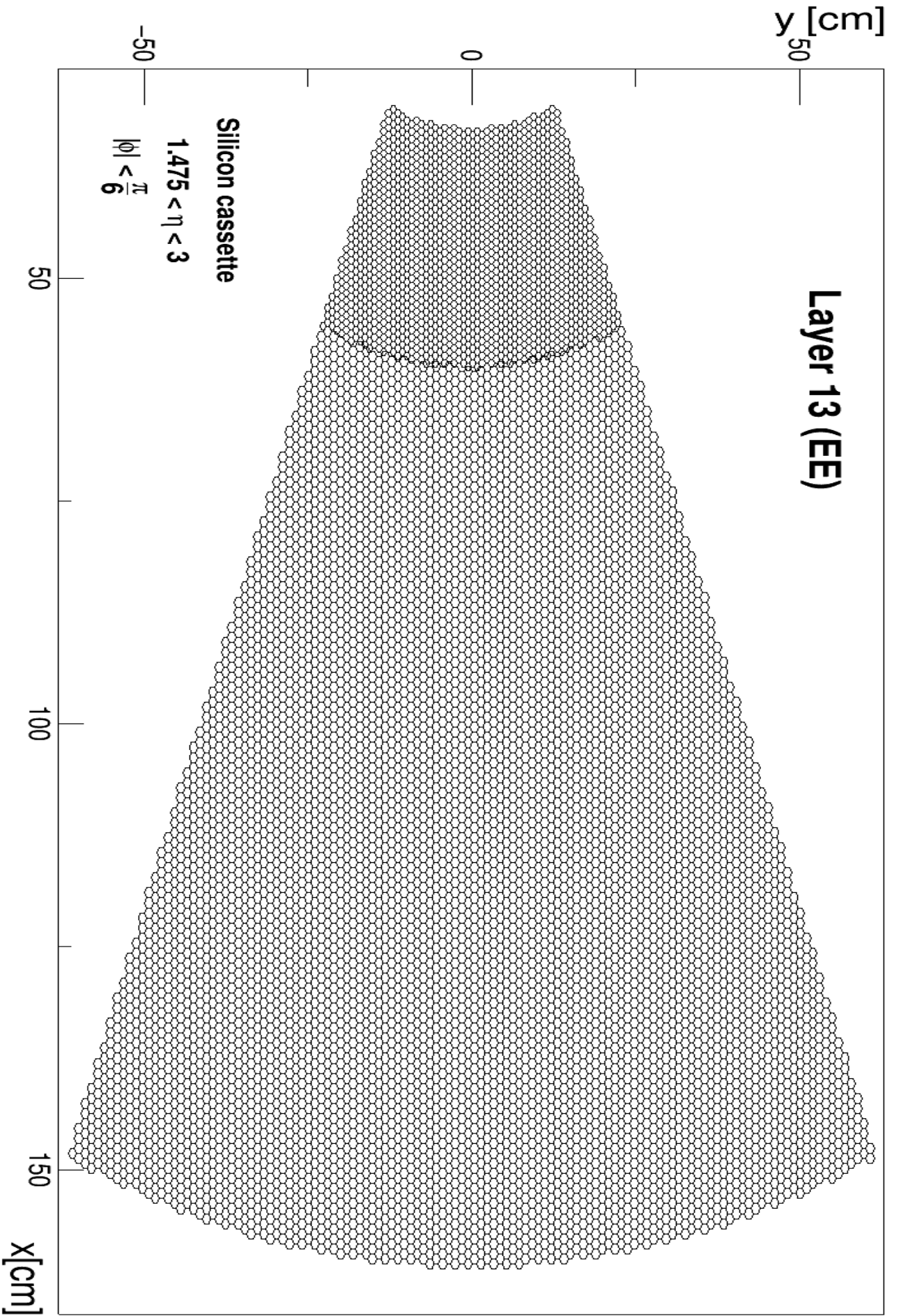


Figure A.2 – Silicon layer as implemented in the HGCal fast simulation.

The small (0.53 cm^2) and large (1.18 cm^2) hexagonal cells are visible.

The limit between the two regions (around 60 cm) shows the holes and cell overlaps.

This geometry corresponds to the 2016 design, frozen for the TDR studies, at the period of the FastSim implementation.

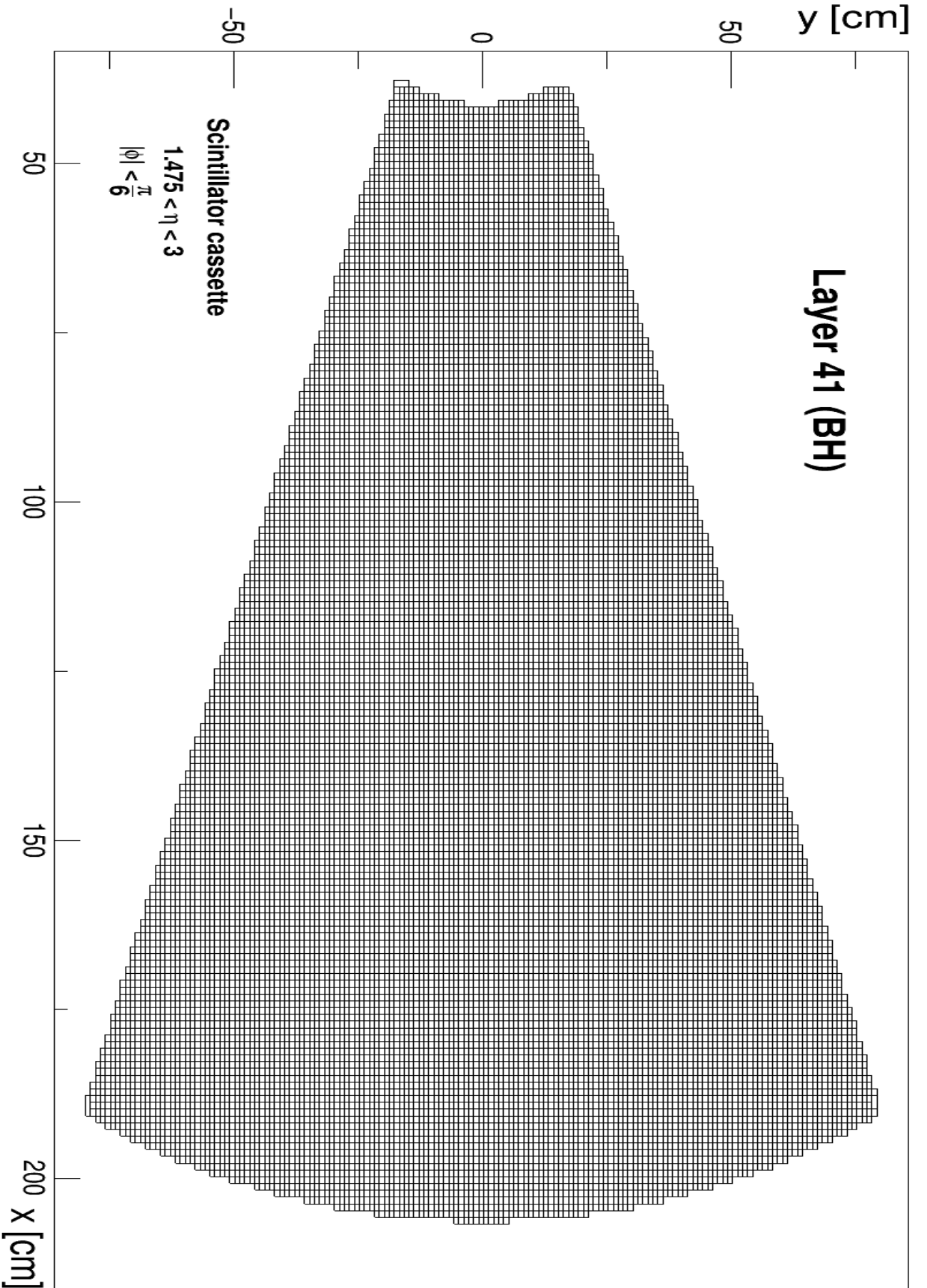


Figure A.3 – Scintillator layer as implemented in the HGCal fast simulation.

This layer has only one type of cells, square cells with dimension $3\text{ cm} \times 3\text{ cm} \times 3\text{ mm}$.

This geometry corresponds to the 2016 design, frozen for the TDR studies, at the period of the FastSim implementation.

Appendix B

Complements to the W mass measurement at FCC-ee

B.1 Relation between the FOM and the W mass statistical uncertainty

N_{1i} = bin content of the i -th bin for the distribution $M_W + 1 \text{ GeV}/c^2$
 N_{2i} = bin content of the i -th bin for the distribution $M_W - 1 \text{ GeV}/c^2$

$$\begin{aligned} sNi &= N_{1i} + N_{2i}, \\ dNi &= N_{1i} - N_{2i}, \end{aligned} \tag{B.1}$$

are the sum and the difference of the content in the bin i -th.

The expected number of events of i -th bin is then:

$$\frac{sNi}{2} \tag{B.2}$$

end the expected statistical uncertainty of i -th bin is:

$$eNi = \sqrt{\frac{sNi}{2}} \tag{B.3}$$

The expected extrapolated statistical uncertainty on M_W from the event contents of i -th bin is:

$$\Delta M_{wi} = \frac{DM}{DN} \Delta N \tag{B.4}$$

where $DM = 2 \text{ GeV}$ is this study (M_W simulated at $\pm 1 \text{ GeV}$). DN is the expected variation due to the variation DM and is equal to dNi . ΔN is the extrapolated statistical uncertainty of the event content and $\Delta N = eNi$.

From these definitions, Equation B.4 becomes:

$$\Delta M_{wi} = \frac{DM \sqrt{\frac{sNi}{2}}}{dNi} \tag{B.5}$$

The uncertainty on M_W is next given combining all bins. As the errors are statistical (independent), the statistical uncertainty on M_W is:

$$\begin{aligned}
\frac{1}{\Delta M^2} &= \sum^{bin} \left(\frac{1}{\Delta M_{wi}^2} \right) \\
&= \sum^{bin} \left(\frac{1}{\left(\frac{DM \sqrt{\frac{sNi}{2}}}{dNi} \right)^2} \right) \\
&= \sum^{bin} \left(\frac{2 \times dNi^2}{DM^2 \times sNi} \right) \\
&= \frac{2}{DM^2} \sum^{bin} \frac{dNi^2}{sNi}
\end{aligned} \tag{B.6}$$

$$\Delta M^2 = \frac{DM^2}{2} \frac{1}{\sum^{bin} \frac{dNi^2}{sNi}} \tag{B.7}$$

$$\Delta M = \frac{DM}{\sqrt{2}} \frac{1}{\sqrt{\sum^{bin} \frac{dNi^2}{sNi}}} = \frac{DM}{\sqrt{2 \sum^{bin} \frac{dNi^2}{sNi}}} \tag{B.8}$$

If the normalised FOM is defined as:

$$FOM = \frac{2 \sum sNi}{\sum \frac{dNi^2}{sNi}}$$

Hence:

$$\begin{aligned}
\sum \frac{dNi^2}{sNi} &= 2 \frac{\sum sNi}{FOM} \\
\sqrt{2 \sum \frac{dNi^2}{sNi}} &= 2 \sqrt{\frac{\sum sNi}{FOM}}
\end{aligned}$$

Then ΔM is linked to the FOM with:

$$\Delta M = \frac{DM}{2} \frac{\sqrt{FOM}}{\sqrt{N_{tot}}}$$

B.2 Kinematic fit procedure

The full kinematic fit procedure as described in Chapter 7.1.2 is summarised on Figure B.1.

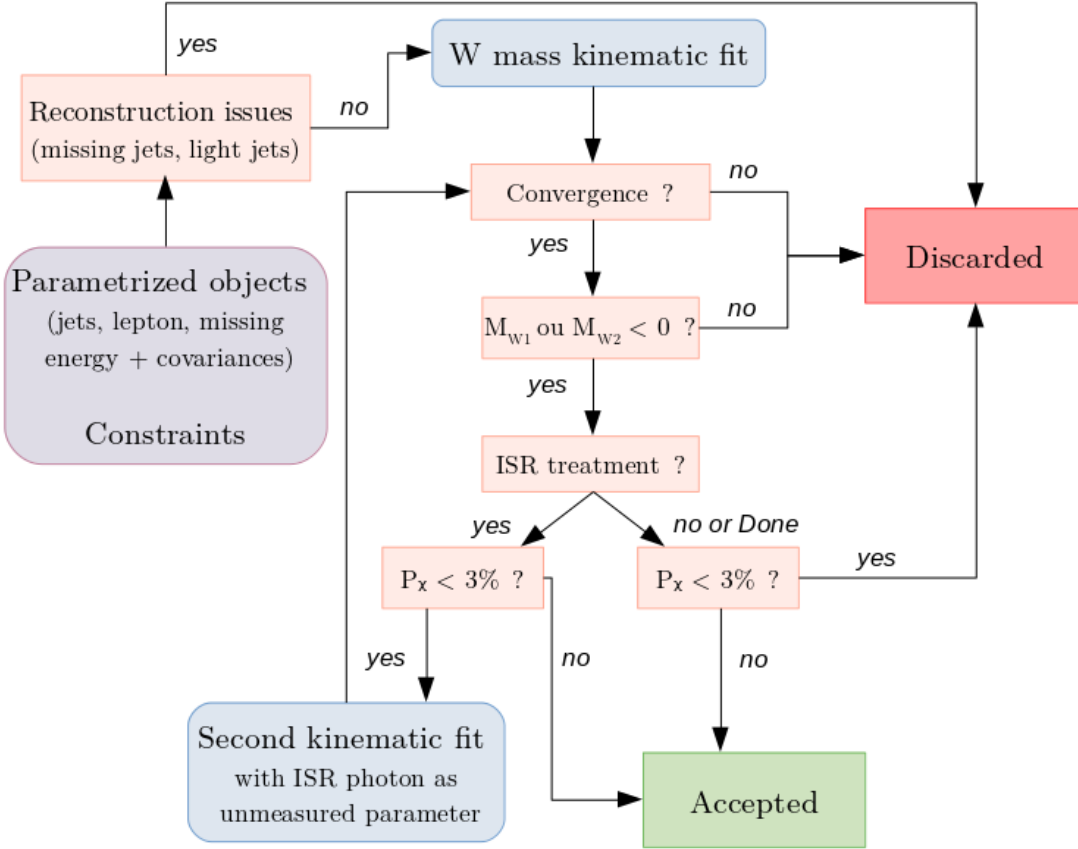


Figure B.1 – Full flowchart of the kinematic fit procedure as used in the current study of W mass reconstruction at FCC-ee.

Steps followed by each hadronic or semi-leptonic event during the kinematic fit procedure.

The objects representing particles and their constraints are first introduced. The event is discarded if reconstruction issues are detected. If not, the partial derivatives and other quantities are computed before to be passed on to a fitting object. The iterative procedure is processed:

1. The current values of the constraints are passed on to the fitting object
2. The derivative of the constraints and particles are computed and transferred to the fitter
3. The derivatives are corrected
4. The convergence criteria are checked. If they are not fulfilled, the procedure is resumed to step 1
5. At the end of the process, i.e. convergence or convergence criteria reached, the procedure is stopped. In case of convergence, the fit results correspond to the last iteration values, else the event is discarded.

If the ISR treatment is activated and the convergent event has a fit probability smaller than 3%, a second fit is processed following the steps presented above and including the photon parametrization in the list of the input objects. At the end of the second fit, only events with a fit probability larger than 3% are kept.

B.3 Off-diagonal terms covariance matrix

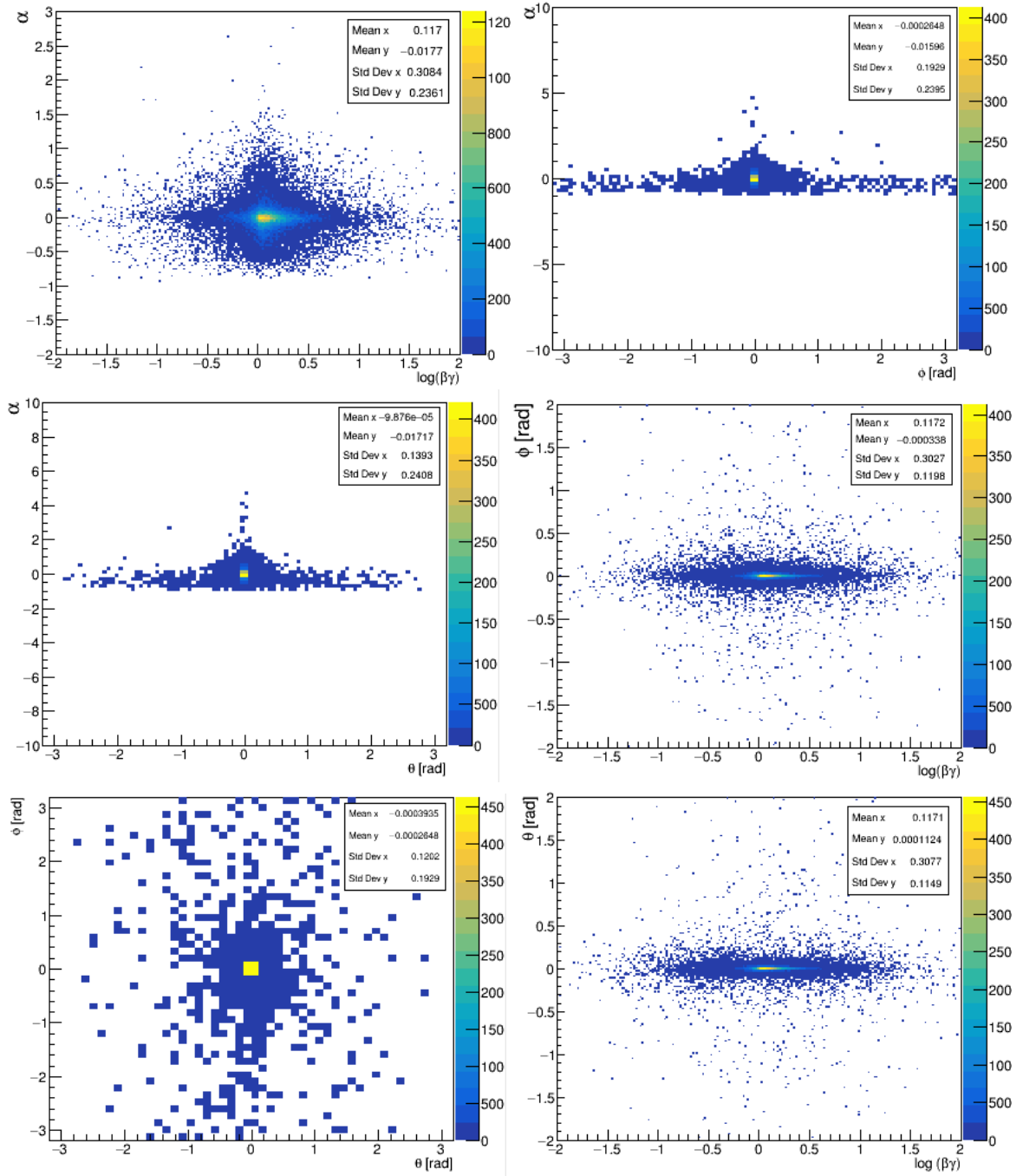


Figure B.2 – Off-diagonal terms of the covariance matrix of the kinematic fit ($\sqrt{s} = 162.6$ GeV)

B.4 Comparison before/after cut in probability

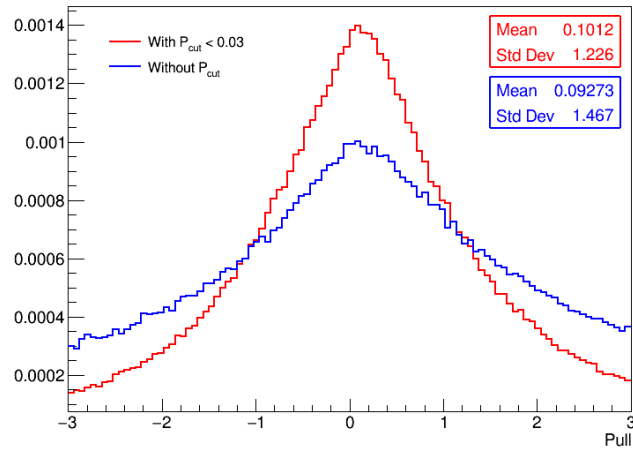


Figure B.3 – Comparison pull before and after cut

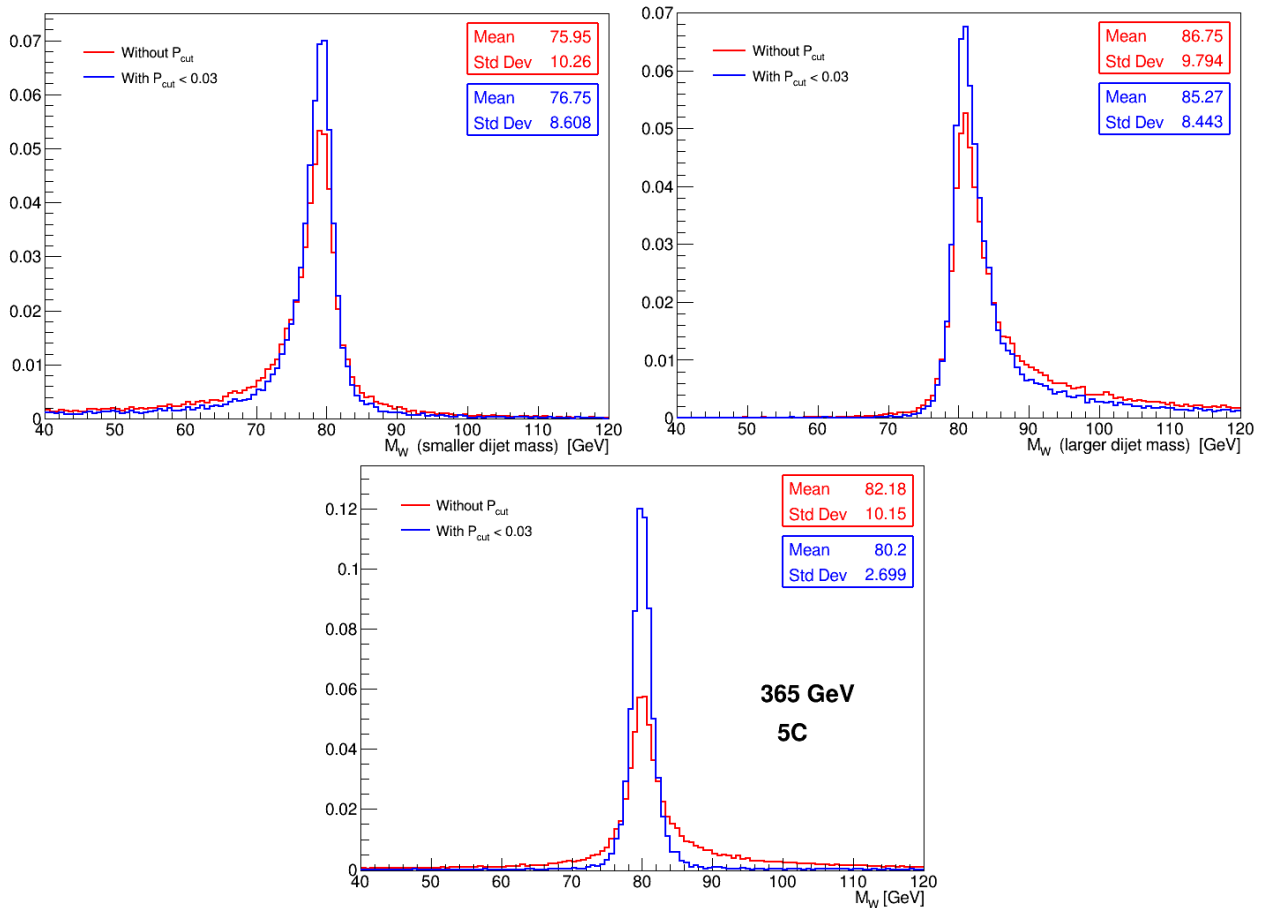


Figure B.4 – Comparison W mass distributions reconstructed with the kinematic fit 4C (top figures) and 5C (bottom figure), adding or not the cut in fit probability ($P < 0.03$) at $\sqrt{s} = 365$ GeV

Appendix C

Résumé en français

Les bosons W et Z découverts en 1983 suite à la transformation du SPS en collisionneur protons-antiprotons, confirmèrent la théorie électrofaible prédite par Glasgow, Wienberg et Salam. Depuis, plusieurs accélérateurs se sont succédés, permettant de mesurer les caractéristiques de ces bosons en collisions e^+e^- (LEP), $p\bar{p}$ (Tevatron) et pp (LHC).

La mesure précise de la masse du boson W est un paramètre fondamental pour tester la cohérence du Modèle Standard et mettre indirectement en évidence une nouvelle physique. Jusqu'à présent aucune déviation des mesures expérimentales par rapport aux prédictions du fit global du secteur électrofaible n'a été observée dans la limite de leurs incertitudes. Cependant, la mesure de la masse du boson W étant largement dominée par les incertitudes expérimentales et théoriques, les efforts se concentrent donc désormais sur leur réduction à un niveau inférieur au $1 \text{ MeV}/c^2$.

La mesure précise de la masse du boson W a été étudiée dans le cadre de deux futures expériences au CERN : l'expérience CMS avec un nouveau calorimètre à haute granularité (HGCAL) pour la phase HL-LHC, et un futur détecteur pour le projet FCC-ee.

Ce résumé présente brièvement l'étude qui a été menée. Il se focalise majoritairement sur les résultats obtenus, les détails sont donnés dans le texte. Les méthodes de mesure de la masse du boson W dans le cadre de différents types de collisions sont d'abord énoncées puis le contexte expérimental de l'étude est présenté. Les études effectuées pour mesurer la masse du boson W avec précision à CMS puis à FCC-ee sont ensuite résumées.

Le boson W

Collision hadronique

En collision hadronique, le boson W est produit via l'annihilation d'un quark et d'un antiquark issus des hadrons entrant en collision. Il se désintègre ensuite rapidement en une paire fermion-antifermion. A cause du bruit QCD généré par les autres produits de l'interaction (recoil), sa décomposition en paire de quarks est difficilement discernable ; en collision hadronique, un boson W est identifié par son canal leptonique de désintégration uniquement ($l\nu$ avec l étant un électron ou un muon). Celui-ci est caractérisé par un lepton de haute énergie et une énergie manquante importante, emportée par le neutrino indétecté. La plupart des résidus hadroniques de la collision échappant à la détection le long de l'axe des faisceaux, l'impulsion longitudinale du neutrino (énergie manquante longitudinale) ne peut pas être mesurée et seules les composantes transverses de l'événement sont utilisables.

La masse du boson W peut être reconstruite à partir des distributions des moments transverses du lepton, p_T^ℓ et du neutrino, p_T^ν , montrant un pic jacobien à $M_W/2$. Ces deux variables sont cependant sensibles au moment transverse du boson W , p_T^W , qui introduit une incertitude systématique sur la mesure de la masse. La masse transverse est un meilleur estimateur de M_W car sa dépendance à p_T^W peut être régulée en la calculant à partir du recul :

$$\frac{M_T^2}{2} = p_T^\ell(p_T^\ell + |\vec{p}_T^\ell + \vec{h}|) + \vec{p}_T^\ell \cdot \vec{h}. \quad (\text{C.1})$$

La masse et la largeur du boson sont ensuite extraites à partir de la distribution de la masse transverse, présentant un maximum à $M_T = M_W$, par un ajustement de distributions générées pour plusieurs valeurs de la masse et de la largeur (templates) avec un simulateur Monte-Carlo (MC).

Collision leptonique

En collision leptonique, le boson W est produit par paires, à partir de $\sqrt{s} = 2M_W$, par un processus d'annihilation électron-positron. Les bosons se désintègrent ensuite rapidement donnant lieu à un état final à quatre fermions : hadronique ($q\bar{q}'q'\bar{q}$), leptonique ($l\nu l'\nu'$) et semi-leptonique ($qq'l\nu$). Le processus $e^+e^- \rightarrow W^+W^- \rightarrow 4f$ peut également être accompagné d'émission de photons dans les états initiaux (ISR), intermédiaires (interaction de coulomb) et finaux (FSR). Dans l'état final hadronique des effets de reconnections peuvent se produire : reconnection de couleur (CR) et corrélation de Bose-Einstein (BEC).

Lorsqu'il est produit par paires, la masse du boson W peut être déterminée de deux façons différentes :

- Proche du seuil de production de paire de W , la masse et la largeur peuvent être obtenues à partir de la mesure de la section efficace totale de production de paires. Cette mesure est possible grâce à l'augmentation rapide de la section-efficace autour de 160 GeV et sa sensibilité à la masse ainsi qu'à la largeur du boson. Une fois l'énergie optimale déterminée, la masse peut être mesurée seule (à une énergie) ou simultanément avec la largeur (au à moins deux énergies) par comparaison de la section-efficace mesurée avec des templates MC. Tous les canaux de désintégration de la paire WW peuvent être utilisés dans cette mesure.
- L'état final de la collision e^+e^- est très propre et la cinématique de l'événement est complètement déterminée ; ainsi la masse invariante peut être reconstruite à partir des moments des produits de désintégration de la paire. La masse et la largeur du W sont ensuite extraites en ajustant la distribution de la masse invariante avec des templates MC. Cette méthode requiert beaucoup de statistique et est plutôt utilisée au-delà du seuil de production de paires. À FCC-ee, le niveau de statistique serait suffisant pour utiliser cette méthode à toutes les énergies. Seuls les canaux de désintégrations hadroniques et semi-leptoniques sont cependant utilisables pour cette mesure car lors des désintégrations purement leptoniques les quadri-vecteurs des deux neutrinos émis ne peuvent être reconstruits.

Contexte expérimental

HL-LHC et HGCAL

Le LHC (27 km) est le plus grand collisionneur de particules au monde. Il fait entrer en collisions des protons à 7 TeV (i.e. une énergie dans le centre de masse de 14 TeV) au coeur de quatre grandes expériences, dont le détecteur CMS, l'une de ses deux expériences générales. CMS est un détecteur cylindrique centré sur l'axe du faisceau qui mesure 15 m de diamètre, 28.7 m de long et pèse 14 t. À partir du point de collision, au centre du détecteur, les principaux sous-détecteurs sont : le trajectomètre, le ECAL, le HCAL, le solénoïde (4T) et le spectromètre à muon. Pour exploiter entièrement les capacités du LHC, le collisionneur va être amélioré pour produire dix fois plus de données qu'à l'heure actuelle. Cette phase (HL-LHC) commencera vers 2030. Augmenter la luminosité de la collision signifie aussi augmenter le nombre moyen de collisions par paquets de protons (pile-up) ainsi que le niveau de radiation au sein du détecteur. Pour maintenir d'excellentes performances, les détecteurs vont devoir être mis à niveau. Dans CMS, le bouchon du calorimètre va être remplacé par le HGCAL, un calorimètre regroupant les parties électromagnétique et hadronique, dont la structure est montrée sur la Figure C.1.

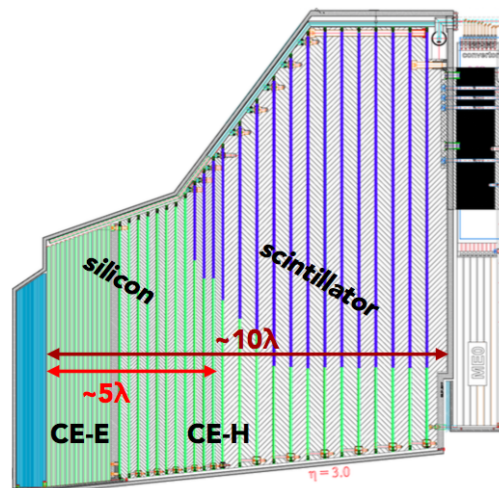


Figure C.1 – Coupe longitudinale (partie haute) de l'un des deux HGCAL. La partie électromagnétique (CE-E), la plus proche du point d'interaction, est suivie de la partie hadronique (CE-H)

Les capteurs en silicium (vert) sont disposés dans la région à plus fort taux de radiation et les scintillateurs (bleu) occupent la région à faible radiation. [85]

Il est composé de 50 plaques (couches) recouvertes de capteurs. Les couches CE-E sont composées intégralement de capteurs silicium et celles de CE-H sont des couches hybrides composées de capteurs silicium dans les régions à haut niveau de radiations (proche de l'axe du faisceau) et de scintillateurs ailleurs. Les capteurs silicium sont des hexagones de différentes tailles (0.52 et 1.18 cm²) et épaisseurs (120, 200 et 300 μm). Les scintillateurs sont des tuiles de plastique carrées dont la taille varie de 4 à 32 cm². Les caractéristiques des deux types de capteurs, sont imposées par le niveau de radiation.

Ce détecteur possèdera des segmentations longitudinale et transversale très fines, ainsi qu'une très bonne capacité de séparation temporelle, permettant d'identifier et reconstruire précisément les différentes particules en cas de fort pile-up.

FCC-ee et CLD

FCC est un projet post-LHC de 100 km qui serait intégré dans l'actuel complexe des faisceaux du CERN. FCC-ee, un collisionneur d'électrons-positrons à haute luminosité, serait l'éventuelle première étape d'un collisionneur de hadrons à 100 TeV, FCC-hh. FCC-ee commencerait à fonctionner vers 2040 et quatre programmes différents seraient suivis : au seuil de production du boson Z ($\sqrt{s} \sim 91$ GeV), au seuil de production d'une paire de W ($\sqrt{s} \sim 160$ GeV), au seuil de production du Higgs via la production de paires ZH ($\sqrt{s} \sim 240$ GeV) et au seuil de production d'une paire de top quarks ($\sqrt{s} \sim 350 - 365$ GeV). Toutes ces particules seraient produites à des quantités très importantes permettant d'étudier les interactions forte et électrofaible avec de très grande précisions. FCC-ee aurait deux expériences (potentiellement quatre), CLD et IDEA, au centre desquelles les leptons entreraient en collision avec un angle de 30 mrad pour limiter les rayonnements synchrotrons dans le détecteur.

Le détecteur CLD, utilisé dans cette étude, aurait une structure cylindrique composée de sous-détecteurs disposés dans le même ordre que ceux de CMS dans un champ magnétique homogène de 2T. Il mesurerait 12 m de diamètre, 10.6 m de longueur.

Simulation et reconstruction d'événements

Plusieurs logiciels ont été utilisés pour simuler la création de bosons W à partir des interactions e^+e^- et pp (événement) et leurs désintégrations. Ces pseudo-données sont ensuite traitées comme des données réelles et reconstruites en pseudo-données à l'aide de logiciels simulant le détecteur. Le logiciel de simulation MC utilisé pour générer les événements est Pythia, les logiciels de reconstruction utilisés dans cette étude sont les suivants.

Le logiciel CMSSW est l'outil de simulation complet du détecteur CMS basé sur Geant4. Il est utilisé pour simuler et reconstruire les données de CMS et peut-être utilisé avec des données réelles ou obtenues par simulation MC. Toutes les caractéristiques du détecteur y sont précisément implémentées.

Les particules sont reconstruites avec un algorithme (Particle-Flow (PF)) dont le principe est le suivant. Les traces des particules chargées et les amas de cellules collectant du signal dans les calorimètres (clusters) sont d'abord reconstruits. Les différents éléments sont ensuite connectés formant ainsi des blocs utilisés pour l'identification des particules. Les particules générées sont utilisées dans d'autres algorithmes de reconstruction pour créer les objets de la collision (jets et neutrino par exemple).

CMSSW est en cours d'évolution pour simuler des événements dans le HGCal. Le même PF est utilisé pour reconstruire les particules dans le HGCal. Pour l'instant, le moment des particules chargées est intégralement dérivé du moment de la trace, ce qui donne lieu à une détérioration de la résolution des jets lorsque le p_T augmente. Une implémentation en cours combinera les informations venant des traces et des clusters pour bénéficier de la résolution du détecteur de traces (à faible énergie) et des calorimètres (à haute énergie).

Le logiciel Delphes a également été utilisé pour simuler la désintégration $W \rightarrow l\nu$ à 13 TeV dans le détecteur CMS. L'algorithme de reconstruction des particules est basé sur celui de CMS. Après avoir vérifié la reconstruction du lepton et du recul par comparaison avec les distributions générées par CMSSW, les pseudo-données ainsi produites ont été utilisées dans l'étude de la reconstruction du recul décrite plus bas.

Pour l'étude de la masse à FCC-ee, l'interaction des pseudo-données à travers le détecteur CLD a été émulée par le simulateur heppy. Il s'agit d'un logiciel de simulation rapide qui a été créé pour l'étude des détecteurs de FCC-ee. L'algorithme de reconstruction des particules est basé sur celui de CMSSW. Les événements ont été intégralement reconstruits dans heppy. Les jets ont été reconstruits avec l'algorithme $ee-k_T$ (Durham), contraignant les particules reconstruites à former un nombre de jets imposé (quatre en canal hadronique et deux en semi-leptonique). Les leptons issus du W sont identifiés comme étant les leptons les plus énergétiques et les photons compatibles avec un photon FSR émis par le lepton lui sont associés. Enfin, le neutrino, indétecté, est associé à l'énergie manquante calculée à partir de la conservation du moment et de l'énergie de la collision.

Outil de simulation rapide pour le HGCal

Le HGCal est très précisément implémenté dans le logiciel CMSSW. Cependant, dans le but d'optimiser ses paramètres ou de générer un nombre important d'événements, il peut être nécessaire d'avoir recours à un logiciel de simulation rapide. Un logiciel de simulation rapide pour le HGCal (FastSim) a donc été implémenté en complément de la simulation complète de CMSSW (FullSim).

La FastSim a été développée au moment de la période de conception du HGCal, pendant laquelle la géométrie du détecteur avait été gelée à la version de 2016. Depuis, quelques paramètres géométriques ont évolué, notamment la nature des capteurs sur les couches.

La géométrie de la structure du HGCal est d'abord construite couche par couche et chaque particule générée est associée à la cellule correspondante. L'association particle-cellule a été optimisée grâce à un algorithme basé sur une structure de données en Quadtree. Cette structure permet de comparer efficacement chaque particule à une liste réduite de cellules plutôt qu'à la liste complète des cellules. Avec cette approche l'association se fait beaucoup plus rapidement (en $\mathcal{O}(\log(n))$ au lieu de $\mathcal{O}(n)$) et l'outil de simulation atteint un taux de génération de 2,6 kHz.

Dans les simulations, une part importante est dédiée à la simulation des particules à travers les calorimètres, la FastSim utilise donc une paramétrisation des gerbes électromagnétique et hadronique. Ces gerbes sont très précisément décrites dans la FullSim. Les paramétrisations ont donc été déterminées à partir des distributions longitudinales et transversales pour différentes particules.

La simulation des particules dans la structure a ensuite été rendue plus réaliste en dégradant la résolution en énergie du calorimètre. Dans un premier temps le nombre de particules générées dans la couche a été corrigé en prenant en compte son caractère Poissonien. Ensuite, le bruit électronique (extrait de la FullSim) a été ajouté aux cellules enregistrant un signal.

Le logiciel développé a ensuite été validé par comparaison avec des distributions obtenues avec la FullSim. La Figure C.2 montre les distributions de l'énergie reconstruite, du profil moyen longitudinal ainsi que l'évolution des rayons contenant 68% et 95% de l'énergie de la gerbe dans les différentes couches, pour un pion de 100 GeV avec les FullSim et avec la FastSim. Les mêmes vérifications ont été faites pour un électron et un photon générés à 50 GeV. À partir de ces distributions, on peut conclure que, pour les objets étudiés, la FastSim émule la FullSim avec un niveau acceptable si le but est d'optimiser des paramètres du HGCal.

Les changements de géométrie effectués depuis la validation du logiciel, n'ont eu que très peu d'impact sur les résultats de la FullSim. Ainsi bien que la grande flexibilité de la FastSim permettrait d'implémenter rapidement la nouvelle géométrie, aucune modification de celle-ci n'est nécessaire. Elle est donc considérée comme toujours valide et est en attente d'implémentation dans

le logiciel CMSSW.

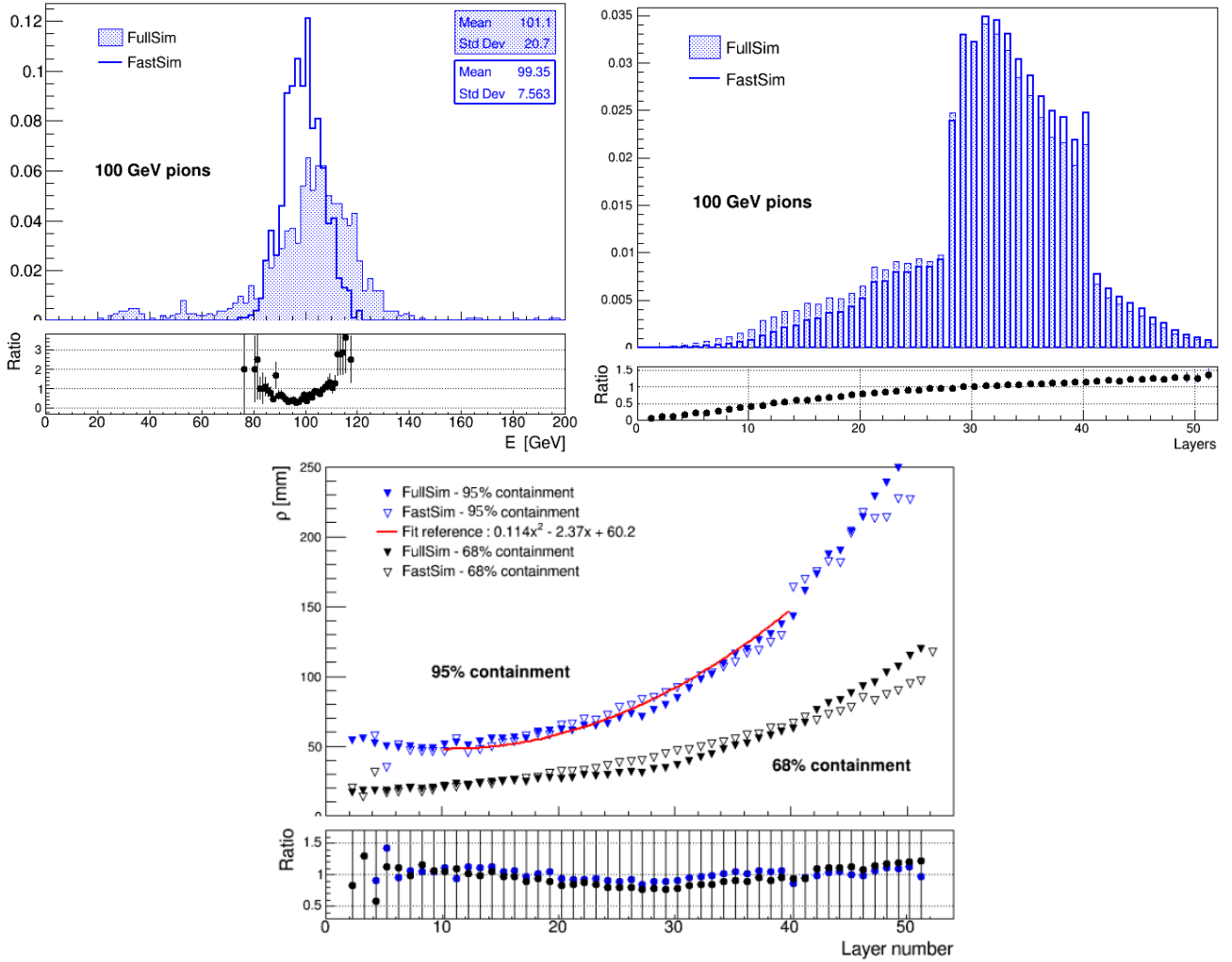


Figure C.2 – Comparaison des distributions obtenues avec la FastSim et la FullSim pour des pions générés à 100 GeV

Haut : énergie reconstruite de la particule. *Milieu*: profil moyen longitudinal dans les couches du HGCAL. *Bas*: évolution des rayons contenant 68% et 95% de l'énergie de la gerbe dans les différentes couches.

Mesure de la masse du boson W à CMS

Le boson W, produit dans les collisions hadroniques, est identifié à partir de sa désintégration leptonique uniquement. Cette désintégration est accompagnée du recul, reconstruit à partir de toutes les particules produites dans la collision sauf le lepton. La masse du boson W est reconstruite à partir des moments transverse du lepton, \vec{p}_T^l , et du recul dans le plan transverse, \vec{h} . \vec{p}_T^l étant précisément reconstruit, la précision sur la masse est donc directement corrélée à la précision de la mesure du recul. Cette précision dépend principalement de la définition utilisée pour décrire le recul ainsi que des effets du détecteur.

Dans sa définition traditionnelle, le recul est décrit par un vecteur à deux dimensions, égal et opposé

au moment du boson W . Comme il s'agit d'un objet non-local reconstruit à partir des particules de la collision (distribuées dans tout le détecteur), sa définition n'est pas triviale. Il existe deux modèles principaux:

- Le recul reconstruit à partir des particules reconstruites par PF. Bien que cette définition implique l'ensemble des particules reconstruites, elle est limitée par la contamination du pile-up.
- Le recul reconstruit à partir des traces des particules chargées issues du premier vertex. Cette définition ne prend pas en compte l'ensemble de l'événement mais est insensible à la contamination du pile-up et montre un bon accord entre les données et la simulation MC.

La définition impliquant les traces est robuste contre le pile-up, mais cette définition présente deux inconvénients : une limitation plus importante de l'acceptance et une perte de réponse. Sa résolution est également affectée par le fait de n'utiliser qu'une partie de l'événement. Une définition plus complète, basée sur des techniques de machine learning en utilisant une régression quantile multivariée a donc été utilisée.

La régression multivariée a pour but de prédire événement par événement une cible à partir de plusieurs paramètres la décrivant. La régression quantile est un estimateur plus robuste permettant de mieux décrire le lien entre les paramètres utilisés et d'écarter les éventuelles données erronées. Pour cela la médiane de la distribution de la cible mais aussi ses dispersions statistiques autour de deux quantiles (16% et 84% ici) sont estimées.

Ici, le recul n'a pas été directement pris pour cible dans la régression car il est préférable d'utiliser une cible présentant une stabilité d'un événement à l'autre et ayant une distribution peu étalée pour une convergence plus rapide de la régression. Les corrections aux paramètres du recul, magnitude, h , et direction, ϕ , définis par l'Équation C.2 où $true$ désigne le vrai recul, et TK le recul défini par les traces, ont donc été prises pour cible par la régression.

$$\begin{aligned} \ln(e_1) &= \ln\left(\frac{|h_{true}|}{|h_{TK}|}\right), \\ e_2 &= \phi_{true} - \phi_{TK}, \end{aligned} \tag{C.2}$$

Les paramètres qui ont été utilisés (liste non exhaustive) dans la régression dans le cas où le pile-up n'est pas inclus dans la simulation sont :

- le nombre de vertex,
- le nombre de jets,
- le nombre de traces,
- la densité d'énergie médiane,
- l'angle azimuthal, la sphéricité, le moment transverse et la magnitude du recul modélisé par : les traces, les particules reconstruites par le PF ainsi qu'en utilisant les particules neutres du PF,
- les paramètres régressés $\ln(e_1)$ et e_2

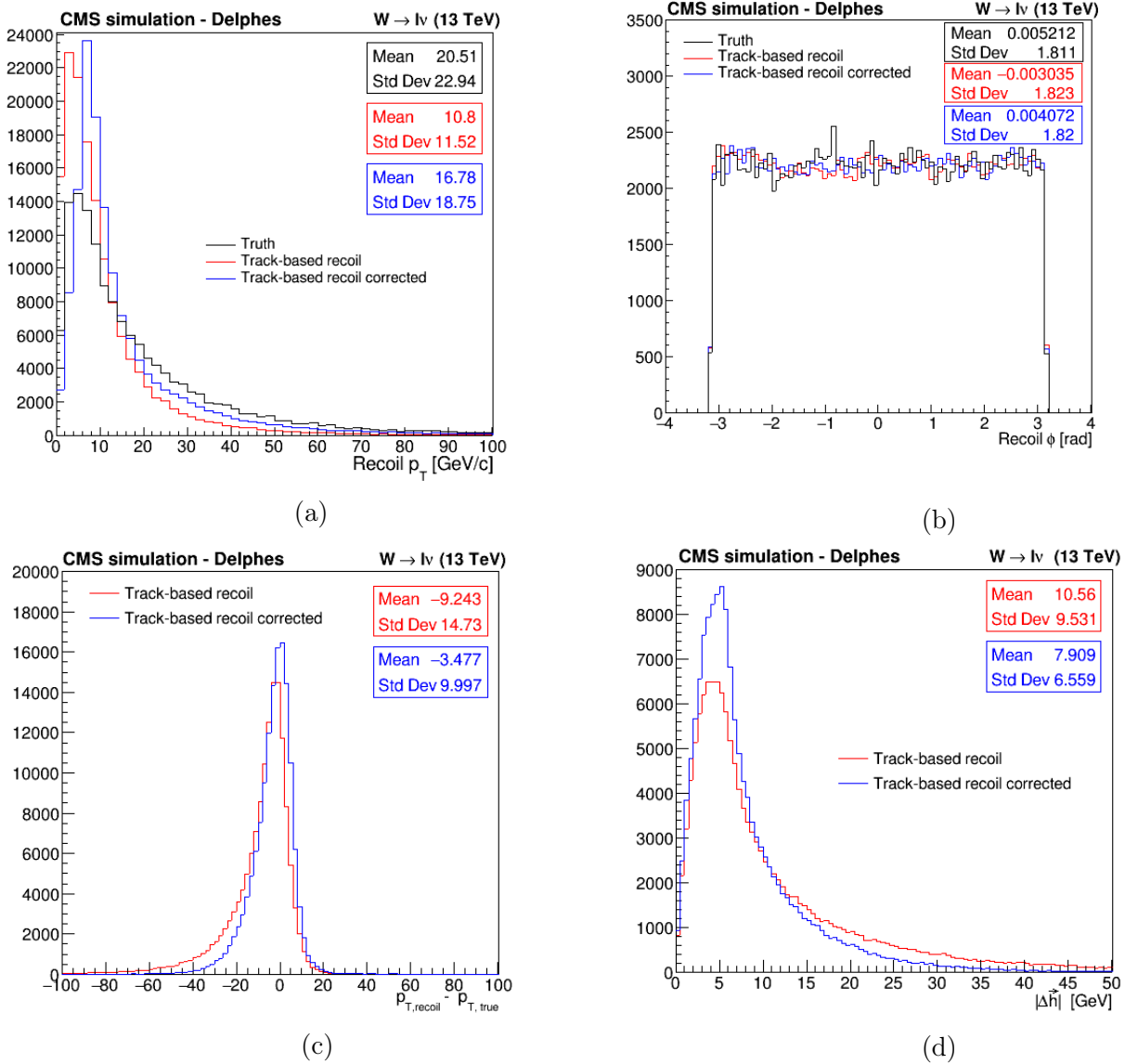


Figure C.3 – Corrections du recul défini à partir des traces en utilisant la régression quantile multivariée

Les figures (a) et (b) montrent l'amélioration des composantes du recul, la magnitude et la direction. La figure (c) compare le recul reconstruit au vrai recul avant et après corrections. La figure (d) montre l'amélioration de la résolution du recul. Le pile-up n'est pas simulé.

La Figure C.3 montre l'amélioration de la reconstruction du recul défini par les traces des particules chargées grâce à l'utilisation d'un grand nombre d'informations du détecteur.

Une étude en cours permettra d'étudier l'effet de l'acceptance, de la résolution et de la granularité du HGCal sur le recul ainsi reconstruit. La précision pouvant être atteinte sur la masse du W à HL-LHC pourra être évaluée.

Mesure de la masse du boson W à FCC-ee

Estimation de l'incertitude statistique

Dans cette étude de production de paires de bosons W dans les collisions leptoniques, la masse du W a été reconstruite directement à partir des produits de désintégration de la paire à toutes les énergies prévues à FCC-ee, 162,6 GeV, 240 GeV et 365 GeV.

Dans ce type de collision, l'énergie dans le centre de masse est mesurée très précisément. Les incertitudes attendues sur la masse et la largeur ont donc été estimées dans les canaux hadronique et semi-leptonique de désintégration en utilisant un fit cinématique contraint. Cette méthode est un processus itératif permettant varier des paramètres dans leurs incertitudes dans le but de minimiser la déviation entre leurs valeurs mesurées et fittées tout en répondant à un certain nombre de contraintes. La méthode des multiplicateurs de Lagrange a été utilisée pour résoudre ce problème et la fonction minimisée est ¹ :

$$L = \Delta \mathbf{y}^T V^{-1} \Delta \mathbf{y} + 2 \sum_{i=1}^4 \lambda_i f_i(\mathbf{y}, \mathbf{a}), \quad (\text{C.3})$$

où \mathbf{y} (\mathbf{a}) est le vecteur contenant les paramètres mesurés (non mesurés) à varier, V est la matrice de covariance contenant les incertitudes sur ces paramètres, λ_i correspondent aux multiplicateurs de Lagrange et f_i sont les contraintes à satisfaire.

Dans cette étude les objets utilisés dans le fit cinématique sont les moments des jets, le lepton et le neutrino des canaux hadronique et semi-leptonique. Ils ont été paramétrisés en fonction des paramètres à varier pour répondre aux contraintes. Les paramètres utilisés dans la description de ces moments sont:

- Jets : le coefficient de mise à l'échelle $\alpha = E_j/E_i$ où E_i correspond à l'énergie mesurée et E_j à l'énergie corrigée, la vitesse ($\log(\beta\gamma)$) et les angles polaire et azimuthal. Tous ces paramètres sont mesurés;
- Lepton : seule l'énergie mesurée du lepton est utilisée;
- Neutrino : l'énergie manquante ainsi que la direction manquante. Ces paramètres ne sont pas mesurés.

La matrice de covariance V contient les incertitudes sur les paramètres mesurés. Elle a été prise diagonale en supposant une absence de corrélation de ces paramètres.

Les contraintes imposées dans le fit sont la conservation de l'énergie et du moment (fit 4C pour le canal hadronique et 1C pour le canal semi-leptonique). Pour une meilleure reconstruction de la masse l'égalité des masses des deux W a également été ajoutée (fit 5C pour le canal hadronique et 2C pour le canal semi-leptonique).

Dans le cas du canal hadronique, la masse a aussi été estimée par conservation de l'énergie et du moment des produits de désintégration. Cette méthode est inutilisable en canal semi-leptonique car le neutrino est déjà reconstruit selon cette contrainte. La Figure C.4 montre la plus petite des

¹Les caractères en gras sont des vecteurs

masses du canal hadronique ainsi que la masse leptonique du canal semi-leptonique reconstruites à 240 GeV en utilisant les différents estimateurs présentés ci-dessus. La masse obtenue directement à partir des données brutes (raw mass) est donnée pour la comparaison.

Les incertitudes sur la masse et la largeur ont été estimées via un fit binné du maximum de vraisemblance à partir des masses invariantes reconstruites. Dans les deux canaux le fit le plus contraint (5C/2C) donne la meilleure incertitude statistique. Pour chaque énergie, l'incertitude estimée sur la masse est en dessous du niveau du MeV.

Étude de l'effect des interactions dans l'état final du canal hadronique

À LEP, la mesure de la masse du boson W était limitée par l'incertitude statistique. À FCC-ee, avec une précision statistique en dessous du niveau du MeV à toutes les énergies, cette mesure serait dominée par l'incertitude systématique. La plus large source d'incertitude systématique à LEP était due aux effets de QCD (FSI) entre les produits de désintégrations du canal hadronique : CR et BEC.

Les CR ont été simulées en utilisant les modèles SKI et SKII, deux scénarios implémentés dans Pythia lors de l'étude des CR à LEP. Un seul modèle permet de décrire les BEC pour tous les types de collisions.

À ALEPH, une des méthodes utilisée pour réduire cette incertitude consistait à rejeter toutes les particules en dehors d'un cône centré sur l'axe du jet ayant un angle d'ouverture de 0.4 radian lors de la construction des jets. Ce traitement permettait de supprimer les particules à faible impulsion, responsables de la modification de l'angle du jet sous l'effet des FSI. Le même cône a été utilisé dans cette étude. La perte d'information engendrée par la suppression de ces particules va avoir pour effet de détériorer la distribution de la masse du W et par conséquent l'incertitude statistique. Les niveaux de détérioration de la masse et de son incertitudes statistiques sont indiqués dans le Tableau C.1.

Il est cependant attendu que ces pertes soient compensées par la diminution de l'incertitude systématique. Il a été estimé qu'en présence de CR et de BEC, le cône devrait diminuer l'incertitude systématique de 50%. Les FSI ajouteront une incertitude supplémentaire sur l'incertitude statistique, en plus des détériorations engendrées par le cône sur les incertitudes statistiques indiquées dans le Tableau C.1. Cependant le niveau de perte a été considéré comme acceptable étant donnée la correction de l'incertitude systématique sur la masse.

Différentes études de la précision attendue sur la masse du boson W aux futures expériences ont été présentées.

Un outil flexible, fiable et rapide a été développé en complément de la simulation complète de CMS

Table C.1 – Détérioration de la masse et de son incertitude statistique due à l'ajout d'un cône de sélection sur les jets

| \sqrt{s} GeV | M_W | $\sigma_{M_W,stat}$ |
|----------------|-------|---------------------|
| 162,6 | 2,9 % | % |
| 240 | 6,7 % | 10% |
| 365 | 16,9% | 15% |

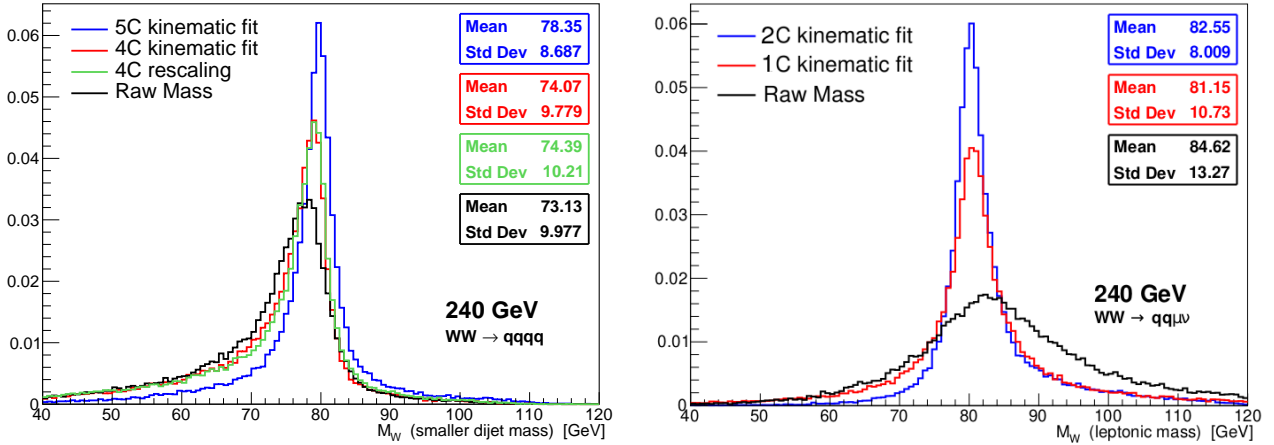


Figure C.4 – Masse invariante de la plus petite des masses du canal hadronique (gauche) ainsi que la masse leptonique (droite) du canal semi-leptonique reconstruites à 240 GeV en utilisant les différents estimateurs.

pour l’optimisation des paramètres du détecteur HGCal. Bien que performant, plusieurs aspects pourraient être améliorés comme une description plus complète du développement des gerbes électromagnétiques dans la structure du HGCal, ou encore l’implémentation d’éléments physiques tels que le champ magnétique ou encore le pile-up.

En collision hadronique la mesure précise de la masse, dépend de la reconstruction du recul. Une nouvelle définition de cet objet, basée sur des méthodes de Machine Learning, a été développée pour améliorer sa mesure. Une étude en cours permettra d’évaluer l’effet des paramètres du HGCal sur cette mesure.

La masse du W à FCC-ee a été reconstruite via un fit cinématique dans les canaux hadronique et semi-leptonique de désintégration de la paire de W à 162,6 GeV, 240 GeV et 365 GeV. L’incertitude statistique obtenue sur la masse avec cette méthode est de l’ordre du MeV pour les deux modes de désintégrations et pour toutes les énergies. La mesure serait donc dominée par les effets systématiques. Une étude de l’incertitude due aux effets de QCD dans le canal hadronique, la plus grande incertitude systématique à LEP, a été menée. Il a été estimé que cette incertitude pourrait être réduite de 50% en utilisant un cône lors/ de la reconstruction des jets. Ce cône pourrait avoir un effet sur l’incertitude statistique mais il a été conclu que la diminution de l’incertitude systématique balancerait largement la dégradation de l’incertitude statistique.

Titre: Calorimétrie et mesure de la masse du W pour les futures expériences

Mots clés: Boson W, HGCal, FCC-ee, simulation rapide, recul, incertitude statistique

Résumé: La mesure précise de la masse du boson W est une composante essentielle pour tester la cohérence globale du Modèle Standard, dont une défaillance pourrait mettre à jour la nouvelle physique. Avec des millions de bosons W prévus, les futures expériences seront des usines à bosons permettant de mesurer sa masse avec une précision inégalée. La mesure de la masse du W est discutée dans le contexte de deux expériences : l'amélioration du détecteur CMS au LHC, le HL-LHC, avec un nouveau bouchon calorimétrique, le HGCal, et à un détecteur pour FCC-ee, un projet circulaire post-LHC.

En collision proton-proton, la mesure précise de la masse du boson W dépend de la précision de la mesure du recul hadronique. Cette précision dépend principalement de la définition du recul et des effets induits par le détecteur. La définition du recul est améliorée par des méthodes de machine learning, en utilisant une régression quantile multivariée. Les effets de la granularité, de l'acceptance et de la résolution du HGCal sur le recul sont évalués. Cette étude donne une estimation de la précision sur la masse du

boson W qui pourrait être atteinte au HL-LHC. Avant d'estimer les effets de la performance du détecteur sur le recul, la géométrie complète et les paramètres du détecteur ont été ajustés et optimisés. Un fidèle outil de simulation rapide, complément au logiciel de simulation complet de CMS, implémenté pour mener cette étude, est présenté.

En collision électron-positron, la masse du boson W peut être déterminée à partir du produit de désintégration de la paire de W. Les incertitudes statistiques sur la masse et la largeur sont estimées en utilisant la méthode du fit cinématique, dans les canaux de désintégration hadronique et semi-leptonique à 162,6 GeV, 240 GeV et 365 GeV. Atteignant une incertitude statistique inférieure au niveau du MeV/c^2 à toutes les énergies et pour les deux canaux, la mesure de la masse du W devient limitée par les incertitudes systématiques. Un traitement pour réduire l'incertitude systématique engendrée par les effets QCD, la plus large source d'incertitude systématique à LEP, et son impact sur l'incertitude statistique sont également étudiés.

Title: Calorimetry and W mass measurement for future experiments

Keywords: W boson, HGCal, FCC-ee, Fast simulation, recoil, statistical uncertainty

Abstract: The precise measure of the W boson mass is an essential input to a crucial test of the overall consistency of the Standard Model, whose failure might reveal the emergence of new physics. With millions of W bosons expected, future experiments will be W boson factories allowing the measurement of the W mass with unparalleled precision. The W mass measurement is discussed in the context of two experiments: the upgrade of CMS at the LHC, the HL-LHC, with a new endcap calorimeter, the HGCal, and a detector for the FCC-ee, a circular post-LHC project.

In proton-proton collisions, the precise measurement of the W mass relies on a precise measurement of the hadronic recoil. Its accurate measurement mainly depends on its definition model and detector effects. The recoil definition is improved with machine learning techniques, using a multivariate quantile regression. The effects of the HGCal granularity, acceptance and resolution on the recoil reconstruction are evaluated. This study gives an estimate of the precision that

might be reached on the W mass measurement at HL-LHC. Before evaluating the effect of the detector performance on the recoil, the full geometry and parameters had to be tuned and optimised. An accurate fast simulation tool, complement to the full CMS simulation, implemented to undertake such a study, is presented.

In electron-positron collisions, the W mass can be determined from the W-pair decay products. The statistical uncertainties on the W mass and width are estimated using a kinematic fit technique in the hadronic and semi-leptonic channels at 162.6 GeV, 240 GeV and 365 GeV. Reaching a statistical precision below the MeV/c^2 level at all energies for both channels, the W mass measurement becomes limited by the systematic uncertainties. A treatment to reduce the systematic uncertainty coming from QCD effects, the largest source of systematic uncertainty at LEP, and its impact on the statistical uncertainty are also studied.

